

Compositional and Mechanistic Studies of Cu-zeolites for the Direct Activation of Lower Alkanes

Dissertation for the Degree of Philosophiae Doctor

KAROLINE KVANDE



Department of Chemistry

Faculty of Mathematics and Natural Sciences

University of Oslo

May 2023

© **Karoline Kvande, 2023**

*Series of dissertations submitted to the
Faculty of Mathematics and Natural Sciences, University of Oslo
No. 2633*

ISSN 1501-7710

All rights reserved. No part of this publication may be
reproduced or transmitted, in any form or by any means, without permission.

Cover: UiO.

Print production: Graphic Center, University of Oslo.

«Det har jeg aldri gjort før,
så det klarer jeg helt sikkert!»

- Pippi Langstrømpe

Acknowledgements

The work presented in this thesis has been carried out as a part of work package 5 (WP5) in the iCSI (industrial Catalysis Science and Innovation) Centre for Research-based Innovation, which receives financial support from the Research Council of Norway under contract no. 237922. The project was performed at University of Oslo with a 6-month research stay at the University of Turin. This PhD project has been an invaluable experience that has been both very rewarding and challenging at times. In the end, I am left with a toolbox filled with important skills, both scientific and personal, that I bring with me for my future endeavors.

I would like to thank my supervisor, Prof. Stian Svelle, for giving me this opportunity and for supporting and challenging me along the way. I would also like to thank you, Stian, for your valuable feedback on the papers, which has really helped me grow as a writer. Thank you to my co-supervisors, Dr. Pablo Beato, Prof. Elisa Borfecchia, and Prof. Unni Olsbye, for your continued support, help, and feedback on the different experiments and papers. I am grateful to Prof. Silvia Bordiga for always providing invaluable feedback on the spectroscopy experiments and for hosting me at the University of Turin for 6 months. Your dedication and warmth is inspiring and made my stay in Turin truly enjoyable, both scientifically and personally. A special thanks to Stian, Unni, Kine, Bjørn, Simon, Chris, and Sebastian for reading and providing feedback on various parts of this thesis. Your contributions were truly appreciated.

I am thankful to all the people of the iCSI WP5 team for the discussions and support along the way. A special mention to the Oslo team, Bjørn and Sebastian, for always being eager to chat about our findings. Gabriele and Matteo, I thank you for your invaluable help during my stay in Turin, all the fun during my time there, and for sharing my frustrations towards equipment like the “Shitty oven”. Bea and Elisa, I sincerely appreciate your work on the XAS data analysis and for making my stays at the synchrotron so enjoyable.

Moses Mawanga, I would like to thank you for performing the microcalorimetry experiments and for the nice discussions on that paper.

I am so grateful that I have gotten to know so many great people during my time at the Chemistry department. A special thanks to the “Gin-appreciation Alliance”. You provided much-needed fun during the Covid shutdown and in the years after when we spread across the world. I would also like to thank the whole Catalysis group for all the fun times and friendship I have gained over the years. I have loved the eagerness to knowledge-sharing within the group, the long lunch discussions, the coffee breaks and all the after-work fun. Thank you!

Inga, my dear German friend, thank you for bringing so much fun to my time at the University. I am really going to miss talking about life and music, our way-to-long coffee dates and the too-few game nights (but there will be more!).

I also want to thank you, Kine, for always being there and all the fun times we’ve had ever since we started our B.Sc. We made it! Your passion for the things you enjoy and believe in is such an inspiration, and I am so happy to call you my maid of honor.

My dear friends, Kari, Ina, Hilde, Olav, and Jeanette, thank you for always cheering me on, and all the talks and laughs! I am so lucky to have you all.

I want to express my deepest gratitude towards my family. I could not have chosen a better. I have cherished all your support and happiness for my accomplishments. It means so much to me, and it has given me the support and foundation I need to reach for my present and future goals.

Above all, I need to thank my best friend and husband, Simon. You have been my rock through it all. My person to discuss, cry, and laugh with over all the little (and big) things in life. I am so thankful to have you by my side. Always.

My dear nieces and nephews: Liv, Ingvild, Emma, Caleb, Matheo, Magnus, and Elise. This thesis is for you. I hope you will always follow your dreams.

Abstract

Direct activation routes for lower alkanes have been explored over the last decades as more sustainable solutions for the production of key building blocks to use in the chemical industry. Production of methanol from methane (MTM) is one such reaction route that has received a lot of attention. In this thesis, we have explored a stepwise, stoichiometric reaction protocol for MTM. With such a reaction route, the products are hindered from over-oxidization due to the complete separation of gas-phase oxygen and reactants/products. Despite the high product selectivity seen with this reaction, the process still suffers from extensive reaction times and low fraction of active Cu-sites that coupled with a long reaction time gives low overall methanol production rate. These drawbacks can be addressed by seeking to understand more about the nature of activated Cu_xO_y -species within the zeolite framework and the mechanism of the reaction. To that end, combined with various characterization and spectroscopy techniques, the topic of this thesis has been to investigate hitherto unexplored zeolite frameworks and different Cu exchange methods in attempts to understand more about the structure–activity relationships in the MTM reaction. The results indicate that the Cu speciation and environment within the framework have a significant impact on methanol productivity. To shed more light on the behavior of the Cu_xO_y -sites during the C–H activation step, X-ray absorption spectroscopy coupled with temperature-programmed reaction experiments in different reducing atmospheres (methane, ethane, CO) was performed. The findings indicate that the consumption of reactant can be directly linked to the reduction of Cu. Further, the reactivity of other alkanes in this established reaction route for MTM was studied. The fundamental study on ethane activation demonstrated that ethane can be selectively converted to ethylene already at 150 °C over Cu-mordenites using the same cyclic protocol. Our systematic study of the reaction route has led to a broader understanding of the nature of the Cu species and their role in C–H activation.

Sammendrag

På veien mot en fungerende sirkulær økonomi er vi nødt til å utnytte de råmaterialene vi har på en renest mulig måte. Naturgass er sett på som et overgangsmateriale til fornybare ressurser i energiproduksjon, da metan, hovedkomponenten i naturgass, brenner renere og har en høyere energitetthet enn alternativer som kull eller større hydrokarboner. Ytterligere er naturgass en potensiell kilde til å danne viktige byggesteiner som trengs i kjemisk industri. I tillegg til metan består naturgass hovedsakelig av andre lave alkaner som etan og propan. Alkaner er lite reaktive, blant annet på grunn av sterke C–H bindinger, og dagens eksisterende metoder for å utnytte alkaner er energikrevende og kostbare. Dette gjør det vanskelig å prøve å utnytte naturgass på avsidesliggende steder. En følge av dette er at naturgass som kommer opp som et biprodukt av for eksempel oljeproduksjon ofte brennes av til potente drivhusgasser som CO₂ og H₂O i stedet for å bli utnyttet. Dersom vi hadde klart å funksjonalisere alkanene i naturgass til byggesteiner i kjemisk industri på en måte som krever mindre energi enn dagens metoder, ville vi kunne utvide bruksområdet for naturgass parallelt med at vi forhindrer store utslipp av CO₂ til atmosfæren. En måte som er foreslått er å omdanne metan til metanol (CH₃OH). Metanol er et viktig startmateriale for produksjon av et arsenal av forbruksvarer slik som medisiner, plastikk og drivstoff. I tillegg er metanol væske ved romtemperatur som vil senke kostnaden med å frakte produktet fra avsidesliggende steder. I denne avhandlingen har vi jobbet med en stegvis, støkiometrisk metode for å direkte konvertere metan til metanol (MTM) over kobberfylte zeolitter som er oksidert med oksygen. I MTM vil reaktanter og produkter være forhindret fra å interagere, noe som øker selektiviteten mot metanol da vi forhindrer metanol fra å reagere videre med oksygen. Noen av ulempene med denne reaksjonen så langt er at lang reaksjonstid og få aktive seter fører til lav produksjonsrate av metanol. For å utvikle og forstå reaksjonen bedre er vi nødt til å forstå mer om blant annet hvordan de oksiderte

kobbersetene ser ut. I tillegg bør vi forstå mer om hvordan kobbersetene endrer seg underveis i reaksjonen, samt finne undersøkende metoder som gir nytt lys på den totale reaksjonsmekanismen. Vi har i denne avhandlingen angrepet problemstillingen fra tre forskjellige perspektiver. Først, så kombinerte vi forskjellige karakteriserings- og spektroskopiteknikker for å undersøke materialer og synteseteknikker som tidligere har vært lite testet i MTM for å finne sammenhenger mellom struktur og aktivitet i reaksjonen. Resultatene fra dette indikerte at miljøet rundt kobbersetene i zeolitten og deres spesifikke sammensetning har en stor påvirkning på metanolproduksjonen. Videre forsøkte vi å se næyere på hvordan kobbersetene endret seg når de blir utsatt for alkaner (CH_4 og C_2H_6) eller andre oksiderende materialer (CO). For å se på kobbersetene, ble røntgen absorpsjonsspektroskopi tatt i bruk. Dette ble gjort samtidig som vi utsatte de kobberholdige zeolittene for reaktantene under en temperaturøkning, noe som ga en indikasjon på hvor sterk interaksjonen mellom setene og reaktantene var. Fra dette forsøket lærte vi blant annet at interaksjonen med reaktantene og kobbersetene er direkte koblet sammen med reduksjon av kobber fra oksidasjonstall 2+ til 1+. Til slutt undersøkte vi hvordan et annet alkan, etan (C_2H_6), ville reagere i en lignende reaksjonsprotokoll for å utvide horisonten basert på den etablerte litteraturen innenfor MTM reksjonen. Denne fundamentale studien viste at etan kan selektivt funksjonaliseres over kobbersetene ved dannelse av en dobbeltbinding slik at vi danner eten (C_2H_4). Eten, er på samme måte som metanol, et veldig viktig startmateriale for kjemisk industri, og brukes spesielt i dannelse av polyetylen (plastikk). Denne studien har blant annet utvidet bruksmulighetene til kobberholdige zeolitter og gitt oss fornyet innsikt i de spesifikke stegene underveis i C–H aktiveringsreaksjoner. Oppsummert så har vi i denne avhandlingen tilført litt mer forståelse til C–H aktiveringsreaksjoner som i lengden forhåpentligvis kan utnyttes for å hjelpe samfunnet nærmere en sirkulær økonomi.

List of Publications

- I. **Comparing the Nature of Active Sites in Cu-loaded SAPO-34 and SSZ-13 for the Direct Conversion of Methane to Methanol.** Karoline Kvande, Dimitrios K. Pappas, Michael Dybala, Carlo Buono, Matteo Signorile, Elisa Borfecchia, Kirill A Lomachenko, Bjørnar Arstad, Silvia Bordiga, Gloria Berlier, Unni Olsbye, Pablo Beato and Stian Svelle, *Catalysts*, 2020, 10, 191.
- II. **Microcalorimetry on Cu-MCM-22 reveals structure-activity relationships for the methane-to-methanol reaction.** Karoline Kvande, Moses Mawanga, Sebastian Prodinge, Bjørn Gading Solemsli, Jia Yang, Unni Olsbye, Pablo Beato, Edd Anders Blekkan, and Stian Svelle, *In peer-review at Industrial & Engineering Chemistry Research (I&EC)*.
- III. **Copper-zeolites prepared by solid-state ion exchange - characterization and evaluation for the direct conversion of methane to methanol.** Karoline Kvande, Sebastian Prodinge, Fabian Schlimpen, Pablo Beato, Patrick Pale, Stefan Chassaing, Stian Svelle, *Topics in Catalysis*, 2022, DOI: 10.1007/s11244-022-01763-7
- IV. **Understanding C-H activation in light alkanes over Cu-MOR zeolites by coupling advanced spectroscopy and temperature-programmed reduction experiments.** Karoline Kvande, Beatrice Garetto, Gabriele Deplano, Matteo Signorile, Bjørn Gading Solemsli, Sebastian Prodinge, Unni Olsbye, Pablo Beato, Silvia Bordiga, Stian Svelle, and Elisa Borfecchia. *In peer-review at Chemical Science*.
- V. **Cu-loaded zeolites enable the selective activation of ethane to ethylene at low temperatures and pressure.** Karoline Kvande, Sebastian Prodinge, Bjørn Gading Solemsli, Silvia Bordiga, Elisa Borfecchia, Unni Olsbye, Pablo Beato, and Stian Svelle, *ChemComm*, 2023, DOI: 10.1039/D3CC00948C

The Author's Contributions

- I. Planning and acquiring activity tests of samples at higher CH₄ temperature, Analysis/Interpretation of the high CH₄ temperature test results, and CH₄-TPR data. The author performed the visualization of all figures and tables. Writing – original draft + review & editing based on feedback from co-authors, Submitted to journal, and performed major changes after review.

- II. Cu-exchange of the zeolites, Investigation/acquisition of activity testing, SEM images, XRD collection (of Cu-exchanged zeolites), N₂-physisorption, CO-adsorption FT-IR, n-Propylamine TPD, XAS, and TGA, Analysis/interpretation of the acquired data except for n-Propylamine TPD, Strong involvement in the interpretation of the microcalorimetry data, Participated in the XAS synchrotron campaign, Visualization of all figures and tables, Writing – original draft + review & editing based on feedback from co-authors, Submitted to the journal.

- III. Investigation/acquisition of MTM activity and CH₄-TPR experiments, pXRD measurements, and CO-adsorption FT-IR experiments, Analysis/interpretation of all data. Visualization of figures and tables, Writing – original draft + review & editing based on feedback from co-authors, Submitted to journal and performed major changes after review.

- IV. Investigation/acquisition and analysis of UV-vis CH₄-TPR and FT-IR CO-TPR, Acquisition of synchrotron beam time. Synchrotron experiment planning and administration. XAS data acquisition at the synchrotron campaign. Discussing and interpreting the XAS results. Visualization of figures and tables related to MS data, UV-vis, and FT-IR results, Writing – original draft + review & editing after feedback from co-authors, Submitted to the journal.
- V. Conceptualization of the experiment, Built/redesigned the test setup needed for activity testing, performed the activity testing and FT-IR spectroscopy measurements. Ion exchanged SiO₂ and SiO₂/Al₂O₃, Analyzed/Interpreted all data. Visualization of figures and tables, Writing – original draft + review & editing based on feedback from co-authors, Submitted to journal and performed major changes after review.

Publications not included in the thesis

- i. **Advanced X-ray absorption spectroscopy analysis to determine structure-activity relationships for Cu-zeolites in the direct conversion of methane to methanol.** Karoline Kvande, Dimitrios K Pappas, Elisa Borfecchia and Kirill A Lomachenko., *ChemCatChem*, 2020, 12, 2385-2405.

- ii. **Influence of Cu-speciation in mordenite on direct methane to methanol conversion: multi-technique characterization and comparison with NH₃ selective catalytic reduction of NO_x.** Dimitrios K Pappas, Karoline Kvande, Maria Kalyva, Michael Dyballa, Kirill A Lomachenko, Bjørnar Arstad, Elisa Borfecchia, Silvia Bordiga, Unni Olsbye, Pablo Beato and Stian Svelle., *Catal. Today*, 2021, 369, 105-111

- iii. **Synthesis–Structure–Activity Relationship in Cu-MOR for Partial Methane Oxidation: Al Siting via Inorganic Structure-Directing Agents.** Sebastian Prodinger, Karoline Kvande, Bjørnar Arstad, Elisa Borfecchia, Pablo Beato and Stian Svelle., *ACS Catal.*, 2022, 12, 2166-2177

List of Conference Contributions

- i. *Direct Conversion of Methane to Methanol – A More Sustainable Solution.*
Poster Presentation at «PhD Day at UiO», November 2019.
- ii. Direct methane to methanol conversion: comparing the activity of Cu-SAPO-34 and Cu-SSZ-13. Karoline Kvande, **Oral Presentation** at Norwegian Catalysis Symposium, December 2019.
- iii. *Fight for a better future.* Karoline Kvande. **Video Contribution** to “Kjemi Grand Prix”, a popular science competition at the Department of Chemistry, January 2021.
- iv. *Methane to methanol conversion over Cu-zeolites – structure performance relationships,* Karoline Kvande, Dimitrios K. Pappas, Michael Dybala, Elisa Borfecchia, Andrea Martini, Silvia Bordiga, Pablo Beato and Stian Svelle. **Virtual Oral Presentation** at “8th Conference of the Federation of European Zeolite Associations (FEZA 2021)”, July 2021.
- v. *Direkte konvertering av metangass – en mer bærekraftig løsning for industrien.* Karoline Kvande. **Virtual Oral Presentation** at “Faglig Pedagogisk dag”, a National Teachers Day at the Department of Chemistry, November 2021.
- vi. *Reducing flaring and emissions of methane by creating everyday products.* Karoline Kvande. **Oral Pitch** at BI Green Growth Conference, May 2022.

- vii. *Cu-loaded mordenites for the activation of ethane to ethene in a stepwise, cyclic conversion protocol.* Karoline Kvande, Silvia Bordiga, Pablo Beato, Stian Svelle. **Oral Presentation** at the 19th Nordic Symposium on Catalysis, Espoo, June 2022.
- viii. *Employing TPR to describe activity differences in the Methane-to-Methanol reaction over two different Cu-MOR.* Karoline Kvande. **Virtual Oral Presentation** at International Symposium on Heterogeneous and Homogeneous Catalysis. June 2022.
- ix. *Structural and mechanistic investigations of Cu_xO_y - sites in zeolites and their role in the direct activation of lower alkanes.* Karoline Kvande, **Oral Presentation** at Norwegian Catalysis Symposium, December 2022.

Table of Contents

Acknowledgements	iii
Abstract.....	vii
Sammendrag.....	ix
List of Publications.....	xiii
The Author's Contributions	xv
Publications not included in the thesis	xix
List of Conference Contributions.....	xxi
List of abbreviations	xxix
1. Introduction.....	1
1.1. C–H Activation	4
1.1.1. C–H Activation of Methane.....	7
1.2. Direct Methane to Methanol Conversion	9
1.3. Zeolites.....	12
1.3.1. Brønsted Acid Sites and Ion Exchange	13
1.3.2. Zeolites Applied in the Present Study	15
2. MTM over Cu-exchanged Zeolites.....	21
2.1. Status of the Field	25
2.1.1. Cu-Speciation.....	25
2.1.2. Effects from Zeolite Synthesis and Ion Exchange	31
2.1.3. Reaction Mechanism.....	35
2.1.4. Structure-Reducibility Relationships	36
2.1.5. Co-Feed Studies.....	38
2.1.6. Open Questions.....	39
2.2. Ethane Activation	41
3. Experimental Methods.....	45
3.1. Material Preparation	45
3.1.1. Ion Exchange.....	46
3.2. Physicochemical Characterization	47
3.3. Performance Testing	51
3.4. Microcalorimetry (NH ₃ and CH ₄)	54

3.5.	Temperature-programmed Desorption (TPD).....	55
3.6.	CH ₄ -Temperature-programmed Reduction (TPR)	56
3.7.	Fourier Transform Infrared (FT-IR) Spectroscopy	57
3.8.	Resonance Raman (rRaman) Spectroscopy	58
3.9.	<i>In situ</i> X-ray Absorption Spectroscopy (XAS)	59
	Synopsis of Results	63
4.	Searching for Structure-Activity Relationships.....	63
4.1.	SAPO-34 vs SSZ-13.....	65
4.1.1.	Utilizing Spectroscopy to Investigate the Cu-Speciation.....	65
4.1.2.	Comparing the CH ₄ Consumption.....	68
4.1.3.	Direct Methane to Methanol Conversion	69
4.2.	MCM-22: An Unexplored Zeolite Framework for MTM.....	73
4.2.1.	FT-IR Spectroscopy Provide Insight on the Cu-Speciation.....	74
4.2.2.	NH ₃ -Adsorption Microcalorimetry	77
4.2.3.	The effect of Cu on Framework Acidity	81
4.3.	Evaluating Cu-zeolites Prepared by SSIE for MTM.....	85
4.3.1.	Performance Studies in the MTM Reaction.....	85
4.3.2.	Investigating the Reducibility of the Samples	87
5.	C–H Activation: Understanding the Cu-Speciation	93
5.1.	<i>In situ</i> XANES TPR: Finding Spectroscopic Fingerprints of Different Cu-Species.....	94
5.2.	Coupling Cu ^{II} Reduction with Reactant Consumption and Product Formation	98
5.3.	Complementary <i>in situ</i> UV-vis TPR Experiments	101
5.4.	Confirming the Formation of Cu ^I -CO with <i>in situ</i> FT-IR Spectroscopy Measurements.....	103
6.	C ₂ H ₆ Activation	107
6.1.	C–H Activation in a Stepwise Reaction Protocol.....	108
6.2.	Screening of the Material Properties	109
6.3.	Mechanistic Insight from FT-IR Spectroscopy	111
6.4.	Reaction Pathways	112
6.5.	Elaborating on the Cu-oxo Site Requirements	114

6.6. Systematic Study of the Reaction Parameters	116
7. Conclusions and Perspectives.....	121
7.1. Cu Speciation.....	121
7.2. Confinement and Acidity Effects	123
7.3. Unlocking Activity Through Structural Insight.....	126
7.4. C–H Activation	128
8. Suggestions for Further Work.....	129
References.....	131
APPENDIX.....	151

List of abbreviations

BET	Brunauer–Emmett–Teller
BSE	Backscattered Electrons
CCD	Charge-Couple Device
CHA	Chabazite
D6R	Double 6-ring
DFT	Density Functional Theory
EDH	non-oxidative Dehydrogenation of Ethane
EDX	Energy-Dispersive X-ray spectroscopy
EFAI	Extra-Framework Aluminium
EPR	Electron Paramagnetic Resonance
ERI	Erionite
ESRF	European Synchrotron Radiation Facility
ETE	Ethane-to-Ethylene
EXAFS	Extended X-ray Absorption Fine Structure
FAU	Faujasite
FCC	Fluid Catalytic Cracking
FER	Ferrierite
FID	Flame Ionization Detector
FT	Fourier Transform
GC	Gas Chromatograph
GUI	Graphical User Interface
IR	Infrared
IZA	International Zeolite Association
LCF	Linear Combination Fitting
LIE	Liquid Ion Exchange
LMCT	Ligand-to-Metal Charge Transfer
LN ₂	Liquid Nitrogen
MAZ	Mazzite
MCR-ALS	Multivariate Curve Resolution Alternating Least Square

MCT	Mercury-Cadmium-Telluride
MDA	Methane Dehydroaromatization
MFC	Mass Flow Controller
MMO	Methane Monooxygenase
MOF	Metal Organic Framework
MOR	Mordenite
MP-AES	Microwave Plasma Atomic Emission Spectroscopy
MS	Mass Spectrometer
MTH	Methanol To Hydrocarbons
MTM	Methane To Methanol
MTO	Methanol To Olefins
NMR	Nuclear Magnetic Resonance
NTNU	Norwegian University of Science and Technology
OCM	Oxidative Coupling of Methane
ODH	Oxidative Dehydrogenation of Ethane
PBU	Primary Building Unit
PC	Principle Component
PDF	Pair-Distribution Function
pMMO	particulate Methane Monooxygenase
pXRD	Powder X-ray Diffraction
rRaman	Resonance Raman
RT	Room Temperature
SBU	Secondary Building Unit
SCR	Selective Catalytic Reduction
SDA	Structure Directing Agents
SEM	Scanning Electron Microscopy
SI	Supporting Information
SM	Substitution Mechanism
sMMO	soluble Methane Monooxygenase
SNBL	Swiss-Norwegian Beamline
SSIE	Solid State Ion Exchange

TGA	Thermogravimetric Analysis
TM	Transition Metals
TPD	Temperature Programmed Desorption
TPR	Temperature Programmed Reduction
UiO	University of Oslo
UniTo	University of Torino
UV-vis	Ultraviolet-visible
XANES	X-ray Absorption Near Edge Structure
XAS	X-ray Absorption Spectroscopy
WL	White-Line
WT	Wavelet Transform

1. Introduction

Almost a decade ago, in 2015, the World Bank started the Zero routine flaring initiative. This initiative calls to end all routine natural gas flaring by 2030, i.e. burning of natural gas to CO₂ and H₂O, and has been signed by a total of 54 oil companies and 35 governments [1]. Still, only minuscule reductions in the amount of natural gas flaring have been seen worldwide from the start of the initiative until today [2]. Indeed, at the end of 2021, 143 billion cubic meters of gas were still flared all over the world, which amounts to 270 Mt of CO₂, or almost 1% of the world's annual CO₂ emissions released directly into the atmosphere [3]. The main component of natural gas is methane and although the natural gas is burned through flaring, it is still estimated that about 240 Mt CO₂-eq of methane escapes combustion and is directly released into the atmosphere in the process [3]. Methane is an abundant chemical and has high potential as feedstock in the chemical industry. Instead of being flared from remote oil production sites, it could be utilized to make important products for our everyday life, like medicines, plastics, and fuels. When natural gas is found together with oil it is often referred to as associated gas, while separate natural gas wells, e.g. shale gas, are called non-associated gas. Both associated and non-associated gas are often found in remote areas.

Today, the dominant method for converting methane to industrially important chemicals is via the formation of synthesis gas (CO and H₂) [4]. Synthesis gas production is an energy-intensive reaction (700-1000 °C) and requires large production plants that are impractical to install on-site for remote areas like the oil-production sites [5]. Transporting gas from remote areas is also a very costly process, and the cost-benefit of utilizing the associated gas is therefore often poor [6]. One ideal solution to this conundrum would be implementation of a small-scale operated process to convert natural gas directly to a liquid product or products (e.g. methanol or acetic acid), which is a solution to which extensive

research efforts have been devoted over the past decades [7]. Still, most reactions have yielded low conversion to the desired products. In two recent review articles, the groups of Hutchings [7] and Miliordos [8] ask the very important question of whether it is still worth exploring the field of methane activation. As they point out, in addition to the slow research progression on converting natural gas to liquid, there are also the environmental aspects to take into consideration. In line with the Paris Agreement goal of keeping global warming temperature change below 1.5 °C compared to pre-industrial levels [9], a large portion of today's use of fossil fuels must be phased out in favor of other resources to reach net-zero CO₂ emissions before 2050 [10]. Methane is considered a gateway option for producing heat and electricity on our path to net-zero emissions. That is because, compared to other fossil fuels, combustion of methane produces more heat per mass and fewer byproducts. However, natural gas is still a fossil fuel and by continuing to search for methods to also utilize natural gas, in addition to using it for energy, one consequence might be that the transition period towards net-zero emission is slowed down. One could ask if the current ways instead should be completely disrupted, and the stranded fossil sources be left where they are. Unfortunately, this would be hard to achieve as the world's population is going to continue to need energy and resources like fuel and chemical reactants also in the years to come. For example, the demand for methanol and its derivatives has since the beginning of 2000s grown from around 40 to 106 million tons in 2021 [11, 12]. Beyond using synthesis gas for methanol synthesis, some progress has been made in synthesizing methanol from other sources. Methanol can for example be produced from biomass or CO₂, which would meet some of the industrial methanol needs, however, these reactions are still early stage and require time for development [12]. It should also be kept in mind that the secondary components of natural gas are other light alkanes like ethane and propane (0-20 mol%). These alkanes are raw materials for the formation of ethylene and propylene, which are two very important backbones in the chemical industry [13]. An overview of

important building blocks for the chemical industry that are derived from natural gas is given in Figure 1. Since all the possible methods for converting light alkanes to useful chemicals require increasingly more energy- and cost-efficient pathways to be environmentally friendly and industrially viable, we surmise, just as Hutchings [7] and Miliordos [8], that it remains highly important to focus on and understand the fundamentals of C–H activation.

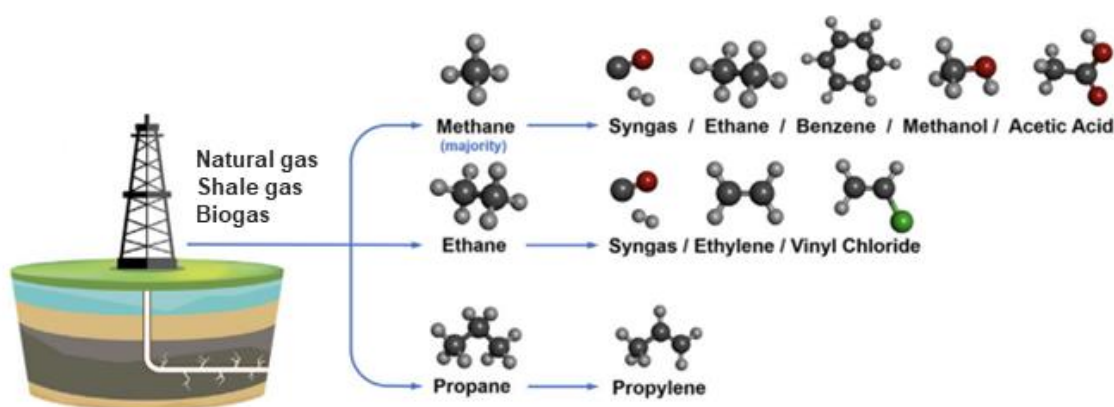


Figure 1. The main components (alkanes) found in associated and non-associated natural gas, as well as the main products that can be derived from these alkanes. The figure is adapted from [14].

Light alkanes are symmetric molecules with no dipole moment and strong bonds giving them an inert behavior [15]. Light alkanes are therefore difficult to selectively convert to desired products. Half a century ago, selective C–H activation was named one of chemistry’s “Holy Grails” [16]. Not only because of the potential environmental and economic benefit of mastering this reaction but also because of the potential academic impact such a reaction would have on the general understanding and development of the research into the broad field of C–H bond activation reactions.

The scope of this thesis is to build on the growing research about the functionalization of the C–H bond in alkanes by especially focusing on the stepwise conversion of methane to methanol over Cu-exchanged zeolites. Upon exploring various zeolite frameworks and Cu exchange techniques we aim to

elucidate structure-activity relationships that provide more fundamental knowledge about the important factors needed for C–H activation and methanol production. Moreover, we use different spectroscopy techniques to thoroughly examine the nature of Cu during C–H activation and oxidation. Finally, we use the knowledge gained to explore how Cu-zeolites can aid in other alkane activation reactions, e.g. ethane activation. The following introduction will give the reader background information on which the work in this thesis is based, as well as insight into the current status of the field.

1.1. C–H Activation

C–H activation and functionalization is a broad field spanning several branches of chemistry. In the field of organometallic chemistry, “C–H activation” traditionally refers to the direct cleavage of a C–H bond of any hydrocarbon-based molecule with the help of a transition metal, leading to the formation of a carbon-metal bond [17]. Functionalization, however, indicates a replacement of H in the C–H bond with another element or functional group. In literature, these terms are often intertwined, which is consistent with the fact that the mechanism for C–H functionalization often proceeds *via* a C–H activation step [17, 18]. For simplicity in the scope of discussions within this thesis, the term “C–H activation” will be used more as a general description of the process of breaking the C–H bond.

Herein, the focus is on the activation of light alkanes due to their high potential as feedstock for the chemical industry. Alkanes, generally have very strong C–C (e.g. $\text{H}_3\text{C}-\text{CH}_3 = 377 \text{ kJ/mol}$) and C–H (e.g. $\text{H}_3\text{C}-\text{H} = 439 \text{ kJ/mol}$) bond strengths [19]. In addition to strong bonds, alkanes also have very low polarizability, electron affinity, and no functional groups, rendering them very stable molecules. Among the alkanes, methane is the most extreme case, and Figure 2 shows the fully symmetric methane molecule and its molecular orbital diagram. With no electrons in the antibonding orbital, σ^* , and fully occupied σ

orbitals, there are no available sites for easy reaction. This causes unfavorable conditions when we want to selectively convert alkanes into functionalized molecules [20]. First, a strong local electric field in the attacking molecule is needed to allow for either a nucleophilic/electrophilic attack or reduction/oxidation reactions [21]. Second, the desired products almost always have higher reactivity than the alkane itself, easily leading to over-oxidation towards CO₂ and H₂O [22, 23].

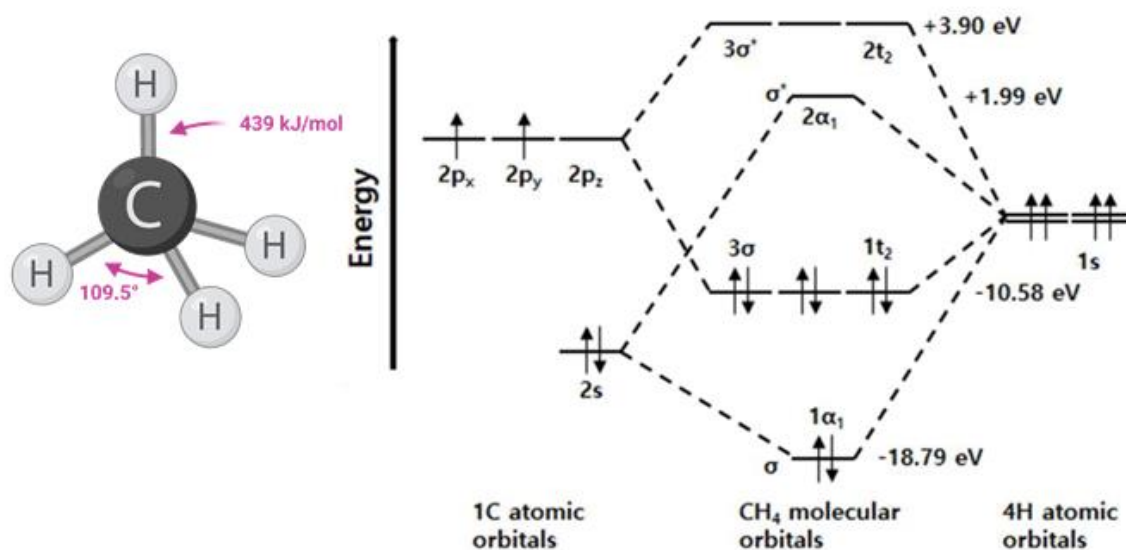


Figure 2. Representation of the methane molecule and its (valence) molecular orbital diagram. The figure is adapted from [20]

To overcome the energy needed to activate the C–H bond, the industrialized methods for C–H activation in lower alkanes, other than exploiting the energy obtained from full combustion reactions to CO₂ and H₂O for heat and electricity, are often very energy-intensive [24]. Natural gas, with its main component being methane (70-90%) [25], is usually converted to synthesis gas, or syngas for short (i.e. a mixture of CO and H₂), *via* steam methane reforming (1), an endothermic process ($\Delta H_{298K}^0 = +206$ kJ/mol) requiring high reaction temperatures (700-1000 °C) [5] to push the thermodynamic equilibrium towards CO and H₂.



In a side reaction, CO could also react further with H₂O to produce CO₂ and H₂ in what is called the water-gas shift reaction ($\Delta H_{298K}^0 = -41 \text{ kJ/mol}$) [5]. The water-gas shift reaction is exothermic and the stoichiometry between CO and H₂ in the reaction feed can therefore be controlled by adjusting the temperatures and pressure. Syngas is used to produce several important chemical products like pure H₂, methanol, NH₃, and synthetic fuels [25]. An overview of the various pathways for methane conversion, both direct and indirect, is given in Figure 3.

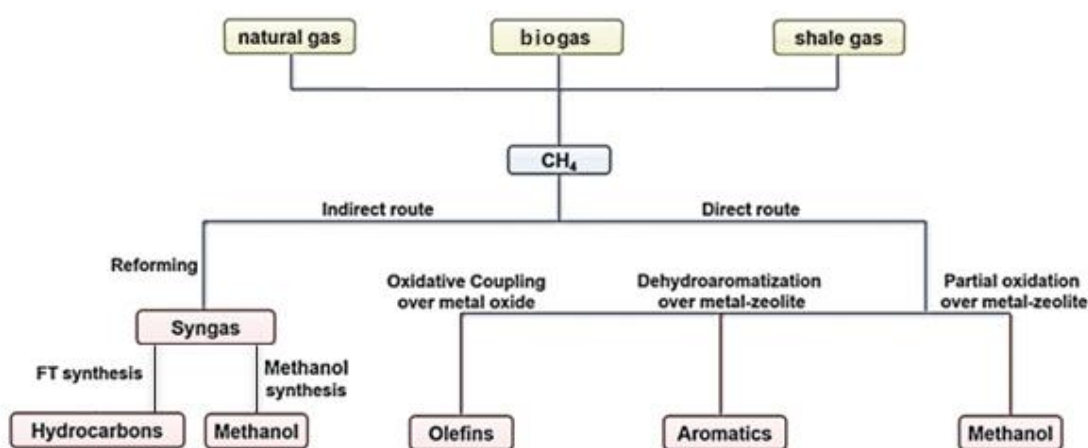


Figure 3. Overview of various methane feedstocks and main conversion paths. The figure is adapted from [26].

For alkanes larger than methane, steam cracking (of ethane) and selective dehydrogenation (of propane and isobutane) are industrially applied methods for their conversion into valuable products like alkenes [5]. The usage of ethane directly in steam cracking to form ethylene instead of higher hydrocarbons, like naphtha obtained from oil production, has become even more feasible over the years with the increasing abundance of (wet) natural gas reserves (e.g. shale gas). However, both steam cracking and dehydrogenation reactions are endothermic and, therefore, require high temperatures to steer the reaction thermodynamics towards the product side. Higher temperatures ($> 600 \text{ }^\circ\text{C}$) can easily lead to gas-

phase radical reactions and the product selectivity over the catalyst material is consequently reduced [5].

Both methane activation and the activation of other light alkanes would benefit greatly from a C–H activation reaction that would lower the energy requirement. The most straightforward path to achieve less energy-intensive paths is to use a reaction protocol that is overall exothermic as heat is not required to push the thermodynamic equilibrium toward the products. Some elevated temperatures would instead be necessary to increase the reaction kinetics, which also can be influenced by the choice of catalyst material. With methane being the major component of natural gas and the main focus of this thesis, the rest of the introduction will concentrate on the advances and materials used in the direct activation of methane. In the last section (2.2) the C–H activation of ethane as another light alkane will briefly be described.

1.1.1. C–H Activation of Methane

Considering the limitations of syngas production, several pathways have been suggested for the direct conversion of methane, i.e., functionalizing the C–H bond in methane instead of breaking it down to CO and H₂ first. As transition metals have shown to be very useful in activating bonds in other small and stable molecules like olefins and CO, they are also widely used in the attempt of activating the C–H bond [17, 23]. One of the major research efforts in this direction has been the oxidative coupling of methane (OCM) to larger hydrocarbons (i.e. exothermic reactions), which started with a report by Keller and Bhasin in 1982 [27]. OCM has been tested over a variety of catalysts, e.g. metal oxides and doped oxides, and is performed at temperatures between 650-880 °C [28, 29]. As the reaction intermediates and products are more reactive than methane, the main issue with OCM has been to obtain high product selectivity at high conversion. Ethylene yields above 40 % has therefore shown to be difficult to achieve [28].

Although an endothermic reaction, nonoxidative methane dehydroaromatization (MDA) was suggested as an alternative to overcome the issue of selectivity. With MDA, studies have shown the benefit of using a bifunctional catalyst with metal sites for dehydrogenation and acid sites for oligomerization [30], making metal-exchanged zeolites a great option. The most active catalyst was Mo/ZSM-5, where a benzene yield of about 10% at 17% methane conversion was achieved [21]. MDA is however far from commercialization due to relatively low methane conversion and short catalyst lifetime due to coking [21]. Beyond the formation of hydrocarbons, other methane activation reactions have also been proposed. Among them is the possibility of coupling methane with CO₂ or CO/H₂O to produce acetic acid [31-33], or directly reacting methane with oxygen in a partial oxidation reaction to produce methanol and formaldehyde [7, 15, 34]. Aromatization, acetic acid formation, and partial oxidation of methane to methanol would all be extremely beneficial reactions in more remote areas where both associated and non-associated natural gas is found due to the cost-efficiency benefit of transporting liquids compared to gas. However, in contrast to aromatization and acetic acid formation, partial oxidation of methane to methanol (2) is an exothermic reaction ($\Delta H_{298K}^0 = -130.5$ kJ/mol) with the subsequent potential for being less energy intensive by operating at lower reaction temperatures. A lower energy requirement increases the potential industrial applicability and environmental impact of the reaction.



Vast research efforts have been devoted to the partial oxidation of methane to methanol over the last decades, and in the next chapter, we will take a deeper look into the major reaction protocols proposed to selectively activate the C–H bond in methane to form methanol.

1.2. Direct Methane to Methanol Conversion

Partial oxidation of methane to methanol in the gas phase has been studied already for a century and is typically operated at high pressures (20-100 bar) and medium temperatures (350-500 °C) due to the exothermic nature of the reaction [7]. Given the higher reactivity of the products compared to methane, a highly fuel-rich atmosphere is needed relative to oxygen, to maintain a high selectivity towards methanol [35]. This compromises greatly the conversion rates, in the same manner as observed for OCM. The reported results in the literature are imprecise [34], rendering some uncertainty to the efficiency of the reaction. However, methanol selectivity close to 60% at 13% methane conversion has been reported [36].

The shortcomings of partial oxidation led the research community to search for methods where a higher selectivity control could be achieved and, therefore, some low-temperature liquid-based reactions have been proposed [37]. The first attempt was already in 1905, when formic acid, made from reacting CH_4 with $\text{HO}_2/\text{FeSO}_4$, was converted to different C_1 oxygenates [38]. Periana et al. then demonstrated in the 1990s that it is possible to convert methane to methanol in a two-step process with concentrated sulfuric acid in the presence of an Hg^{2+} or Pt^{2+} bidiazine catalyst [39, 40]. The reaction proceeds via the formation of a methyl bisulfate intermediate, which then can react with water to form methanol as the final product. Due to the effective stabilization of the intermediate state before the reaction with water, they achieved a methanol yield above 70% with an 81% selectivity [39, 40]. Although the reaction proposed by Periana et al. reports high methanol selectivity, there are some obvious drawbacks, as it includes costly catalyst material and a corrosive atmosphere. Given the homogeneous nature of the reaction, it will require product separation, making it less feasible for industrial scale-up. More recently, Hutchings and co-workers reported that H_2O_2 could be used as an oxidant to convert methane to methanol at high selectivity (> 90%) and 10% conversion in a catalytic reaction loop over Fe-Cu-ZSM-5 zeolites [41, 42].

Furthermore, to address the cost of H₂O₂, both the Hutchings group and others have shown that various catalysts based on Au/Pd mixtures as alloys or supported on TiO₂ or zeolites can make H₂O₂ *in situ* from H₂ and O₂, which then participate in the oxidation of the methane molecules [43-46]. Also, aqueous catalytic processes over Rh [47, 48] and Ir [49] exchanged zeolites without the need for H₂O₂ have been proposed in recent years. Although some advancements have been shown with the use of H₂O₂ and unexplored transition metals, the reaction schemes still require rather costly materials, and the homogeneous catalytic pathways complicate the process scale-up.

To find a selective pathway towards methanol that would not include an aqueous state, scientists have looked to nature, where there is an enzyme called methane monooxygenase (MMO) found in methanotrophic bacteria that can very selectively, and with a high yield, convert methane to methanol solely with O₂ as oxidant [50-52]. There are two versions of the MMO enzyme, namely a soluble (sMMO) based enzyme with well-understood bis(μ -oxo)diiron active sites [50-53], and a membrane-bound particulate (pMMO) enzyme where the active site is suggested to be Cu based, although the speciation is not completely understood [50-52, 54, 55]. In addition to understanding the specific active site of pMMO, researchers have also aimed to utilize the knowledge to find enzymatic and more inorganic biomimetic systems like metal organic frameworks (MOF), to convert methane to methanol [56-60].

Groothaert et al. were the first to suggest a selective gas-phase reaction pathway inspired by the pMMO Cu active site [61]. Similar to the reaction route suggested by Periana et al. (see above), Groothaert et al. also suggested a multi-step process. In the first step, O₂ was used to form active Cu^{II}-oxo centers at moderate temperatures (450 °C) in a Cu-exchanged ZSM-5 zeolite. The active Cu^{II}-oxo sites were then reacted with CH₄ in the following step at lower temperatures

(200 °C) to form stable intermediate species. Only upon H₂O exposure was methanol desorbed as a product.

The publication by Groothaert et al. laid the foundation for decades of research into what we will refer to in this thesis as the stepwise conversion of methane-to-methanol (MTM). The stepwise reaction promises a moderate to low-temperature partial oxidation of methane to methanol over abundant, non-hazardous, and cheap materials (e.g. Cu, zeolites) already widely used in numerous industrial applications. It is additionally a heterogeneous reaction, leading to simpler downstream product separation. There are at least, but not limited to, two major drawbacks of this reaction scheme [62]. First, the stepwise nature of the reaction renders it less favorable for the chemical industry, as it requires several temperature steps and a continuous re-activation of the Cu-loaded zeolites at higher temperatures [63]. Second, the reaction scheme relies on a stoichiometric amount of methanol produced due to the limited number of Cu-oxo sites that can be formed in each cycle [64]. Notwithstanding these limitations, numerous publications have addressed the MTM reaction over the last two decades and have already spurred quite a few comprehensive reviews on the topic [7, 8, 15, 21, 24, 63-71]. The focus in the literature has been especially, but not exclusively, on understanding the Cu speciation of the active sites at different steps of the reaction, unraveling the full reaction mechanism, as well as finding structure-activity relationships, all in attempts to both optimize the reaction protocol and the active sites.

Advancements in MTM research have been the main focus of this thesis, with the target area being on disentangling ambiguous results and unanswered questions related to the reaction. Before we explore the unanswered questions, background knowledge on (Cu-)zeolites and the MTM reaction is provided.

1.3. Zeolites

Zeolites have several important qualities (*vide infra*), rendering them useful materials for applications such as catalysis, ion exchange, and adsorption technologies. They were introduced for industrial use already at the beginning of 1960 when Mobil (now ExxonMobil) applied a faujasite (FAU) zeolite as a catalyst for fluid catalytic cracking (FCC) [72]. Since then, zeolite catalysts are being used in various processes like isomerization, hydrogenation, and methanol to hydrocarbons (MTH) reactions [73, 74]. Zeolites are three-dimensional crystalline aluminosilicates built from Si and Al coordinated with oxygen to form tetrahedra ($[\text{SiO}_4]^{4-}$ and $[\text{AlO}_4]^{5-}$). The central atom of the tetrahedra is referred to as the T-atom (e.g. Si/Al) [75]. The tetrahedra are the primary building units (PBUs) of zeolites and are covalently linked in the corners (sharing an O-atom) to form larger structures known as secondary building units (SBUs) (Figure 4).

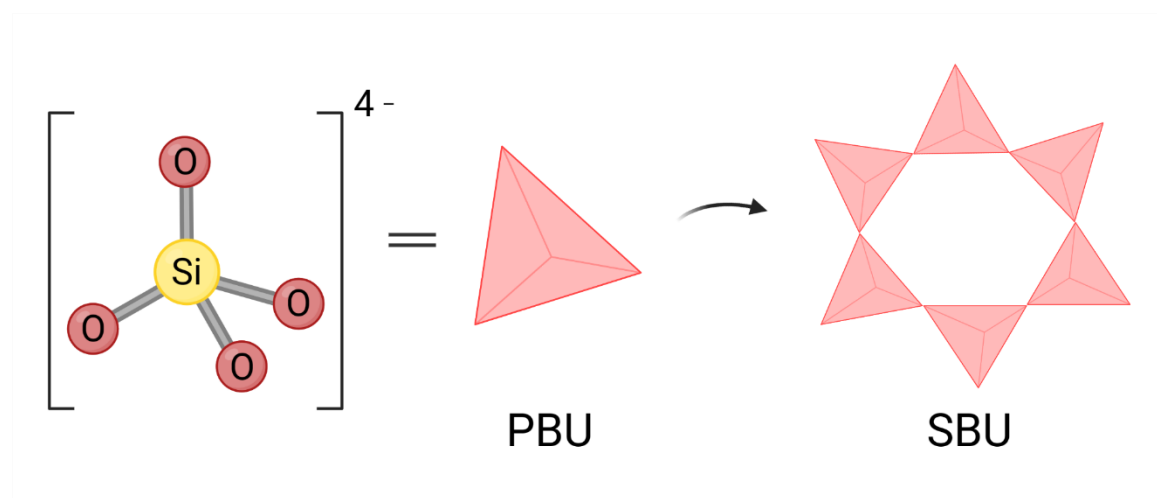


Figure 4. Representation of the composition of a primary building unit (PBU) and an example of a secondary building unit (SBU).

The unit cell of a unique zeolite is designed by stacking specific SBUs in a particular order. The unit cell is then repeated indefinitely to form crystals of different shapes and sizes. The specific stacking of SBUs forms micro-sized (≤ 2 nm) pores and channels through the zeolite, leading to a large internal surface area

[76]. As heterogeneous catalysis often occurs on a surface, the large internal surface areas are one of the reasons why zeolites are good catalyst materials. Especially because the pores and cavities that are formed are perfectly sized for smaller molecules to diffuse through. Due to all the possible stacking combinations with different SBUs, as many as 260 different zeolite structures are proposed in the international zeolite association (IZA) database [77]. The channels and cavities differ in size, depending on the final zeolite structure. These properties give zeolites shape-selectivity properties, perfect for e.g. gas separation and refinement [78].

1.3.1. Brønsted Acid Sites and Ion Exchange

Zeolites are often used in acid-catalyzed reactions. This is possible due to the presence of $[\text{AlO}_4]^{5-}$ tetrahedra. As aluminium has an oxidation state of +III, and silicon has an oxidation state of +IV, for every Al^{3+} tetrahedra present in the material a negative charge is introduced. The negative charge needs to be balanced with a cation, e.g. NH_4^+ , H^+ , Na^+ , K^+ , or Ca^{2+} [75]. The cations can be readily exchanged, and when the cation is a proton, the site gets Brønsted acidic properties. The placement of $[\text{AlO}_4]^{5-}$ tetrahedra must follow Loewenstein's rule, which states that two $[\text{AlO}_4]^{5-}$ tetrahedra cannot be neighbors, i.e. sharing an O atom [79]. When the zeolite structure is built from other T-atoms than Si and Al, the resulting materials are called zeotypes. The most common zeotype is aluminophosphates (AlPOs), where the neutral framework is built from alternating $[\text{AlO}_4]^{5-}$ and of $[\text{PO}_4]^{3-}$ tetrahedra instead of $[\text{SiO}_4]^{4-}$. Then, to create a Brønsted acid site in an AlPO, Si^{4+} can be incorporated in the position of P^{5+} [75]. Zeotypes have a different framework polarity induced by the altered atomic composition compared to zeolites and can in that way affect a potential reaction in a different manner than an isostructural zeolite framework.

In addition to Brønsted acidity, also Lewis acid sites can take form in zeolites. These can be formed by introducing heteroatoms into the framework or by processes that lead to hydrolysis of the Si-O-Al bonds in the zeolite framework so that extra framework Al³⁺ (EFAl) sites are generated [80]. Several structures and positions are possible for EFAl sites, which lead to a variety of sites with different strength. With the right strength, these sites can sometimes also take part in a reaction as electron-pair acceptors, however the nature of the sites are not well understood [80].

The Brønsted sites can also be exchanged with transition metals (TMs), leading to coordinated metal sites within the pores available for reduction/oxidation reactions. With the growth in application area for zeolites in catalysis and the chemical industry, the TMs potential as hosts for reactive guest molecules has also been broadly explored. TM-exchanged zeolites have been investigated in the last decades to create new or improve existing reaction mechanisms for more environmentally friendly applications in reduction/oxidation chemistry [26, 81, 82]. Some potential applications are alkane dehydrogenation, syngas conversion, biomass conversion, CO₂ capture, and conversion, as well as H₂ storage and production [26, 81]. A reaction that has reached industrial application is the use of Cu-exchanged SSZ-13, a Chabazite (CHA) type zeolite, as a catalyst for NH₃-selective catalytic reduction (SCR) of NO_x, greatly minimizing the NO_x emissions from the automotive sector [82].

1.3.2. Zeolites Applied in the Present Study

In this thesis, six different zeolite frameworks are tested. All framework types are displayed in Figure 5. The CHA framework was explored in **Paper I**, while **Paper II** focuses on the MWW (MCM-22) framework. The mordenite (MOR) framework was explored in both **Papers IV and V**, while in **Paper III**, four different frameworks were compared, namely MOR, MFI (ZSM-5), FAU, and Beta (BEA). Beta is a disordered framework structure leading to a family of intergrowths. The intergrowth does not substantially influence the pore accessibility, but could sometimes affect the connectivity of the pores [83].

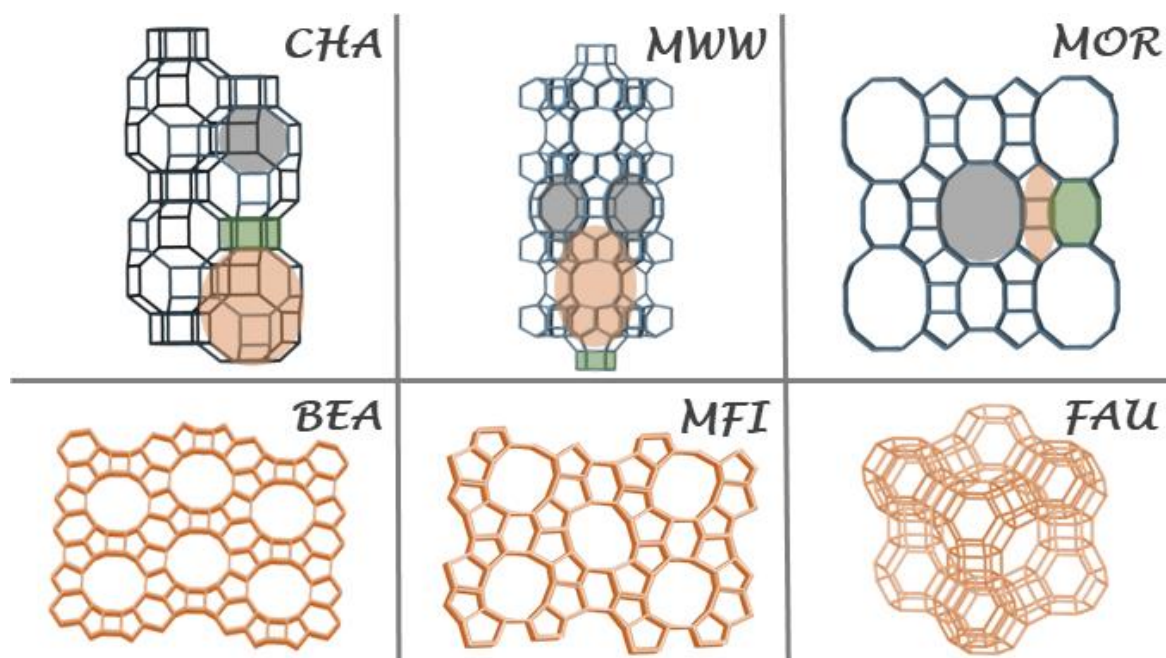


Figure 5. Schematic of all zeolites studied in this thesis. The top row shows the three main zeolites studied herein. MFI, FAU and BEA compared with MOR in **Paper III**. The marked areas in MWW, MOR, and CHA highlight important details in the zeolite framework. See details in-text.

As CHA, MOR, and MWW are the main focus of this work, their composition will be explained in more detail below. In Table 1, the main characteristics of all six zeolites, like channel access, dimensions, and the number of unique T-sites are given.

Table 1. Structural characteristics of the zeolite framework types applied in this thesis.

Framework type	Name	Channel dimensions (Å)	Channel access	Channel systems	Unique T-sites	Ref.
MWW	MCM-22	Sinusoidal 10-ring (4.1x5.1) Supercage (d = 7.1)	10-ring 10-ring	2D	8	[77, 84]
MOR	MOR	12-ring channel (6.5x7.0) 8-ring channel* (2.6x5.7)	12-ring 8-ring	1D	4	[77, 85]
CHA	SSZ-13 SAPO-34	Cavity channel (d = 7.4)	8-ring	3D	1	[77]
MFI	ZSM-5	Sinusoidal 10-ring (5.1x5.5) 10-ring channel (5.3x5.6)	10-ring 10-ring	3D	12	[77, 86]
FAU	FAU	Sodalite cage* (d = 6.3) Supercage channel (d = 11.2)	6-ring 12-ring	3D	1	[77, 87]
*BEA	BEA	Sinusoidal 12-ring (6.5x5.6) 12-ring channel (7.5x5.7)	12-ring 12-ring	3D	9	[77, 88]

CHA

The CHA framework consists of double 6-rings (D6R) stacked in an ABC-sequence and interconnected with 4-rings. The D6R is indicated with a green shade in Figure 5. The stacking of D6R and 4-rings results in cavities (brown shade) that are interconnected and accessible through 8-ring windows (grey shade). CHA is an ideal framework to work with, as the framework only has one crystallographically unique T-site [89, 90]. Four different ion exchange sites have been identified in the CHA framework. Three of them point toward the center of the cavity, around the 8-ring window, while one is in a more constrained position pointing into the D6R [63]. CHA exists in two important atomic compositions. One is the zeolite (aluminosilicate), SSZ-13, and the other is the silico aluminophosphate (SAPO), SAPO-34. The density of Brønsted acid sites in SAPO-34 is determined by the Si content. The incorporation may follow three different substitution mechanisms (SM). SM1 substitutes Si with an Al, which is unlikely because it for one, leads to the introduction of a positive charge that would need to be balanced, and two, the [Si-O-P] linkage that would form is known to be unstable [91]. SM2 substitutes P and leads to the formation of one Brønsted acid site per Si incorporated. SM3 introduces 2 Si, and substitutes both Al and P, usually forming a Si-rich patch [91, 92]. SM2 and SM3 are illustrated in Figure 6.

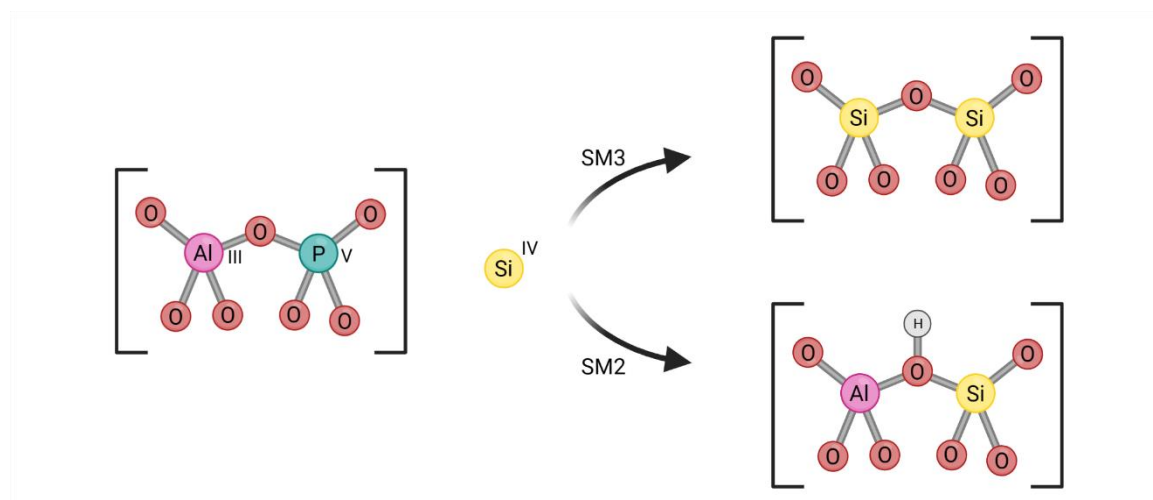


Figure 6. Scheme representing the substitution mechanisms (SM2 and SM3) for Si in SAPO-34.

Whether Si follows mostly the SM2, SM3 or a combination of these mechanisms depends on the synthesis procedure [93]. Because of the different substitution mechanisms, the amount of Si in the SAPO-34 framework will most likely not correlate directly to the amount of ion exchange sites. SSZ-13 has been tested extensively in the MTM reaction [94-103]. However, literature is scarce on the isostructural zeotype material SAPO-34. To the best of our knowledge, only Wulfers et al. have tested SAPO-34 in the stepwise MTM conversion [104]. SAPO-34 is, however, an industrial-scale catalyst for the conversion of methanol to olefins (MTO) [73], and has been widely investigated in the search for a Cu-loaded catalyst in NH₃-assisted selective catalytic reduction (NH₃-SCR) of NO_x [105].

MCM-22

The MCM-22 zeolite has an MWW-type framework and consists of 10-ring pore openings and two independent channels [84]. One is a sinusoidal 10-ring channel (Figure 5 – grey shade), while the other consists of layered supercages with a 12-ring diameter (brown shade), interlinked by D6Rs (green shade), and accessible through 10-ring channels. Even though the largest pore opening in MCM-22 is a 10-ring, the zeolite is often compared to and found to have similar properties as 12-ring pore systems like MOR, FAU, and mazzite (MAZ) zeolites [106]. However, one main difference is the complexity of the MCM-22 structure, causing the zeolite to have no less than 8 different T-sites, while the others mentioned have 4, 1, and 2, respectively. MCM-22 has additionally an outer surface that consists of pockets formed by half of a supercage. These pockets have been shown to hold some of the active sites for MCM-22 [107]. Other possible sites for Al speciation are inside the sinusoidal 10-ring, centered on the supercage walls, and in the D6R at the bottom of the supercage [108]. Previously, MCM-22 has been tested extensively as a large pore zeolite system for methylation reactions [109, 110], however, before the work

presented in this thesis, MCM-22 was an unexplored zeolite framework for the MTM reaction.

MOR

MOR consists of a 12-ring channel (Figure 5 – grey shade) and a distorted 8-ring channel, parallel to the 12-ring pore (green shade) [85]. Due to the nature of the 8-ring pore (see Table 1), it is inaccessible from the main window. However, perpendicular to the 12-ring, there is an 8-ring side pocket (3.4x4.8 Å), that gives access to the parts of the 8-ring channel (brown shade). In conclusion, given the sterically hindered nature of the 8-ring channel, MOR is considered a 1D zeolite consisting of a 12-ring channel with an 8-ring side pocket. MOR is a widely tested zeolite for MTM and is shown to be one of the most active materials [61, 111-115].

2. MTM over Cu-exchanged Zeolites

Ever since the stepwise MTM conversion was suggested by Groothaert et al. [61], Cu-exchanged zeolites have been extensively investigated for the reaction. Major efforts have also been directed toward the reaction design, where the most applied approach for the MTM reaction is a three-step process that are repeated to create a cyclic process (Figure 7) [61, 111, 116-120]. The Cu-zeolites are first activated at high temperatures ($> 400\text{ }^{\circ}\text{C}$) in the presence of O_2 to form Cu^{II} -oxo moieties. Then, the temperature is lowered, typically between 150 and $200\text{ }^{\circ}\text{C}$, where the Cu-sites are exposed to CH_4 , upon which both the C–H bond is activated and methoxy intermediates are stabilized by the Cu and/or H^+ (Brønsted acid sites) present in the zeolite cavity. Finally, H_2O is used to extract methanol, either on-line [111] or by quenching the products in a solvent trap for off-line analysis [121].

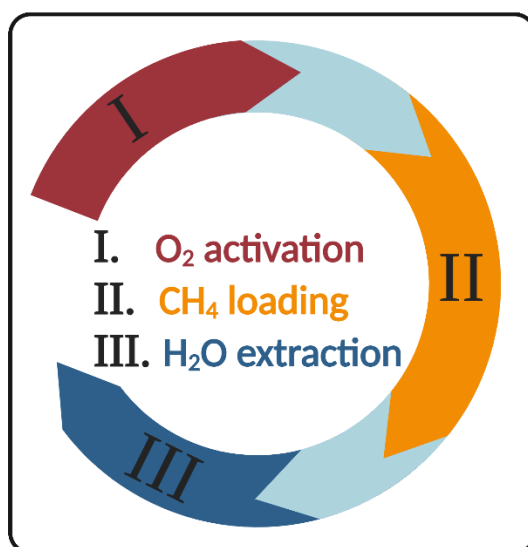


Figure 7. Representation of the MTM sequence over Cu-exchanged zeolites.

Some groups have demonstrated the use of other oxidants like NO [122], N_2O [122-124], and H_2O [125, 126] for activating Cu-zeolites. Also other TMs have been explored for gas-phase, stepwise MTM conversion, and among them are Fe [95, 127-131], Ni [132], and Co [133, 134]. Instead of high-temperature activation, a

stepwise route that proceeds isothermally at around 200-300 °C has also been proposed [64, 122, 135-138]. In the isothermal approach, it seems a higher methane partial pressure (8-37 bar) can circumvent the need for high O₂ activation temperatures. Although this approach introduces a need for high pressure, it lowers the energy requirements of the high-temperature step and simplifies the protocol for industrial use. Herein, the scope has been on understanding the C–H activation mechanism, and we have thus focused our attention on the most applied route in literature, namely the stepwise route over Cu-zeolites that proceeds *via* high-temperature O₂ activation.

Before the initiation of this thesis, but within the same project (iCSI), important contributions have been provided to the field of MTM by Svelle and coworkers. In a 2017 publication, Pappas et al. derived an optimal protocol for MTM over Cu-SSZ-13 [94]. They found that both a prolonged time in O₂ (8 h) and CH₄ (6 h) were necessary, indicating a slow rate of active site formation and C–H activation. In the same study, they also found an interesting correlation between the reduction of the Cu-species from Cu^{II} to Cu^I when activated in He to the activity of the Cu-zeolites in MTM. Such a correlation has also been shown for other zeolite systems [139, 140]. Then, in another key study on Cu-MOR that resulted in several papers [114, 120, 141-143], a highly productive material was found (0.18Cu,H-MOR(11)). With an intermediate Cu-loading (Cu/Al = 0.18) and high Al-content (Si/Al = 7), 0.18Cu,H-MOR(11) showed a productivity of 0.47 mol_{MeOH}/mol_{Cu} (175 μmol_{MeOH}/g). If we hypothesize a dimeric Cu^{II}-oxo site as the active site for MTM (*vide infra*), the productivity obtained is close to the maximum achievable in one reaction cycle. Pappas et al. also investigated a Ferrierite (FER) zeolite type for MTM [140, 144]. The Cu-exchanged FER zeolites showed good productivity (e.g. 0.33 mol_{MeOH}/mol_{Cu}), and interestingly, under CO-adsorption experiments with Fourier transform (FT) infrared (IR) spectroscopy, it was shown that the sample with more freely coordinated Cu-motifs (e.g. 3-fold vs 4-fold), exhibited higher

productivity for methanol. As this work has set the baseline for the work presented herein, and we apply similar reaction protocols and setups, a summary of the MTM activity for the three zeolite systems studied by Svelle and coworkers is reported in Figure 8 for reference.

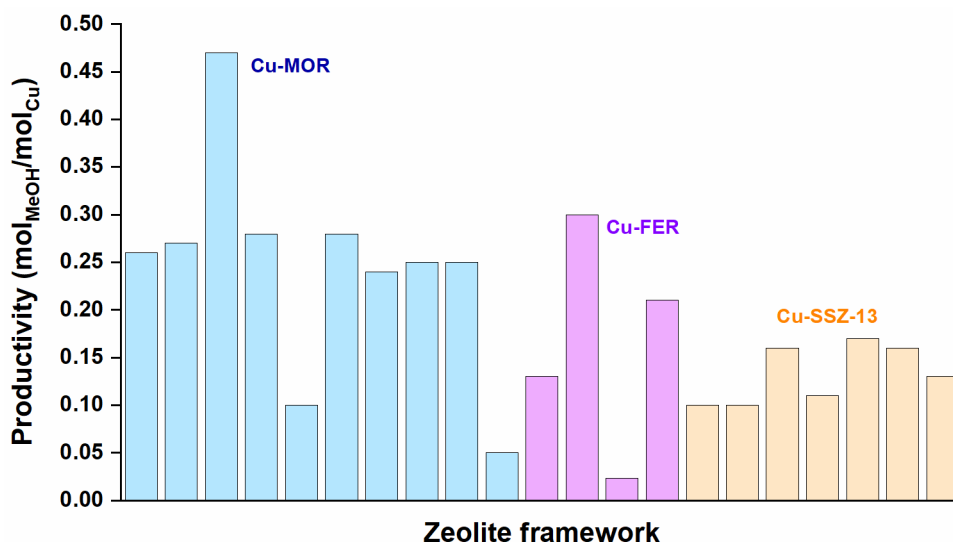


Figure 8. Summary of MTM productivity obtained previously in the iCSI project.

Over several decades, a library of other zeolites has been tested in the MTM reaction. In a recent review, Newton et al. summarized the highest productivity obtained in literature for a number of zeolite frameworks (Figure 9) [67]. Among the most active samples when normalized to the Cu content, we find CHA, FER, MOR, and MAZ. It should be noted from Figure 9 that although FAU also exhibits high productivity, this has only been obtained with higher reaction temperatures and pressure [136]. With CH₄ exposure at 200 °C, FAU was virtually inactive. The top five frameworks range from small pore systems like CHA, MAZ, and FER with (8-ring channels) to medium (10-ring channel in FER), and large pore systems (12-ring channels in FAU, MOR, and MAZ). At first sight, no apparent correlation between channel size and activity is observed. However, upon close examination of the MOR framework, it should be noted that there is a side pocket in the 12-ring channel that is accessible through an 8-ring window, as explained in the previous

chapter. Upon excluding FAU, which needs higher activation temperatures, there appears to be a weak correlation between the methanol productivity at low methane activation temperatures and the presence of stabilizing confinement, like the cavities in CHA, or the MOR side pocket. This is also suggested as an important factor by recent studies on the cavity and confinement effect [71, 145-147].

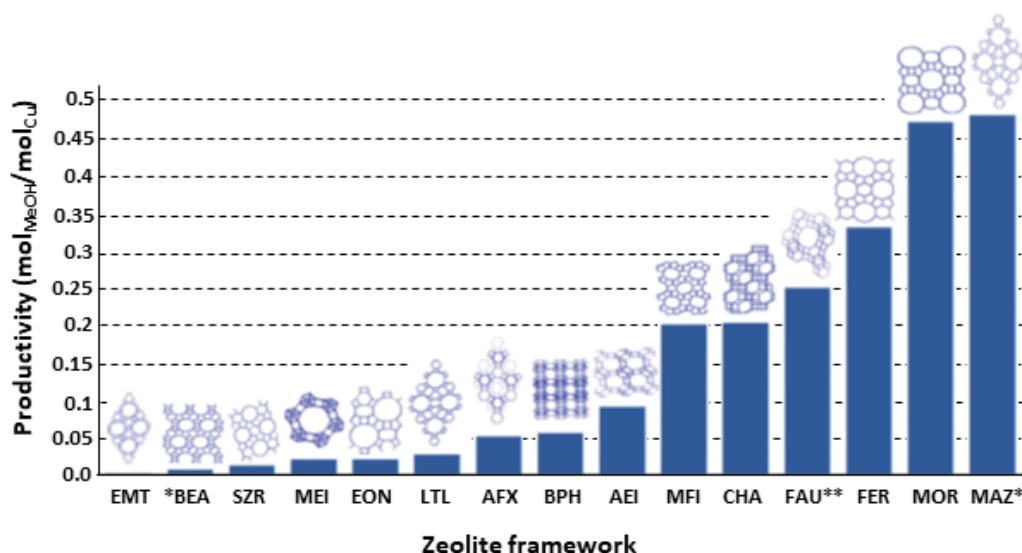


Figure 9. Schematic of different copper zeolites systems tested in MTM, with a comparison of their productivity. The figure is adapted from [67].

In addition to the zeolite frameworks summarized in Figure 9, Cu-exchanged Erionite (ERI), another previously unexplored zeolite system has recently been investigated by Zhu et al. [148]. The material had a mid-high methanol productivity of 0.23 mol_{MeOH}/mol_{Cu} in an isothermal reaction protocol at 300 °C (with 30 bar CH₄ pressure). Like Cu-exchanged FAU zeolites, the Cu-ERI sample demonstrated improved activity at higher temperatures. The need for high temperature was attributed to a stronger interaction between Brønsted sites and methoxy intermediates by the authors.

In the following chapter, a review of some key research advancements made in the field of MTM is provided. Finally, several key points are summarized that remain ambiguous or not fully understood with regard to the literature.

2.1. Status of the Field

In the stepwise conversion of methane to methanol (MTM) over Cu-zeolites, three main components affect the reaction outcome; Cu speciation, the zeolite framework, and the reaction design. Since the reaction is stoichiometric and does not reach a steady-state, it is not possible to break down the reaction mechanism from normal kinetic studies. Because of this, a wide variety of tools have been used in the literature to unravel key information on the process including, but not limited to, FT-IR spectroscopy, ultraviolet-visible (UV-vis) spectroscopy, X-ray absorption spectroscopy (XAS), and adsorption/desorption experiments. Some groups have also recently used time- and temperature-dependent spectroscopy experiments in attempts to unravel the kinetic parameters of the reaction [149, 150]. Herein I will highlight the main overall findings related to Cu-speciation, framework effects, and mechanistic understanding. For more details on the direct output of the various techniques, I refer the reader to some extensive reviews on the topic. In a review by Newton et al., the impact of several techniques has been discussed and scrutinized [67]. For a deeper insight into the use of XAS to advance our understanding of the systems, I refer the reader to my own review on the topic [68].

2.1.1. Cu-Speciation

When Cu-zeolites are exposed to an oxidant at high temperatures, any impurities and water present in the zeolite before heating desorb, and the Cu species binds to oxygen and anchors to the exchange sites. Understanding the nature of these

species has been a large focus area in the MTM research, as this would allow optimization of materials, and thus increase the yield. Initially, a bis- μ -oxo dicopper(III) species was proposed as the active site in ZSM-5 [61]. The assignment was primarily based on a Cu-Cu distance of 2.8 Å as observed with extended X-ray absorption fine structure (EXAFS) on the O₂-activated ZSM-5 and a UV-vis band observed at 22 700 cm⁻¹ that was consumed when the O₂-activated Cu-zeolite was exposed to methane. Bands in this region were correlated to charge transfer from O ligands to Cu already in the early 2000s because of the research focus at the time on both decomposition of NO over Cu-zeolites and studies of the active sites in pMMO [151-153]. As more studies have appeared, the understanding of the Cu-oxo sites developed. In 2009, Woertink et al. re-evaluated the assignment of the 22 700 cm⁻¹ band to be linked with a mono- μ -oxo dicopper(II) site (Cu-O-Cu) instead of bis- μ -oxo dicopper(III) (Cu-(O₂)-Cu) species [118]. This reassignment was based on a combination of resonance Raman (rRaman) spectroscopy and density functional theory (DFT) calculations with the UV-vis measurements. By probing the O₂-activated Cu-zeolite with visible light in the rRaman experiments corresponding to the region of the band observed in UV-vis (22 700 cm⁻¹ = 441 nm), the authors could see resonance-enhanced Cu-O vibrations that were unambiguously assigned to a Cu-O-Cu species.

In later studies on Cu-loaded SSZ-13 by Ipek et al. evidence was found for both trans- μ -1,2-peroxo dicopper(II) (Cu-(O-O)-Cu) and mono- μ -oxo dicopper(II) [97]. Furthermore, in another study on Cu-SSZ-13, Pappas et al. combined results from rRaman, XAS, and FT-IR spectroscopy to study the Cu-speciation after O₂-activation. Based on their results, they suggested that Cu^{II}-OH, as well as end-on and side-on superoxo monocopper(II) species (Cu-(O₂)'), were formed in addition to the two dimeric species proposed by Ipek et al. [94]. Cu^{II}-OH was proposed as an active species for MTM theoretically by Kulkarni et al. [154]. However, Pappas et al. did not find evidence for the Cu^{II}-OH species after prolonged exposure to O₂

and suggested it was an intermediate for dimeric species. To fit a two-electron process, some of the monocopper species were proposed to recombine or bridge to form either trans- μ -1,2-peroxo dicopper(II) or mono- μ -oxo dicopper(II) as the active sites for CH₄ activation [94]. None of the Cu-CHA studies indicated the formation of trimeric Cu-species, and in the study by Pappas et al., an observed lower productivity than 0.5 (maximum productivity in a dimeric site scheme) was instead linked with a set of inactive Cu-sites in the D6R of Cu-SSZ-13. The fraction of Cu occupying the D6R site is shown to increase with increasing Al content and has also been shown to be preferentially occupied at low Cu loadings [155-157]. However, the formation of Cu^{II}-OH species is also suggested to occur in Cu-MOR zeolites. Sushkevich et al. compared compositionally different Cu-MOR zeolites and found that a sample with low Al content (Si/Al = 46) formed primarily isolated Cu-OH species due to the lack of Al-pairs [126], while the samples with higher Al-content also formed Cu^{II} dimers.

In 2015, the existence of trimeric Cu species ($[\text{Cu}_3(\mu\text{-O})_3]^{2+}$) in Cu-MOR zeolites was proposed to exist by Grundner et al. [158]. This was based on three key pieces of evidence where they first showed a linear correlation fitting a slope of 0.33 between the methanol yield and Cu content up to a certain Cu-loading. Then, EXAFS fitting of O₂-activated samples indicated that a trimeric site gave the best fit, which was corroborated by DFT calculations indicating that a trimeric site was the most stable species. Following up with purely theoretical studies, Li et al. showed the likelihood of a trimeric Cu-oxo cluster to be the most active species in ZSM-5 [159], while Mahyuddin et al. showed the same for a Cu-MAZ zeolite [160]. More recently, Lercher and coworkers found evidence that the formation and activity of trimeric Cu species in MOR are reliant on the activation protocol [161], as well as the chemical potential. A higher methane partial pressure (40 bar) allowed for one $[\text{Cu}_3(\mu\text{-O})_3]^{2+}$ species to activate two CH₄ molecules [138]. The stronger chemical potential was found to facilitate the conversion of methane over

Cu clusters anchored on extra-framework Al^{3+} [162, 163]. Some theoretical studies propose larger Cu clusters to form and be more stable than the smaller species [164, 165]. Figure 10 gives an overview of the different Cu-species proposed to form in Cu-zeolites over recent years.

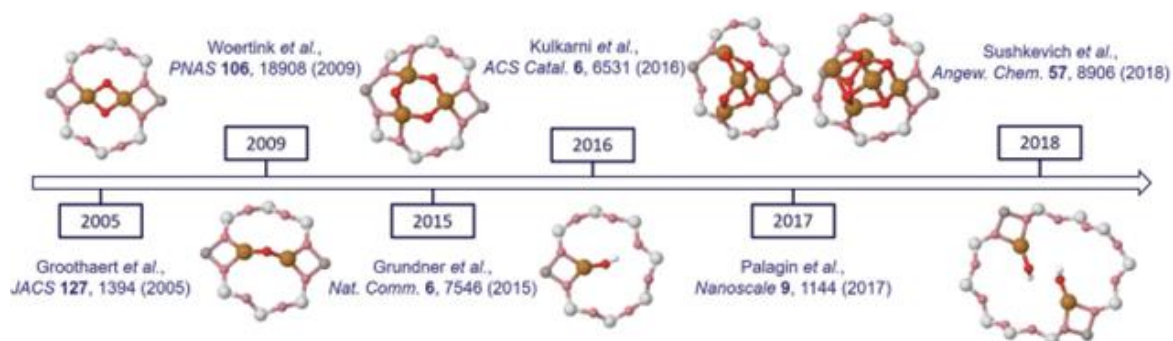


Figure 10. Overview of different Cu_xO_y-moieties proposed to form in Cu-exchanged zeolites over the last two decades. The figure is adapted from [67].

Many studies contradict the idea of trimeric Cu-sites and rather propose mono- μ -oxo dicopper(II) species as the active sites [112, 120, 137, 149]. In this regard, the studies by Svelle and coworkers on Cu-MOR zeolites should be highlighted. In a study of various Cu-MOR compositions by Dybala et al., a highly active Cu-MOR zeolite (0.18Cu,H-MOR(11)) was found [114]. Upon comparing 0.18Cu,H-MOR(11) to a MOR with different composition with the use of High-energy resolution fluorescence-detected X-ray absorption near edge structure (XANES), Pappas et al. were able to correlate the high activity observed over 0.18Cu,H-MOR(11) to the higher presence of a pure dimeric Cu-component (PC5 in Figure 11). PC5 was found to be more present in 0.18Cu,H-MOR(7) after O₂ activation up to 500 °C [120]. PC5 was derived with multivariate curve resolution alternating least square (MCR-ALS) analysis, a technique that has been revolutionized by Martini et al. to explore Cu-speciation based on XANES spectra [156, 166]. The PC5 species was found to be the active species for MTM and

attributed to a three-fold coordinated dimeric Cu^{II}-oxo species, being either mono- μ -oxo dicopper(II) or trans- μ -1,2-peroxo dicopper(II) (not presented in Figure 10).

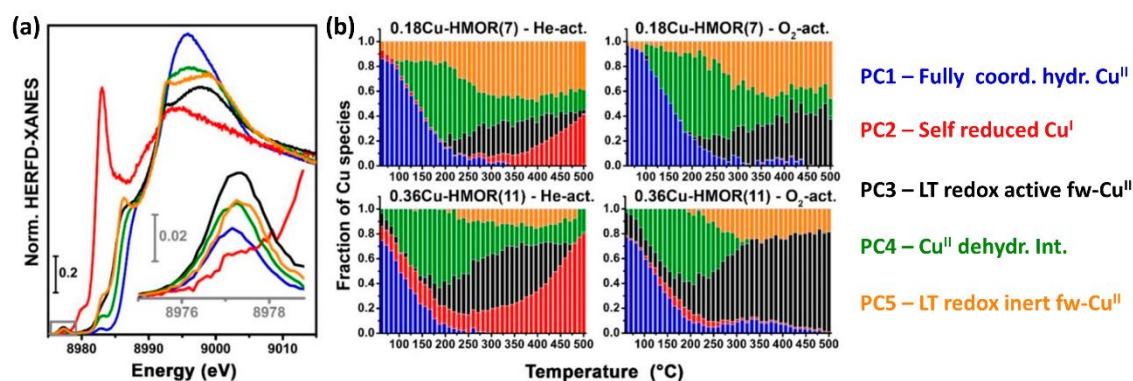


Figure 11. (a) Pure HERFD XANES spectra obtained from MCR-ALS analysis of data collected from O₂- and He-activation of Cu-MOR (Cu/Al = 0.18, Si/Al = 7) and Cu-MOR (Cu/Al = 0.36, Si/Al = 11). The fraction of different Cu-species, given by PC1-PC5, during (b) He-activation and O₂-activation obtained from the pure spectra reported in (a) are given as a function of the data collection temperature. The color code given for the principal components (PC1-PC5) is the same throughout the figures. Figure adapted from Pappas et al. [120], for publication in [68].

Knorpp et al. have provided two studies on Cu-MAZ zeolites for methane to methanol that also support the idea of dimeric or two monomeric sites as active sites. Cu-MAZ was shown to be among the most active materials for MTM (Figure 9), with about the same methanol productivity as the 0.18Cu-MOR(7) sample [167]. Using FT-IR spectroscopy, the authors showed that MAZ had an inferior selectivity to methanol compared to a MOR zeolite [167]. X-ray diffraction combined with EXAFS revealed the nature of the Cu species. They found evidence that a pair of Cu^{II}-OH are situated in 6-rings across from each other pointing into the 8-ring channel of MAZ, hence forming very stable Cu sites for the methoxy species [168]. By comparing different MOR compositions with several different techniques like UV-vis, electron paramagnetic resonance (EPR), EXAFS, and NO-adsorption with FT-IR, Sushkevich et al. found spectroscopic and kinetic evidence of two different Cu species [149]. One was a copper dimer, associated with a UV-

vis band at $26\,100\text{ cm}^{-1}$, while the other was a $\text{Cu}^{\text{II}}\text{-OH}$ monomer, associated with a UV-vis band at $16\,900\text{ cm}^{-1}$. The authors found evidence that $\text{Cu}^{\text{II}}\text{-OH}$ monomers form first, and as the Cu content increases, more Cu-dimers form in the materials. In another recent study by Deplano et al. however, evidence from a set of XAS measurements showed that the Cu-Cu distance fits the formation of dimeric Cu-species [169]. The authors based their experiment on the fact that NH_3 has been shown to both relocate Cu species, but also influence the final activity after O_2 activation. Therefore, they exposed the zeolite to a variety of reducing agents before O_2 activation to see its effect on the final Cu^{II} speciation. With the help of a wavelet transform (WT) EXAFS analysis, the authors quantitatively correlated the amount of Cu pairs to the number of Cu^{II} sites found with linear combination fitting. The use of wavelet transform analysis is a technique that has been explored lately for MTM as a powerful technique to more unambiguously interpret the Cu-Cu single scattering that contributes to the high R range in an EXAFS signal [143, 170, 171].

Since the first studies by Pappas et al. on Cu-FER (mentioned above) [140, 144], Tao et al. have provided some additional insight [172]. They achieved approximately the same productivity as Pappas et al. ($\sim 0.30\text{ mol}_{\text{MeOH}}/\text{mol}_{\text{Cu}}$) and based on the combination of rRaman, NO-adsorption with FT-IR, XAS, and UV-vis spectroscopy measurements, the authors showed that only Cu exchanged into the 8-ring is active towards methanol formation. Their results indicate that they have a bridged Cu-O species with a constrained angle so that the most likely species is a resonance structure of bis- μ -oxo dicopper(III) and μ - η^2, η^2 -peroxo-dicopper(II). This assignment is interestingly taking the field back – full circle – to the species first proposed to form in ZSM-5 by Groothaert et al. in 2005 [61].

As of now, there is still debate in the literature on the exact nature of the active sites. The broad picture of Cu species examined in the literature shows the complexity behind determining said nature, and it is clear that depending on the

zeolite structure, Si/Al, and Cu/Al ratio, different types of Cu species can form, with often a mix of species present within the same sample. In the next section, we will therefore look into the attempts that have been made to optimize materials for specific Cu-speciation.

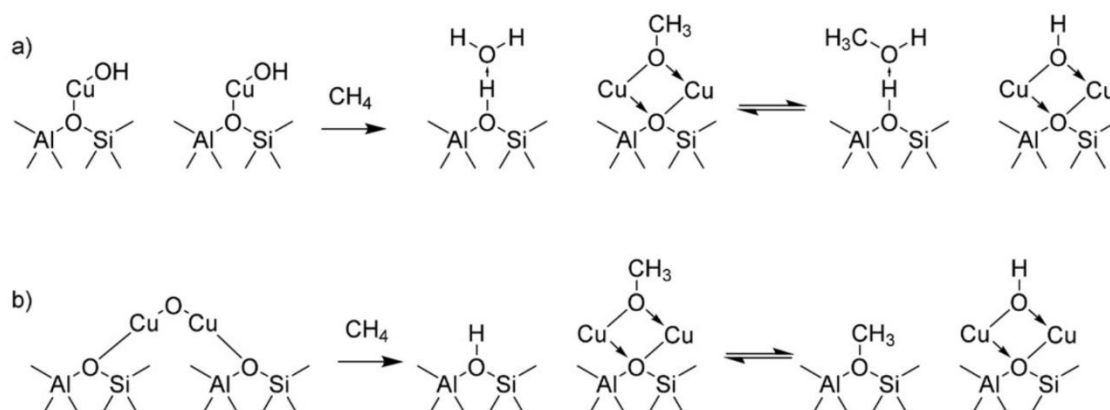
2.1.2. Effects from Zeolite Synthesis and Ion Exchange

The previous section highlights the importance of the Cu-speciation on the methanol activity. The Cu-speciation is affected by several factors like the zeolite framework, synthesis techniques, and ion exchange methods.

The most common synthetic routes for ion-exchanging metals in zeolites are liquid ion exchange (LIE), incipient wetness, and solid-state ion exchange (SSIE). During LIE, a Cu solution (e.g. $\text{Cu}(\text{Ac})_2$) is mixed with the zeolite, and the cations (e.g. H^+ , Na^+ , and NH_4^+) present in the zeolite after synthesis are displaced by Cu complexes. Repeated exchanges and fine-tuning parameters like Cu-precursor, temperature, and pH can ultimately affect the final Cu concentration and its dispersion in the zeolite framework [65, 85, 114, 117, 137, 173]. Incipient wetness, although sometimes called SSIE [114], is a solution-based method, where the solution volume equals the pore volume of the zeolite, and the solution enters the pores because of capillary effects. SSIE is rather a solid mixture with a zeolite and a solid precursor salt (e.g. CuCl_2). Then, upon heating, Cu is exchanged with the cationic sites and a chloride-containing gas is produced. In literature, the Cu loading into zeolites is mostly performed *via* liquid ion exchange or incipient wetness methods with Cu^{II} salts, both giving well-dispersed Cu-zeolites, however only in lab-scale quantities [99, 114]. For industrial applications, it would be much more beneficial to use a simpler exchange method like SSIE to produce larger amounts of material. SSIE is also relevant for the selective catalytic reduction of NO_x with NH_3 , and to that end, Vennestrøm and Shwan et al. have previously investigated a novel method to perform SSIE with $\text{CuO}/\text{Cu}_2\text{O}$ in an atmosphere of

NO/NH₃ [174, 175]. Therein, they suggested that the Cu-oxo species are formed at low temperatures due to the formation of mobile [Cu(NH₃)₂]⁺ complexes. Le *et al.* have previously shown that SSIE with Cu^{II}(acac)₂ instead of Cu^ICl over mordenite leads to a higher yield of methanol [176]. However, when exchanging Cu^I ions instead of Cu^{II} ions into the zeolites, it is theoretically possible to obtain a Cu/Al = 1, thus maximizing the possible Cu-oxo sites. A similar protocol using SSIE with Cu^ICl to exchange H-MOR zeolite for the MTM reaction was previously applied by Bozbag *et al.*, however, they did not explore the possibility of fully exchanging the materials and used maximum Cu/Al ratios around 0.35 [113].

Contrasting the idea of covering the zeolite with Cu to form a maximum amount of Cu-oxo species is the literature showing that Brønsted acid sites are beneficial for the MTM performance, as they are shown to prevent overoxidation [177]. It has also been shown with solid-state nuclear magnetic resonance (NMR) and FT-IR spectroscopy studies that the Brønsted sites play a crucial role in stabilizing the methoxy species after CH₄ activation [178, 179]. Examples of how this might proceed are shown in Scheme 1. In support of this theory, it has been shown that H-exchanged zeolites produce a higher methanol yield than Na-zeolites [114, 177, 180]. Interestingly, for Cu-FER zeolites, it has been found that a combination of Na and H as co-cations led to the most active sample [140].



Scheme 1. An example of oxidation pathways for methane over dimeric and monomeric Cu-oxo species. The scheme was originally reported in [179].

Over the last decade, advancements have also been made concerning zeolite synthesis in attempts to control the Al siting. A special focus has been on controlling the formation of isolated (Al separated by three or more Si) or paired Al sites (Al atoms separated by one or two Si atoms). In e.g. SSZ-13, more Cu²⁺ in paired Al sites have been shown to induce a better hydrothermal stability in the zeolite framework, which subsequently increase the performance of Cu-SSZ-13 zeolites in the NH₃-SCR of NO_x at higher temperatures [181]. In the MTO reaction on the other hand it is shown that paired Al in SSZ-13 has a negative effect on the catalyst lifetime and the wanted MTO product selectivity [182]. Proposed synthesis routes take advantage of the electrostatic interactions between various organic structure-directing agents (SDAs) with negatively charged sites in the framework [183]. Depending on the zeolite structure, the choice of SDA has been shown to influence the Al siting in zeolites (e.g. FER, SSZ-13, and ZSM-5) [184-189]. For SSZ-13, also a top-down approach has been suggested to control the number of paired Al sites by performing an interzeolite conversion synthesis starting with an Al-rich FAU zeolite [190].

In a recent contribution from our group, we showed that using various Al salts as precursors in the synthesis of MOR zeolites would influence the pH of the synthesis gel, furthermore affecting the final Al siting [85]. This was enough to affect the methanol productivity of the Cu-MOR, where the sample with a higher fraction of Al in the 8-ring had lower productivity than the MOR sample with more Al in the 12-ring. From these results, it could be hypothesized that the Al siting affected the position of the Cu species and that Cu-species forming in the 12-ring lead to more redox active sites that are more active in the MTM reaction.

Another route to controlling the Al siting is shown to be possible with the use of specific co-cations. K⁺ and Cs⁺ are large cations that have been shown to selectively block the access to the 8-ring side pocket of MOR and thereby tune the Cu siting [191].

In attempts to simplify the understanding of the Cu-speciation and reaction mechanism, Meyet et al. have also shown in recent years the possibility of converting methane to methanol over well-dispersed Cu^{II} sites placed on an alumina support [192]. Based on spectroscopic evidence from EPR, UV-vis, FT-IR, and EXAFS the authors proposed the active sites to be three-coordinated bare Cu^{II} monomers, and by combining spectroscopy, DFT, and activity experiments, they proposed a mechanism where two monomers work together in pairs to convert methane to methanol. Without zeolite confinement, these samples still produce 0.06-0.12 mol_{MeOH}/mol_{Cu}. Although this productivity is moderate compared to zeolites (Figure 9), the contribution sheds important insight into the mechanism occurring in the zeolite “black box”.

2.1.3. Reaction Mechanism

The partial oxidation of methane to methanol (eq. (2)) is a two-electron process. What this means is that the C atom in methane is oxidized from an oxidation state of -IV to an oxidation state of -II, while each O in O₂ on the other side is reduced from an oxidation state of 0 to -II. Within the broad picture of Cu-sites presented thus far, there are two general types of mechanisms that can occur. This was summarized very nicely in a figure by Newton et al., which is reproduced in Figure 12 [67]. The bottom pathway represents the idea of a redox mechanism over a Cu^{II}/Cu^I pair. In this pathway, two Cu^{II} species are reduced to fulfill the two-electron rule. Upon reduction, the C–H bond in methane is cleaved, and a methoxy species is formed. The methoxy species may be stabilized directly on Cu, but based on the literature, it is more likely that the methoxy group is stabilized either on an extra-framework O-ligand or on a nearby Brønsted acid site (Scheme 1). Dimeric Cu^{II} sites, or possibly two monomeric species close by are the species that fit best such a mechanism. The mechanism presented in the top row is based on theoretical calculations and could occur on both dimeric and trimeric Cu sites [159, 193]. In trimeric species, we find a mixed valence Cu^{II/III} oxidation state for at least two of the Cu atoms after O₂ activation. However, by resonance, the positive charge could also be situated at the O atoms giving them a radical, oxyl character [159]. Recent DFT calculations suggest that Cu is mostly present as Cu^{II} [193] and that it is the highly reactive radical O atoms, [O[•]], that cleave the C–H bond in methane by homolytic C–H bond cleavage. One possible mechanistic route for cleaving the C–H bond is the formation of a gas-phase methyl radical in addition to a bridging OH species. Then, methanol is formed e.g. by a rebound step with the bridging OH species [159]. In the overall radical pathway, there is no need for the reduction of Cu^{II} to Cu^I however, which is a bit of a conundrum, as substantial research indicates that Cu^{II} is reduced upon CH₄ exposure and that the Cu^I formation is directly linked with the amount of CH₃OH produced [120, 142, 167, 194].

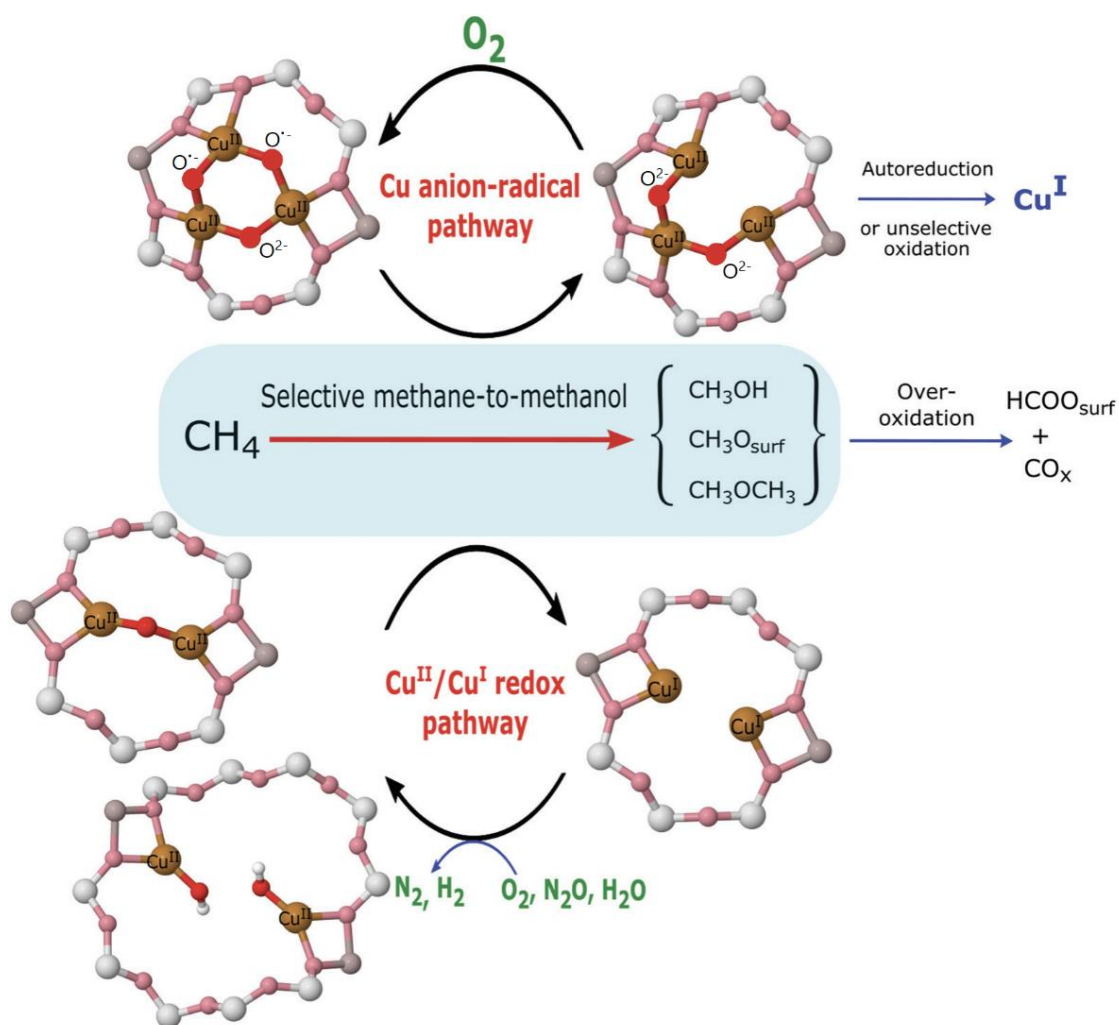


Figure 12. Illustration of two possible reaction mechanisms for oxidation of methane to methanol over Cu-zeolites. In the top row, the oxidation proceeds *via* the formation of oxyl radicals, while the bottom row shows the reaction occurring over a $\text{Cu}^{\text{II}}/\text{Cu}^{\text{I}}$ redox pair. Adapted from [67].

2.1.4. Structure-Reducibility Relationships

In support of the idea that the Cu^{I} -fraction is linked with methanol production, several studies have shown important activity-reducibility effects in recent years. Pappas et al. compared the reducibility of three Cu-CHA with different Si/Al ratios ($\text{Cu}/\text{Al} = 0.5$, $\text{Si}/\text{Al} = 5$, 15, and 29) and showed a linear correlation between these materials Cu^{I} formation during helium (He) activation (“self-reduction”) and their methanol productivity, indicating an important correlation, and that “self-reduction” in He could be used as a type of descriptor for activity. “Self-reduction”

is a well-documented event occurring upon heat treatment of Cu^{II}-exchanged zeolites [195-199].

Sushkevich et al. then compared the “self-reduction” of Cu-exchanged MOR, MFI, BEA, and FAU. To do so, they first pretreated the samples in O₂ at 400 °C (1 h), before they lowered the temperature to 100 °C, and exposed the samples to He while ramping up the temperature (8 °C/min) [139]. To follow the reduction, they performed linear combination fitting (LCF) analysis of the XANES spectra and found that Cu-FAU and Cu-BEA started to reduce at the highest temperature (~500 °C), Cu-MOR at ~450 °C while Cu-MFI reduced much earlier than the other samples (~330 °C). Then, upon comparing three different Si/Al ratios of MOR, they found that the sample with the highest Al content was the first to reduce. Combining these findings, the authors proposed that “self-reduction” is favored at lower temperatures in materials forming multimeric Cu^{II}-oxo sites. Interestingly, the difference between high and low Si/Al ratios in Cu-MOR is not observed in the Cu-MOR studies by Svelle and coworkers. They showed that the most active sample for MTM has well-distributed dimeric Cu-oxo species with high coordination and uniform bond lengths. The most active sample, with Si/Al = 7, is observed to have a higher fraction of “self-reduction” resistant Cu-species compared to a sample with Si/Al = 11 [120, 141]. This contradicts the findings by Sushkevich et al. [139].

In a continued study on the Cu-exchanged MOR, MFI, BEA, and FAU, Sushkevich et al. used CH₄-TPR (temperature-programmed reduction) to look at the reducibility of the Cu-sites in the real reducing agent. Again, performing LCF analysis of the XANES spectra, the authors found that Cu-sites in FAU reduced at a much higher temperature than the other zeolites. This was similar to the effect observed under “self-reduction” and led the authors to change the reaction protocol for Cu-FAU. Under regular conditions with CH₄ exposure at ~200 °C, Cu-FAU was practically inactive for methanol production, however, by increasing the

temperature to 360 °C, the authors saw a five-fold increase in methanol yield (25 $\mu\text{mol}_{\text{MeOH}}/\text{g}$). The authors varied the CH_4 partial pressure and found that upon increasing the pressure to 15 bar, a yield of 360 $\mu\text{mol}_{\text{MeOH}}/\text{g}$ was observed. This yield is twice that seen for the most productive Cu-MOR zeolite reported by Pappas et al. (175 $\mu\text{mol}_{\text{MeOH}}/\text{g}$), albeit the MOR zeolite was tested at 1 bar CH_4 pressure [120]. The study by Sushkevich et al. emphasizes that the stoichiometric reaction protocol is not one-size-fits-all. Clearly, descriptive techniques like CH_4 -TPR could therefore be key when attempting to optimize both the reaction protocol and zeolite material.

2.1.5. Co-Feed Studies

Some groups have also attempted to go beyond the regular stoichiometric routes and explore the continuous conversion of methane over Cu-zeolites. Narsimhan et al. first proposed a catalytic steady-state process over different Cu-zeolites in 2016 [200]. Upon first activating at a high temperature (550 °C) and then extracting methanol at 210 °C, they continued in a catalytic regime at 1 bar in a flow of 25 ppm O_2 , 3.2% H_2O , and 96.8% CH_4 . SSZ-13 had the highest rate with a site time yield of 0.006 $\text{mol}_{\text{MeOH}}/\text{mol}_{\text{Cu}}/\text{h}$. However, the steady-state process has many of the same issues as the earlier studies on gas-phase partial oxidation, as a very limited amount of O_2 can be present in the feed to obtain a high selectivity, which then compromises the CH_4 conversion. Notwithstanding these limitations, several groups have explored the catalytic protocol in recent years, where the contribution of H_2O has gained focus in the reaction feed [201, 202]. In an isotopic study over Cu-SSZ-13, Koishybay and Shantz found evidence from isotopic labeling experiments that it is H_2O which is the O donor in the MTM reaction [101]. This shed a whole new light on mechanistic studies, especially involving the necessities for active site formation, the desorption process, and the regeneration of active sites. Water as an oxidant was further corroborated by Sun et al., who

studied different parameters and achieved as much as 0.5 mol_{MeOH}/mol_{Cu}/h over a Cu-CHA with 91% selectivity [103]. Compared to the most productive Cu-MOR in the stoichiometric, cyclic regime (Figure 8), the productivity is about 20 times higher (0.18Cu,H-MOR(7) \approx 0.024 mol_{MeOH}/mol_{Cu}/h). In even more exploratory terms, the positive effect of water has recently been shown on non-zeolitic systems like mixed metal oxides (CeO₂/Cu₂O/Ir) and Au nanosheets [203-205].

Sushkevich et al. have likewise shown that water can act as a soft oxidant in the stoichiometric conversion of methane to methanol [125]. A Cu-MOR sample was exposed to He (400 °C), contacted with CH₄ at 7 bar pressure (200 °C), and then methanol was extracted by exposure to H₂O, while slowly reheating the sample to 400 °C. Then the cycle was repeated 5 times, and a stable productivity of 0.2 mol_{MeOH}/mol_{Cu} was obtained. Their studies indicated that activating the samples only at 200 °C led water to “poison” some of the active sites by hydrating them. Interestingly, some activity is regained by increasing the methane partial pressure (25 bars), which facilitates for C–H activation over some of the “poisoned” sites [125, 135].

2.1.6. Open Questions

The key advancements presented here show that considerable ambiguity remains in different areas of the MTM research. Figure 13 summarizes keywords in this regard. To have a better foundation for optimizing materials and the reaction protocol, some parts should be further analyzed and understood. The specific nature of the active sites after activation is still dubious, and everything from monomeric to Cu clusters is proposed. Several different species may likely form among the various frameworks. Regardless of the exact Cu-speciation, moving forward we suggest it is important to focus on understanding which sites are most active towards methane activation and selective methanol formation. In other words, searching for more structure-activity relationships. There should,

furthermore, be an increased focus on unraveling the complete reaction scheme because the dynamic behavior of the Cu-oxo sites in the different steps of the reaction is not fully understood. Other open questions are: 1) Upon methane interaction, which species form and how do they behave when contacted with water? 2) Brønsted sites have been shown to have an important role in stabilizing the methoxy intermediates. Is this the only role of Brønsted sites? 3) What is the nature of the active sites upon regeneration, and how does the oxidant (e.g. O₂ or H₂O) influence the nature of the active sites? 4) What is the effect of higher CH₄ partial pressure on the nature of the active sites?

In this introduction, we have also seen that exploring untested zeolite frameworks for MTM, new synthesis procedures, and ion exchange techniques are other means to learn more about the potential Cu-speciation and improving the overall yield. Understanding the influence material properties, such as Al siting, Cu loading, and T-sites have on the MTM reaction should also unequivocally be a focus area in the imminent future as this will allow us to gain more control over the improvements of the MTM protocol.

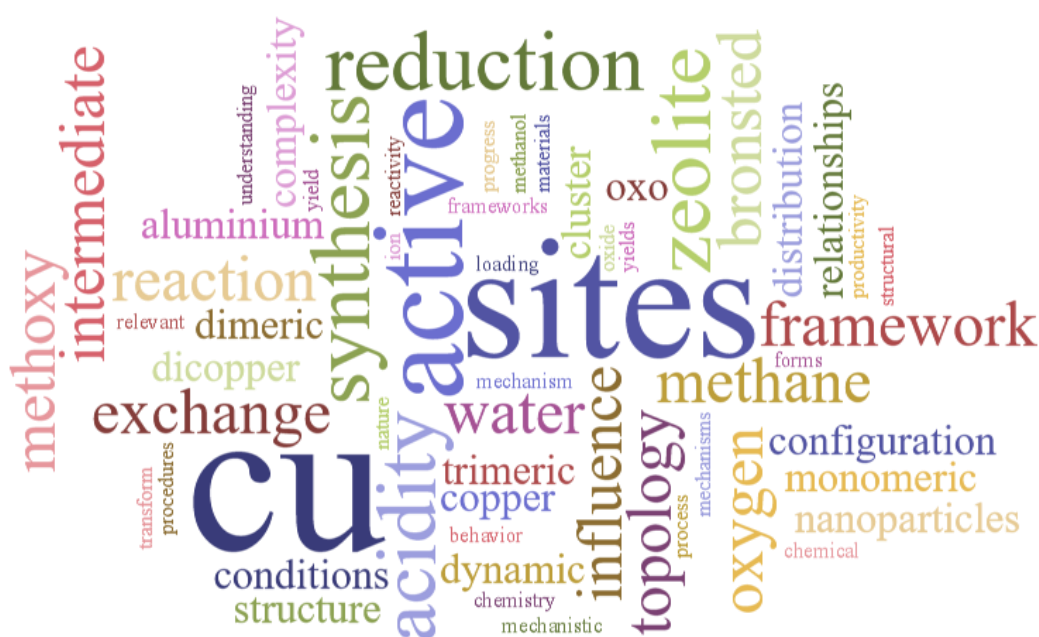


Figure 13. Word cloud summarizing important keywords in the MTM research.

With the results presented in this thesis, I aim to shed light on some of the questions presented above. Among other things, we combine temperature-programmed reduction experiments with *in situ* spectroscopy to learn more about the dynamic nature of the Cu-sites upon exposure to a reductant. In other experiments, we explore the framework composition and structure to obtain new structure-activity insight. Additionally, in an exploratory experiment, we expose the Cu-oxo sites in a zeolite to ethane instead of methane during the stepwise protocol. Such an experiment allows us to compare the behavior of Cu-zeolites in an ethane atmosphere to the well-known MTM process so that we can learn more about the general C–H activation process. The next chapter provides a small overview of the key ethane activation processes that are proposed in the literature thus far.

2.2. Ethane Activation

Since Cu-sites in zeolites can activate methane species, it is natural to explore whether these sites are also capable of activating other hydrocarbons. This was also briefly mentioned by Groothaert et al. in their groundbreaking study on MTM [61]. A fast disappearance of the $22\,700\text{ cm}^{-1}$ band in UV-vis already at room temperature (RT) indicated that the Cu-sites were activating the C–H bond in ethane faster than for methane, which is supported by the lower C–H bond strength in ethane. Upon extraction they obtain ethanol and acetylene, though, the yield is unfortunately not reported. Many pathways have been suggested for direct ethane conversion at lower temperatures to reduce the intensive energy consumption of steam cracking [206, 207]. Some of these pathways are aromatization to ethylene and aromatics, ethane non-oxidative (EDH) and oxidative (ODH) dehydrogenation [208], as well as ammoxidation and partial oxidation to ethylene and oxygenates [208]. The ODH and EDH routes have been investigated extensively. Non-oxidative ethane dehydrogenation typically

requires high temperatures and low pressures to push the reaction equilibrium toward product formation due to its endothermic nature. However, a high temperature could lead to less controllable gas phase reactions between the reactants and products and therefore, these temperature limitations often lead to equilibrium constraints for EDH reactions. Nevertheless, some non-oxidative dehydrogenation reactions to ethylene at medium-high temperatures (~ 600 °C) over e.g. supported Pt and supported Cr_2O_3 has been demonstrated [209, 210]. ODH, however, is exothermic and can therefore be operated at lower temperatures. The typical range is 300-700 °C, and a large variety of supported metals, oxides, and mixed-metal catalysts have been investigated for the reaction [207]. The main drawback of ODH is that measures need to be taken to limit the over-oxidation of the products to CO_2 and it is important to find safe operational modes due to the highly exothermic nature of the reaction. One route to compensate for this has been to perform CO_2 -assisted ODH, but with CO_2 the reaction again become endothermic, and higher reaction temperatures are necessary (>550 °C) [211]. Partial oxidation of ethane with H_2O_2 at 50 °C over Fe and Fe/Cu-loaded zeolites is another interesting pathway that has been suggested by Forde et al. [212]. The authors show that different reaction pathways occur, depending on the ion-exchanged metal. Cu promotes the formation of ethylene, while Fe promotes acetic acid. Ni-Y zeolites have also been shown to selectively activate ethane over a combination of Ni^{2+} and NiO sites. The reaction occurs at the Ni^{2+} sites at temperatures around 600 °C, but with very high selectivity as the authors claim that the NiO sites can be used to oxidize the produced H_2 and thus inhibit the continued oxidation of the desired product [213]. Finally, it is also interesting to note that the partial oxidation of ethane at low temperatures (~ 75 °C) is possible over an iron-based MOF. The MOF form Fe-oxo intermediates from oxidation in N_2O that can be used to activate ethane to form ethanol and acetaldehyde [214].

3. Experimental Methods

3.1. Material Preparation

Below follows an overview of the Cu-zeolites applied in this thesis and their synthesis and ion exchange procedures. Most of the samples were prepared by others, and in those cases, as the synthesis procedure is not a major focus in this thesis, I refer the reader to the specific paper for experimental details of the preparation of these materials. Details on the Cu ion exchange of SAPO-34, MCM-22, SiO₂, and SiO₂/Al₂O₃ is provided herein in section 3.1.1.

Both the synthesis and ion exchange procedure of the Cu-SSZ-13 samples used in **Paper I** and **Paper V** was performed by Haldor Topsøe A/S and details are reported in the works by Pappas et al. [94] and Janssens et al. [215].

The parent MOR zeolites applied in **Paper IV** and **Paper V** were obtained from a commercial supplier. NH₄-MOR(11) (CBV21A) and Na-MOR(7) (CBV10ADS) were both obtained from Zeolyst. The materials were subjected to LIE by Dr. Michael Dyballa and details are given in our previous work [114].

The parent zeolites applied in **Paper III** were all obtained from a commercial supplier: FAU (USY) zeolite (Zeolyst International (CBV500), Si/Al = 2.9), MOR zeolite (CBV21A, Si/Al = 10.3), BEA zeolite (Zeochem International (ZEOCAT PB/H), Si/Al = 12.5-17.5) and ZSM-5 zeolite (Zeolyst International (CBV5020), Si/Al = 25). The samples were ion exchanged using an SSIE method with CuCl by Ph.D. student Fabian Schlimpen from the University of Strasbourg. Details on the ion exchange procedure can be found in **Paper III**. All samples were prepared with an intended Cu/Al ratio ≈ 0.80 , except one Cu-MOR that was made with a lower Cu/Al ratio (~ 0.30) for comparison. Throughout the experimental section, this family of zeolites will be referred to as the SSIE zeolites.

The parent SAPO-34 material was synthesized by SINTEF according to the synthesis route reported by Mertens [216]. Details can be found in **Paper I**.

The parent MCM-22 material was synthesized by an M.Sc. student at the University of Oslo, Markus Sørensen. Details on this synthesis can be found in the supporting information of **Paper II**.

3.1.1. Ion Exchange

2 g of 5wt%-CuSiO₂ and 2.5wt%Cu-SiO₂/Al₂O₃ were prepared with incipient wetness for use in **Paper V** by following the procedure reported by Proding et al. [217]. The Cu-exchanged samples were prepared via wet impregnation. A slurry was made by impregnating SiO₂ or SiO₂/Al₂O₃ with a copper nitrate solution, Cu(NO₃)₂ × 3H₂O. About 3 g of distilled water was used to make the copper nitrate solution as this was the amount needed to make a slurry with the parent material. The slurry was then dried over night at 100 °C, before calcined at 350 °C for 3 h (ramp rate = 10 °C/min) in a static atmosphere. The wt.% of Cu is determined based on the intended ratio between Cu and SiO₂ or aluminium before exchange.

The H-form of SAPO-34 and MCM-22 was obtained by calcining the materials in static air at 600 °C for 15 h. The heating rate was 2 °C/min, starting from RT.

The samples were then ion-exchanged with Cu using LIE. A Cu(Ac)₂-solution (x M) was prepared and stirred with the material (60 ml solution/g of zeolite) at RT for 24 h. The specific concentration of the ion exchange solution is given in Table 2. The pH of the solution was kept in the range of 5.5-6. After stirring, the material was washed and centrifuged three times. For the high-loaded SAPO-34 material, the process was repeated three times with a calcining step between each round (600 °C, 15 h, 2 °C/min) to increase the Cu loading. The Cu(Ac)₂ solution used in the first round was 0.02 M. For the second and third rounds, a Cu(Ac)₂-solution resulting in a Cu/Si ratio of 0.5 was used (0.008 M).

3.2. Physicochemical Characterization

All details on the physicochemical analysis of the previously reported materials, Cu-MOR and Cu-SSZ-13, can be found in the respective papers by Dyballa et al. [114] and Pappas et al. [94]. The relevant elemental composition and MTM activity of these materials are repeated in Table 3.

Powder X-Ray Diffraction (pXRD) is used to verify a material's crystal structure and crystallinity and identify possible intergrowths or phase impurities. Larger Cu nanoparticles or clusters can also be identified by the presence of specific peaks in the diffractogram. pXRD patterns were obtained with a Bruker D8 Discovery diffractometer with Cu K α radiation ($\lambda = 1.5418 \text{ \AA}$). Measurement details and collected pXRD patterns of SAPO-34 (**Paper I**), MCM-22 (**Paper II**), and the SSIE exchanged samples, FAU, MOR, MFI, and BEA (**Paper III**), are found in their respective papers.

With **N₂-physisorption**, the internal surface area of a zeolite can be determined by measuring the monolayer coverage of N₂ in the pores. Cu-SSZ-13, Cu-MOR, and Cu-SAPO-34 were collected on a BelSorp MINI instrument. The materials were first pre-treated in vacuum (1 h at 80 °C, and 2 h at 300 °C). H-MCM-22 were collected on a BELSorp Maxi volumetric gas adsorption instrument (MicroTrac MRB) at -196 °C. Before the measurements, the sample was pretreated in vacuum at 300 °C for 10 h. To obtain the specific surface area, the Brunauer-Emmett-Teller (BET) approximation was used in a p/p_0 range relevant for microporous materials as defined by Llewellyn *et al.* [218].

Scanning Electron Microscope (SEM) images were collected to investigate the crystal morphology and by collecting backscattered electrons (BSE) images, the presence of small Cu nanoparticles could be detected. Images were obtained using a Hitachi SU8230 microscope. The acceleration voltage for SEM images was set to 2 kV and the emission current to 10 μA . For the collection of BSE images, only 0.5 kV was applied. The elemental composition of Cu-MOR, Cu-SSZ-13, and Cu-

SAPO-34 was determined by collecting energy-dispersive X-ray spectroscopy (EDX). A small amount of powder was pressed (5 tons) into a self-supporting wafer before the EDX measurements. Three different areas (200x200 μm^2) were measured with an accelerating voltage of 20 kV and emission current of 30 μA to calculate the average elemental composition.

To obtain the elemental composition of Cu-MCM-22 and the SSIE zeolites, **Microwave Plasma Atomic Emission Spectroscopy (MP-AES)** was applied. Before analysis, 1 mL 15% hydrofluoric acid (HF) was used to dissolve 20 mg of the sample in a Teflon liner for 1 h. The use of hydrofluoric acid requires special precautions (Safety note). A light was centered on the Teflon liner to verify that all solid materials were dissolved. 5 wt% H_3BO_3 was then added to quench excess fluoride anions. The resulting solution was diluted with 50 mL water, and an Agilent 4100 MP-AES instrument was utilized to analyze the solution. External calibration curves based on elemental standards were employed to determine the amount of Si, Al, and Cu in $\mu\text{mol/g}$. As determined by EDX or MP-AES, relevant elemental composition is reported in Table 2 and Table 3.

With **Thermogravimetric Analysis (TGA)**, the water content (in %) of the samples was measured. This was used to determine the dry weight of the samples for effluent quantification. For the measurements of Cu-MOR, Cu-SSZ-13, and Cu-SAPO-34, a Stanton Redcroft furnace was used, while a Netzsch STA 449F Jupiter system was employed for Cu-MCM-22 and the SSIE zeolites. ~ 20 mg of material was added to Pt crucibles and heated to 300 $^\circ\text{C}$ with a ramp of 2 $^\circ\text{C}/\text{min}$. The protocol was performed in a flow of synthetic air.

Table 2. The chemical composition of Cu-exchanged zeolites used in **Papers I, II, and III** and reported in Chapter 4.

Sample	Cu Exchange	Si/Al	Cu/Al	Cu wt.% (%)
0.08CuSAPO-34	LIE [Cu(Ac) ₂] = 0.02 M	14.9 ¹⁾	0.08 ¹⁾	0.5
0.25CuSAPO-34	LIE [Cu(Ac) ₂] = 0.02 M (3x) ²⁾	14.9 ¹⁾	0.25 ¹⁾	1.6
0.50CuSSZ-13	LIE [Cu(Ac) ₂] ³⁾	14.8	0.53	3.4
0.25Cu-MCM-22	LIE [Cu(Ac) ₂] = 0.01 M	15.2	0.25	1.7
0.30Cu-MCM-22	LIE [Cu(Ac) ₂] = 0.02 M	15.2	0.30	2.0
Cu ^I -ZSM-5	SSIE m _{CuCl} → Cu/Al ≈ 0.8	18.4	0.78	4.2
Cu ^I -BEA	SSIE m _{CuCl} → Cu/Al ≈ 0.8	35.7	2.0	5.9
Cu ^I -MOR	SSIE m _{CuCl} → Cu/Al ≈ 0.8	12.0	0.89	7.2
Cu ^I -USY	SSIE m _{CuCl} → Cu/Al ≈ 0.8	2.9	0.74	20.2
0.30Cu ^I -MOR	SSIE m _{CuCl} → Cu/Al ≈ 0.3	11.8	0.31	2.5

¹⁾ For SAPO-34, the Si/Al ratio is given as (Al+P)/Si, while Cu/Al is given as Cu/Si. ²⁾ The CuAc₂ solution used in the first round was 0.02 M. For the second and third rounds, a Cu(Ac)₂-solution resulting in a Cu/Si ratio of 0.5 was used (0.008 M). ³⁾ Exact LIE conditions are reported by Janssens [215].

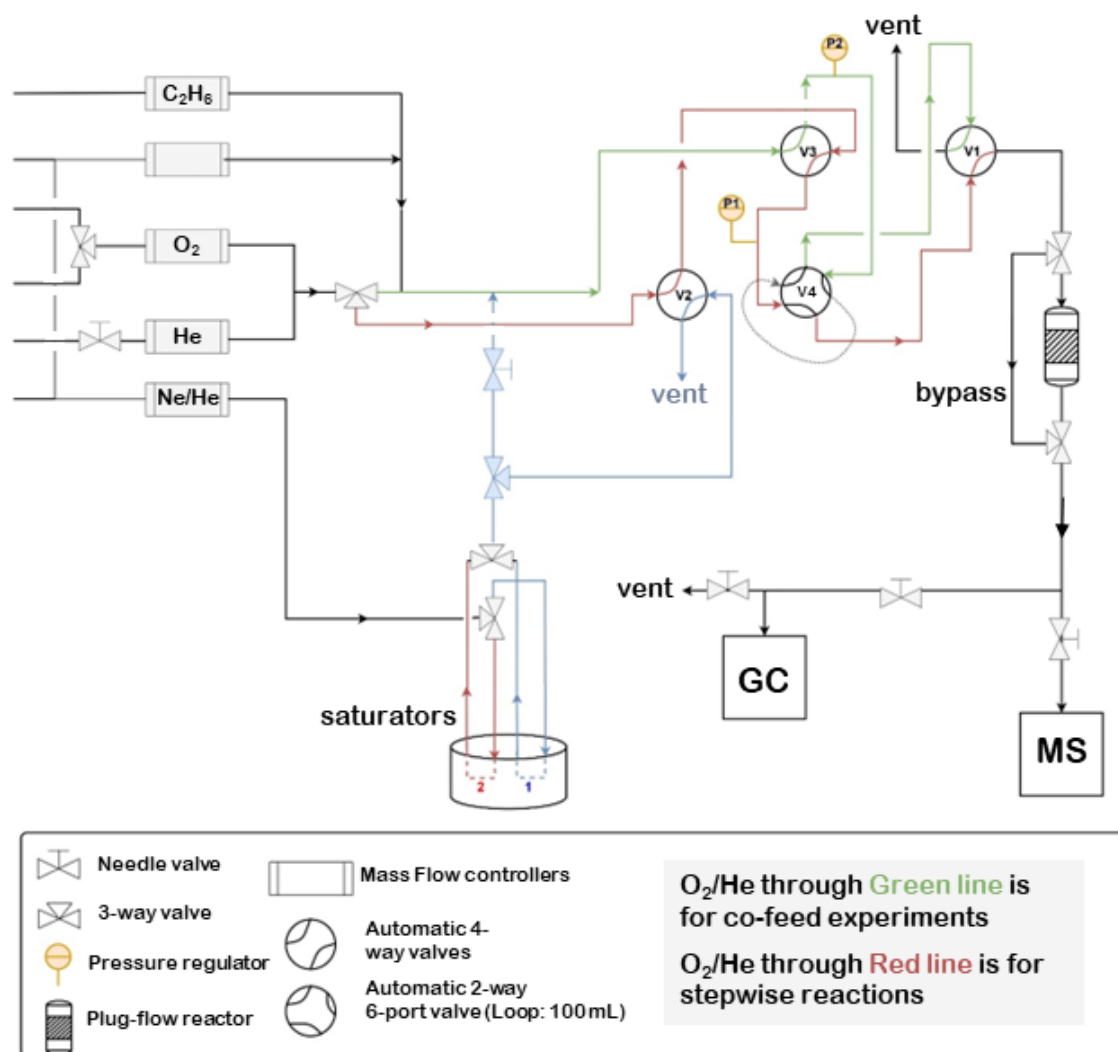
Table 3. Chemical composition and MTM performance of materials used in **Paper V** and reported in Chapter 6. 0.36Cu,H-MOR(11) and 0.18Cu,H-MOR(7) (green shading) were also used in Paper IV (reported in Chapter 5)

Sample name	Si/Al	Cu/Al	Cu wt.% (%)	MTM* Productivity (mol _{MeOH} /mol _{Cu})	MTM* Yield (μmol _{MeOH} /g)
H-MOR(11) ¹⁾	11	-	-	-	-
0.19Cu,H-MOR(11) ¹⁾	11	0.19	1.67	0.24	64
0.36Cu,H-MOR(11) ¹⁾	11	0.36	3.18	0.25	123
0.32Cu,Na-MOR(11) ¹⁾	11	0.32	2.83	0.17	74
0.18Cu,H-MOR(7) ¹⁾	7	0.18	2.33	0.47	172
0.35Cu,H-ZSM-5(11) ²⁾	11.5	0.35	2.88	0.10	43
0.30Cu,H-SSZ-13(12)	12.1	0.34	2.68	0.16	67
2.5wt%-Cu/SiO ₂ /Al ₂ O ₃	14.6	0.38	2.5	-	-
5wt%-CuSiO ₂	-	-	5	-	-

¹⁾ Elemental composition, such as Si/Al, Cu/Al, and Cu wt.%, along with the MTM productivity and yield of the Cu-exchanged MOR zeolites and the 0.30Cu,H-SSZ-13(1) sample have been determined by Svelle and co-workers in previous publications [94, 114, 120]. ²⁾ The MTM activity of 0.35Cu,H-ZSM-5(11) was measured following Test #1 (Table 4). The elemental composition was previously reported by Deplano et al. [219].

3.3. Performance Testing

Methane activation tests were performed on a purpose-designed setup [94, 120, 140, 220] with an online mass spectrometer (MS) monitoring the effluent. For ethane activation tests another setup was built where the effluent was monitored both by an online MS and a gas chromatograph (GC) equipped with a flame ionization detector (FID). In both reaction schemes, 100 mg of sample was weighed, sieved (425 – 250 μm), and placed in a linear quartz tube reactor (i.d. = 6 mm). A thermocouple inside the oven was used to control the temperature. The temperature setpoints were calibrated in an initial test experiment by placing a thermocouple inside a quartz sheet and touching the sample bed while following a full protocol. A stepwise protocol was applied for the experiments. The gases were kept separate with the help of different mass flow controllers (MFCs) for each gas, as well as stop- and 4-way valves (The flow scheme of the reactor setup designed for ethane activation is reported in Scheme 2 as an example). The reference protocol for methane activation follows the following protocol: the sample is first ramped up to 500 °C in O₂ (100%) before it is activated for 8 h. Then the temperature is lowered (5 °C/min) to 200 °C, and He (100%) is sent onto the sample (~45 min) to flush the system. Then CH₄ (100%) is sent onto the sample (3 h), before a second flushing step in He (~45 min) is initiated. Finally, a Ne/He (10%/rest) flow saturated with 10% water was sent onto the sample (2 h). All flows were kept at 15 ml/min. The water concentration was controlled by a bubbler immersed in an oil bath (silicon oil) kept at 45 °C. Test #1 and #2 in Table 4 summarize the respective key parameters for the reference methane and ethane activation protocols.



Scheme 2. Flow scheme of the multi-purpose reaction set-up designed for ethane activation experiments. The setup is designed with the possibility of performing both stepwise and co-feed (steady-state) experiments. It is also made with options to perform pulsing and SSITKA experiments.

An online quadrupole mass spectrometer (MS) (Omnistar GSD320, Pfeiffer) was connected to the outlet of the reactor to analyze the effluent from methane activation (Test #1). The quantitative analysis of the product yields related to methane activation (CH₃OH ($m/z = 31$), CH₃OCH₃ ($m/z = 46$), CO ($m/z = 28$), and CO₂ ($m/z = 44$)) in $\mu\text{mol/g}$ was obtained with the help of an external calibration bottle with known amounts of the products. The material performance in the MTM reaction is reported either as the total yield of methanol produced per gram of zeolite (3) or normalized to the Cu content (4). To determine the selectivity, the

yields of CH₃OH and CH₃OCH₃ (MeOH) are divided by the total conversion of methane (5). The additional components are CO₂ and some CO (CO_x).

$$Yield_{MeOH} (\mu\text{mol}/g) = Yield_{CH_3OH} + (2 \times Yield_{CH_3OCH_3}) \quad (3)$$

$$Productivity (mol_{MeOH}/mol_{Cu}) = \frac{Yield_{MeOH}}{Cu (\mu\text{mol}/g)} \quad (4)$$

$$Selectivity (\%) = \frac{Yield_{MeOH}}{Yield_{MeOH} + Yield_{CO_x}} \times 100 \quad (5)$$

In **Paper I**, the results from test #1.1 (Table 4) were analyzed with the online MS as described above, while the results from test #1 were analysed with a GC-MS similar to Cu-SSZ-13 and Cu-MOR reported previously [94, 114]. The GC-MS was a Hewlett Packard 6890/6972 equipped with a Supel-Q PLOT capillary column and used He as carrier gas. Effluent analysis was conducted isothermally at 125 °C and the analysis time was 3.5 min. Samples were injected every 4 minutes and repeated 30 times during the extraction step. Combined, the chromatography and mass selective detector allowed separation and accurate analysis of all relevant components in the effluent.

Since ethylene was found to be a key product from ethane activation, an online MS was not enough to separate the m/z fragments. A test setup including a gas chromatograph (GC 6890N, Agilent) equipped with a Plot U column and an FID detector with He as the carrier gas, was therefore employed to quantitatively analyze the product yields by separating the responses from ethane and ethylene by their retention times. For quantitative analysis of ethylene, a low-temperature sampling method was used where the analysis time was 5.5 min at 40 °C, and this was repeated about every 6 min for 2 h. For qualitative analysis of the effluent, a longer method was applied to capture all possible products. The long method included an initial step of 6 min at 40 °C, before the column was heated to 150 °C (20 °C/min) and then kept at 150 °C for 5 min.

The quantitative analysis of the C₂H₄ yield in μmol/g (yield_{C₂H₄}/g) was calculated with the help of an external calibration curve made with a calibration bottle with known amounts of the products. The Productivity was determined by normalizing to the Cu content (mol_{C₂H₄}/mol_{Cu}). Other C₂₊ products (e.g. C₄H₈ and CH₃CH₂OH) were determined from the long analysis method by their relative peak area to the area of the ethylene peak. Test #2 (Table 4) is the reference condition for ethane activation. Alterations to the parameters reported here are specifically explained in the results.

Table 4. Reference test conditions applied for methane and ethane activation.

Test	Process Steps	Temperature (°C)	Time (h)
#1 Reference CH₄- activation	1) 100% O ₂	500	8
	2) 100% CH ₄	200	3
	3) 10% H ₂ O/(Ne/He)	200	1.5
#1.1	1) 100% O ₂	500	8
	2) 100% CH ₄	300	3
	3) 10% H ₂ O/(Ne/He)	200	1.5
#2 Reference C₂H₆- activation	1) 100% O ₂	500	8
	2) 5% C ₂ H ₆ in He	150	3.5
	3) 10% H ₂ O in Ne/He	150	2

3.4. Microcalorimetry (NH₃ and CH₄)

NH₃-microcalorimetry, a powerful technique providing information on the heats of adsorption of various acidic sites as well as the adsorption isotherms were applied to study H- and Cu-MCM-22 (Subchapter 4.2). The microcalorimetry

experiments were carried out by Ph.D. student, Moses Mawanga at the Norwegian University of Science and Technology (NTNU). Instrumental details can be found in **Paper II**. Before each adsorption experiment, the samples were pretreated and activated with the following protocol. Typically, 0.2-0.3 g of sample was placed in a quartz calorimetric cell maintained at 80 °C. The sample was dried in argon at 160 °C for 1-3 hours, followed by a temperature ramp in pure oxygen at 5 °C/min to 500 °C. The sample was held at 500 °C for 480 minutes before cooling to 200 °C in oxygen flow. Once at 200 °C the flow was switched back to argon for 60 minutes and later cooled to room temperature and isolated from the external atmosphere to avoid exposing the activated sample to atmospheric humidity. The sample containing cell was transferred to the calorimeter, well maintained at 80 °C, and outgassed to a dynamic vacuum of 10^{-8} mbar until a stable baseline was achieved. Successive micromolar doses of NH_3 were introduced to the sample until the sample became saturated (i.e., no noticeable changes in the heat flow signal with more doses). Between the primary and secondary adsorption, the sample was outgassed at 80 °C for ~10 h until the heat flow curve returned to baseline.

The same protocol was followed for CH_4 adsorption, except that the adsorption temperature was set to 300 °C.

3.5. Temperature-programmed Desorption (TPD)

n-Propylamine-temperature programmed desorption (TPD) experiments to study the amount of Brønsted acid sites of both the protonic and Cu-exchanged material were performed on a homemade flow set-up. The effluent from the desorption was detected by an online Pfeiffer Omnistar quadrupole mass spectrometer. About 30 mg sample was activated in a flow of synthetic air (50 ml/min) for 1 h at 500 °C (ramp rate = 10 °C/min). The sample was then cooled to 170 °C before being exposed to N_2 gas flow (50 mL/min) saturated with n-propylamine vapors for 1 h. All excess n-propylamine was flushed from the system with N_2 (66 ml/min, 4 h)

before the desorption protocol was initiated (ramping 10 °C/min in 66 ml/min N₂ up to 500 °C). The total amount of propene (m/z = 41) released from the system was quantified using a calibration gas that was sent into the system at the end of the experiment.

NH₃-TPD was performed to study both Lewis and Brønsted acid sites. Ca. 30 mg pelletized protonic and Cu-exchanged zeolite was used comparably to the n-propylamine-TPD. After an initial activation step in synthetic air, the sample kept at 170 °C was exposed to 2% NH₃ in N₂ (50 ml/min) for 4 h. This was followed by flushing in inert N₂ (66 ml/min) for 4 h before heating to 575 °C (10 °C/min) in N₂. The amount of NH₃ released (m/z = 16) was quantified using the calibrant 2% NH₃ in N₂ upon stabilizing at the end of the adsorption step.

3.6. CH₄-Temperature-programmed Reduction (TPR)

Two different setups in the University of Oslo (UiO) laboratory were used for CH₄-TPR experiments on Cu-SAPO-34/SSZ-13 (**Paper I**) and the SSIE zeolites (**Paper III**). *In situ* UV-vis CH₄-TPR experiments were additionally performed on the Cu-MOR zeolites (**Paper IV**) at the University of Turin (UniTo) (*vide infra*). An overview of the experiments is presented here, while the reader is referred to the respective paper for specific experimental details. The experiments were performed using quartz fixed bed reactors, while the effluent was monitored with an online Pfeiffer MS. About 100 mg of material was used for the measurements. CH₄ (5% in He), He (100%), and O₂ (100%). The reaction protocol consisted of heating the material at 500 °C in O₂ (100%) for 8 h before the reactor was cooled to 100-120 °C and flushed with He (100%) for about 1 h. Then CH₄ was introduced, while the temperature was ramped (5 °C/min) to 550-650 °C. The temperature was recorded simultaneously with a thermocouple placed on top of the sample bed. The output of the reactor was analyzed with an online MS.

By following the CH₄-TPR experiments with UV-vis spectroscopy, details on the Cu-coordination environment can be obtained from the observation of specific absorption energies from d-d electron transition as well as ligand-to-metal charge transfer (LMCT). The transition from Cu^{II} to Cu^I should also be possible to follow as Cu^{II} has a d⁹ electron configuration and will absorb light by d-d electron transitions while this is not possible in Cu^I, as Cu^I has completely filled d-orbitals (d¹⁰). In the UV-vis experiments the UV probe is placed into the middle of an oven, touching the tubular quartz reactor (9 mm i.d.) perpendicular to the reactor bed. The spectra were recorded in reflectance (%) mode on an Avantes AvaSpec-ULS2048XL-EVO fiber optics spectrometer (100 μm slits) with an Avantes AvaLight-DH-S light source (including both a deuterium and a halogen lamp). For the collection of diffuse reflected light from the sample, a custom high-temperature resistant fiber optic with a high-OH fused silica core (diameter = 100 μm) was used. Polytetrafluoroethylene (PTFE) powder was measured at room temperature (RT) as a 100% reflectance reference before the TPR experiments. UV-vis spectra were collected continuously at all steps of the protocol. For the TPR ramp, one spectrum, obtained as the average of 50 scans with 10 ms integration time each, was collected every 50 s.

3.7. Fourier Transform Infrared (FT-IR) Spectroscopy

With FT-IR spectroscopy, the vibrational fingerprint of different functional groups can be detected. By probing a zeolite with small molecules, their interaction with different parts of the zeolite framework can provide valuable information on the active sites. C₂H₄- and CO-adsorption experiments on the zeolite samples were performed at RT and measured on a Bruker Vertex 70 instrument equipped with a Mercury-Cadmium-Telluride (MCT) detector cooled with liquid nitrogen (LN₂). A thin, self-supporting wafer (~10 mg/cm²) of each sample was prepared and fitted inside a gold envelope. The envelope was placed in a low-temperature vacuum

cell with KBr windows before being heated to 450 °C and kept for 1.5 h. After being cooled to RT, incremental doses of C₂H₄/CO were exposed to the sample. An IR spectrum was collected after every dose. In the C₂H₄ atmosphere, after dosing, the samples were cooled with LN₂, before slowly outgassed and consecutively heated back to RT.

The CO-TPR experiment reported in chapter 5 was conducted on a Bruker Vertex 80 instrument equipped with an MCT detector. The material was pressed into a self-supporting wafer (7.5 mg/cm²) and placed inside an AABSPEC cell with low free volume (model #CXX), where both temperature and gas flow can be controlled. The sample was heated to 500 °C (5 °C/min) in a flow of O₂ (100%), before being cooled down to 120 °C (10 °C/min), where He (100%) was purged on the sample for 1 h. Then, the gas flow was switched to CO (10% in He) and ramped up to 500 °C (10 °C/min). A spectrum was collected every 40 s. To calculate the CO concentration (in μmol/g), the following form of Lambert-Beer law was applied:

$$A = \varepsilon \times C \times \rho \quad (6)$$

where A (cm⁻¹) is the integrated absorbance defined in a specific spectral region, ρ (mg/cm²) is the pellet density, ε (cm/μmol) is the molar attenuation coefficient (11.5 cm/μmol) obtained from Deplano *et al.* [219], and C (μmol/g) is the concentration of CO.

3.8. Resonance Raman (rRaman) Spectroscopy

By probing a Cu-zeolites with specific wavelengths that Cu-sites are known to absorb from UV-vis spectroscopy, the vibrations coming from Cu-O species can be resonance enhanced in a rRaman spectrum. rRaman spectroscopy measurements were used herein to investigate Cu-O and O-O vibrations in the Cu exchanged SAPO-34 and SSZ-13 materials. The samples were investigated at RT, both as-synthesized (hydrated), as well as in sealed capillaries after activation in a static

air atmosphere. The sealed capillaries were prepared by filling boron-silicate glass capillaries (0.5 mm diameter and 0.01 mm wall thickness). The capillaries were then heated to 550 °C, with a 3 °C/min ramp, and kept overnight (14 h) at the same temperature. The capillaries were then sealed with a flame gun while hot, and then slowly cooled to RT. The rRaman spectra were collected with a blue laser (488 nm) and recorded with a Horiba LabRamanHR microscope, equipped with a Coherent Sapphire laser. The signal was dispersed over a grating with 1800 lines/mm on a thermoelectrically cooled charge-coupled device (CCD) detector. The excitation beam was focused on the sample with a 50x objective lens.

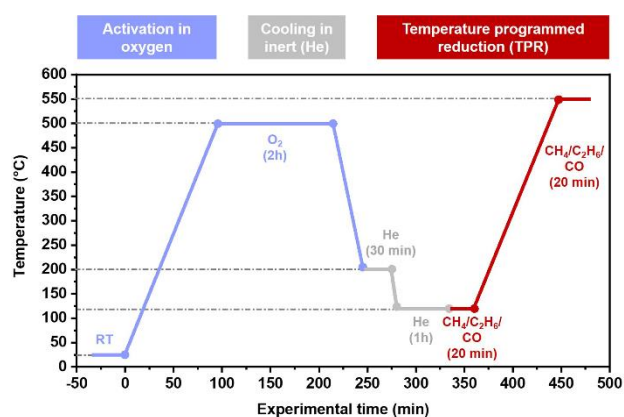
3.9. *In situ* X-ray Absorption Spectroscopy (XAS)

The XAS experiments reported herein were collected at the Swiss Norwegian beamline (SNBL), BM31, at the European Synchrotron Radiation Facility (ESRF). X-ray absorption spectroscopy is a powerful, bulk-averaging, element-specific technique. The X-ray Absorption Near Edge Structure (XANES) region can provide important information on the oxidation state and coordination number and geometry of the element. Then, from the Extended X-ray absorption Fine Structure (EXAFS) information on the absorber's environment can be obtained, e.g. neighboring atoms and bond lengths.

The Cu K-edge *in situ* XAS data were collected in transmission mode on the BM31 beamline of the European Synchrotron Radiation Facility (ESRF, Grenoble, France) [221]. The beamline was equipped with a water-cooled double-crystal monochromator (flat Si[111] pair) and ionization chambers, filled with a He/Ar mixture, was used for the detection of the incident (I_0) and transmitted photons (I_1) [222]. All the XAS spectra were collected with an acquisition time of ca. 3 min/scan.

TPR experiments were conducted in thin capillary reactors simultaneously as X-ray absorption spectra were collected. About 6 mg of sample were pressed

and sieved (160-125 μm) and placed into a quartz capillary (1.5 mm i.d. and 0.01 mm thickness) with a quartz wool plug at each end of the bed. The capillary was then glued to a special-designed bracket so that gas could flow through. The capillary was heated with a heat blower placed directly under the reactor bed. The temperature set points were calibrated with a thermocouple placed inside an empty capillary before the experiments. Three MFCs together with automatic 4-way valves (kept at 120 $^{\circ}\text{C}$ to remove traces of moisture) were used to control the flows of He (100%), O_2 (100%), and either CH_4 (2% in He), C_2H_6 (3% in He), or CO (5% in He). All flows were set to 5 ml/min, and the effluent was analyzed with an online MS. The reaction protocol is depicted in Scheme 3. Before the TPR ramp, the samples were heated to 500 $^{\circ}\text{C}$ in O_2 and kept in these conditions for 2 h before it was first cooled (10 $^{\circ}\text{C}/\text{min}$) to 200 $^{\circ}\text{C}$ and subjected to He for 30 min to clean away possible contaminants when switching the automatic 4-way valve between O_2 and He. Then the samples were cooled further to 120 $^{\circ}\text{C}$ and kept in inert treatment (He) for 1 h before being exposed to the reducing agent. After reaching a steady trace (~ 20 min) in the MS, the samples were heated at 5 $^{\circ}\text{C}/\text{min}$ up to 550 $^{\circ}\text{C}$.



Scheme 3. Experimental protocol for *in situ* XAS during TPR experiments over Cu-MOR samples. The protocol consists of activation in oxygen at 500 $^{\circ}\text{C}$, followed by two cooling steps. First, the sample was cooled in oxygen until 200 $^{\circ}\text{C}$ before a second cooling step to 120 $^{\circ}\text{C}$ in inert (He). Then the samples were exposed to a reductive atmosphere (either CH_4 , C_2H_6 , or CO) while the temperature was ramped up (5 $^{\circ}\text{C}/\text{min}$) to 550 $^{\circ}\text{C}$.

The obtained data were treated by M.Sc. student, Beatrice Garetto, at the UniTo. The data were normalized to unity edge jump at the Cu K-edge by the Athena software from the Demeter suite [223]. XAS uniquely gives access to local structural information without any need for long-range order in the Cu site distribution [224, 225]. However, in presence of different Cu species in the zeolite, the technique will provide an average signal over all the Cu sites in the mixture. In this regard, Multivariate Curve Resolution - Alternating Least Squares (MCR-ALS) analysis represents a powerful method to deepen the characterization, by resolving individual contributions from pure Cu species. MCR-ALS allows the decomposition of an experimental matrix D into pure contributions, such as spectra S matrix and the corresponding concentration profile C matrix: $D = C \cdot S^T$. Initially, the number of principal components (PCs) must be determined following a critical assessment of the results in terms of spectroscopic and chemical-physical meaningfulness [226-228]. The principal results that MCR-ALS returns are concentration profiles and spectra of pure components. The generation of the pure components was performed by initial guesses efficiently managed by specific methods, such as SIMPLISMA [229]. In this work, the whole experimental energy range (8800-9727 eV), including both the XANES and the EXAFS spectral regions, of normalized and energy-aligned XAS spectra was analyzed by MCR-ALS. To determine the pure spectra, the normalized $\mu(E)$ XAS spectra, starting from the pretreatment step under static conditions in O₂ at 500 °C, were organized in three datasets according to the reducing agent used during the TPR step, combining the datasets related to the two investigated Cu-MOR samples. MCR-ALS reconstruction was carried out using the MATLAB-based MCR-ALS Graphical User Interface (GUI) developed by Jaumot *et al.*, using Matlab R2022a [230]. For further details on the specific method implementation and the ALS quality control parameters, the interested reader is referred to the supporting information (SI) of **Paper IV**.

Synopsis of Results

4. Searching for Structure-Activity Relationships

Chapter 4 is the first of three chapters summarizing the results obtained in this thesis. Each chapter focuses on different parts of the uncharted territories in the research field of direct C–H activation over Cu-zeolites. In chapter 4, the reader is guided through a set of smaller stories, where the aim is to shed light on structure-activity relationships found when investigating different framework compositions, topology, and acidity effects, as well as Cu-exchange and positioning. Many different spectroscopic and adsorption/desorption techniques have been applied to investigate the “black box”. The chapter is built up from **Papers I, II, and III**, and aims to summarize and connect the key findings from each paper in the bigger picture of methane-to-methanol research.

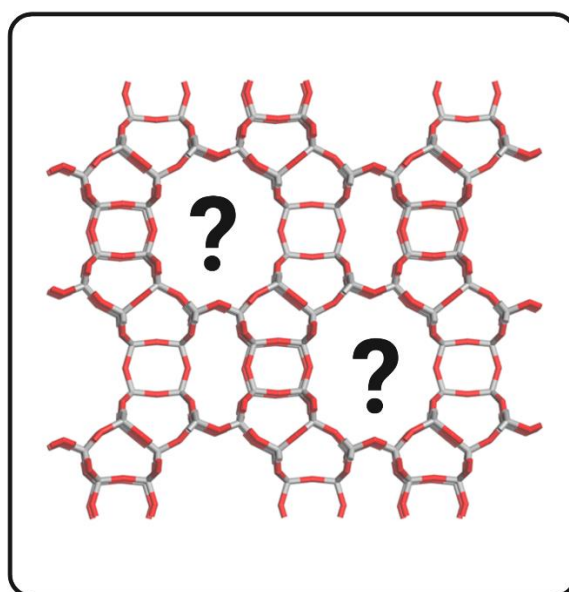


Figure 14. Illustration of the idea behind chapter 4. Unraveling the zeolite “black box”.

4.1. SAPO-34 vs SSZ-13

SAPO-34 is isostructural to SSZ-13, which has been tested in several studies for the MTM reaction [94, 96, 97, 103, 119, 200]. The SBUs in SAPO-34 are built from different elements than in SSZ-13 and SAPO-34 consequently has a slightly different framework polarity. Additionally, it is likely that the substitution mechanisms of Si in SAPO-34 leads to a different distribution of acid sites compared to SSZ-13. The zeotype SAPO-34 was investigated to understand the effect another composition could have on the Cu-speciation and consequently the MTM reaction, as most studies have focused on Cu-exchanged zeolites.

H-SAPO-34 was received by SINTEF, and with the use of $\text{Cu}(\text{OAc})_2$ LIE, two samples, namely 0.08CuSAPO-34 and 0.25CuSAPO-34 with a Cu/Si = 0.08 and 0.25, respectively, was prepared. Herein, the Cu-exchanged SAPO-34 material was compared with a Cu-loaded SSZ-13 (Cu/Al = 0.50), named 0.50CuSSZ-13. All physicochemical analyses results of the SAPO-34 samples can be found in the SI of **Paper I**. Physicochemical data on 0.50CuSSZ-13 is reported previously by Pappas et al. [94] and Janssens et al. [215].

4.1.1. Utilizing Spectroscopy to Investigate the Cu-Speciation

To study the nature of the Cu sites, several spectroscopic techniques were applied. rRaman was used to study the Cu species in an O_2 -activated state. With a blue laser (488 nm), several studies have reported the resonance effect of Cu-oxo species in zeolites, making rRaman a great technique to see fingerprints of Cu_xO_y -moieties. FT-IR was applied to study the difference between the accessibility and reducibility of the Cu-sites in SAPO-34 and SSZ-13 by following the interaction of “self-reduced” Cu^{I} with CO at RT to selectively probe the Cu sites [231, 232]. Finally, *in situ* XAS was applied to support the findings made with rRaman and FT-IR.

rRaman spectra of activated, sealed capillaries were collected with a blue laser (488 nm) at RT. The resulting spectra of hydrated and activated 0.25CuSAPO-34 (red) and 0.50CuSSZ-13 (blue) (measured previously by Pappas et al. [94]) are shown in Figure 15 (a). When comparing the spectra collected at RT to the spectra collected after O₂ activation, several new bands are observed. These bands are correlated to Cu^{II}-oxo species that are resonantly enhanced by the blue laser. Frequencies and reasonable assignments are summarized in the SI of **Paper I** and are based on previous assignments on other Cu-zeolites [94, 97, 118, 233].

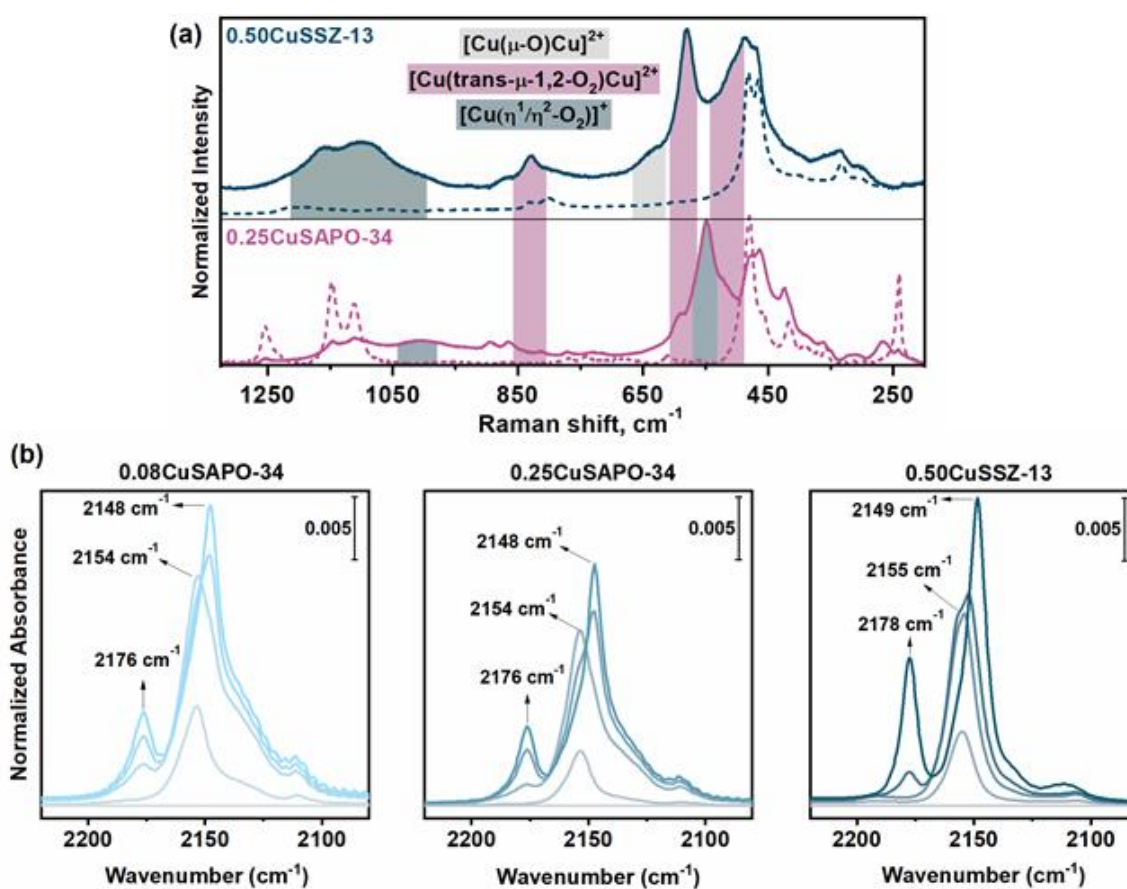


Figure 15. (a) rRaman spectra of hydrated (dashed) and activated (solid) 0.50CuSSZ-13 (top panel) and 0.25CuSAPO-34 (bottom panel). The contributions from different Cu_xO_y moieties are marked. Pink shading: [Cu(trans-μ-1,2-O₂)Cu]²⁺, light grey shading: [Cu(μ-O)-Cu]²⁺ and dark grey shading: [Cu(η¹/η²-O₂)]⁺. (b) FT-IR spectra of adsorbed CO at RT on 0.08CuSAPO-34 (light blue), 0.25CuSAPO-34 (blue), and 0.50CuSSZ-13 (dark blue). The CO pressure was increased from 20 μbar to 20 mbar. The materials were activated for 1 h at 150 °C, 300 °C, and 450 °C. The spectra are

background subtracted and normalized to the framework overtones as well as to the Cu content ($\mu\text{mol/g}$).

In total, four distinct Cu^{II} -oxo species with different spectroscopic vibrations were detected. The bands at 812, 524, and 587 cm^{-1} were assigned to a three-fold coordinated dicopper species, $[\text{Cu}(\text{trans-}\mu\text{-1,2-O}_2)\text{Cu}]^{2+}$, while the shoulder at 620 cm^{-1} is assigned to the closely related $[\text{Cu}(\mu\text{-O})\text{-Cu}]^{2+}$ [94]. The other two vibrational features were assigned to monomeric end-on and side-on superoxo Cu^{II} species ($[\text{Cu}(\eta^1/\eta^2\text{-O}_2)]^+$) [94, 118, 233]. In Cu-SAPO-34, only the vibrations of $[\text{Cu}(\text{trans-}\mu\text{-1,2-O}_2)\text{Cu}]^{2+}$ and $[\text{Cu}(\eta^2\text{-O}_2)]^+$ were detected. Additionally, even though Raman vibrations do not allow for any quantitative analysis of the Cu-species distribution, it is conspicuous that the most intense vibration in Cu-SAPO-34 comes from a four-fold coordinated monocopper species ($[\text{Cu}(\eta^2\text{-O}_2)]$). This result indicates that the Cu-speciation is different in the two CHA-type frameworks. SAPO-34 appears to form only long-distance dimeric and isolated monomeric Cu^{II} -oxo species. We conjecture this to be related to the more constrained distribution of Si in SAPO-34, leading to fewer Brønsted sites in proximity, which subsequently affects the Cu speciation.

The vibrations related to CO being perturbed by the Cu^{I} sites are depicted in Figure 15 (b) and show the evolution of mono- and dicarbonyl species on Cu. Already at small doses of CO, a band is evolving at 2154/2155 cm^{-1} related to the vibration of monocarbonyl adducts ($\text{Cu}^{\text{I}}\text{-CO}$) [231, 232, 234]. The normalized intensity of the $\text{Cu}^{\text{I}}\text{-CO}$ is more intense in the 0.08CuSAPO-34 sample compared to both the higher loaded Cu-SAPO-34 and the isostructural Cu-SSZ-13, indicating that a higher fraction of Cu^{I} sites is accessible by CO in the low-loaded Cu-SAPO-34. It may also be the case that some of the Cu-sites in the high-loaded SAPO-34 and/or SSZ-13 samples are more resistant to self-reduction and therefore remain as Cu^{II} [120]. This is also supported by a higher “self-reduction” behavior in Cu-SAPO-34, as observed with XAS performed during He-activation (See **Paper I**).

The bands at 2176/2178 cm^{-1} and 2148/2149 cm^{-1} develop with increasing CO pressure and are assigned to the symmetric and antisymmetric stretching vibration of dicarbonyl adducts ($\text{Cu}^{\text{I}}\text{-(CO)}_2$) [231, 232, 234]. These species are more easily formed in 0.50CuSSZ-13, as seen from the higher intensity of the bands. The increased amount of dicarbonyl adducts suggests that 0.50CuSSZ-13 has more freely coordinated Cu^{I} species where the Cu has only two or three oxygen framework neighbors. These results corroborate the findings from rRaman spectroscopy, suggesting that more of the Cu in SAPO-34 exist as monomeric isolated Cu-sites, compared to SSZ-13.

4.1.2. Comparing the CH_4 Consumption

Recently, temperature programmed reduction experiments with CH_4 have been shown to be useful for optimizing reaction parameters based on material composition. By monitoring CH_4 -TPR on a set of zeolites (BEA, FAU, MOR, and ZSM-5) with XANES, van Bokhoven and coworkers showed that the Cu-sites in an FAU framework needed a higher temperature to be reduced [136]. With the support from NO and H_2 adsorption studies with FT-IR, they were able to allocate the higher reduction temperature to more isolated Cu-sites [139]. As our spectroscopy results on Cu-loaded SAPO-34 and SSZ-13 imply that SAPO-34 develops more monomeric Cu-sites, we similarly performed CH_4 -TPR on the samples to see if a difference could be observed. The consumption of CH_4 is shown in Figure 16 (left panel), while the total oxidation to CO_2 is reported in the right panel. The results affirm that the CH_4 consumption starts at a substantially lower temperature in 0.50CuSSZ-13 (ca. 200 $^\circ\text{C}$) than in 0.08CuSAPO-34 and 0.25CuSAPO-34 (ca. 280 and 300 $^\circ\text{C}$, respectively). This is supported by a later onset of the CO_2 production temperature in Cu-SAPO-34 (right panel). The higher CH_4 consumption temperature in Cu-SAPO-34 does mark a striking similarity to the behavior of Cu-FAU as observed by Sushkevich et al. [136], and supports the hypothesis of more isolated Cu-species in SAPO-34. It should be noted that both

the higher Al concentration in FAU zeolites, and the different framework polarity in SAPO-34 are both inducing a lower acidity of the Brønsted sites [235, 236], which we surmise to have the biggest impact on the different Cu-speciation observed.

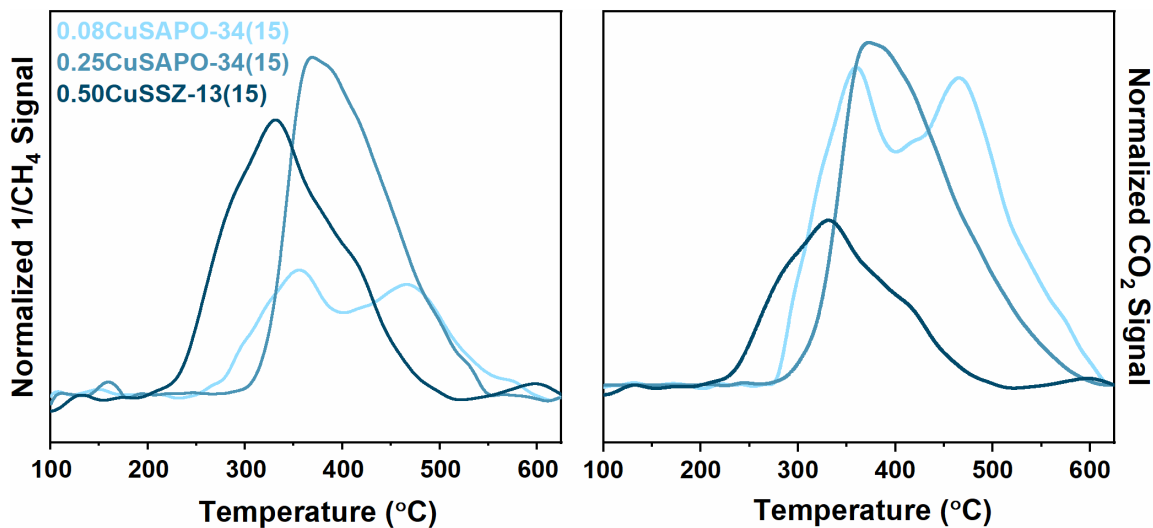


Figure 16. Inversed CH_4 consumption of 0.50CuSSZ-13, 0.08CuSAPO-34, and 0.25CuSAPO-34 measured by an online MS during a flow of CH_4 while heating from 100 to 650 °C (ramp: 5 °C/min). The materials were activated at 500 °C in O_2 for 8 h before the CH_4 -TPR experiment. The graphs have been normalized to the sample weight.

4.1.3. Direct Methane to Methanol Conversion

Having observed that the exchanged Cu-SAPO-34 behaved differently than 0.50CuSSZ-13 in the presence of CH_4 , we decided to study the materials with two different protocols in the MTM reaction. As Pappas et al. have previously performed a study on the MTM reaction parameters over Cu-SSZ-13 [94], the optimized reaction procedure found there was used as a reference herein. Then, a second test was performed with a CH_4 loading at 300 °C, instead of 200 °, as the CH_4 -TPR results showed that SAPO-34 needed a higher temperature to activate CH_4 . The complete test protocols are described in Table 4 in the experimental section, and the results are reported in Figure 17. In the left panel, the total yield of methanol ($\mu\text{mol}_{\text{MeOH}}/\text{g}$) is shown as a function of the Cu content. The right panel shows the productivity, where the total amount of methanol is normalized to the

Cu content. The selectivity is not reported due to systematic errors affecting the quantification of CO_x species, however, qualitatively, it seemed only minor fractions of CO/CO₂ were observed in the effluent during methane loading and H₂O-assisted extraction. From the results reported in Figure 17, it is evident that the Cu-loaded SSZ-13 outperforms the Cu-SAPO-34 materials in the reference reaction (CH₄ @ 200 °C). This is also in line with previous results obtained for the MTM conversion over Cu-SSZ-13 and SAPO-34, reported by Wulfers et al. [63]. The low productivity of Cu-SAPO-34 at the reference conditions also corresponds well with the presence of more highly coordinated monomeric Cu-sites in SAPO-34, as these sites are assumed to be less active for CH₄-activation [94], compared to dimeric three-fold coordinated Cu^{II} species.

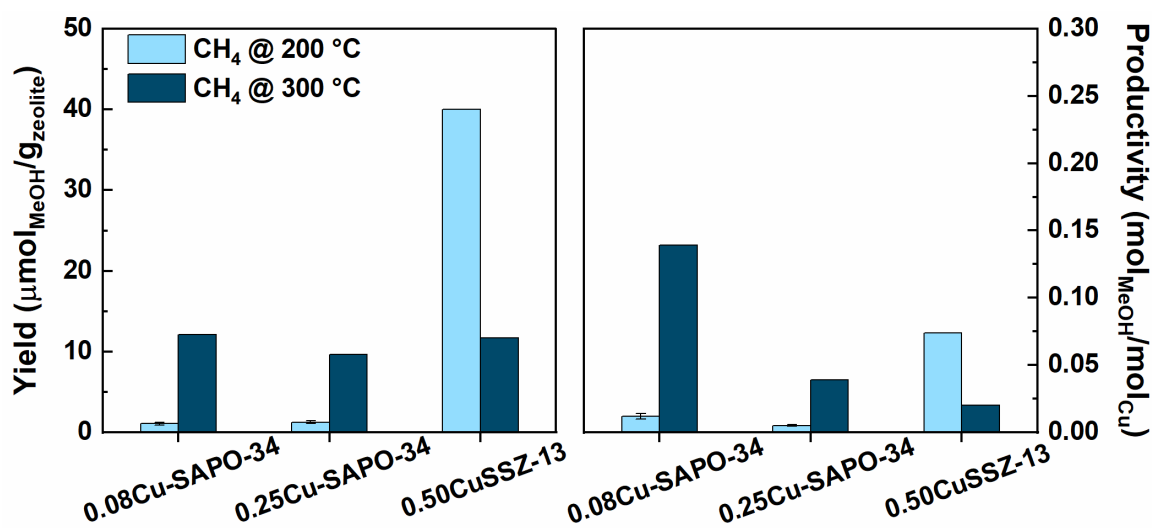


Figure 17. Representation of the performance of 0.08CuSAPO-34, 0.25CuSAPO-34, and 0.50CuSSZ-13 at the reference conditions (CH₄ @ 200 °C) and high-temperature CH₄ loading (CH₄ @ 300 °C). The panel on the left shows CH₃OH yield in μmol per gram of zeolite. The panel on the right gives the CH₃OH yield normalized to the Cu content (mol_{MeOH}/mol_{Cu}). The estimated error from MTM conversion over Cu-SAPO-34 is shown as black error bars inside the bars.

The performance observed after increasing the CH₄-loading temperature was remarkable. A tenfold increase in the CH₃OH yield over 0.08CuSAPO-34 and 0.25CuSAPO-34 was observed. Contrary, the CH₃OH yield from 0.50CuSSZ-13 decreases significantly, indicating a loss in selectivity. The lower selectivity is

supported by the CH₄-TPR experiments on 0.50CuSSZ-13 reported above, where the CO₂ production is already at a large extent at 300 °C (Figure 16). The reported values for methanol production over Cu-SAPO-34 are in the lower range of Cu-zeolites, however, the difference between the productivity after CH₄ activation at 300 °C vs 200 °C is significant and verifies the potential of CH₄-TPR experiments being a descriptor for the reaction parameters and possibly the Cu-speciation.

4.2. MCM-22: An Unexplored Zeolite Framework for MTM

The previous section (4.1) gave insight into the effect a different framework elemental composition could have on the MTM activity. Another important measure is to investigate the effect structural differences among zeolites have on Cu-speciation and methanol productivity. As mentioned in the introduction, there are nearly 260 different zeolite structures with different combinations of SBUs leading to varying topologies. Thus far, there is still some uncertainty as to whether large or small pore ring systems are most effective for methane activation.

In this subchapter, we have focused on a hitherto untested material for MTM, namely MCM-22. With the use of LIE, two Cu exchanged samples were prepared, namely 0.25Cu-MCM-22 and 0.30Cu-MCM-22. The Cu-loading was 0.26 and 0.31 mmol/g, respectively. A range of characterization techniques like MP-AES, N₂-physisorption, SEM, pXRD, TGA, and XAS was applied to verify the integrity of the MCM-22 synthesis and Cu ion exchange. Details on this can be found in **Paper II**. The samples were tested in the conversion of methane to methanol following the reference conditions reported in the experimental section, and the yield shows that the sample with the highest Cu content also has the highest methanol activity (27 vs 20 $\mu\text{mol}_{\text{MeOH}}/\text{g}$). However, when comparing the normalized productivity, the samples are much more similar (0.09 vs 0.08 $\text{mol}_{\text{MeOH}}/\text{mol}_{\text{Cu}}$). When comparing the values obtained herein to other tested Cu-zeolites for methane to methanol, the values are lower than what is reported when using the same reaction protocol and setup. Depending on the framework, exchange method, Si/Al, and Cu/Al ratio, the productivities previously obtained for Cu-zeolites are in the range of about 0.10 – 0.47 [94, 114, 140]. The selectivity was about 75% for both samples, which is also in the lower region of what is typically observed with this reaction protocol over other Cu-zeolites [94, 114, 140].

Previously, MCM-22 has been shown to be quite active for the MTO reaction by exhibiting a high selectivity towards propene [237]. In the MTO mechanism, there are generally two pathways suggested for methylation, a concerted and a stepwise route [238]. The latter leads to the formation of a methoxy intermediate, however, due to the complex channel structure of MCM-22 it is still debatable which of the mechanisms is dominant in this material [239]. A stepwise mechanism for MTO could indicate that the material can form and stabilize methoxy species at least on Brønsted sites, which do suggest that the material should be a candidate for the MTM reaction. Since our material characterization presented above indicate that the materials have been properly synthesized and exchanged with Cu, it became obvious that more investigations were needed to understand the reason for the low methanol production of these materials. As the two Cu samples had very similar Cu-loading and methanol productivity, we will mostly focus our discussion on the differences observed between the Cu-forms and the H-form.

4.2.1. FT-IR Spectroscopy Provide Insight on the Cu-Speciation

As with the Chabazite materials in subchapter 4.1, we performed CO-adsorption at RT with FT-IR spectroscopy on “self-reduced” samples to study the accessibility and reducibility of the Cu-species. In Figure 18, we show the region of interest (2250 – 2080 cm^{-1}) from the experiments. Bands related to both monocarbonyl (2158/2151 cm^{-1}) and dicarbonyl (2180/2176 cm^{-1} and 2151 cm^{-1}) adducts are observed at different CO coverage. The two bands observed for dicarbonyl species are due to the symmetric and asymmetric stretch, respectively. Two distinct bands appear for the $\text{Cu}^{\text{I}}\text{-CO}$ species as well as in the symmetric stretch of $\text{Cu}^{\text{I}}\text{-(CO)}_2$. While usually only one band is observed for the monocarbonyl species in Cu-zeolites [140, 141, 220, 232], this behavior has also been seen over Cu-BEA zeolites previously [232]. The two distinct bands indicate that in MCM-22 there are at least two structurally different Cu-sites, which is coherent with the sample having at least three major positions for Cu to be positioned, namely in the sinusoidal 10-

ring channel, within the supercage, or on the external surface in the super cage half-cups. Frolich et al. have suggested that the low-frequency monocarbonyl band at 2151 cm^{-1} is linked to a higher coordinated Cu species than the high-frequency band [240]. The authors propose that the band at 2151 cm^{-1} is from Cu in the D6R at the bottom of the supercage, while the high-frequency band at 2158 cm^{-1} is coming from a more freely coordinated species situated at the center of the supercage. If the low-frequency band is from Cu in the D6R, this could lead to inactive sites for MTM, as has been shown in CHA zeolites [94, 155]. This could help explain why the Cu-MCM-22 samples have such a low C–H activation capacity.

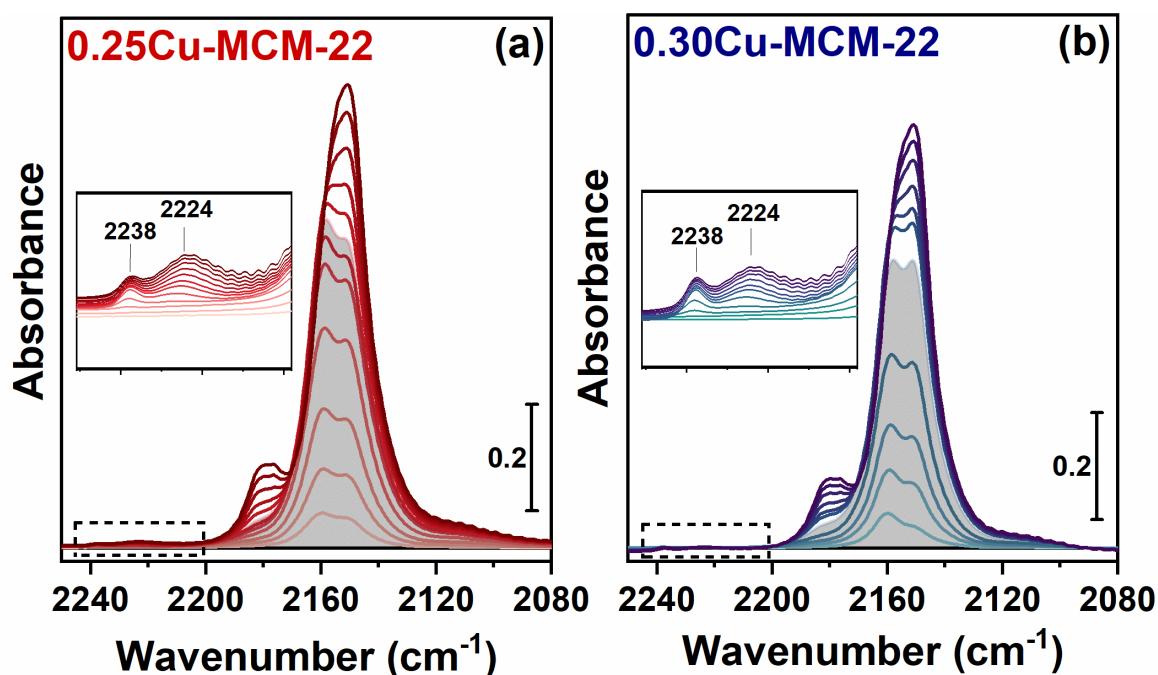


Figure 18. FT-IR spectra of the -CO stretch region after exposure to CO of the two Cu-exchanged MCM-22 samples, 0.25Cu-MCM-22 (a) and 0.30Cu-MCM-22 (b). The spectra are collected at RT after stabilization of the equilibrium pressure at incremental doses of CO from $\sim 50\text{ }\mu\text{bar}$ to 8 mbar. The samples were pre-treated in vacuum at $450\text{ }^{\circ}\text{C}$ (1.5 h). The spectra are background subtracted by dividing on the pre-treated spectra and normalized to the framework overtone, as well as Cu-content. The insets give a closer view of the marked area where the CO vibrations on Al^{3+} are found.

In addition to the typical bands appearing for CO interacting with Cu^{I} , there are also two smaller bands appearing at slightly higher wavenumbers (2238 and

2224 cm^{-1}). These bands are positioned at typical energies for CO interacting with extra-framework Al^{3+} (EFAl) sites [234, 241]. The observation of these bands suggests that there is some EFAl in the zeolite, which minimizes the number of Brønsted sites in the sample. This could have at least two potential implications on the MTM reaction. First, fewer Brønsted sites could minimize the amount of Cu exchanged in the samples. Indeed, LIE with both 0.01 and 0.02 M $\text{Cu}(\text{OAc})_2$ solution led to very similar amounts of Cu exchanged. Although other methods to increase the Cu exchange was not attempted as higher loadings often lead to Cu clusters and nanoparticles, the similarity between the two materials obtained with different LIE solutions suggests that we have reached a maximum of Cu exchange sites. Secondly, it has been shown that the presence of Brønsted sites is important for stabilizing methoxy intermediates [178, 179], and if the accessibility to the remaining sites is somewhat blocked by the EFAl, this could both minimize the availability for Cu exchange but also reduce the stabilizing effect of Brønsted acid sites. Based on this, we will in the following section further investigate the effect of acid site distribution in the MCM-22 framework and by extension its effect on the Cu siting to unravel more about the influence these parameters have on the MTM reaction.

4.2.2. NH₃-Adsorption Microcalorimetry

To study the changes in acidic properties of MCM-22 before and after Cu exchange, NH₃- and CH₄-microcalorimetry experiments were performed in a joint project by PhD student Moses Mawanga at NTNU. These experiments were very important for discussing the full picture and have therefore been included herein. The results are reported in Figure 19. In the left panel, we show the differential heats of adsorption (ΔH_{ads}) vs the amount of adsorbed NH₃, obtained for H-MCM-22 (a), 0.25Cu-MCM-22 (b), and 0.30Cu-MCM-22 (c). Both a primary (solid squares) and a secondary (open triangles) adsorption experiment were performed for all three samples. If we first look at the differential heat of adsorption measured for the Cu-free sample, there are three regions of interest marked with alternating light and dark grey colors. Initially, at very low coverage, there is a strong heat of adsorption (> 160 kJ/mol), which decreases sharply as the coverage increases. This is typically related to strong Lewis acid sites [242]. The second region of interest is a narrow area around $\Delta H_{\text{ads}} \approx -135 \pm 15$ kJ/mol that we allocate to the Brønsted acid sites [242]. The Al concentration of the H-MCM-22 applied herein is about 1.1 mmol/g, and as the second region diminishes already at about 0.25 mmol/g of adsorbed NH₃, it is evident that the amount of homogeneously strong Brønsted acid sites is lower in this sample, compared to what would be expected from a zeolite with similar Al content. Indeed, this region has previously been reported to be stable up to at least 0.8 mmol/g in an H-MOR with similar Al content (1.1 mmol/g) as our samples [243]. After the high enthalpy area, we enter the third region, where the heat of adsorption decreases gradually until the enthalpy for condensation of NH₃ is reached ($\Delta H_c = -23.4$ kJ/mol) at 1.4 mmol/g, close to the total Al value of 1.1 mmol/g. The gradual decrease is linked with a set of heterogeneous acid sites [242], indicating that a large portion of the total amount of Al in the sample is either present as EFAl, as indicated already by the FT-IR spectra above, or more Brønsted sites in positions that lead to lower heats of adsorption.

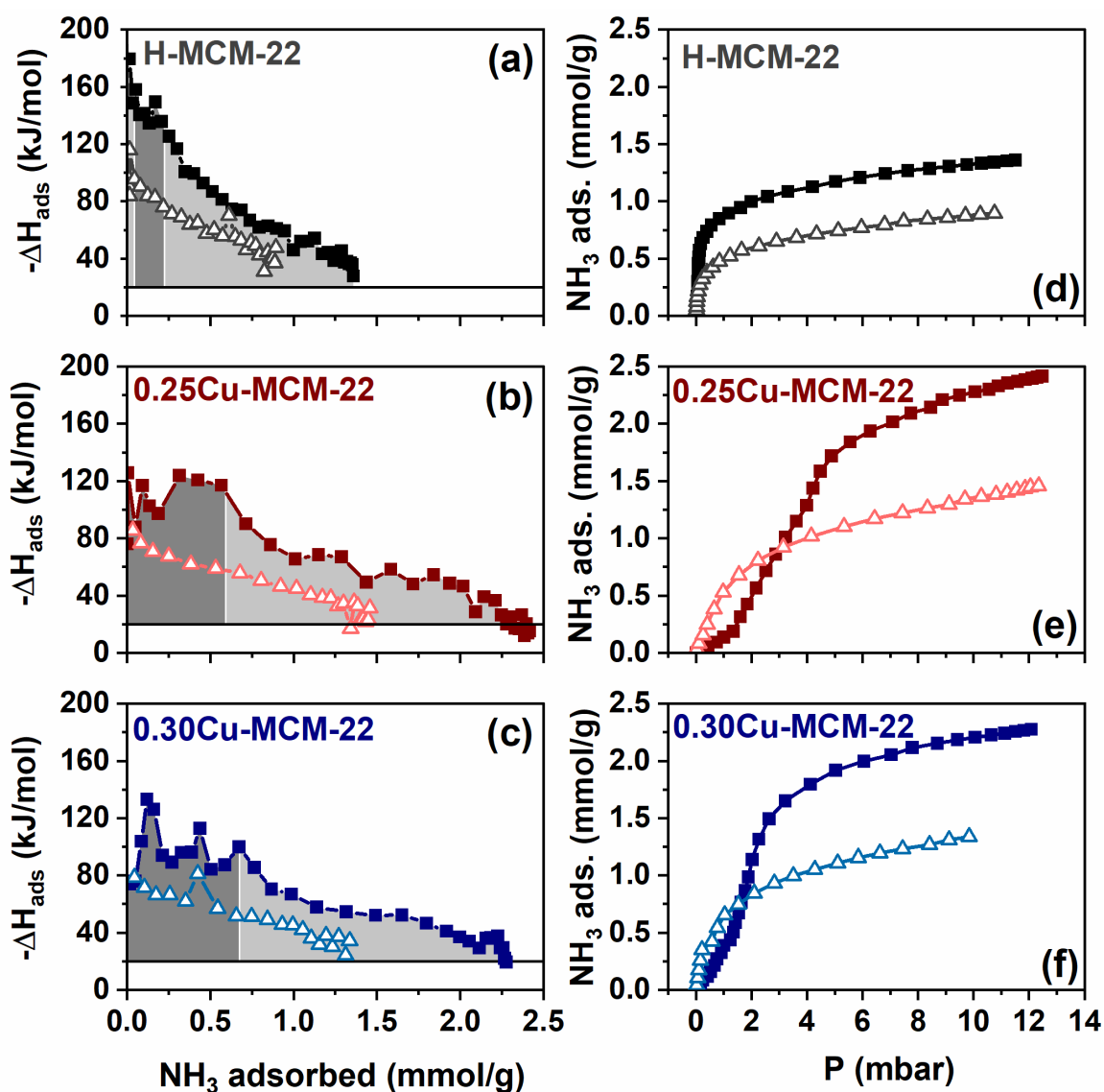


Figure 19. Differential heats of adsorption (a-c) and adsorption isotherms (d-f) for NH_3 on the three MCM-22 samples (a-c). Both primary (dark color, filled symbol) and secondary (light color, open symbol) heat of adsorption curves adsorption isotherms is reported. The differential heats of adsorption (kJ/mol) are plotted against the NH_3 adsorbed in $\mu\text{mol/g}$. The sharp horizontal line is representing the enthalpy for NH_3 condensation. The adsorption isotherms are given as adsorbed NH_3 in $\mu\text{mol/g}$ per absolute pressure (mbar).

If we shift our focus onto the Cu-exchanged samples, a broader region of heterogeneous sites is observed in a region of intermediate strength with $\Delta H_{\text{ads}} \approx -100 \pm 20$ kJ/mol up to about 0.6-0.7 mmol/g of adsorbed NH_3 . The “spikes” observed are linked with the oxidation of NH_3 on the pre-oxidized Cu-sites and the subsequent formation of Cu^{I} and mobile diamine Cu^{I} complexes [244-246].

Since the strong Brønsted site enthalpy region is non-existing in the Cu-exchanged samples, we conjecture that Cu is exchanged first with the strongest Brønsted sites and possibly the few strong Lewis sites. This is very much in line with an earlier study by Chen et al., where the authors found evidence from NH₃-TPD experiments that the strongest Brønsted sites are consumed in favor of a Cu site of intermediate strength [247]. As discussed above, the number of strong Brønsted acid sites observed herein was found to be much less than e.g. in a MOR with a similar Si/Al ratio. Given the high methanol productivity observed over Cu-MOR zeolites [120], we conjecture that adequately strong Brønsted sites are needed to form the active Cu-oxo species for MTM. The less strong acid sites likely lead to Cu-species that are either less active or inactive for methanol production. It could be that the Cu species are situated in less accessible positions like the sinusoidal 10-ring, or that the Cu is positioned in the double 6-ring at the bottom of the supercages as conjectured from the FT-IR spectroscopy results. A third possibility is that the Cu is positioned on the outer surface in the half “cups” of the supercage and that there is not enough confinement or available Brønsted sites in these positions for the methoxy intermediates to stabilize on the Cu-sites. This hypothesis is supported by previous studies revealing the half cups to be one of the more likely sites for methylation reactions over MCM-22 [107]. In the Cu exchanged samples, the NH₃ adsorption proceeds up to as much as twice the Al content, reaching an adsorption of around 2.3 mmol/g for both samples. If we expect some NH₃ to still be adsorbed on the remaining Brønsted sites, as verified by FT-IR (see SI of **Paper II**) the higher amount of NH₃ suggests that about three to four NH₃ molecules are adsorbed per Cu site at our adsorption conditions (80 °C). This high NH₃ to Cu ratio cannot be explained solely by the formation of linear diamine Cu^I complexes (Z[Cu(NH₃)₂]⁺), and we, therefore, surmise that a combination of this and a four coordinated Cu^{II} complex (e.g. Z₂[Cu(NH₃)₄]²⁺) are forming. This is supported by a thermodynamic study over Cu-SSZ-13 by Paolucci et al., where they find that Z₂[Cu(NH₃)₄]²⁺ and Z[Cu(NH₃)₂]⁺ are the most stable

species ($\Delta G \approx -90$ kJ/mol) formed at 80 °C in an NH_3 atmosphere [155]. Also, other forms of the tetraammine complex have been shown to exist where some of the NH_3 ligands are switched out with oxygen-derived species like $-\text{OH}$ groups [248].

In the right panel of Figure 19 (d-f), we have reported the ammonia adsorption isotherms. Both the primary and secondary adsorption are plotted. If we first view the adsorption isotherm for H-MCM-22 (d), the shape suggests that the adsorption follows a typical Langmuir isotherm or an L-shaped isotherm based on the classification by Giles et al. [249]. The secondary adsorption has the same shape, however reaching the plateau indicating saturation at less ammonia adsorbed than for the primary. For the Cu-exchanged samples, the primary adsorption isotherm has instead a peculiar S-shape. An S-shaped isotherm is usually consistent with a scenario where there are two or more competing mechanisms at play during the adsorption [250]. For the two Cu-exchanged samples herein, we conjecture two feasible scenarios. 1) Since NH_3 adsorbs on both H-sites and Cu-sites, and we have seen two distinct Cu-sites from CO-adsorption with FT-IR, the S-shape may come from a varying site selectivity depending on the coverage [250]. 2) The slow initial adsorption could also be due to the initial binding and complexation of NH_3 at the strongly adsorbing Cu-sites [251]. Then, as the level of adsorbate increases and the negative effect caused by complex formation subsides, faster adsorption is observed at higher pressures, where also the Brønsted sites are covered. Whether it is scenario 1) or 2) that is occurring would need further investigations beyond the scope of this study, although, it cannot be ruled out that it is a combination of the two. Interestingly, it seems like the negative effect is no longer present for the second isotherm, and the shape is much more similar to the H-MCM-22 sample. Even so, the adsorption amount is still much higher in the Cu samples, indicating that both NH_3 adsorbed to Brønsted sites and some of the NH_3 ligands coordinated to Cu are desorbed during outgassing.

4.2.3. The effect of Cu on Framework Acidity

To further support our findings from NH₃-calorimetry, we also performed n-propylamine TPD experiments on the three samples. n-Propylamine can be used to solely titrate the Brønsted acid sites of a zeolite due to an acid-catalyzed Hoffmann elimination of chemisorbed n-propylamine that releases propene (C₃=) and NH₃. The column named "C₃=" in Table 5 gives the total amount of desorbed propene from the reaction. With the total Al in H- and Cu-MCM-22 being about 1.0-1.1 mmol/g, and the quantity of propene observed only 0.46-0.66 mmol/g, we surmise that a large fraction of Al in the samples has to be EFAl sites. This is also in line with the FT-IR spectroscopy and microcalorimetry results presented above. The amount of propene desorbed is slightly decreasing from 0.66 mmol/g for the H-MCM-22 as the Cu-content increases. Specifically, 0.15 and 0.20 mmol/g reduction for 0.25 and 0.30Cu-MCM-22, respectively. This is consistent with Cu exchanging some of the H-sites, however, given that the Cu concentration of the two samples is 0.26 and 0.31 mmol/g, we do speculate that Cu also exchanges some strong EFAl sites like the strongly adsorbing Lewis acid sites observed in the first region of the NH₃ microcalorimetry results (Figure 19). Additionally, some propene could be confined within the zeolite framework or was subjected to undesired side reactions as we have observed to be possible over Cu-zeolites for another study in our lab, and also recently reported by Lashchinskaya et al. [252].

NH₃ TPD was also employed as NH₃ can titrate both the Lewis and Brønsted acid sites in the samples. The NH₃ desorption (TPD) values are in the range of 0.57 – 0.76 mmol/g, with the desorbed NH₃ amount slightly increasing with increasing Cu content. The values are a bit low considering the Al content (~1.1 mmol/g), although in the same range and following the same trend as the values obtained from subtracting the primary and secondary isotherm to get the irreversible NH₃ adsorption with NH₃ calorimetry (0.44 – 0.84 mmol/g). As the samples have either

been outgassed at 80 °C (adsorption) or 170 °C (desorption), we surmise that the “missing” acid site concentration is due to very weakly binding Lewis acid sites.

Table 5. Density of acid sites obtained by n-propylamine TPD and NH₃-TPD together with the irreversible NH₃ adsorbed measured with calorimetry. The Al and Cu content is also reported for comparison.

Sample name	Al (mmol/g)	Cu (mmol/g)	Density of acid sites (n-propylamine TPD)	Density of acid sites (NH ₃ TPD)	Irreversible NH ₃ adsorption (calorimetry)
			C ₃₌ (mmol/g)	NH ₃ (mmol/g)	NH ₃ (mmol/g)
H-MCM-22	1.07	-	0.66	0.57	0.44
0.25Cu-MCM-22	1.03	0.26	0.51	0.64	0.82
0.30Cu-MCM-22	1.03	0.31	0.46	0.76	0.84

Lastly, it is also of interest to point out the peak desorption temperatures during the NH₃-TPD experiments. As reported in Figure 20, the H-MCM-22 sample has a broad peak (maximum at 350 °C) assigned to Brønsted acid sites. Note, the broad nature of the peak is in line with the heterogeneity of acid site strengths first observed with NH₃ calorimetry on the H-form. The two Cu exchanged samples, however, have three major peaks, specifically at 275, 350, and 450 °C. This is similar to what has been observed on a set of Cu-loaded MCM-22 materials previously by Chen et al. [247]. The peak at 350 °C reduces with increasing Cu-loading, supporting that this desorption temperature is linked with Brønsted acid sites. Based on the discussion above, we infer that the other two peaks come from NH₃

molecules being desorbed from the $Z[\text{Cu}(\text{NH}_3)_2]^+$ and $Z_2[\text{Cu}(\text{NH}_3)_4]^{2+}$ complexes residing after adsorption. According to the phase diagram reported by Paolucci et al. on Cu-SSZ-13 [155], and *in situ* XAS TPD experiments by Borfecchia et al. [248], we surmise that the low-temperature peak is mostly from NH_3 desorbing from tetraammine derived complexes. This peak is stronger in the 0.30Cu-MCM-22 which indicates that a higher concentration of Cu leads to more sites available for tetraammine complexation. As this requires more space, we could presume that this site is more easily accessible than the site forming diammine complexes. The broad high-temperature peak however is coming from a variety of sites stronger than the Brønsted acid sites and is likely the remaining NH_3 desorbing from both diammine and tetraammine Cu complexes [155].

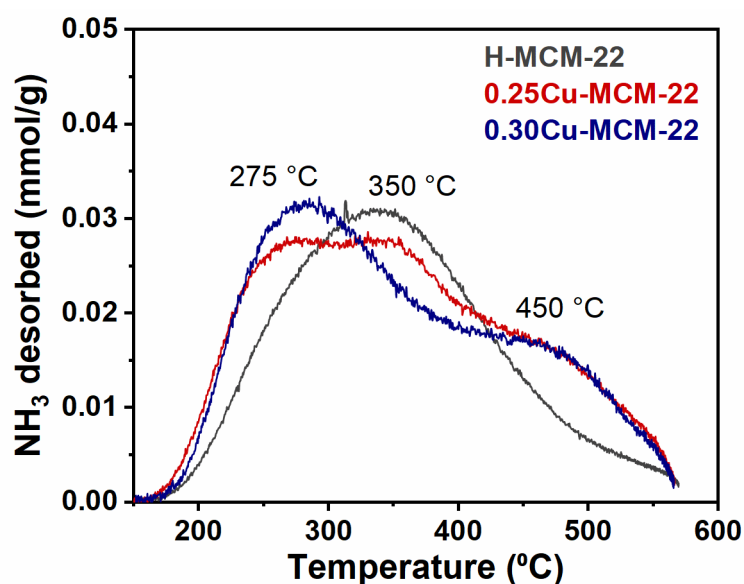


Figure 20. NH_3 -TPD profiles of H-MCM-22, 0.25Cu-MCM-22 and 0.30Cu-MCM-22.

4.3. Evaluating Cu-zeolites Prepared by SSIE for MTM

To this point, I have shed light on structure-activity relationships coming from alterations to the framework composition. However, another important component of the puzzle is the Cu exchange. In this subchapter, I highlight the work of **Paper III**, where four different zeolite frameworks (MOR, BEA, ZSM-5, and FAU) are ion-exchanged using an alternative method to LIE that has been the preference in the field. SSIE is industrially a much simpler synthesis process than the various solution-based exchange procedures. Furthermore, by performing SSIE with Cu^I salts, it should be possible to obtain a higher exchange degree of Cu in the zeolite, possibly leading to a larger concentration of proximal Cu ions. Their proximity could make the formation of active sites for C–H activation more feasible.

Details on the standard characterization of the solid-state ion-exchanged materials can be found in **Paper III**, but to summarize, techniques like MP-AES and EDX were used for elemental analysis, N₂-physisorption to determine the specific surface area, and pXRD, SEM, and backscattered images to search for Cu outside the frameworks. The results showed that there is a heterogeneous distribution of Cu in the samples and possible pore blockage by larger agglomerates present. It was therefore surmised that even though the exchange led to a Cu/Al ratio of 0.8, it is not likely that all the Cu present in the samples contributes to C–H bond activation. It was, however, still of interest to look a bit more into the effect this high loading had on the nature of the Cu-sites, and consequently the methanol productivity.

4.3.1. Performance Studies in the MTM Reaction

The propensity of Cu^I-zeolites towards producing methanol from methane was investigated by following Test #1 reported in Table 4 in the experimental section. The methanol yield ($\mu\text{mol}_{\text{MeOH}}/\text{g}$) and selectivity (%) of the four highly exchanged

Cu^I-zeolites as well as 0.30Cu^I-MOR (targeted during SSIE at Cu/Al = 0.30) are presented in Figure 21. CH₃Cl was observed as a product of the reaction but has not been included in the quantified yield or selectivity. Cl is a remnant from SSIE, and in an EDX analysis after testing, it was observed that a large fraction of the Cl in the framework disappeared after one test, as shown in the SI of **Paper III**. All four highly exchanged samples show the ability to produce methanol, with Cu^I-MOR having the highest yield. This is in line with what has been observed previously for this set of Cu-exchanged zeolite frameworks at similar reaction conditions [114, 136].

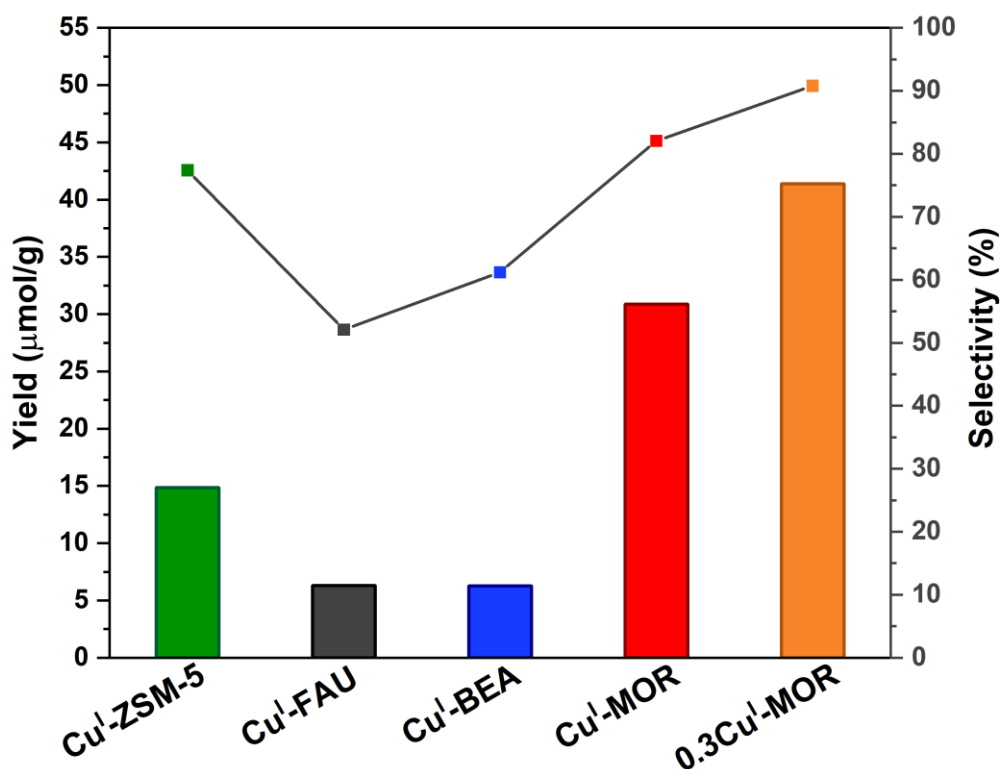


Figure 21. Activity data for the methane to methanol reaction over the Cu^I-zeolites. The left axis gives the yield in µmol of the total amount of methanol per gram of zeolite. On the right axis is the selectivity. In the reaction protocol, the materials were exposed to the following gas flows (15 ml/min) and temperatures; 100% O₂ (500 °C, 8 h), 100% He (200 °C, 1 h), and then, isothermally, 100% CH₄ (3 h), 100% He (1 h), and 10% H₂O in 10% Ne/He (~2 h).

When comparing the highly exchanged samples with 0.30Cu^I-MOR, an even higher yield is observed. This becomes more evident if we compare the

normalized productivity as 0.30Cu^I-MOR has much less Cu in the system. The productivity of Cu^I-MOR and 0.30Cu^I-MOR is 0.03 and 0.10 mol_{MeOH}/mol_{Cu}, respectively. The increase in productivity can likely be attributed to the formation of fewer nanoparticles and Cu agglomerates in the 0.30Cu^I-MOR sample. Alternatively, one could also argue that the increased productivity is related to a higher fraction of Brønsted sites present in this sample compared to the higher Cu-loaded samples.

To place the yields obtained in this study into perspective, the MOR zeolites can be compared with a thorough study by Dyballa et al. on MOR zeolites exchanged with LIE and incipient wetness [114]. When comparing the productivity of the SSIE MOR zeolites studied herein to the productivity obtained by Dyballa et al. (0.06 > 0.47), it is apparent that the SSIE exchanged MOR zeolites achieve only moderate methanol productivity. From these initial results, we find that a more precise method is likely necessary to obtain a high fraction of active sites. In the following subsection, we shall focus on the two Cu^I-MOR samples to clarify how the high Cu exchange affected the Cu-speciation besides forming Cu nanoparticles and agglomerates. To do so, we have investigated the samples with FT-IR spectroscopy to study the Cu^I formation and accessibility, as well as the Brønsted acidity. Finally, CH₄-TPR, being so efficient for elucidating differences for different Cu-CHA framework types (subsection 4.1), was used to understand more about Cu reducibility.

4.3.2. Investigating the Reducibility of the Samples

The effects of the very high exchange degree achieved for the four zeolites (Cu/Al ratio of 0.8) on Cu speciation were studied using FT-IR spectroscopy. Figure 22 (a) depicts the $\nu(\text{OH})$ stretching region of the spectra of Cu^I-MOR at RT after pretreatment at 450 °C in vacuum. The O–H stretching band connected to the Brønsted site (Si(-OH)Al) should be found at 3611 cm⁻¹, as shown by the parent MOR zeolite in the figure. The lack of bands in this region indicates that all

Brønsted sites are covered by Cu. This is important to note, as it has previously been suggested that Brønsted sites are necessary to produce methanol [178, 179]. The evidence from the FT-IR spectra combined with the above-mentioned observation of methanol might suggest that some Cu-species are capable of selectively converting methane to methanol without facilitation by Brønsted sites. Yet, the formation of some Brønsted sites during the reaction protocol or possibly not detected in the FT-IR spectra cannot be ruled out at this point.

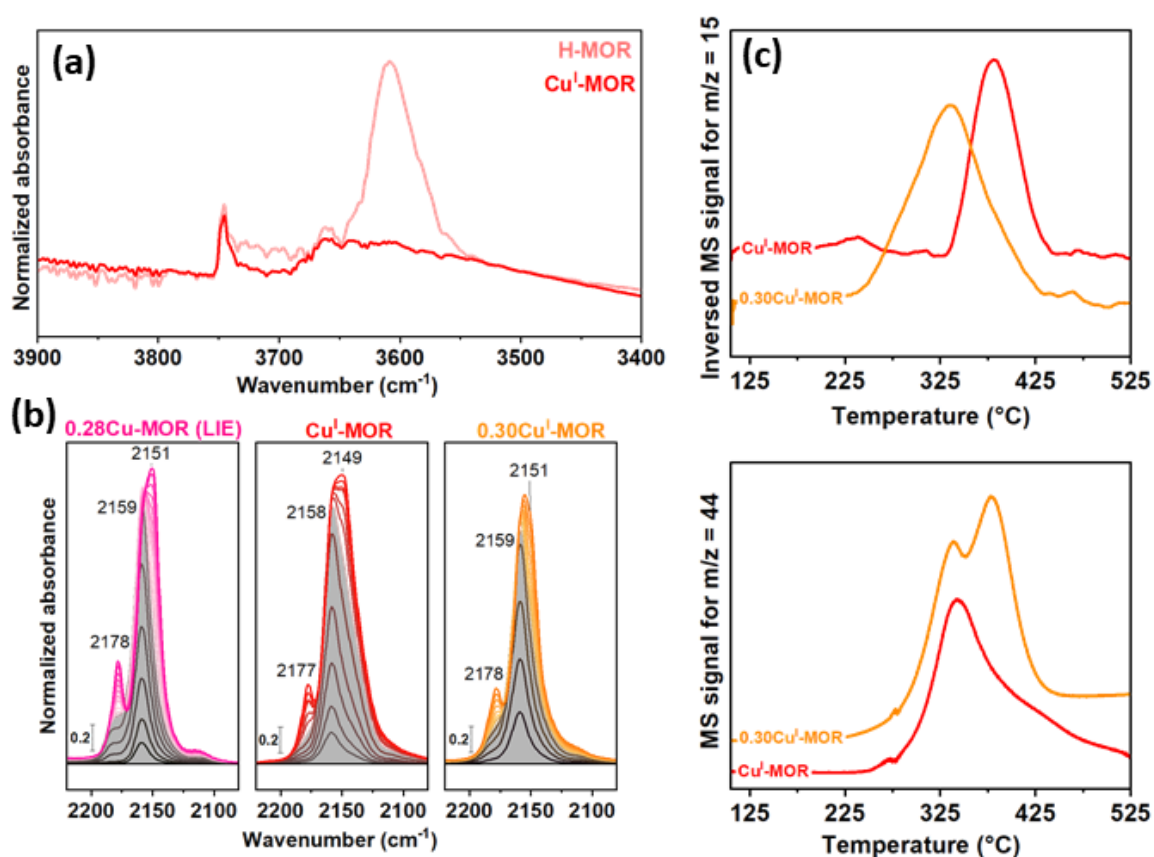


Figure 22. (a) FT-IR spectra showing the $\nu(\text{OH})$ stretching region of the H-MOR and Cu^I-MOR after pretreatment in vacuum at 450 °C. (b) FT-IR spectra showing the $\nu(\text{CO})$ stretching region of Cu^I-MOR, low loaded Cu^I-MOR (0.30Cu^I-MOR), and a LIE Cu-MOR (0.28Cu-MOR (LIE)), during CO adsorption. The spectra have been collected with increasing CO pressure (up to 8 mbar). All spectra are normalized to their framework overtone and background subtracted. The grey area represents the monolayer coverage. (c) CH₄ consumption and CO₂ production during TPR for Cu^I-MOR and 0.30Cu^I-MOR. The graphs have been vertically adjusted for easier comparison.

To investigate the nature of the Cu-sites, CO-adsorption with FT-IR was performed. The samples were pretreated in vacuum to induce “self-reduction” of potentially oxidized Cu to Cu^I before being exposed to CO at RT to selectively probe the Cu^I-sites [195-199]. In this summary, we focus on the comparison between the highly exchanged (Cu^I-MOR) and the low exchanged MOR (0.30Cu^I-MOR) samples, and their comparison to a sample prepared by LIE (Cu/Al=0.28 and Si/Al = 11) also previously published [141]. The evolution of mono- and dicarbonyl adducts (not normalized to Cu content) is depicted in Figure 22. The band related to the formation of monocarbonyl species (2158/59 cm⁻¹) is highlighted with a grey background [232]. As more CO is dosed onto the samples, a band starts appearing at 2177/78 and 2149/51 cm⁻¹. These are the symmetric and asymmetric stretch of Cu^I-(CO)₂, respectively, and are related to the formation of dicarbonyl species. In Cu^I-MOR, the band at 2149 cm⁻¹ is distorted by a broad tail from the formation of a band/shoulder at around 2135 cm⁻¹, which is likely due to the presence of Cu₂O nanoparticles formed during the exchange procedure [232]. When comparing the intensity of the different stretches in Cu^I-MOR, 0.30Cu^I-MOR, and 0.28Cu-MOR (LIE), it is evident the highly exchanged Cu^I-MOR sample has more available Cu^I to form monocarbonyl adducts, as the band intensity for monocarbonyl is higher, compared to 0.30Cu^I-MOR. However, when comparing the symmetric dicarbonyl band at 2178 cm⁻¹, the two SSIE exchanged samples show approximately the same intensity, indicating that the same amount of Cu^I-(CO)₂ is formed on the two samples. Albeit, as the spectra are not normalized to the Cu content, it is apparent that 0.30Cu^I-MOR has a higher ratio of Cu sites available for dicarbonyl formation. When matching both samples to the LIE sample, however, the LIE sample has markedly higher bands for the dicarbonyl adducts, even though it has the same Cu content as 0.30Cu^I-MOR. Higher Cu^I-(CO)₂ intensities have been previously attributed to Cu-zeolites with a higher number of low-coordination Cu sites that are more likely to be able to activate the C-H bond in methane [140]. This is also supported by much higher methanol productivity

measured for this sample ($0.25 \text{ mol}_{\text{MeOH}}/\text{mol}_{\text{Cu}}$) [114]. These findings indicate that the SSIE method, used for the Cu^I-zeolites herein, yields fewer Cu sites that are in a coordination state and position preferred for reaction with methane. We infer this to partially be due to less accessibility to the sites because of nanoparticle formation blocking the pores. This is supported by a significant lowering in the specific surface area measured for all the zeolites when exchanged with Cu. Another possibility is that some of the Cu sites are still coordinated to Cl (used for Cu exchange), thus limiting the coordination environment available for CO and only allowing for monocarbonyl species to form. The latter is corroborated by the observation of CuCl₂ nanoparticles with pXRD after testing.

To further explore the propensity of the samples for reaction with methane, CH₄-TPR experiments were used. CH₄-TPR results over all four highly exchanged zeolites is found in **Paper III**. To summarize, it is noteworthy that the onset of CH₄ consumption for the highly exchanged MOR, BEA and ZSM-5 seems to start around the same temperature, whereas the methane consumption occurs at considerably higher temperature for FAU. Sorting the materials based on the temperature of their maximum consumption rate gives Cu^I-ZSM-5 < Cu^I-MOR < Cu^I-BEA << Cu^I-FAU. This order is in line with the results previously reported by Sushkevich and van Bokhoven for CH₄ consumption on ion-exchanged Cu-zeolites [136]. Further, a considerably larger quantity of methane is consumed over Cu^I-MOR and Cu^I-FAU compared to the other two materials. Interestingly are FAU and MOR also among the most active zeolites for MTM (Figure 9).

The CH₄ consumption (top panel) and CO₂ production (bottom panel) during CH₄-TPR of Cu^I-MOR and 0.30Cu^I-MOR are depicted in Figure 22 (c). A few key observations are made when focusing on the most distinct differences that can be observed between the samples. First, the highly exchanged Cu^I-MOR has a significantly higher onset temperature for CH₄ consumption compared to 0.30Cu^I-MOR. Secondly, when investigating CO₂ production, it can be observed that the

production of CO₂ occurs as two peaks for the highly exchanged sample, with the onset of CO₂ release occurring before appreciable methane consumption. Over 0.30Cu^I-MOR, on the other hand, there is one main peak occurring at the time of CH₄ consumption with just a broad shoulder towards higher temperatures. As there is a shift of methane consumption to higher temperatures for the Cu^I-MOR vs 0.30Cu^I-MOR, we presume that it is the second CO₂ peak, which overlays well with the CH₄ consumption, that is the CO₂ production peak linked to CH₄ oxidation over MTM active species in Cu^I-MOR, and that the first peak is more likely to be from undetectably consumed methane that oxidizes and desorbs faster due to Cu nanoparticles or possibly the remaining Cl from SSIE. The late onset of CH₄ consumption in Cu^I-MOR vs 0.30Cu^I-MOR is similar to what we observed for SAPO-34 when compared to SSZ-13, in subchapter 4.1. There, like Sushkevich et al. [136], we allocated the temperature difference to a higher fraction of monomeric Cu active sites, which require a higher temperature to activate methane. We could therefore conjecture that the higher Cu-loading in Cu^I-MOR has led to more monomeric Cu active sites. Another possibility that should be considered is that the higher amount of Brønsted sites in 0.30Cu^I-MOR aids in the reactivity towards methane, and that this is the reason behind the clear difference in CH₄ consumption temperature between the two MOR we observe herein, and not necessarily the formation of different types of Cu-oxo sites. Since it has been shown previously that Brønsted sites are important for stabilizing the methoxy intermediates, this is a plausible scenario [178].

5. C–H Activation: Understanding the Cu-Speciation

In the previous chapter, we showed that the use of TPR experiments could elucidate important material differences that affected the MTM activity. Moreover, coupled with the right characterization tools, TPR experiments have the potential to shed some light on the otherwise slow dynamic changes in the Cu-speciation when exposed to CH_4 . The following chapter is based on the results reported in **Paper IV** and has two target areas. First, we have used TPR experiments coupled with different spectroscopic techniques like UV-vis, FT-IR, and XAS, to search for minor differences within the same zeolite system (Cu-MOR) affecting the Cu-speciation and subsequent methanol productivity. Secondly, to understand more about the mechanism during Cu^{II} reduction, both CH_4 -, C_2H_6 -, and CO -TPR was performed.

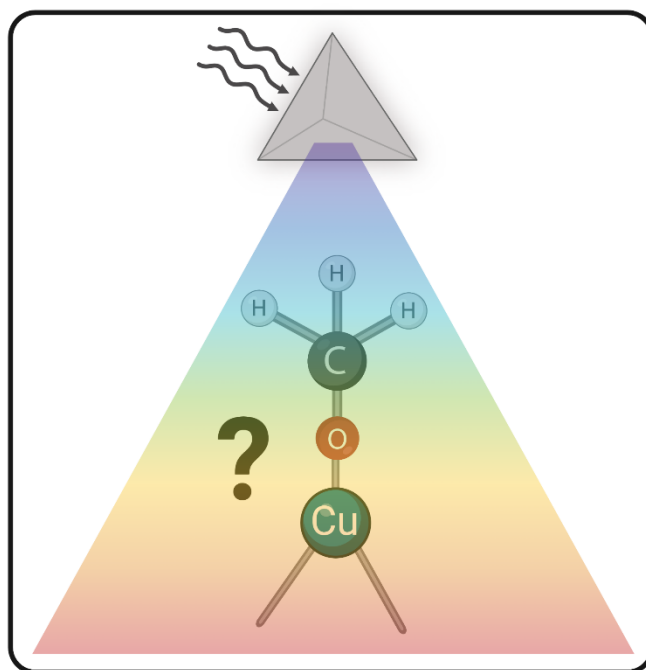


Figure 23. Illustration of the idea behind chapter 5. Different spectroscopic techniques are applied to shed light on Cu speciation during C–H exposure.

5.1. *In situ* XANES TPR: Finding Spectroscopic Fingerprints of Different Cu-Species

The Cu-MOR materials applied herein have been well-tested in the MTM reaction and have been through various extensive characterization in a range of previous studies [94, 114, 120, 141, 142, 253]. 0.36Cu-MOR(11) and 0.18Cu-MOR(7) have different Si/Al and Cu/Al ratio, as well as different methanol productivity in the MTM reaction (Table 3 in the experimental section). Given the broad characterization history of these materials and their productivity difference, they presented as good candidates for the present study.

At BM31 (ESRF), the samples were subjected to three different TPR protocols, by following Scheme 3, given in the experimental section. CH₄, C₂H₆, and CO-TPR were performed accordingly, and XAS spectra were collected throughout the entire experiment. A qualitative overview of the obtained scans can be found in **Paper V**. As part of her master thesis, Beatrice Garetto (M.Sc.), at UniTo performed the MCR-ALS analysis on the *in situ* XAS data, and from that we obtained quantitative information on the Cu-speciation throughout the TPR experiments as this advanced data analysis technique provides detailed insight into the speciation and dynamics of the Cu species inside the zeolite [68, 254]. The MCR-ALS analysis yielded a total of six principal components. The pure XANES spectra of the six components are reported in Figure 24 (a), while their concentration profiles in the different experiments are reported in Figure 24 (b). A pictorial representation of possible Cu-species linked with the pure XANES spectra discussed is finally provided in Figure 24 (c). Firstly, focusing on the O₂ activation step of the protocol, two high-temperature (HT) Cu^{II} species, **Cu^{II}_HT_a** and **Cu^{II}_HT_b**, are recognized with very similar XANES signatures. The biggest difference is the shape and intensity of the WL, supporting a conserved coordination motif with only subtle differences in the first-shell bond distances and angles. It is plausible that they could stem from the same Cu-moiety, e.g., a

mono- μ -oxo dicopper(II) core, but docked at distinct exchange sites, also featuring different accessibility. The third Cu^{II} species, $\text{Cu}^{\text{II}}_{\text{LT}}$, is described as a low-temperature (LT) Cu^{II} species since it increases in concentration with a decrease in temperature. $\text{Cu}^{\text{II}}_{\text{LT}}$ is likely to be more highly coordinated than the high-temperature species, based on the higher white-line (WL) intensity observed for this species. Interestingly, the growth of $\text{Cu}^{\text{II}}_{\text{LT}}$ appears to correlate with a decrease in the concentration of $\text{Cu}^{\text{II}}_{\text{HT}_a}$, while $\text{Cu}^{\text{II}}_{\text{HT}_b}$ remains almost stable. We conjecture that the concentration of $\text{Cu}^{\text{II}}_{\text{LT}}$ increases with decreasing temperature due to a dynamic change in some of the $\text{Cu}^{\text{II}}_{\text{HT}_a}$ species, leading to a change in coordination motif from three-fold to four-fold. The chemical nature of this four-fold coordinated Cu^{II} species, seen to increase in abundance also, once the feed is switched from O_2 to He in the final cooling step before TPR, is puzzling. A tentative assignment starting from a mono- μ -oxo dicopper(II) core could entail bis- μ -hydroxo dicopper(II) formed upon interaction with residual H_2O traces, favored as temperature decreases. This hydroxo-bridged dicopper(II) species is specifically discussed in enzymatic systems and complex formation [255, 256], but a similar hydration event forming trimeric Cu species in zeolites has also been suggested [159]. Alternatively, μ - η^2, η^2 -peroxo-dicopper(II) species could be proposed as a way for the system to prevent self-reduction by using O_2 molecules supplied in the first part of the cooling step. A minor peak in the typical Cu^{I} energy region (8983 eV) is visible in the pure $\text{Cu}^{\text{II}}_{\text{LT}}$ XANES spectrum and is highlighted with an asterisk (*). This spurious spectral feature is an artifact from the MCR-ALS analysis due to a high abundance of Cu^{I} in the mix of Cu species, previously documented by Martini et al. [257]. When comparing the concentration profile for $\text{Cu}^{\text{II}}_{\text{HT}_a}$ and $\text{Cu}^{\text{II}}_{\text{HT}_b}$ between 018Cu-MOR(7) and 036Cu-MOR(11) during the O_2 activation, they behave similarly throughout all experiments, however, with a higher concentration of $\text{Cu}^{\text{II}}_{\text{HT}_b}$ in 018Cu-MOR(7). Importantly, this is fully consistent with previous results by Pappas et al., where a framework-coordinated Cu^{II} species with a Cu K-edge spectral signature consistent with $\text{Cu}^{\text{II}}_{\text{HT}_b}$, was

found to be more abundant in the more productive 018Cu-MOR(7) sample, and tentatively associated with the active site for the MTM reaction [120].

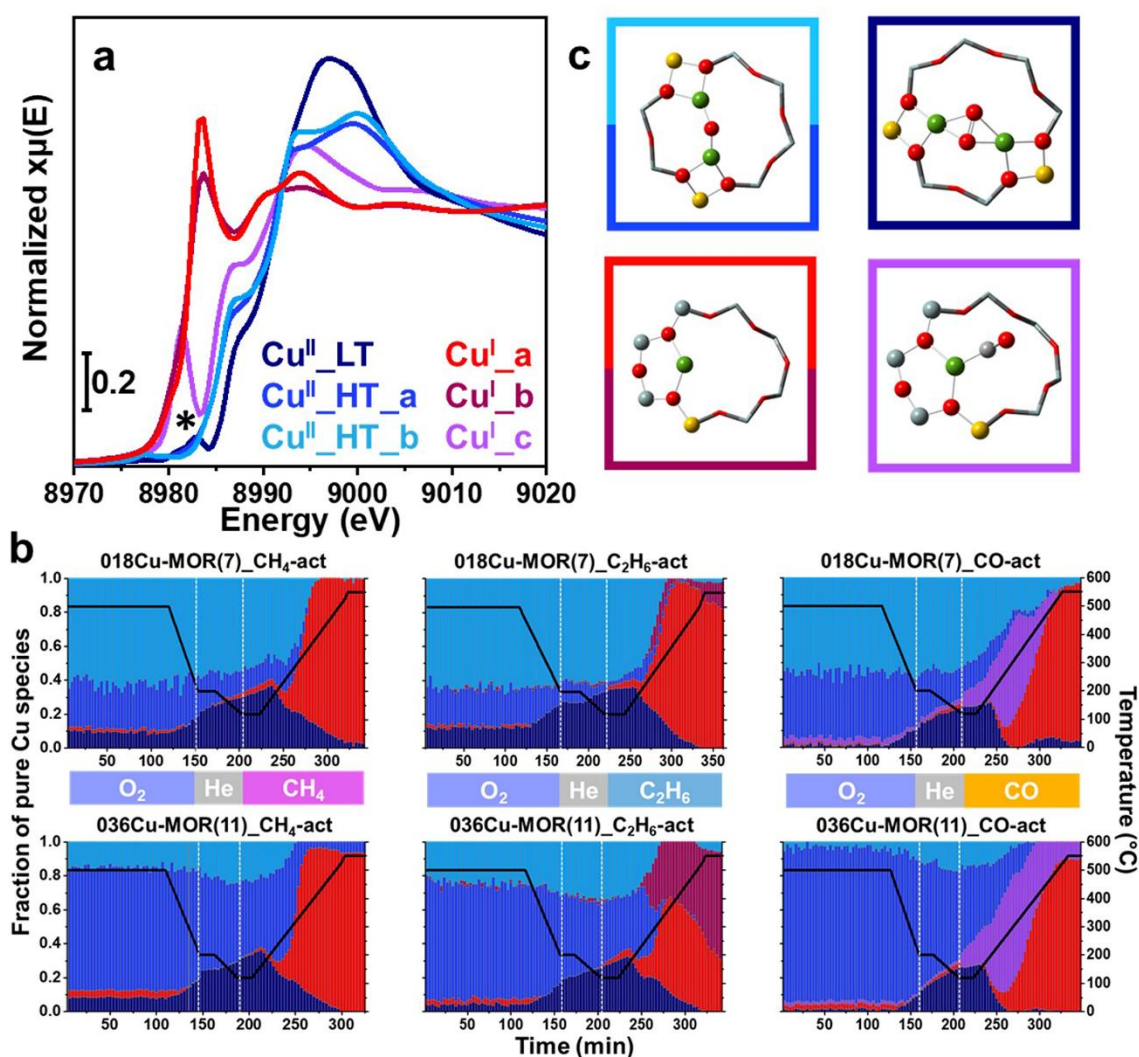


Figure 24. (a) Global representation of the pure XANES spectra of Cu species obtained by MCR analysis, performed considering the whole dataset except for the ramp from RT to 500 °C during the activation step. The * symbol indicates an MCR reconstruction artifact. (b) Corresponding temperature-dependent concentration profiles for each Cu species, (c) Pictorial representation of the Cu species proposed to form during the experiment. Atoms color code: Cu, green; O, red; C, purple; Si, grey; Al, yellow.

When focusing on the TPR step of the protocol, we note that new Cu-species develop, as Cu^I species form at the expense of Cu^{II}. Depending on the experiment, three distinct principal components were detected, where **Cu^I_b** and **Cu^I_c** formed exclusively in C₂H₆ and CO, respectively. The two species denoted as **Cu^I_a** and

Cu^I_b show similar spectral features, with a typical rising edge peak assigned to the $1s \rightarrow 4p$ transition of Cu^I , and no trace of the $d^9 1s \rightarrow 3d$ pre-edge peak (Figure 24 (a)). The WL intensity is significantly lower than for the Cu^{II} species, indicating Cu sites with lower coordination numbers. Indeed, the spectral features are very similar to (quasi) linear Cu sites coordinated with two lattice oxygen atoms [258]. The minor modifications in the XANES spectral shape between **Cu^I_a** and **Cu^I_b** are likely related to small induced differences in bond length and/or minor rearrangements when the sites are perturbed by the different gaseous species (CH_4 vs C_2H_6). The XANES spectrum of the third Cu^I species, **Cu^I_c**, has very different spectral features from the other two, where the $1s \rightarrow 4p$ peak is shifted towards lower energy values. When studying the concentration profile, Figure 24 (b), we observe how the species reaches a maximum of about 260 °C species and then slowly diminishes up until ~400 °C. Due to the change in the coordination environment of this species compared to **Cu^I_a** and **Cu^I_b**, we conjecture the species is related to mono- or dicarbonyl complexes forming in the presence of CO, as CO is known to be stable on Cu^I species in zeolites [219, 259]. A small fraction of **Cu^I_c** appears to be stable above 400 °C for 036Cu-MOR(11), however, this quantity falls within the uncertainty typically associated with MCR-ALS reconstruction (~10% of total Cu), and can therefore not be ascertained as a stable species [257].

Lastly, we note that when the Cu^I species start forming in the CH_4 - and C_2H_6 -TPR experiments, we see the consumption of **Cu^{II}_HT_b** slightly before the consumption of **Cu^{II}_HT_a**. This observation indicates that **Cu^{II}_HT_b** is more easily reduced upon alkane activation, and as this is the dominant Cu^{II} species in the most MTM active 018Cu-MOR(7) sample, we hypothesize the Cu reducibility to be linked with the activity of the samples. This hypothesis is considered even more closely in the following section when we attempt to look more meticulously at the overall reduction trends during the TPR ramp.

5.2. Coupling Cu^{II} Reduction with Reactant Consumption and Product Formation

To elucidate more easily the minor differences in the TPR protocol between the two MOR compositions and the different substrates, we looked into the reduction of Cu^I as a function of temperature. The data points were derived by summing the fractions of all the pure Cu^I species as determined by the MCR-ALS analysis above for each XANES spectrum collected. Herein, we report the first derivative of the trace ($d(\text{Cu}^{\text{I}} \text{ tot.})/dE$) to emphasize the reduction rate. The Cu^{II} reduction is also compared to the reactant consumption and (over-oxidized) product formation. The results are given in Figure 25. Foremost, comparing the rate of Cu^{II} reduction, we observe that the onset of Cu reduction varies depending on the substrate in the order of $\text{CO} < \text{C}_2\text{H}_6 < \text{CH}_4$, where the CH_4 atmosphere leads to the highest reduction temperature. This is quite natural given the stronger bond dissociation energy of CH_4 (439 kJ/mol) compared to C_2H_6 (422 kJ/mol) [19]. As the behavior of Cu in CO is so different, we will discuss further the CO-TPR event at the end of the section, and for now, focus on the results obtained with the two alkanes as reducing agents. Interestingly, we observe that 018Cu-MOR(7) appears to have a marginal temperature region initially, where Cu is reduced faster than for 036Cu-MOR(11). This is consistent with the **Cu^{II}_HT_b** species reducing faster than the other Cu^{II} species, as observed in the previous section. This earlier reduction behavior in 018Cu-MOR(7) could be sought-after evidence of more readily reducible species in the highly active Cu-MOR material [114, 120]. A high “self-reduction” potential has been linked directly to the materials’ methanol productivity in other framework topologies like Cu-exchanged FER and CHA [94, 140]. This however, has not been observed for the Cu-MOR zeolites presented herein, as previously reported results have indicated that 018CuMOR(7) has more “self-reduction” resistant species, which then were coupled with well-distributed Cu-oxo species with high coordination and uniform bond lengths [120, 141]. It should be noted,

however, that the above-mentioned studies concern the reducibility of Cu-zeolites in either vacuum or inert atmosphere. Conversely, herein we are linking the high methanol productivity of 018Cu-MOR(7) directly to the reducibility of the Cu species in a methane atmosphere. This elucidates the importance of working with as relevant conditions as possible. Moreover, the higher reducibility observed for 018Cu-MOR(7) herein is in full agreement with Lomachenko et al. who found that more Cu^{II} reduced to Cu^I after methane loading for the 018CuMOR(7) material compared to 036Cu-MOR(11), when investigating the samples with XAS in a full MTM cycle [142].

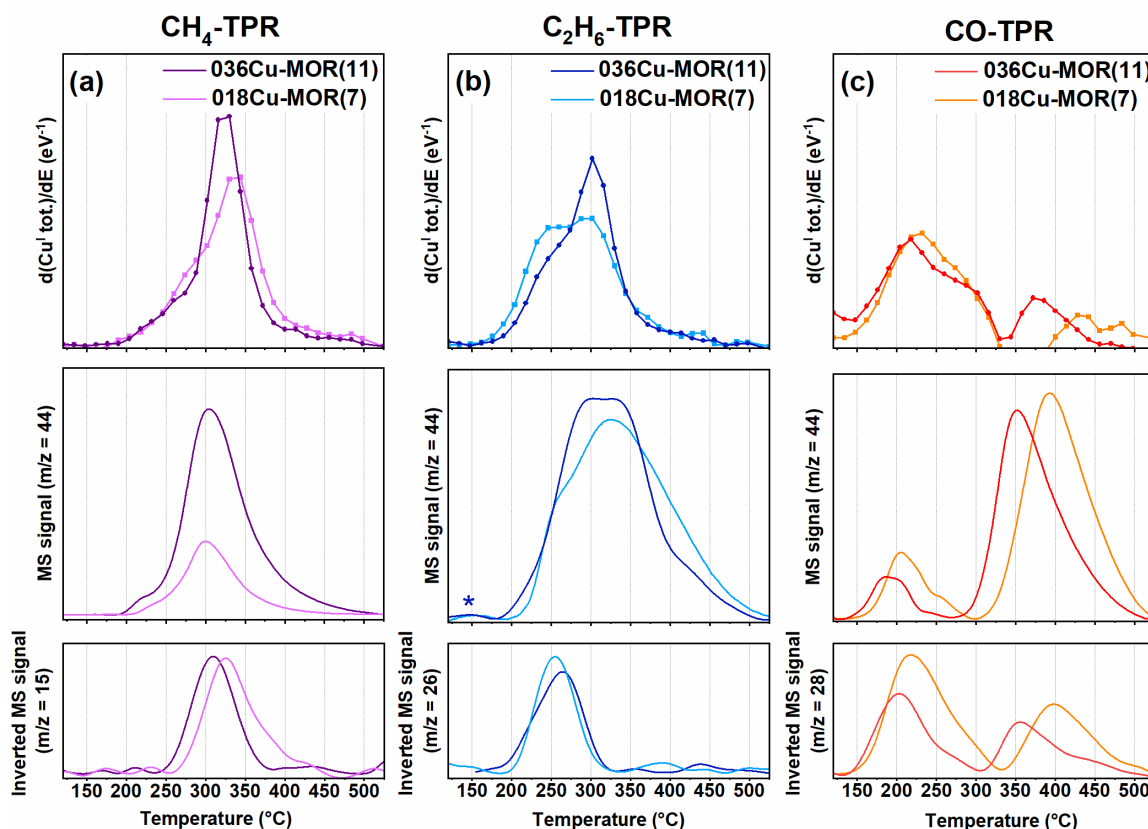


Figure 25. (a-c) Comparison of the first derivative of the Cu^I-fraction (top panel) to the CO₂ formation (middle panel) and reactant consumption (bottom panel) during the TPR protocol with (a) CH₄, (b) C₂H₆, and (c) CO. The MS trace used for CO₂ is m/z = 44, while m/z = 15, 26, and 28 is used for CH₄, C₂H₆ and CO, respectively. The MS traces have been normalized to the sample weight and Cu content. *The CO₂ trace for 0.36Cu,H-MOR(11) during C₂H₆-TPR has been collected in a parallel experiment in the home laboratory, due to technical problems with the trace obtained during the XAS experiment.

Upon comparing the reduction rate of Cu^{II} to the substrate consumption and CO_2 production obtained simultaneously (Figure 25), interesting features are found. First, during CH_4 -TPR, both CO_2 , as well as the consumption of CH_4 , appear in the same temperature window as the Cu^{I} formation. This direct link between CH_4 consumption, CO_2 production, and Cu^{I} formation contrasts with previously reported results by Sushkevich et al. [136]. They observed a temperature region where CH_4 was consumed before CO_2 production over Cu-MOR ($200 > 325$ °C) and signified this window to be linked with oxidation processes of partially oxidized methane intermediates. However, as we observe the complete oxidation occurring simultaneously with Cu^{I} formation and CH_4 consumption, we speculate that with a continuous temperature ramp, the over-oxidation occurs too fast to be singled out from the CH_4 consumption and Cu^{II} reduction in a meaningful way. Nevertheless, about 10% of the total Cu^{I} fraction is forming before the onset of CH_4 consumption (< 250 °C). We postulate this minor Cu^{I} fraction, yet very close to the uncertainty of the MCR-ALS method, to possibly come from a “self-reduction” of Cu^{II} to Cu^{I} , as made possible by an electron-rich environment after O_2 activation where O^{2-} ions have remained stabilized in the framework [260]. We must point out that the results also show small traces of CO_2 produced in this low-temperature window. However, we allocate this to an effect of the low signal resolution caused by the small amounts of material and gas flows used in the experiment. Also due to this, we cannot exclude the possibility that some CH_4 (not visible in the CH_4 trace) is being consumed already from around 200 °C when Cu is being reduced. Regardless, some Cu^{I} is forming before consumption also during C_2H_6 -TPR, especially discernible for 018Cu-MOR(7), supporting the “self-reduction” event suggested above. Another intriguing observation during C_2H_6 -TPR is that there is a secondary region, where no more ethane is being consumed, but there is still a reduction of Cu, as well as continued production of CO_2 . This behavior indicates that when ethane acts as a substrate, there are secondary oxidations with ethane

derivatives that are less potent reducing agents, reacting on remaining Cu^{II} sites that did not react directly with ethane or were somehow not accessible to ethane.

Coming back to the CO-TPR protocol, two reduction regions are observed. The primary reduction starts directly upon contact with CO and leads to ca. 80% of reduced Cu^{II}. Then as the temperature increases, a secondary reduction event happens at higher temperatures, involving the residual fraction of ca. 20% of total Cu. In contrast to the behavior of the Cu-zeolites in an alkane atmosphere, it appears the Cu-sites in 036Cu-MOR(11) reduce overall in a lower temperature range than 018Cu-MOR(7). Focusing on the Cu^{II} reduction, we surmise that the first, broad reduction peak is linked with the above-suggested formation of Cu^I-(CO)_x (x = 1 or 2). This is also well supported by a clear consumption of CO, and a smaller CO₂ production coming from the oxidation at the Cu-oxo sites. Then, during the high-temperature reduction event, we do see a much larger fraction of CO₂ being produced in combination with a smaller consumption of CO. As most Cu already has been reduced to Cu^I at this point, we postulate that the production of CO₂ is linked with trapped CO₂ being released as the temperature increases, or possibly the release and oxidation of CO from Cu^I-carbonyls. This could proceed *via* a reaction with residual O²⁻ present, or by a disproportionation reaction between two CO molecules in a Boudouard reaction [261]. As we do not have any evidence for the formation of elemental C, the latter reaction pathway is only speculations by the authors at this point.

5.3. Complementary *in situ* UV-vis TPR Experiments

To support the observations presented in the previous sections, a complementary experiment was performed in-house with a purpose-designed *in situ* UV-vis setup. The UV-vis spectra were obtained in diffuse reflectance mode during a CH₄-TPR experiment for both 018Cu-MOR(7) and 036Cu-MOR(11) and are reported in Figure 26. Interestingly, we are seeing the biggest changes in the UV-vis spectra in

the same temperature window as for the XANES results presented above. It can be observed that at about 250 °C, three bands at 20250, 16850, and 13000 cm⁻¹ grow, reaching a maximum at about 325 °C. This is also approximately the temperature at which a maximum is observed for CH₄ consumption and Cu^I formation rate during the XAS experiment. At 325 °C, the bands decrease again, giving the biggest evidence of reduction from Cu^{II} to Cu^I, as this is to be expected when the Cu ion goes from a d⁹ to a d¹⁰ configuration and the d-d electron transfer becomes forbidden. When the temperature reaches about 400 °C, the changes slow down, and mostly temperature-induced shifts in the LMCT region (25000-45000 cm⁻¹) are observed from 450-550 °C [116].

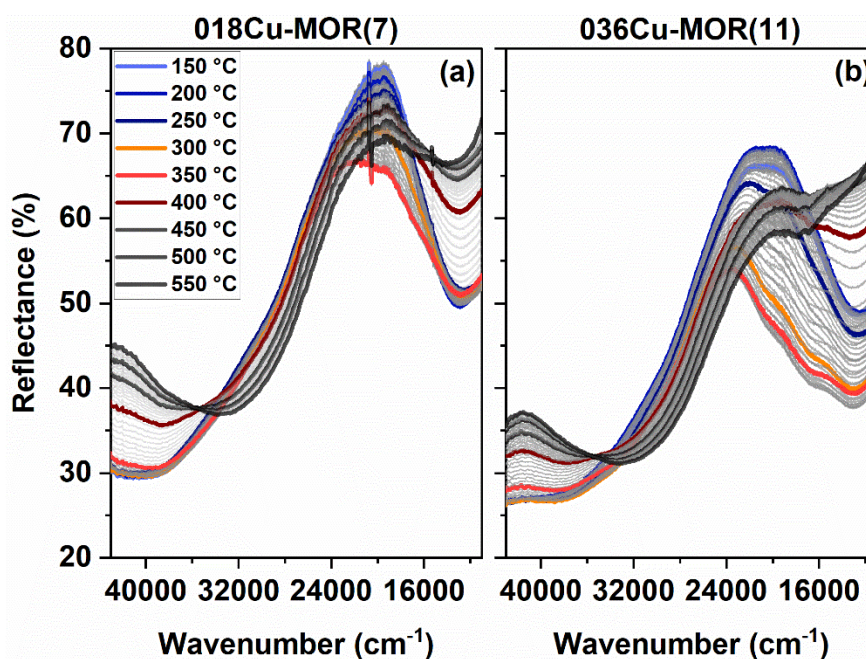


Figure 26. *In situ* UV-vis spectra were obtained during a TPR protocol with CH₄ for the two Cu-MOR samples. The spectra are overlaid, with a thicker line and different colors used for every 50 °C to clarify the change in the spectra throughout the protocol. Blue colors are for low temperatures, red for intermediate temperatures, and dark grey for high temperatures.

The growth of the bands in the d-d region between 250 and 325 °C, especially visible in 036Cu-MOR(11), is counter-intuitive, as it could be interpreted as an increase in the abundance of Cu^{II} species. However, the combination of these three bands shares similarities with the so-called “multiplet” formation also

observed previously in Cu-CHA during O₂ activation [232]. The literature suggests that the multiplet formation is linked with a diluted Cu^{II} species with a very strong extinction coefficient [262]. Interestingly, it is evident from the band at 38500 cm⁻¹ that the species must also affect the LMCT region, as there is no evidence of reduction here before the temperature reaches 325 °C. Nevertheless, we conjecture that even though this species is forming, it is likely to involve a minor fraction of total Cu ions, and there is still a reduction process occurring before T = 325 °C, as evidenced by the XAS experiments. To the best of our knowledge, the observation of a multiplet has not previously been reported for Cu-MOR. The Cu^{II} species is temperature dependent, and forms, contrary to Cu-CHA, in a CH₄ atmosphere. Why this species is much more prominent in 036Cu-MOR(11) than in 018Cu-MOR(7) would only be subject to speculation at this point, but it is alluring to suggest it is linked with the **Cu^{II}_HT_b**, as this is much more abundant in the 036Cu-MOR(11) sample.

5.4. Confirming the Formation of Cu^I-CO with *in situ* FT-IR Spectroscopy Measurements

To verify that the **Cu^I_c** component indeed is from Cu^I-(CO)_x formation, and whether it is linked with mono- or dicarbonyl species, we performed *in situ* CO-TPR experiments coupled with FT-IR spectroscopy on a pre-oxidized 018Cu-MOR(7) sample. The results are reported in Figure 27 (a). As the CO atmosphere is introduced to the sample, a band associated with Cu^I-CO adducts on Cu-MOR zeolites is evolving slowly at 2158 cm⁻¹ [234]. Additionally, we observe the presence of the gaseous CO molecules by the presence of rotational-vibrational branches on either side of the Cu^I-CO band. The maximum intensity of these branches is marked with an asterisk (*). Then, as the temperature increases, the monocarbonyl band increases, until a maximum is reached at about 350 °C. The intensity of the band at 2158 cm⁻¹ reflects both the amount of Cu^I (growing according to the reducing effect of CO) and the stability of the Cu^I-CO adducts. For this reason, it is

not directly coinciding with the evolution of the $\text{Cu}^{\text{I}}_{\text{c}}$ component, which is found to have a maximum at about 300 °C (Figure 24 (b)), however, clearly present up to at least 400 °C. The formation of a $\text{Cu}^{\text{I}}\text{-CO}$ band on a Cu zeolite with no Cu^{I} as evidenced by XAS, suggests that at 120 °C, CO is instantaneously able to reduce some Cu^{II} species to Cu^{I} , that are then able to form the $\text{Cu}^{\text{I}}\text{-CO}$ adduct and form CO_2 . This is consistent with the reduction of Cu^{II} , the early consumption of CO, and the subsequent formation of CO_2 , as observed above when performing the parallel CO-TPR/XAS experiment.

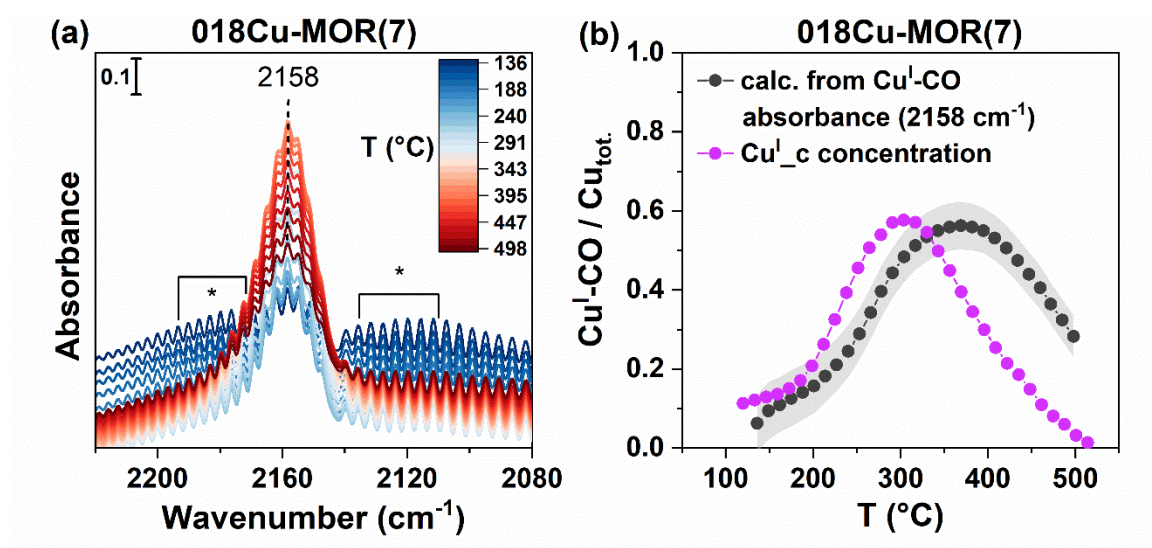


Figure 27. (a) FT-IR spectra obtained during CO-TPR. Spectra are background subtracted. (b) A comparison of the fraction of $\text{Cu}^{\text{I}}\text{-CO}$ species found with XAS throughout the TPR protocol ($\text{Cu}^{\text{I}}_{\text{c}}$), and the corresponding $\text{Cu}^{\text{I}}\text{-monocarbonyl}$ fraction calculated from Beer-Lambert law by integrating the band 2158 cm^{-1} . The error bars (grey band) are given as the standard deviation determined from three different baseline positions on the rotational-vibrational features when obtaining the integrated area.

To more quantitatively compare the 2158 cm^{-1} band from FT-IR to the $\text{Cu}^{\text{I}}_{\text{c}}$ component, we calculated the CO concentration from the integrated feature at 2158 cm^{-1} by applying Lambert-beers law given in eq. (6), Deplano et al. recently determined the molar attenuation coefficient, ϵ , for monocarbonyl species forming on Cu-ZSM-5 zeolites [219], and as long as the band shape of the $\text{Cu}^{\text{I}}\text{-CO}$ band is

similar, this value should be somewhat comparable for other zeolite systems. We therefore used this value for our calculations herein. By dividing the calculated CO concentration by the total Cu concentration of the system we indirectly find the fraction of Cu^I-CO species with FT-IR. The results are reported in Figure 27 (right panel) and inadvertently give a strong correspondence with the Cu^I_c concentration determined by XAS. Both traces give a maximum Cu^I-CO formation (~300 °C) of about 55% of the total Cu concentration in 018Cu-MOR(7). At this temperature, almost 80% of the Cu in the sample has become Cu^I (Figure 25), indicating that some CO species have already desorbed, leaving bare Cu^I sites. The CO reduction on Cu^{II} sites is a two-electron process, and should therefore only be possible on Cu-dimers, or possibly two isolated Cu^{II} species nearby [263]. WT-EXAFS results, performed by Beatrice Garetto at UniTo and reported in **Paper IV**, revealed that all detectable Cu^{II} species in the sample after O₂ activation were dicopper(II) moieties (or proximal Cu^{II} monomers), also in line with previous literature proposals [15, 120, 170, 171]. Overall, these results show that a very large fraction of the Cu^{II} species in MOR are dimeric species after O₂ activation, and do not need to be made mobile with e.g. an NH₃ molecule to form the dimers, as suggested for other zeolite systems, like CHA [264, 265]. We note that there is a small shift in the temperature profile for the CO/Cu trace (calc. from absorbance) compared to Cu^I_c, however, we allocate this to the different setups utilized, causing small variations in the measured temperature. Additionally, we explain the slower CO desorption in the FT-IR setup to the vast difference in the sample environment. FT-IR was measured on a thin wafer, while XAS was performed on a pelletized sample in a capillary reactor. The different pellet morphology and sample environment leads likely to a slower diffusion through the sample in the FT-IR cell compared to the capillary.

6. C₂H₆ Activation

In chapters 4 and 5, we investigated the structural and mechanistic effects the zeolite framework and Cu-speciation can have on the MTM reaction. This research has added input to the methane activation literature. As we observed in chapter 5, the Cu-zeolites can also activate the C–H bond in other alkanes at an even lower temperature than in CH₄. In this third chapter, we use the understanding obtained for MTM in the work presented herein, but also over the last two decades by other groups, to expand on the use of Cu-zeolites towards other C–H reactions, specifically, the activation of ethane. This chapter is based on the results reported in **Paper V**, and in this fundamental study, we report a new pathway for ethane conversion over Cu-zeolites by exploring the structural and compositional requirements for an effective reaction.

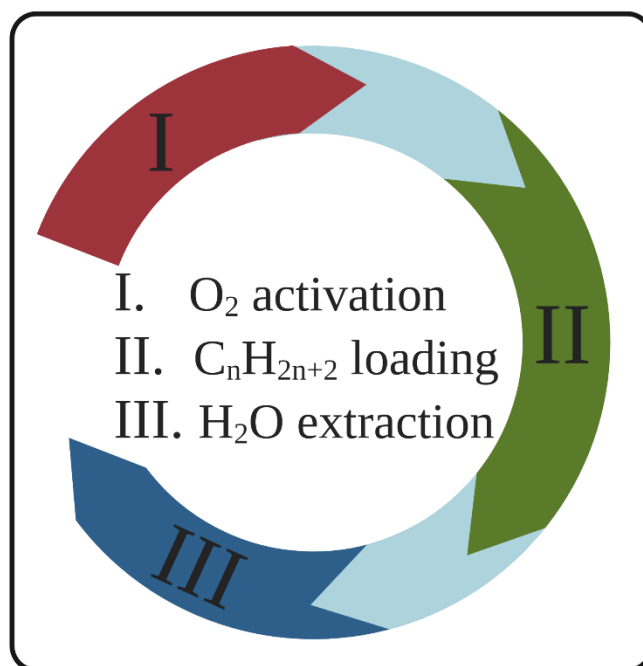


Figure 28. Illustration of the idea behind chapter 6. Expanding the MTM stepwise reaction mechanism towards other C–H activation reactions.

6.1. C–H Activation in a Stepwise Reaction Protocol

For ethane activation, 0.36Cu,H-MOR(11), also used for the TPR study in chapter 5, has been the reference sample. Furthermore were Cu-ZSM-5, Cu-SSZ-13, and a range of MOR zeolites with different compositions tested for ethane activation. All samples have been tested in the MTM reaction, and are well characterized [94, 114, 219]. Relevant elemental composition and MTM activity of the materials are summarized and reported in the SI of **Paper V**.

The protocol applied for ethane activation is based on the optimized MTM protocol by Pappas et al. [94], altered with a slightly lower activation time (3 h vs 6 h) and temperature (150 vs 200 °C). The full protocol (Test #2) is given in Table 4 in the experimental section. Already from our initial results on 0.36Cu,H-MOR(11), it was evident that the sample was able to activate the C–H bond in ethane. As reported in Figure 29 (a), The main product was ethylene, with ~95% hydrocarbon selectivity. When following the productivity throughout three reaction cycles, the reactivity seems to be quasi-stable, with only a small decrease in ethylene yield (Figure 29 (b)).

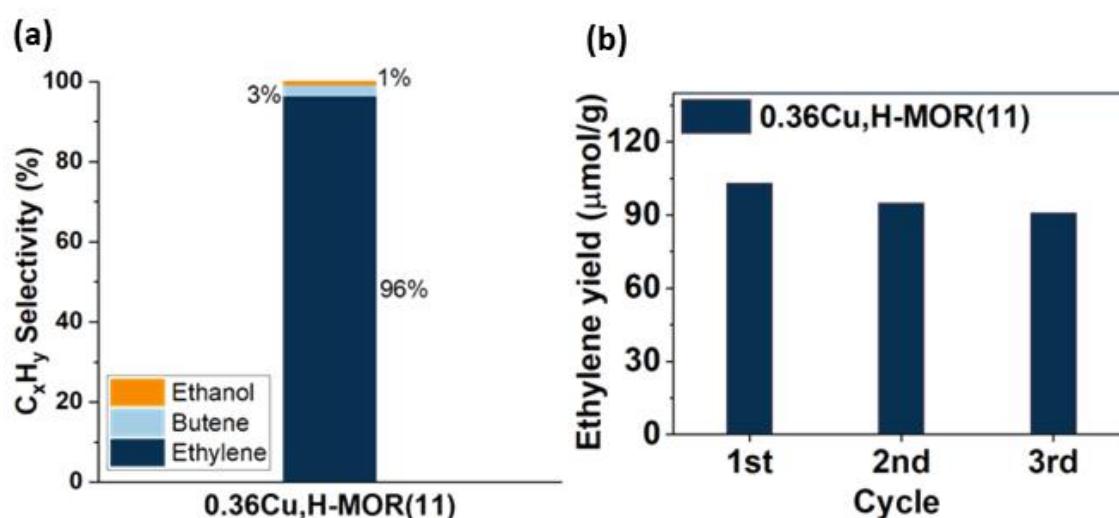


Figure 29. (a) Hydrocarbon selectivity as determined with an FID detector. (b) Ethylene yield ($\mu\text{mol}_{\text{C}_2\text{H}_4}/\text{g}$) obtained for three consecutive reaction cycles.

6.2. Screening of the Material Properties

Having shown that we produce ethylene over a Cu-zeolite, we set forth to elucidate the necessary site requirements for ethylene production. To do so, 0.36Cu,H-MOR(11) was used as reference material and compared to a variety of materials. Figure 30 shows the yield of ethylene obtained over different material topologies and zeolite compositions and several interesting features of the reaction can be observed. 0.36Cu,H-MOR(11) is used as reference material for the discussion. First, the reaction was performed over three test materials. A Cu-loaded silica (5wt%Cu-SiO₂) containing CuO clusters, a Cu-loaded silica alumina with similar Al and Cu content as the reference material that contains [AlO₄]⁻ for Cu and H exchange, and an H-MOR zeolite (a porous zeolite framework with acid sites, but no Cu). They all yielded negligible amounts of ethylene and other products, confirming that both well-defined Cu sites and the zeolite framework with restricted exchange sites, are necessary to promote the activation of ethane. Further, a Na-based, Cu-exchanged MOR zeolite (0.32Cu,Na-MOR(11)) with similar Cu-content as the reference material, but less Brønsted sites, displayed a similar ethylene yield and product distribution. This implies that the Brønsted sites are not that crucial for ethylene production. This contrasts with previous findings for the MTM reaction that show that the Brønsted sites play an important part in stabilizing methoxy intermediates for methanol production [178, 179]. A Cu-loaded ZSM-5 with similar Cu/Al and Si/Al as our reference material produced a significantly lower yield, and thus lower productivity (0.10 mol_{C₂H₄}/mol_{Cu}). This is somewhat surprising, as ZSM-5 has been proposed in other ethane activation reactions, e.g. exchanged with Pt, Zn, Ga, or Fe [212, 266-268]. Nevertheless, the same trend between the zeolites has also been observed in the MTM reaction [269], highlighting the similarity of the two reactions. Also a Cu-loaded SSZ-13 was tested in the reaction and proved less productive than both MOR and ZSM-5 (0.07

mol_{C₂H₄}/mol_{Cu}). This evidences a trend, where the productivity increases with increasing pore size: CHA (8r) < MFI (10r) < MOR (12r).

When employing a Cu-MOR with both a lower Si/Al and Cu/Al ratio (0.18Cu,H-MOR(7)) that previously has been found to be a quintessential material for methanol production in the MTM reaction [120], unremarkable results are found when ethane is the reactant. This indicates that the Cu species in 0.18Cu,H-MOR(7) are more efficient at activating methane than ethane, which is surprising given the higher reactivity of ethane (the bond dissociation energies of the first C–H bond in CH₄ and C₂H₆ are 439 vs 422 kJ/mol, respectively [19]). Based on this conspicuous difference, and the lack of a detrimental effect of Na, we conjecture that there might be some subtle differences in the site requirements for methane and ethane activation.

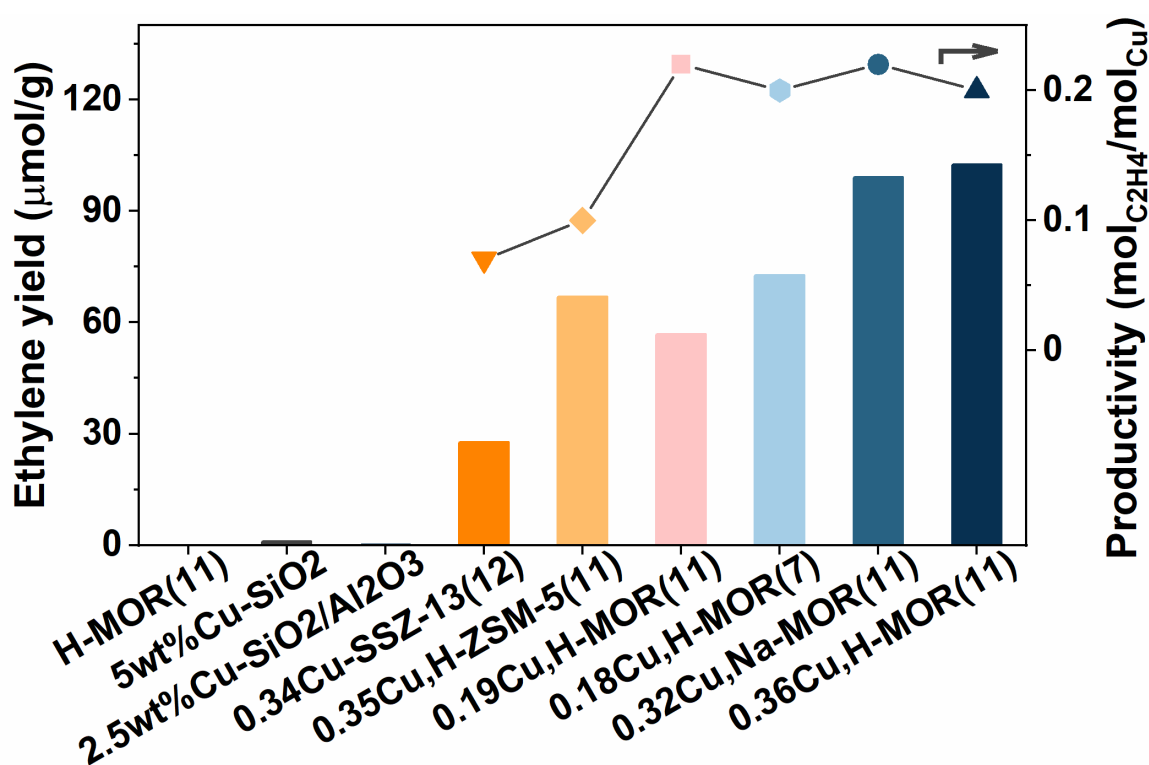


Figure 30. (left axis) Bar plot comparing the ethylene yield (μmol_{C₂H₄}/g) produced over different materials. On the right axis, the ethylene productivity (mol_{C₂H₄}/mol_{Cu}) is plotted against the Cu content. The line connecting the symbols is for visual guidance.

When comparing the reference to a sample based on the same zeolite but with lower Cu content (0.19Cu,H-MOR(11)) it is evident that 0.36Cu,H-MOR(11) has the highest yield. The normalized ethylene productivity of the Cu-loaded zeolites ($\text{mol}_{\text{C}_2\text{H}_4}/\text{mol}_{\text{Cu}}$) is plotted on the right axis of Figure 30. The productivity is the same for all four MOR samples ($\sim 0.20 \text{ mol}_{\text{C}_2\text{H}_4}/\text{mol}_{\text{Cu}}$), suggesting that regardless of Si/Al ratio or Cu content, the number of active sites increases linearly with the amount of Cu present. In contrast, a volcano-type behavior is typically observed within the same range of Cu content for MTM with the productivity peaking at intermediate Cu-loadings [85, 120]. This major difference between the two reactions again indicates different Cu site requirements for C–H activation in ethane vs methane.

6.3. Mechanistic Insight from FT-IR Spectroscopy

To study the interaction of the ethylene product with the materials, 0.36Cu,H-MOR(11) and H-MOR were investigated with FT-IR spectroscopy upon incremental doses of ethylene. The full spectra, including a more detailed description, are reported in SI of **Paper V**, while the $\nu(\text{C-H})$ stretch region is shown in Figure 31. Below 3000 cm^{-1} , several new bands evolve for H-MOR(11), but not for the Cu-containing sample. These bands are related to the formation of saturated CH_2 (2928 and 2857 cm^{-1}) and CH_3 (2960 and 2873 cm^{-1}) groups, indicating that ethylene starts to be polymerized in the H-MOR zeolite. This has also been shown to occur over other H-zeolites [270]. Interestingly, this behavior is only observed in the pure, protonic zeolite, and not in the Cu-containing sample, even though 0.36Cu,H-MOR(11) still has a significant amount of Brønsted sites. We posit that the ability of the Cu-exchanged zeolites to suppress oligomerization might be the key to the high ethylene selectivity. When Cu-zeolites are used in the ethane-to-ethylene (ETE) reaction, the ethylene-derived intermediates are stabilized on the Cu-sites, thus preventing further oxidation or chain growth.

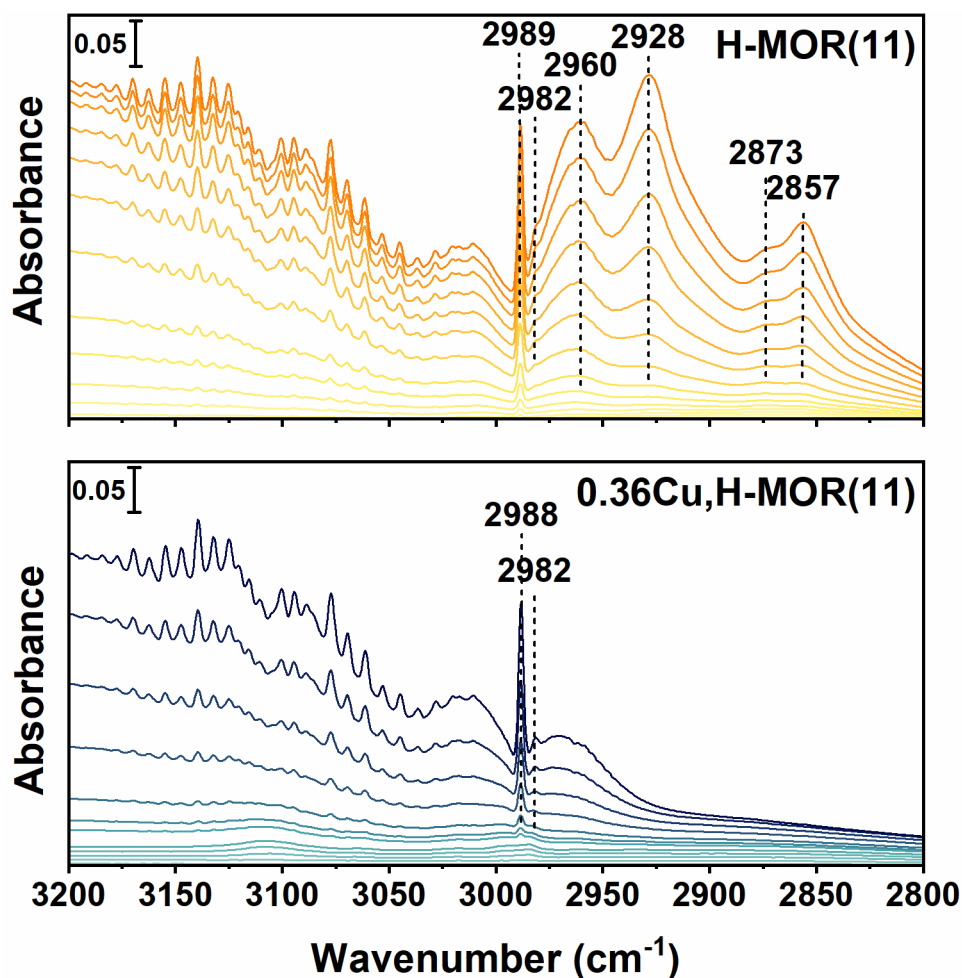


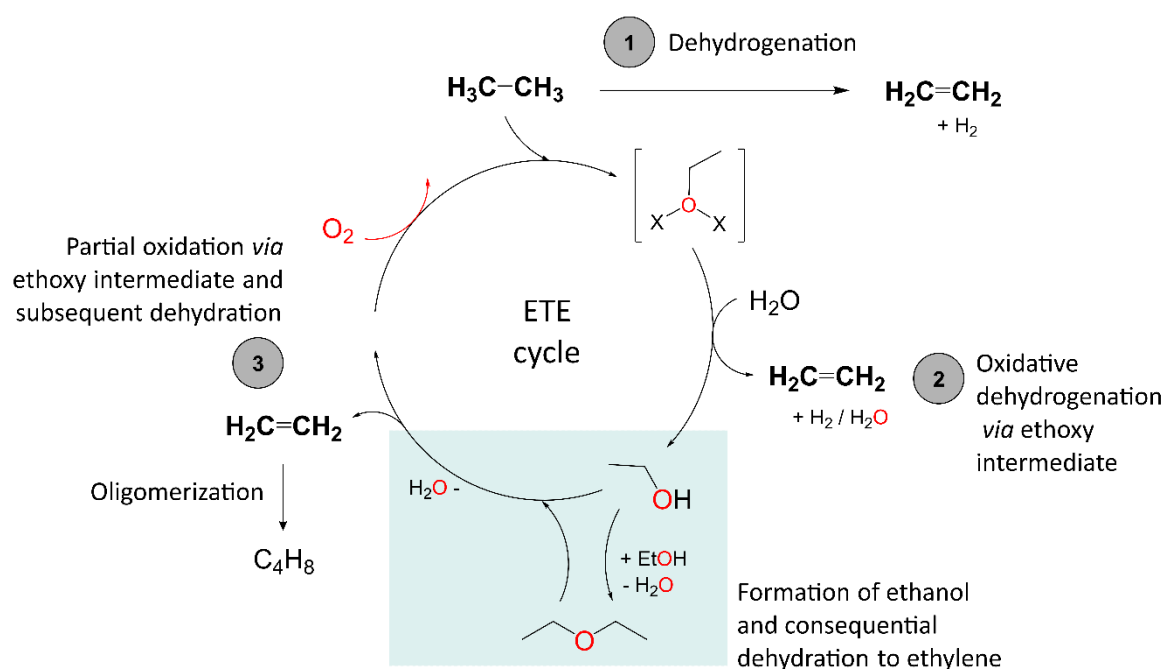
Figure 31. Normalized and background subtracted FT-IR spectra of the $\nu(\text{C-H})$ stretch region obtained for adsorbed ethylene at RT on H-MOR(11) (top panel) and 0.36Cu,H-MOR(11) (bottom panel).

6.4. Reaction Pathways

Based on the experimental data obtained, we have tried to identify possible reaction routes for ethylene formation from ethane over activated Cu-sites. The reaction pathways considered are displayed in Scheme 2. There are in principle three pathways for ethylene formation, marked (1) – (3) in Scheme 2. Pathway (1) involves the direct dehydrogenation of ethane and the formation of molecular hydrogen in an endothermic reaction. However, as we have shown that oxidized Cu species are an important factor for ethylene production, and since also C_2 oxygenates are observed as (minor) byproducts, it is considerably more likely that

the reaction proceeds *via* an ethoxy intermediate. Accordingly, two exothermic, oxidative reaction pathways, (2) and (3), are proposed. Analogous to methoxy formation in the MTM reaction, ethane could react with some type of Cu_xO_y -moieties leading to ethoxy formation. Pathway (2) is a direct oxidative dehydrogenation of ethane via ethoxy intermediate species. Water facilitates the desorption of ethylene, and H_2O (or possibly H_2 if the Cu is re-oxidized in this step) is formed as the byproduct.

Scheme 4. Possible routes derived from the experimental data obtained herein for the ETE reaction. The colored box marks the dehydration process.



Pathway (3) involves C_2 oxygenates (ethanol and possibly diethyl ether (DEE) from dehydration) as free intermediates. Initially formed ethoxy species are detached from the active site upon contact with water. Then, a dehydration process occurs, either instantaneously at the acid sites or some point down the bed and ethylene is the main product detected in the effluent. To confirm the likelihood of dehydration, we exposed $0.36\text{Cu}_x\text{H.MOR}(11)$, $0.32\text{Cu}_x\text{NaMOR}(11)$, and H-

MOR(11) directly to ethanol after activation in oxygen, which indeed led to a significant formation of ethylene over all three materials. Pathway (3) is supported by the observation of trace amounts of ethanol in the effluent. We consider it unlikely that ethanol is formed from acid-catalyzed hydration of ethylene in pathway (2) as the product distribution was found to be the same over both Na-based and H-based Cu-MOR and thus unaffected by the density of Brønsted acid sites. Additionally, since an oxidative dehydrogenation to ethylene, as suggested by pathway (2), should be feasible without the addition of H₂O, it is more conceivable that the reaction is proceeding *via* ethanol formation (pathway (3)). Consequently, the main experimental observations favor reaction pathway (3), and we surmise that the reported ethane activation protocol results in the formation of ethoxy intermediates. We note that this might lay the foundation for a search for a process to form ethanol directly from ethane, by looking for the right reaction conditions and metal-zeolite.

6.5. Elaborating on the Cu-oxo Site Requirements

Beyond what we report in **Paper V**, we have also looked into the effect of different activation treatments. The initial screening of materials and diverging productivity trends demonstrated the likelihood of different Cu-sites being active for ETE and MTM. The consensus in the field of MTM research is for Cu_xO_y-moieties to form in the framework after O₂ activation, and that these are the species responsible for methane activation [67]. Recently, it has been suggested that the oxygen in methanol comes from a reaction with H₂O in the extraction step, and not the Cu_xO_y-sites [101-103, 125], leading to a new-found insight into the reaction mechanism and the role of the Cu sites. To study more deeply the nature of the Cu sites in the ETE reaction, 0.36Cu,H-MOR(11) was subjected to three consecutive activation cycles in an inert atmosphere (He) instead of oxygen. It has been shown that activating Cu-zeolites in He leads partially to the “self-reduction” of Cu^{II} to Cu^I. Based on this, the hypothesis would be that activating Cu-zeolites in He leads to

fewer Cu^{II} sites and subsequently lower productivity. And indeed, for several Cu-zeolite systems in the MTM reaction, this is the case [94, 140]. The results obtained after He activation for three cycles are presented in Figure 32, directly compared to the corresponding results from O₂ activation that was also presented in Figure 29. Quite remarkably, the yield of ethylene is largely identical for all three cycles, irrespective of the activation procedure. Indeed, the activity with He activation seems even more stable than when the sample was activated with O₂.

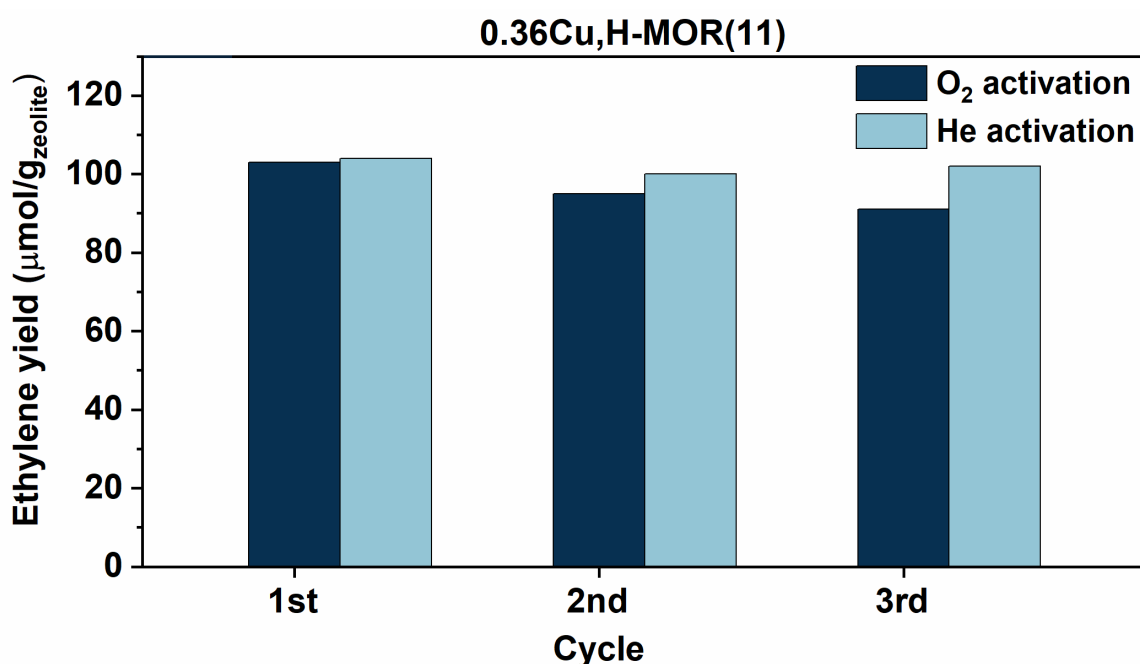


Figure 32. Bar plot comparing the ethylene yield obtained over three cycles when exposed to O₂ or He during the activation step.

These results open up a can of questions that should be discussed. Firstly, if it is assumed that Cu_xO_y-moieties, as suggested in Scheme 4, are necessary to activate ethane and produce ethylene in the Cu-loaded zeolites, the quasi-stable ethylene yield suggests that H₂O may contribute to the formation of the active Cu-oxo sites needed in this reaction. This has also been shown to be possible for the MTM reaction, mostly at higher methane pressures to compensate for some active sites poisoned by water [101, 102, 125, 201]. Although, somewhat difficult to explain is the high activity observed already in the first cycle. This suggests that when activating in He, oxidation would only be possible from moisture in the

atmosphere before loading the reactor, or possibly from small impurities entering the reactor upon cooling after high-temperature treatment. We could speculate at this point that the sites available for ethane activation are less prone to “self-reduction”. Given a productivity of $0.20 \text{ mol}_{\text{C}_2\text{H}_4}/\text{mol}_{\text{Cu}}$, this would be about 40% of the total Cu. Indeed, in chapter 5, Figure 25, we saw that the ethane consumption finished when only half the Cu^{II} sites had been reduced to Cu^{I} , supporting the hypothesis that only a set of sites are capable of ethane activation. It could be imagined that the ethoxy species, being larger than methoxy is only stabilized at certain positions. Similar behavior has been observed also in methanol carbonylation reactions, where it was shown by Corma and coworkers that the T-sites around the 12-ring were not able to stabilize the acetyl intermediate and formed other kinetically favored products [271]. However, if the acetyl intermediate was placed inside the 8-ring side-pocket at the T3 site and pointing out towards the 12-ring channel, it would have enough confinement from the framework, without being sterically hindered, to selectively form acetic acid. With an ethoxy intermediate being about the same size as the acetyl intermediate, this could be a plausible explanation for the low productivity. It should be emphasized here that these are all just speculations at this point and that more investigation on the Cu-speciation during O_2 and He activation is necessary.

6.6. Systematic Study of the Reaction Parameters

The positive effect of water presence in alkane activation over zeolites has also previously been shown in a publication by Hensen et al., where they use DFT calculations to show that water stabilizes the reaction intermediates and thus increases the reaction rate for steady-state alkane activation over Ga-ZSM-5 [272]. To start understanding the requirements, also other parts of the stepwise protocol were scrutinized to find the optimum conditions for ethane activation. All experiments were performed on the reference material, $0.36\text{Cu}_x\text{H-MOR}(11)$ sample, and the reference protocol was the following: O_2 (8 h) at 500°C , flushing

in He (1 h), followed by C₂H₆ (3.5 h) at 150 °C, before the sample was again flushed in He (1 h), and lastly reacted with steam (2 h). The results from changing one parameter at a time are reported in Figure 33, and show the changes in ethylene productivity as an effect of the ethane loading time and temperature, as well as the He activation time and temperature. Since He activation was found to be as effective for productivity as O₂-activation, the effects of changing exposure time and temperature during the activation were only investigated for the He activation protocol.

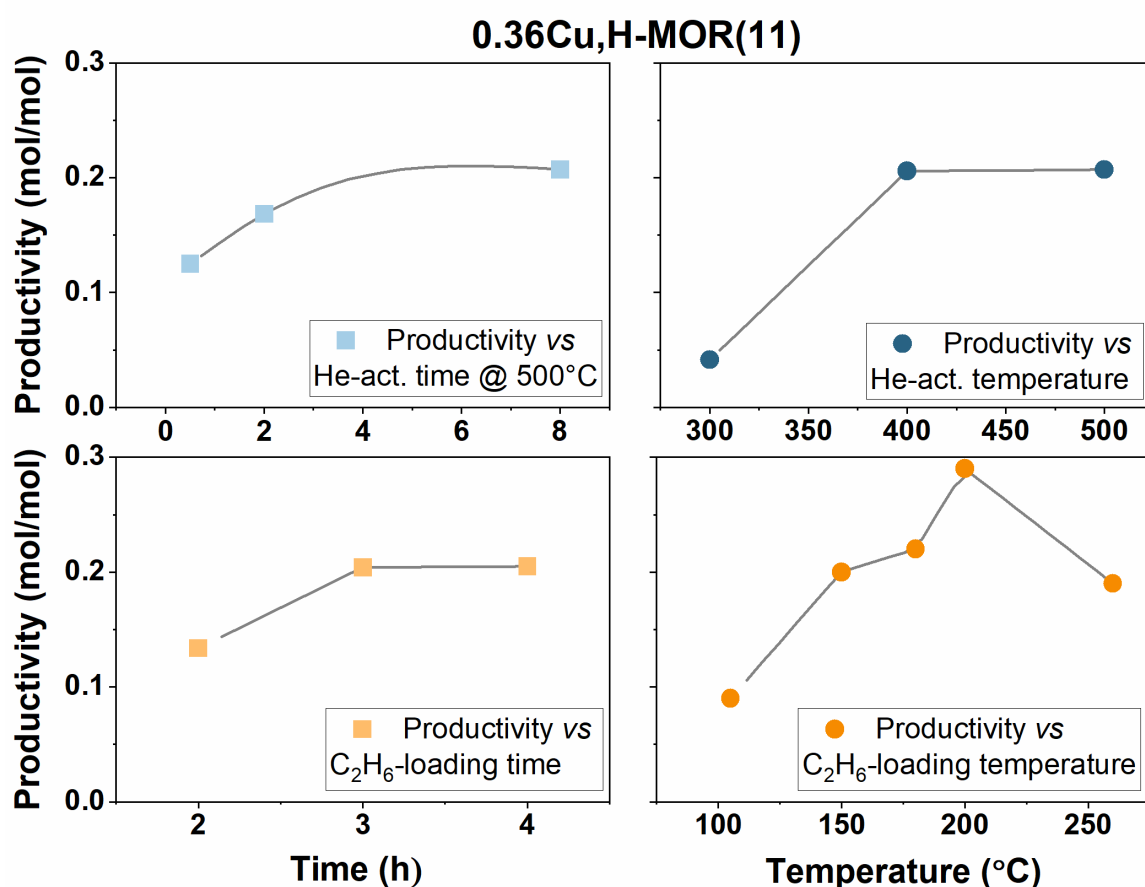


Figure 33. Normalized ethylene productivity (molC₂H₄/molCu) obtained during a systematic study of the reaction conditions. The change in productivity is reported vs the exposure times (left column - squares) and the temperature (right column - circles) for the He activation (top panel - blue) and ethane reaction step (bottom panel - orange). The water extraction step was always kept isothermal to the ethane exposure temperature. The grey lines are only present as a guide for the eye.

The results from altering the exposure time at high temperatures show the importance of a prolonged time at high temperatures to obtain the highest productivity. This indicates that the oxidation process is slow, similar to what has been found for the MTM reaction [94]. One likely reason is that strongly adsorbed water needs a certain temperature to be released or dehydrogenated to form Cu-oxo species, as it otherwise poisons the active sites [273]. Thus, the removal of these strongly bound water species may have a significant impact on Cu-speciation, and consequently, the productivity. Searching for an optimal temperature in the range between 300 and 400 °C could be an aid to find an adequate temperature to perform a continuous or isothermal chemical looping approach for ethane activation over Cu-loaded zeolites with only ethane and H₂O as reactants, while still keeping the selectivity high. Furthermore, when altering the exposure time to ethane, also here, a somewhat lengthy exposure time was necessary. However, the ethane activation observed herein is much faster than methane activation in the same protocol, as Pappas et al. deemed an exposure time of 6 h necessary to optimize the MTM reaction protocol over Cu-CHA [94]. In this study, only 50 mbar partial pressure of ethane was used, and the effect of having a higher partial pressure was not investigated. In the study by Pappas et al. it was shown that a higher partial pressure of methane had a positive effect on the MTM reaction, so this should be kept in mind for future studies on improved productivity, e.g. in the search of a continuous reaction over the Cu-zeolites [94]. Lastly, when comparing the ethane loading temperature, it is evident that the materials can produce some ethylene already at 105 °C. Then, as the temperature increase, there is peak productivity at 200 °C, before it drops again towards 260 °C.

Combined, the results indicate that a steady-state approach could be achievable, however, a compromise must likely be made when searching for the optimal activation temperature while maintaining a decent selectivity toward the desired products.

7. Conclusions and Perspectives

In the following section, the results presented in chapters 4-6 are bound together beyond the individual stories to provide a coherent picture of this work's overall findings and implications (Figure 34).

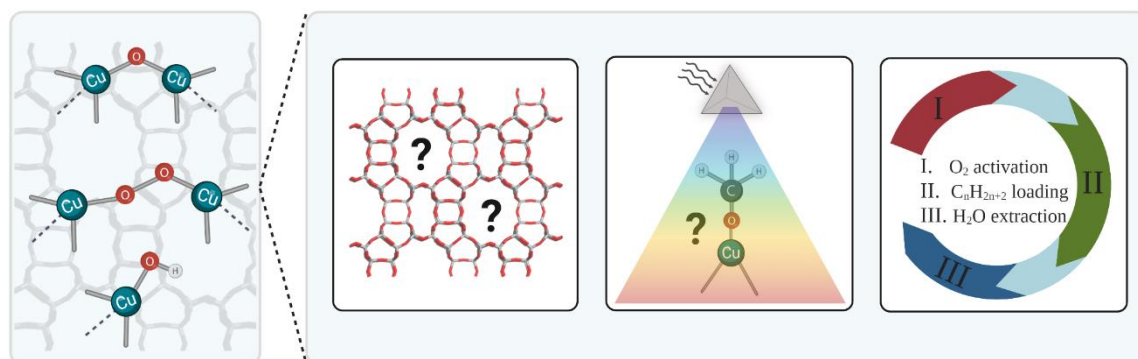


Figure 34. Illustration of the insight obtained with this work for the application of Cu-zeolites in C–H activation and oxidation reactions. Among other things, we have learned more about the Cu-speciation by studying the zeolite framework composition. Spectroscopy studies have shed light on the dynamic behavior of the Cu-sites when exposed to reducing agents. And finally, exploring the activation of another alkane over Cu-zeolites have shown that the versatility of the Cu-sites in C–H activation reactions.

7.1. Cu Speciation

The work presented in this thesis has provided new insight into the debate on Cu-speciation. In our study on Cu-SAPO-34, the spectroscopic evidence from rRaman, FT-IR, and XAS pointed to more isolated and highly coordinated Cu_xO_y-species forming in SAPO-34 vs SSZ-13. With results from rRaman spectroscopy, we could even propose a monomeric side-on superoxo Cu^{II} ([Cu(η²-O₂))] to be the most prominent Cu_xO_y-species forming in SAPO-34. The [Cu(η²-O₂)] species was proposed as the most likely four-coordinated species in SAPO-34 instead of bare Cu^{II} sites coordinated to two framework Al in the D6R. Bare Cu^{II} species have been proposed to form in Cu-SSZ-13 [155], but due to limited options to substitute Si in

the D6R of SAPO-34, it is less likely that highly coordinated species come from such bare Cu^{II} sites.

Upon studying Cu-loaded MCM-22 with CO-adsorption FT-IR spectroscopy, we found evidence of at least two spectroscopically different Cu species forming in the pore structure. One of them was linked with Cu located in the D6R at the bottom of the supercage and based on the inactivity of these sites in CHA zeolites, the formation of these was proposed as one of the reasons why only a moderate C–H activation was observed over the Cu-MCM-22 zeolite.

In chapter 5, we combined information obtained with UV-vis and FT-IR spectroscopy with XAS to study the speciation of Cu-MOR under the effect of a reducing agent. MCR-ALS analysis on the obtained XANES spectra obtained during CH₄-TPR revealed in total three distinct Cu^{II} species with three-/four-fold coordination and one linear Cu^I species. The four-fold coordinated Cu^{II} species was shown with additional EXAFS analysis (**Paper IV**) to be a bis- μ -hydroxo dicopper(II) species formed from the threefold dicopper(II) cores upon interaction with traces of water in the feed when cooling. The bis- μ -hydroxo dicopper(II) species is also proposed in a recent theoretical study to be the most stable site in Cu-CHA at temperatures ≤ 250 °C [274]. During both C₂H₆- and CO-TPR, additional Cu^I species were found. The Cu^I species derived from C₂H₆-TPR is a linear Cu^I species slightly affected by a C₂H₆ atmosphere, while the Cu^I species found during CO-TPR was established as a chemisorbed Cu^I-CO intermediate by the combination of results from XAS and FT-IR. We were also able to verify the number of Cu^I-CO species formed throughout the TPR protocol by quantifying the absorbance observed with FT-IR. The CO results showed that the copper sites are almost completely dicopper species in Cu-MOR before reductant exposure. This was also verified with WT-EXAFS analysis of the pure Cu components (**Paper IV**). From UV-vis, it was observed an evolvement of a “multiplet” in the d-d region of 036Cu-MOR(11). The multiplet bands were loosely assigned to a high-

temperature, threefold Cu^{II} species much more present in 036Cu-MOR(11). With this study, we have pushed the boundaries for how MCR-ALS analysis can be used to explore and learn more about metal species' chemical and structural evolution in complex mixtures. By also coupling this with complementary and strengthening techniques, like UV-vis and FT-IR spectroscopy, we conjecture these tools will continue to be very important in the MTM advancement as well as in many other reactions where the complex superimposition of different phenomena have led to inconclusive results thus far.

In summary, our studies on Cu-speciation show that although different sites are forming depending on the zeolite framework and composition, not all sites are equally active toward methanol formation. The site that best fits the spectroscopic evidence as the most active site for C–H activation at low temperature (200 °C) and ambient pressure is dimeric, e.g. mono- μ -oxo dicopper(II) or possibly two proximal monomeric Cu^{II} -OH sites. The results have also shown that other sites can become more active at higher temperatures, depending strongly on their closest environment. This we will discuss more in the following section.

7.2. Confinement and Acidity Effects

Chapters 4.1 and 4.3 provide insight into the C–H activation processes over different zeolite systems by comparing the onset of CH_4 consumption during CH_4 -TPR. Over Cu-exchanged CHA zeolites, CH_4 is shown to be consumed at a higher temperature over Cu-SAPO-34 compared to Cu-SSZ-13. Additionally, when a zeolite system was fully exchanged with Cu, that being FAU, BEA, ZSM-5, or MOR, a higher CH_4 consumption temperature was observed compared to a sample with less Cu and thus more Brønsted sites present. Correspondingly, the same behavior was also observed when comparing the two SAPO-34 samples with different Cu concentrations, albeit within a smaller temperature range. Sushkevich

et al. have shown that Cu-MOR with lower Al concentration (Si/Al = 11 vs 7) self-reduces in He at higher temperatures while, on the contrary, very small differences were observed when the Si/Al ratio was kept constant and different Cu concentrations were compared [139]. Combined with their observation that FAU zeolites reduce (both in He and CH₄) at higher temperatures compared to BEA, ZSM-5, and MOR [136], the authors assigned the observed higher C–H activation temperature to zeolites that form more isolated Cu-species. Based on the spectroscopic evidence, this also seemed to be a plausible explanation as to why Cu-SAPO-34 reduces at higher temperatures than Cu-SSZ-13. The observation of more isolated Cu-sites, and hence fewer options to form dimeric Cu-species, were allocated to the possibility that the substitution of Si leads to the formation of some neutral Si islands, and thus fewer cation exchange sites and remaining Brønsted acid sites. It is also likely that the different framework polarity in SAPO-34 induced by the different atomic compositions (Al+P vs Si) affects the preferred siting for Cu.

From this picture, two possible explanations for higher C–H activation temperature can be inferred. One option is that the isolated Cu-sites have weaker reactivity possibly induced by a lower electrophilic nature than multimeric species and therefore require higher temperatures to attack the C–H bond. Another explanation is that the Cu-sites' capacity to attack the C–H bond is weakened by a lower stabilization effect in the cages/channels around the Cu-site due to either weaker or fewer Brønsted acid sites. The latter is supported by the observation that SSIE Cu-MOR zeolites fully exchanged with Cu have a higher CH₄-consumption temperature than the same parent material with less Cu and more available Brønsted acid sites. A similar argument can be used for FAU zeolites that Sushkevich et al. showed to have high C–H activation temperatures [136], as the large number of Al sites present in FAU weakens the Brønsted acid site strength [235]. However, we also saw that the fully SSIE Cu-FAU had a higher CH₄

consumption temperature than the other SSIE zeolites (See **Paper III**). This indicates that even with few to null Brønsted sites present, the same trend was observed between FAU and ZSM-5, BEA, and MOR, and is therefore supporting more the idea that isolated Cu-sites lead to a higher C–H activation temperature.

In a small calorimetric study on CH₄-adsorption over Cu-MCM-22 (see details in **Paper II**), we observed that CH₄ interaction with the active sites at around the temperatures needed for C–H activation is very weak (low heats of adsorption). The weak interaction of CH₄ with the Cu-sites support the need for a stabilizing effect around the Cu-sites. We surmise that both the electrophilic nature of the Cu-sites, induced by the specific exchange site and/or the specific shape and composition of the site, and the surrounding Brønsted acid sites affect the capacity of a Cu-site to activate the C–H bond in methane. I.e., in addition to stabilizing intermediates [178, 179], the surrounding Brønsted sites existing in MTM active Cu-zeolites increase somehow the interaction between methane molecules and the active sites so that C–H bond breaking can more easily occur.

The importance of available and sufficiently strong Brønsted acid sites was further corroborated in our study on MCM-22 zeolites. With this work, we showed that there were only a limited number of homogeneously strong Brønsted acid sites in MCM-22 before Cu exchange. These strong Brønsted sites were the first to be exchanged with Cu and were likely the sites leading to a Cu-oxo speciation available for C–H activation. Based on the discussion above related to the effect of Brønsted site strength on C–H activation, it could be hypothesized that the remaining Brønsted acid sites in MCM-22 were too weak or too few to provide the necessary support needed to increase the moderate methanol productivity.

7.3. Unlocking Activity Through Structural Insight

In Figure 35, the productivity obtained over Cu-SAPO-34, Cu-MCM-22, and the SSIE Cu-zeolites is compared to the previously tested Cu-zeolites in this project. The methanol productivities obtained over the hitherto uncharted materials and exchange methods presented in this thesis are moderate, at most, when compared to the previously explored zeolites. Nevertheless, what we have attempted to show with our work is that by searching for the rationale behind the inefficiency, new insight was obtained. Beyond allowing us to understand more about the effect of Brønsted acid sites on the C–H activation, the work presented here has also provided insight into how productivity can be improved.

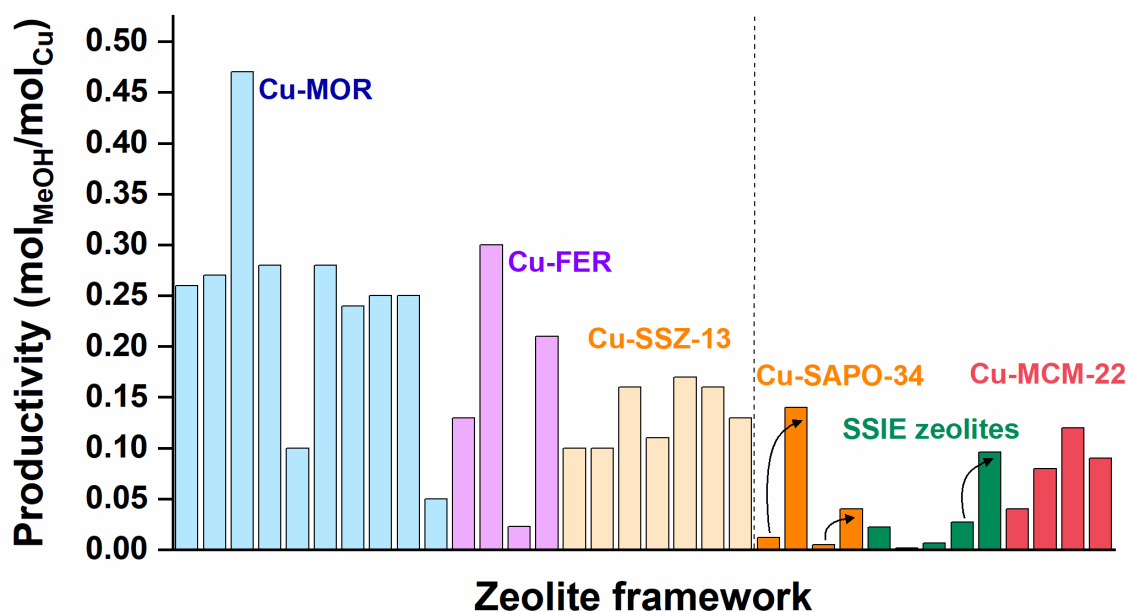


Figure 35. Overview of the methanol productivities obtained over the zeolites presented herein (right side of the stapled line) compared to previously reported data using similar experimental protocols and setup. The arrows indicate improved productivity after specific adjustments (see text).

SSIE-exchanged zeolites had a very low activity towards methanol formation when fully exchanged with Cu^I. Interestingly, however, some productivity was observed, indicating that some sites can activate the C–H bond and stabilize the methoxy species without the need for Brønsted acid sites even at

200 °C. By controlling the amount of Cu exchanged via SSIE, we were able to obtain much higher methanol productivity. With results from elemental analysis, FT-IR spectroscopy, and CH₄-TPR we showed that this was partially due to a higher fraction of active and accessible Cu-oxo species but also due to the presence of more Brønsted sites in the sample with lower Cu concentration.

The higher C–H activation temperature observed over Cu-SAPO-34 led us to consider CH₄-TPR as a possible descriptor for the reducibility of the Cu-sites in zeolites. By changing the CH₄-loading temperature from 200 to 300 °C we observed more than a tenfold increase in methanol yield (from 1 to 12 μmol_{MeOH}/g) for 0.08CuSAPO-34. These results allow us to propose that CH₄-TPR could be an important tool to screen for the most optimal metal-exchanged zeolite catalyst, which could be especially useful upon tuning the reaction conditions, e.g. for steady-state purposes.

In chapter 5, we compare two MOR zeolites with already well-known properties and MTM behavior. Having observed that CH₄-TPR can act as a descriptor for the C–H activation temperature, we wanted to explore the sensitivity of TPR to separate between two zeolites of the same MOR structure where both samples have well-distributed Cu-species and remaining Brønsted acid sites. By coupling the transformation of Cu^{II} to Cu^I, as observed with XAS and complementary UV-vis, with the evolution of the CO₂ and CH₄ MS fragments, we found an unambiguous connection between the spectral changes and the MS traces for both samples, linking Cu reduction directly to CH₄ activation. Additionally, a small but consistent difference was observed between the two MOR compositions. The sample with the highest methane activity in MTM (018Cu-MOR(7)) showed a tendency to have a faster reduction at low temperatures compared to 036Cu-MOR(11). This allowed us to connect reducibility to MTM activity for MOR zeolites, which has previously been dubious due to “self-reduction” resistant Cu species in the highly active 018Cu-MOR(7). Although not elaborated on herein, it

should be mentioned that the observed link between CH₄ activation and Cu^{II} reduction fits well with the literature suggesting that the MTM reaction follows a mechanism involving a Cu^{II}/Cu^I redox pair (see chapter 2 in the introduction).

7.4. C–H Activation

In the last result section, we expand the scope of using Cu-zeolites in C–H bond activation by applying them to another light alkane. For the first time, we report a low-temperature, ambient pressure, and highly selective pathway to form ethylene from ethane. The reaction is akin to the well-investigated, stepwise MTM reaction, with about the same temperature needed for C–H activation, but there are also marked differences between these two reactions. Screening of several Cu-loaded zeolites indicates that the active site requirements are different for the two substrates, which is supported by the trends observed during CH₄- and C₂H₆-TPR experiments presented in chapter 5. There, it was observed that only about half of the Cu^{II} sites were reduced during ethane consumption, while the rest of the Cu species were reduced by secondary oxidation of the ethane derivatives. This behavior was different from CH₄-TPR, where the CH₄ consumption and Cu reduction occurred approximately in the same temperature window. This observation indicates that some sites were either inaccessible or inactive toward C₂H₆ activation. Preliminary studies also show that the active sites for ethane activation can be oxidized by traces of water, as the productivity is persistent across several cycles. This is in contrast to methane activation, where the productivity is reduced when water is the oxygen source unless a much higher chemical potential is used, i.e. by increasing the methane partial pressure [125]. By deducing possible mechanisms, we find that our work is reconcilable with the formation of an ethoxy intermediate.

Overall, these results provide the foundation for the use of Cu-zeolites in C–H activation and oxidation reactions beyond methane activation.

8. Suggestions for Further Work

With the developments of advanced XAS analysis tools like MCR-ALS analysis and WT-EXAFS, we imagine that this can be used to determine the specific nature of the Cu-sites present in the zeolites and thus aid in determining the overall reaction mechanism for C–H activation. To improve the resolution beyond what we have shown in this work, some factors should be considered. 1) To synthesize a Cu-zeolite sample set with much more defined differences so that e.g. one sample has mostly monomeric sites, while another has mostly dimeric. 2) Combine XAS experiments with complementary techniques providing information on the Cu environment like rRaman spectroscopy, UV-vis spectroscopy, or pair-distribution function (PDF) analysis. PDF measurements would provide bond-length information on all possible atomic pairs in the system that, combined with EXAFS spectra, could unravel more specific structural information on the Cu species and their positions. 3) In the work herein, we have shown the importance of “close-to-reality” experiments, and efforts should therefore be taken to find probes and experimental conditions that simulate best the reaction conditions.

Based on the results presented thus far in literature and in this thesis, the effect the choice of oxidant (e.g. H₂O or O₂) has on Cu-speciation and the overall mechanism should be explored further. This could help explain why we are seeing different structure-activity relationships during CH₄ and C₂H₆ activation.

As a topic for further studies on ethane activation, we highlight a more detailed investigation of the reaction parameters that might enable the establishment of a steady-state process, similar to what has been recently described for methane, albeit at very low conversions. Having found that the ETE reaction requires only He/H₂O to oxidize the Cu-zeolites, it could be imagined that the steady-state approach would be possible by co-feeding ethane and H₂O, where H₂O would displace the products and act as a soft oxidant for the reaction.

Based on the hypothesis that the ethane reaction, like CH₄ activation, proceeds via an ethoxy intermediate, we propose that the selective formation of ethanol could be possible by tuning the reaction parameters. Based on the results presented herein, it is likely that a strong stabilization around the active sites is necessary, however, without compromising too much the product diffusion time.

Another application area for Cu-zeolites, and especially Cu,H-MOR zeolites could be the direct activation of methane and CO + H₂O to acetic acid and H₂. This could either be attempted in a co-feeding process or a stepwise mechanism where the methoxy species are formed before exposure to CO and H₂O. The overall reaction thermodynamics are unfavorable, however, the formation of the Cu_xO_y-sites and a stepwise protocol could potentially influence the activation barriers.

To support the acidity discussion above, DFT calculations could be applied to study the effect surrounding Brønsted sites might have on the interaction of CH₄ with the active sites.

Lastly, it should be mentioned that with today's growth in machine learning methods, such techniques should also be developed to explore C–H activation and oxidation reactions over Cu-zeolites from a theoretical perspective. DFT calculations become costly and time-consuming due to the often complex nature of the unit cells, however, with machine learning the experimental time can be significantly shortened and this is, therefore, a potential new tool for the toolbox to use in combination with experiments.

References

- [1] World Bank, Zero Routine Flaring by 2030, <https://www.worldbank.org/en/programs/zero-routine-flaring-by-2030> (accessed: 5 April 2023)
- [2] *Global Gas Flaring Tracker Report*, Global Gas Flaring Reduction Partnership (GGFR), The World Bank, **2023**
- [3] IEA, Flaring Emissions, Paris, License: CC BY 4.0, <https://www.iea.org/reports/flaring-emissions> (accessed: 27 April 2023)
- [4] J. H. Lunsford, Catalytic conversion of methane to more useful chemicals and fuels: a challenge for the 21st century, *Catal. Today* **2000**, 63, 165-174.
- [5] J. A. Moulijn, M. Makkee and A. E. van Diepen, *Chemical Process Technology, Second edition*, John Wiley & Sons Ltd, **2013**.
- [6] G. Molnar, *Economics of Gas Transportation by Pipeline and LNG in The Palgrave Handbook of International Energy Economics*, ed. M. H. G. Luciani, Palgrave Macmillan, Cham, **2022**, 23-57.
- [7] N. F. Dummer, D. J. Willock, Q. He, M. J. Howard, R. J. Lewis, G. Qi, S. H. Taylor, J. Xu, D. Bethell, C. J. Kiely and G. J. Hutchings, Methane Oxidation to Methanol, *Chem. Rev.* **2022**, DOI: 10.1021/acs.chemrev.2c00439
- [8] E. E. Claveau, S. Sader, B. A. Jackson, S. N. Khan and E. Miliordos, Transition metal oxide complexes as molecular catalysts for selective methane to methanol transformation: any prospects or time to retire?, *Phys. Chem. Chem. Phys.* **2023**, 25, 5313-5326.
- [9] UNFCCC, *Paris Agreement*, Paris Climate Change Conference - COP21, **2015**
- [10] IEA, Net Zero by 2050, <https://www.iea.org/reports/net-zero-by-2050> (accessed: 6 April 2023)
- [11] Methanol institute, Methanol price and supply/demand, <https://www.methanol.org/methanol-price-supply-demand/> (accessed: 6 April 2023)
- [12] IRENA AND METHANOL INSTITUTE, *Innovation outlook: Renewable Methanol*, International Renewable Energy Agency, Abu Dhabi, **2021**.
- [13] D. Coombs, *Propylene: The "Other" Olefin*, EVP, Global Olefins and Polyolefins, Goldman Sachs Chemical Intensity Conference: Houston, TX, **2016**
- [14] X. Li, C. Pei and J. Gong, Shale gas revolution: Catalytic conversion of C1–C3 light alkanes to value-added chemicals, *Chem* **2021**, 7, 1755-1801.
- [15] M. Ravi, M. Ranocchiari and J. A. van Bokhoven, The Direct Catalytic Oxidation of Methane to Methanol-A Critical Assessment, *Angew. Chem. Int. Ed.* **2017**, 56, 16464-16483.
- [16] B. A. Arndtsen, R. G. Bergman, T. A. Mobley and T. H. Peterson, Selective Intermolecular Carbon-Hydrogen Bond Activation by Synthetic Metal Complexes in Homogeneous Solution, *Acc. Chem. Res.* **1995**, 28, 154-162.
- [17] K. M. Altus and J. A. Love, The continuum of carbon–hydrogen (C–H) activation mechanisms and terminology, *Commun. Chem.* **2021**, 4, 173.
- [18] R. H. Crabtree, Alkane C–H activation and functionalization with homogeneous transition metal catalysts: a century of progress—a new millennium in prospect, *J. Chem. Soc., Dalton Trans.* **2001**, 17, 2437-2450.

- [19] B. Ruscic, Active Thermochemical Tables: Sequential Bond Dissociation Enthalpies of Methane, Ethane, and Methanol and the Related Thermochemistry, *J. Phys. Chem. A* **2015**, 119, 7810-7837.
- [20] M. S. A. Sher Shah, C. Oh, H. Park, Y. J. Hwang, M. Ma and J. H. Park, Catalytic Oxidation of Methane to Oxygenated Products: Recent Advancements and Prospects for Electrocatalytic and Photocatalytic Conversion at Low Temperatures, *Adv. Sci.* **2020**, 7, 2001946.
- [21] P. Schwach, X. Pan and X. Bao, Direct Conversion of Methane to Value-Added Chemicals over Heterogeneous Catalysts: Challenges and Prospects, *Chem. Rev.* **2017**, 117, 8497-8520.
- [22] A. A. Fokin and P. R. Schreiner, Selective Alkane Transformations via Radicals and Radical Cations: Insights into the Activation Step from Experiment and Theory, *Chem. Rev.* **2002**, 102, 1551-1594.
- [23] J. A. Labinger and J. E. Bercaw, Understanding and exploiting C–H bond activation, *Nature* **2002**, 417, 507-514.
- [24] J. S. Valente, R. Quintana-Solórzano, H. Armendáriz-Herrera and J.-M. M. Millet, Decarbonizing Petrochemical Processes: Contribution and Perspectives of the Selective Oxidation of C1–C3 Paraffins, *ACS Catal.* **2023**, 13, 1693-1716.
- [25] NaturalGas.org, Background, <http://naturalgas.org/overview/background/> (accessed: 6 April 2023)
- [26] Q. Zhang, J. Yu and A. Corma, Applications of Zeolites to C1 Chemistry: Recent Advances, Challenges, and Opportunities, *Adv. Mater.* **2020**, 32, 2002927.
- [27] G. E. Keller and M. M. Bhasin, Synthesis of ethylene via oxidative coupling of methane: I. Determination of active catalysts, *J. Catal.* **1982**, 73, 9-19.
- [28] A. Galadima and O. Muraza, Revisiting the oxidative coupling of methane to ethylene in the golden period of shale gas: A review, *J. Ind. Eng. Chem.* **2016**, 37, 1-13.
- [29] J. H. Lunsford, The Catalytic Oxidative Coupling of Methane, *Angew. Chem., Int. Ed. Engl.* **1995**, 34, 970-980.
- [30] C. Karakaya, S. H. Morejudo, H. Zhu and R. J. Kee, Catalytic Chemistry for Methane Dehydroaromatization (MDA) on a Bifunctional Mo/HZSM-5 Catalyst in a Packed Bed, *Ind. Eng. Chem. Res.* **2016**, 55, 9895-9906.
- [31] C. Tu, X. Nie and J. G. Chen, Insight into Acetic Acid Synthesis from the Reaction of CH₄ and CO₂, *ACS Catal.* **2021**, 11, 3384-3401.
- [32] K. Narsimhan, V. K. Michaelis, G. Mathies, W. R. Gunther, R. G. Griffin and Y. Roman-Leshkov, Methane to Acetic Acid over Cu-Exchanged Zeolites: Mechanistic Insights from a Site-Specific Carbonylation Reaction, *J. Am. Chem. Soc.* **2015**, 137, 1825-1832.
- [33] C. Dong, M. Marinova, K. B. Tayeb, O. V. Safonova, Y. Zhou, D. Hu, S. Chernyak, M. Corda, J. Zaffran, A. Y. Khodakov and V. V. Ordonsky, Direct Photocatalytic Synthesis of Acetic Acid from Methane and CO at Ambient Temperature Using Water as Oxidant, *J. Am. Chem. Soc.* **2023**, 145, 1185-1193.
- [34] E. M. Turan, E. van Steen and K. P. Möller, Comparison of mechanisms for the direct, gas phase, partial oxidation of methane to methanol, *Chem. Eng. Sci.* **2021**, 241, 116718.
- [35] Q. Zhang, D. He and Q. Zhu, Recent Progress in Direct Partial Oxidation of Methane to Methanol, *J. Nat. Gas Chem.* **2003**, 12, 81-89.

- [36] Q. Zhang, D. He, J. Li, B. Xu, Y. Liang and Q. Zhu, Comparatively high yield methanol production from gas phase partial oxidation of methane, *Appl. Catal., A* **2002**, 224, 201-207.
- [37] S. J. Freakley, N. Dimitratos, D. J. Willock, S. H. Taylor, C. J. Kiely and G. J. Hutchings, Methane Oxidation to Methanol in Water, *Acc. Chem. Res.* **2021**, 54, 2614-2623.
- [38] D. Lance and E. G. Elworthy, *Process for the Manufacture of Methyl-alcohol from Methane*, 352687, French Patent, France, **1905**.
- [39] R. A. Periana, D. J. Taube, E. R. Evitt, D. G. Löffler, P. R. Wentrcek, G. Voss and T. Masuda, A Mercury-Catalyzed, High-Yield System for the Oxidation of Methane to Methanol, *Science* **1993**, 259, 340.
- [40] R. A. Periana, D. J. Taube, S. Gamble, H. Taube, T. Satoh and H. Fujii, Platinum catalysts for the high-yield oxidation of methane to a methanol derivative, *Science* **1998**, 280, 560-564.
- [41] C. Hammond, M. M. Forde, M. H. Ab Rahim, A. Thetford, Q. He, R. L. Jenkins, N. Dimitratos, J. A. Lopez-Sanchez, N. F. Dummer, D. M. Murphy, A. F. Carley, S. H. Taylor, D. J. Willock, E. E. Stangland, J. Kang, H. Hagen, C. J. Kiely and G. J. Hutchings, Direct Catalytic Conversion of Methane to Methanol in an Aqueous Medium by using Copper-Promoted Fe-ZSM-5, *Angew. Chem. Int. Ed.* **2012**, 51, 5129-5133.
- [42] C. Hammond, N. Dimitratos, R. L. Jenkins, J. A. Lopez-Sanchez, S. A. Kondrat, M. H. ab Rahim, M. M. Forde, A. Thetford, S. H. Taylor, H. Hagen, E. E. Stangland, J. H. Kang, J. M. Moulijn, D. J. Willock and G. J. Hutchings, Elucidation and Evolution of the Active Component within Cu/Fe/ZSM-5 for Catalytic Methane Oxidation: From Synthesis to Catalysis, *ACS Catal.* **2013**, 3, 689-699.
- [43] Z. Jin, L. Wang, E. Zuidema, K. Mondal, M. Zhang, J. Zhang, C. Wang, X. Meng, H. Yang, C. Mesters and F.-S. Xiao, Hydrophobic zeolite modification for in situ peroxide formation in methane oxidation to methanol, *Science* **2020**, 367, 193-197.
- [44] C. Williams, J. H. Carter, N. F. Dummer, Y. K. Chow, D. J. Morgan, S. Yacob, P. Serna, D. J. Willock, R. J. Meyer, S. H. Taylor and G. J. Hutchings, Selective Oxidation of Methane to Methanol Using Supported AuPd Catalysts Prepared by Stabilizer-Free Sol-Immobilization, *ACS Catal.* **2018**, 8, 2567-2576.
- [45] N. Agarwal, S. J. Freakley, R. U. McVicker, S. M. Althahban, N. Dimitratos, Q. He, D. J. Morgan, R. L. Jenkins, D. J. Willock, S. H. Taylor, C. J. Kiely and G. J. Hutchings, Aqueous Au-Pd colloids catalyze selective CH₄ oxidation to CH₃OH with O₂ under mild conditions, *Science* **2017**, 358, 223-227.
- [46] M. H. Ab Rahim, M. M. Forde, R. L. Jenkins, C. Hammond, Q. He, N. Dimitratos, J. A. Lopez-Sanchez, A. F. Carley, S. H. Taylor, D. J. Willock, D. M. Murphy, C. J. Kiely and G. J. Hutchings, Oxidation of Methane to Methanol with Hydrogen Peroxide Using Supported Gold-Palladium Alloy Nanoparticles, *Angew. Chem. Int. Ed.* **2013**, 52, 1280-1284.
- [47] J. Shan, M. Li, L. F. Allard, S. Lee and M. Flytzani-Stephanopoulos, Mild oxidation of methane to methanol or acetic acid on supported isolated rhodium catalysts, *Nature* **2017**, 551, 605.
- [48] Y. Tang, Y. Li, V. Fung, D.-e. Jiang, W. Huang, S. Zhang, Y. Iwasawa, T. Sakata, L. Nguyen, X. Zhang, A. I. Frenkel and F. Tao, Single rhodium atoms anchored in micropores for efficient transformation of methane under mild conditions, *Nat. Commun.* **2018**, 9, 1231.

- [49] M. Li, J. Shan, G. Giannakakis, M. Ouyang, S. Cao, S. Lee, L. F. Allard and M. Flytzani-Stephanopoulos, Single-step selective oxidation of methane to methanol in the aqueous phase on iridium-based catalysts, *Appl. Catal., B* **2021**, 292, 120124.
- [50] S. Sirajuddin and A. C. Rosenzweig, Enzymatic Oxidation of Methane, *Biochem.* **2015**, 54, 2283-2294.
- [51] M. O. Ross and A. C. Rosenzweig, A tale of two methane monooxygenases, *J. Biol. Inorg. Chem.* **2017**, 22, 307-319.
- [52] V. C. C. Wang, S. Maji, P. P. Y. Chen, H. K. Lee, S. S. F. Yu and S. I. Chan, Alkane Oxidation: Methane Monooxygenases, Related Enzymes, and Their Biomimetics, *Chem. Rev.* **2017**, 117, 8574-8621.
- [53] A. S. Hakemian and A. C. Rosenzweig, The Biochemistry of Methane Oxidation, *Annu. Rev. Biochem.* **2007**, 76, 223-241.
- [54] R. L. Lieberman and A. C. Rosenzweig, Biological Methane Oxidation: Regulation, Biochemistry, and Active Site Structure of Particulate Methane Monooxygenase, *Crit. Rev. Biochem. Mol. Biol.* **2004**, 39, 147-164.
- [55] M. O. Ross, F. MacMillan, J. Wang, A. Nisthal, T. J. Lawton, B. D. Olafson, S. L. Mayo, A. C. Rosenzweig and B. M. Hoffman, Particulate methane monooxygenase contains only mononuclear copper centers, *Science* **2019**, 364, 566.
- [56] H. J. Kim, J. Huh, Y. W. Kwon, D. Park, Y. Yu, Y. E. Jang, B.-R. Lee, E. Jo, E. J. Lee, Y. Heo, W. Lee and J. Lee, Biological conversion of methane to methanol through genetic reassembly of native catalytic domains, *Nat. Catal.* **2019**, 2, 342-353.
- [57] S. I. Chan and S. S. F. Yu, Copper protein constructs for methane oxidation, *Nat. Catal.* **2019**, 2, 286-287.
- [58] J. Baek, B. Rungtaweeworanit, X. Pei, M. Park, S. C. Fakra, Y.-S. Liu, R. Matheu, S. A. Alshmiri, S. Alshehri, C. A. Trickett, G. A. Somorjai and O. M. Yaghi, Bioinspired Metal–Organic Framework Catalysts for Selective Methane Oxidation to Methanol, *J. Am. Chem. Soc.* **2018**, 140, 18208-18216.
- [59] J. Zheng, J. Ye, M. A. Ortuño, J. L. Fulton, O. Y. Gutiérrez, D. M. Camaioni, R. K. Motkuri, Z. Li, T. E. Webber, B. L. Mehdi, N. D. Browning, R. L. Penn, O. K. Farha, J. T. Hupp, D. G. Truhlar, C. J. Cramer and J. A. Lercher, Selective Methane Oxidation to Methanol on Cu-Oxo Dimers Stabilized by Zirconia Nodes of an NU-1000 Metal–Organic Framework, *J. Am. Chem. Soc.* **2019**, 141, 9292-9304.
- [60] I. Gerz, S. A. V. Jannuzzi, K. T. Hylland, C. Negri, D. S. Wragg, S. Øien-Ødegaard, M. Tilset, U. Olsbye, S. DeBeer and M. Amedjkouh, Structural Elucidation, Aggregation, and Dynamic Behaviour of N,N,N,N-Copper(I) Schiff Base Complexes in Solid and in Solution: A Combined NMR, X-ray Spectroscopic and Crystallographic Investigation, *Eur. J. Inorg. Chem.* **2021**, 2021, 4762-4775.
- [61] M. H. Groothaert, P. J. Smeets, B. F. Sels, P. A. Jacobs and R. A. Schoonheydt, Selective oxidation of methane by the bis(μ -oxo)dicopper core stabilized on ZSM-5 and mordenite zeolites, *J. Am. Chem. Soc.* **2005**, 127, 1394-1395.
- [62] M. Ravi, V. L. Sushkevich, A. J. Knorpp, M. A. Newton, D. Palagin, A. B. Pinar, M. Ranocchiari and J. A. van Bokhoven, Misconceptions and challenges in methane-to-methanol over transition-metal-exchanged zeolites, *Nat. Catal.* **2019**, 2, 485-494.

- [63] E. Borfecchia, P. Beato, S. Svelle, U. Olsbye, C. Lamberti and S. Bordiga, Cu-CHA - A Model System for Applied Selective Redox Catalysis, *Chem. Soc. Rev.* **2018**, 47, 8097-8133.
- [64] P. Tomkins, M. Ranocchiari and J. A. van Bokhoven, Direct Conversion of Methane to Methanol under Mild Conditions over Cu-Zeolites and Beyond, *Acc. Chem. Res.* **2017**, 50, 418-425.
- [65] P. Vanelderen, J. Vancauwenbergh, B. F. Sels and R. A. Schoonheydt, Coordination chemistry and reactivity of copper in zeolites, *Coord. Chem. Rev.* **2013**, 257, 483-494.
- [66] R. Horn and R. Schlögl, Methane Activation by Heterogeneous Catalysis, *Catal. Lett.* **2015**, 145, 23-39.
- [67] M. A. Newton, A. J. Knorpp, V. L. Sushkevich, D. Palagin and J. A. van Bokhoven, Active sites and mechanisms in the direct conversion of methane to methanol using Cu in zeolitic hosts: a critical examination, *Chem. Soc. Rev.* **2020**, 49, 1449-1486.
- [68] K. Kvande, D. K. Pappas, E. Borfecchia and K. A. Lomachenko, Advanced X-ray Absorption Spectroscopy Analysis to Determine Structure-Activity Relationships for Cu-Zeolites in the Direct Conversion of Methane to Methanol, *ChemCatChem* **2020**, 12, 2385-2405.
- [69] M. B. Park, E. D. Park and W.-S. Ahn, Recent Progress in Direct Conversion of Methane to Methanol Over Copper-Exchanged Zeolites, *Front. Chem.* **2019**, 7, 1-7.
- [70] S. Raynes, M. A. Shah and R. A. Taylor, Direct conversion of methane to methanol with zeolites: towards understanding the role of extra-framework d-block metal and zeolite framework type, **2019**, 48, 10364-10384.
- [71] B. E. R. Snyder, M. L. Bols, H. M. Rhoda, D. Plessers, R. A. Schoonheydt, B. F. Sels and E. I. Solomon, Cage effects control the mechanism of methane hydroxylation in zeolites, *Science* **2021**, 373, 327-331.
- [72] C. J. Plank, E. J. Rosinski and W. P. Hawthorne, Acidic Crystalline Aluminosilicates. New Superactive, Superselective Cracking Catalysts, *Ind. Eng. Chem. Prod. Res. Dev.* **1964**, 3, 165-169.
- [73] U. Olsbye, S. Svelle, M. Bjørgen, P. Beato, T. V. W. Janssens, F. Joensen, S. Bordiga and K. P. Lillerud, Conversion of Methanol to Hydrocarbons: How Zeolite Cavity and Pore Size Controls Product Selectivity, *Angew. Chem. Int. Ed.* **2012**, 51, 5810-5831.
- [74] J. E. Naber, K. P. de Jong, W. H. J. Stork, H. P. C. E. Kuipers and M. F. M. Post, *Industrial applications of zeolite catalysis in Studies in Surface Science and Catalysis*, ed. J. Weitkamp, H. G. Karge, H. Pfeifer and W. Hölderich, Elsevier, **1994**, 2197-2219.
- [75] A. Dyer, *Zeolites in Encyclopedia of Materials: Science and Technology*, ed. Elsevier Science Ltd., **2001**, 9859-9863.
- [76] A. Dyer, *An Introduction to Zeolite Molecular Sieves*, John Wiley & Sons Ltd, **1988**.
- [77] C. Baerlocher and L. B. McCusker, Database of Zeolite Structures, <http://www.iza-structure.org/databases/> (accessed: 27 April 2023)
- [78] S. Teketel, W. Skistad, S. Benard, U. Olsbye, K. P. Lillerud, P. Beato and S. Svelle, Shape Selectivity in the Conversion of Methanol to Hydrocarbons: The Catalytic

- Performance of One-Dimensional 10-Ring Zeolites: ZSM-22, ZSM-23, ZSM-48, and EU-1, *ACS Catal.* **2012**, 2, 26-37.
- [79] W. Loewenstein, The distribution of aluminum in the tetrahedra of silicates and aluminates, *Am. Mineral.* **1954**, 39, 92-96.
- [80] M. Ravi, V. L. Sushkevich and J. A. van Bokhoven, Towards a better understanding of Lewis acidic aluminium in zeolites, *Nat. Mater.* **2020**, 19, 1047-1056.
- [81] P. Sánchez-López, Y. Kotolevich, R. I. Yocupicio-Gaxiola, J. Antúnez-García, R. K. Chowdari, V. Petranovskii and S. Fuentes-Moyado, Recent Advances in Catalysis Based on Transition Metals Supported on Zeolites, *Front. Chem.* **2021**, 9,
- [82] A. M. Beale, F. Gao, I. Lezcano-Gonzalez, C. H. F. Peden and J. Szanyi, Recent advances in automotive catalysis for NO_x emission control by small-pore microporous materials, *Chem. Soc. Rev.* **2015**, 44, 7371-7405.
- [83] T. Lu, W. Yan and R. Xu, Chiral zeolite beta: structure, synthesis, and application, *Inorg. Chem. Front.* **2019**, 6, 1938-1951.
- [84] M. E. Leonowicz, J. A. Lawton, S. L. Lawton and M. K. Rubin, MCM-22: A Molecular Sieve with Two Independent Multidimensional Channel Systems, *Science* **1994**, 264, 1910-1913.
- [85] S. Prodingler, K. Kvande, B. Arstad, E. Borfecchia, P. Beato and S. Svelle, Synthesis–Structure–Activity Relationship in Cu-MOR for Partial Methane Oxidation: Al Siting via Inorganic Structure-Directing Agents, *ACS Catal.* **2022**, 12, 2166-2177.
- [86] M. B. J. Roeflaers, R. Ameloot, M. Baruah, H. Uji-i, M. Bulut, G. De Cremer, U. Müller, P. A. Jacobs, J. Hofkens, B. F. Sels and D. E. De Vos, Morphology of Large ZSM-5 Crystals Unraveled by Fluorescence Microscopy, *J. Am. Chem. Soc.* **2008**, 130, 5763-5772.
- [87] E. Dib, J. Rey, A. Vicente, S. Kunjir, H. Awala, S. Komaty, A. Daouli, T. Bučko, H. El Siblani, R. Bedard, J. Bricker, J.-P. Gilson, M. Badawi and S. Mintova, Access to sodalite cages in ion-exchanged nanosized FAU zeolites probed by hyperpolarized ¹²⁹Xe NMR and DFT calculations, *Microporous and Mesoporous Mater.* **2022**, 338, 111965.
- [88] J. B. Higgins, R. B. LaPierre, J. L. Schlenker, A. C. Rohrman, J. D. Wood, G. T. Kerr and W. J. Rohrbaugh, The framework topology of zeolite beta, *Zeolites* **1988**, 8, 446-452.
- [89] U. Deka, A. Juhin, E. A. Eilertsen, H. Emerich, M. A. Green, S. T. Korhonen, B. M. Weckhuysen and A. M. Beale, Confirmation of Isolated Cu²⁺ Ions in SSZ-13 Zeolite as Active Sites in NH₃-Selective Catalytic Reduction, *J. Phys. Chem. C* **2012**, 116, 4809-4818.
- [90] D. W. Fickel, J. M. Fedeyko and R. F. Lobo, Copper Coordination in Cu-SSZ-13 and Cu-SSZ-16 Investigated by Variable-Temperature XRD, *J. Phys. Chem. C* **2010**, 114, 1633-1640.
- [91] G. Sastre, D. W. Lewis and C. R. A. Catlow, Structure and Stability of Silica Species in SAPO Molecular Sieves, *J. Phys. Chem.* **1996**, 100, 6722-6730.
- [92] I. Pinilla-Herrero, U. Olsbye, C. Márquez-Álvarez and E. Sastre, Effect of framework topology of SAPO catalysts on selectivity and deactivation profile in the methanol-to-olefins reaction, *J. Catal.* **2017**, 352, 191-207.
- [93] J. Woo, K. Leistner, D. Bernin, H. Ahari, M. Shost, M. Zammit and L. Olsson, Effect of various structure directing agents (SDAs) on low-temperature deactivation

- of Cu/SAPO-34 during NH₃-SCR reaction, *Catal. Sci. Technol.* **2018**, 8, 3090-3106.
- [94] D. K. Pappas, E. Borfecchia, M. Dyballa, I. A. Pankin, K. A. Lomachenko, A. Martini, M. Signorile, S. Teketel, B. Arstad, G. Berlier, C. Lamberti, S. Bordiga, U. Olsbye, K. P. Lillerud, S. Svelle and P. Beato, Methane to Methanol: Structure-Activity Relationships for Cu-CHA, *J. Am. Chem. Soc.* **2017**, 139, 14961-14975.
- [95] M. L. Bols, S. D. Hallaert, B. E. R. Snyder, J. Devos, D. Plessers, H. M. Rhoda, M. Dusselier, R. A. Schoonheydt, K. Pierloot, E. I. Solomon and B. F. Sels, Spectroscopic Identification of the α -Fe/ α -O Active Site in Fe-CHA Zeolite for the Low-Temperature Activation of the Methane C–H Bond, *J. Am. Chem. Soc.* **2018**, 140, 12021-12032.
- [96] B. Ipek and R. F. Lobo, Catalytic conversion of methane to methanol on Cu-SSZ-13 using N₂O as oxidant, *Chem. Commun.* **2016**, 52, 13401-13404.
- [97] B. Ipek, M. J. Wulfers, H. Kim, F. Göttl, I. Hermans, J. P. Smith, K. S. Booksh, C. M. Brown and R. F. Lobo, Formation of [Cu₂O₂]²⁺ and [Cu₂O]²⁺ toward C–H Bond Activation in Cu-SSZ-13 and Cu-SSZ-39, *ACS Catal.* **2017**, 7, 4291-4303.
- [98] R. Oord, J. E. Schmidt and B. M. Weckhuysen, Methane-to-methanol conversion over zeolite Cu-SSZ-13, and its comparison with the selective catalytic reduction of NO_x with NH₃, *Catal. Sci. Technol.* **2018**, 8, 1028-1038.
- [99] K. T. Dinh, M. M. Sullivan, K. Narsimhan, P. Serna, R. J. Meyer, M. Dinca and Y. Roman-Leshkov, Continuous Partial Oxidation of Methane to Methanol Catalyzed by Diffusion-Paired Copper Dimers in Copper-Exchanged Zeolites, *J. Am. Chem. Soc.* **2019**, 141, 11641-11650.
- [100] U. Engedahl, H. Grönbeck and A. Hellman, First-Principles Study of Oxidation State and Coordination of Cu-Dimers in Cu-SSZ-13 during Methane-to-Methanol Reaction Conditions, **2019**, 123, 26145-26150.
- [101] A. Koishybay and D. F. Shantz, Water Is the Oxygen Source for Methanol Produced in Partial Oxidation of Methane in a Flow Reactor over Cu-SSZ-13, *J. Am. Chem. Soc.* **2020**, 142, 11962-11966.
- [102] H. Zhang, J. Lv, Z. Zhang, C. Du, S. Wang, J. Lin, S. Wan, Y. Wang and H. Xiong, Oxidation of Methane to Methanol by Water Over Cu/SSZ-13: Impact of Cu Loading and Formation of Active Sites, *ChemCatChem* **2022**, 14, e202101609.
- [103] L. Sun, Y. Wang, C. Wang, Z. Xie, N. Guan and L. Li, Water-involved methane-selective catalytic oxidation by dioxygen over copper zeolites, *Chem* **2021**, 7, 1557-1568.
- [104] M. J. Wulfers, S. Teketel, B. Ipek and R. F. Lobo, Conversion of methane to methanol on copper-containing small-pore zeolites and zeotypes, *Chem. Commun.* **2015**, 51, 4447-4450.
- [105] M. Cortés-Reyes, E. Finocchio, C. Herrera, M. A. Larrubia, L. J. Alemany and G. Busca, A study of Cu-SAPO-34 catalysts for SCR of NO_x by ammonia, *Microporous and Mesoporous Mater.* **2017**, 241, 258-265.
- [106] W. Souverijns, W. Verrelst, G. Vanbutsele, J. A. Martens and P. A. Jacobs, Micropore structure of zeolite MCM-22 as determined by the decane catalytic test reaction, *J. Chem. Soc., Chem. Commun.* **1994**, 14, 1671-1672.
- [107] S. L. Lawton, M. E. Leonowicz, R. D. Partridge, P. Chu and M. K. Rubin, Twelve-ring pockets on the external surface of MCM-22 crystals, *Microporous Mesoporous Mater.* **1998**, 23, 109-117.

- [108] G. Sastre, V. Fornes and A. Corma, Influence of short- and long-range factors in the Brønsted acidity of MCM-22 zeolite, *Chem. Commun.* **1999**, 21, 2163-2164.
- [109] R. Ravishankar, D. Bhattacharya, N. E. Jacob and S. Sivasanker, Characterization and catalytic properties of zeolite MCM-22, *Microporous Mater.* **1995**, 4, 83-93.
- [110] M. Bjørgen, S. Akyalcin, U. Olsbye, S. Benard, S. Kolboe and S. Svelle, Methanol to hydrocarbons over large cavity zeolites: Toward a unified description of catalyst deactivation and the reaction mechanism, *J. Catal.* **2010**, 275, 170-180.
- [111] E. M. Alayon, M. Nachtegaal, M. Ranocchiari and J. A. van Bokhoven, Catalytic conversion of methane to methanol over Cu-mordenite, *Chem. Commun.* **2012**, 48, 404-406.
- [112] P. Vanelderen, B. E. R. Snyder, M.-L. Tsai, R. G. Hadt, J. Vancauwenbergh, O. Coussens, R. A. Schoonheydt, B. F. Sels and E. I. Solomon, Spectroscopic definition of the copper active sites in mordenite: selective methane oxidation, *J. Am. Chem. Soc.* **2015**, 137, 6383-6392.
- [113] S. E. Bozbag, E. M. C. Alayon, J. Pecháček, M. Nachtegaal, M. Ranocchiari and J. A. van Bokhoven, Methane to Methanol over Copper Mordenite: Yield Improvement Through Multiple Cycles and Different Synthesis techniques, *Catal. Sci. Technol.* **2016**, 6, 5011-5022.
- [114] M. Dyballa, D. K. Pappas, K. Kvande, E. Borfecchia, B. Arstad, P. Beato, U. Olsbye and S. Svelle, On How Copper Mordenite Properties Govern the Framework Stability and Activity in the Methane-to-Methanol Conversion, *ACS Catal.* **2019**, 9, 365-375.
- [115] A. J. Knorpp, M. A. Newton, A. B. Pinar and J. A. van Bokhoven, Conversion of Methane to Methanol on Copper Mordenite: Redox Mechanism of Isothermal and High-Temperature-Activation Procedures, *Ind. Eng. Chem. Res.* **2018**, 57, 12036-12039.
- [116] P. J. Smeets, M. H. Groothaert and R. A. Schoonheydt, Cu Based Zeolites: A UV-Vis Study of the Active Site in the Selective Methane Oxidation at Low Temperatures, *Catal. Today* **2005**, 110, 303-309.
- [117] S. Grundner, M. A. Markovits, G. Li, M. Tromp, E. A. Pidko, E. J. Hensen, A. Jentys, M. Sanchez-Sanchez and J. A. Lercher, Single-Site Trinuclear Copper Oxygen Clusters in Mordenite for Selective Conversion of Methane to Methanol, *Nat. Commun.* **2015**, 6, 7546.
- [118] J. S. Woertink, P. J. Smeets, M. H. Groothaert, M. A. Vance, B. F. Sels, R. A. Schoonheydt and E. I. Solomon, A $[\text{Cu}_2\text{O}]^{2+}$ Core in Cu-ZSM-5, the Active Site in the Oxidation of Methane to Methanol, *Proc. Natl. Acad. Sci. USA* **2009**, 106, 18908-18913.
- [119] M. J. Wulfers, S. Teketel, B. Ipek and R. F. Lobo, Conversion of Methane to Methanol on Copper-Containing Small-Pore Zeolites and Zeotypes, *Chem. Commun.* **2015**, 51, 4447-4450.
- [120] D. K. Pappas, A. Martini, M. Dyballa, K. Kvande, S. Teketel, K. A. Lomachenko, R. Baran, P. Glatzel, B. Arstad, G. Berlier, C. Lamberti, S. Bordiga, U. Olsbye, S. Svelle, P. Beato and E. Borfecchia, The Nuclearity of the Active Site for Methane to Methanol Conversion in Cu-Mordenite: A Quantitative Assessment, *J. Am. Chem. Soc.* **2018**, 140, 15270-15278.
- [121] N. V. Beznis, B. M. Weckhuysen and J. H. Bitter, Cu-ZSM-5 Zeolites for the Formation of Methanol from Methane and Oxygen: Probing the Active Sites and Spectator Species, *Catal. Lett.* **2010**, 138, 14-22.

- [122] T. Sheppard, C. D. Hamill, A. Goguet, D. W. Rooney and J. M. Thompson, A low temperature, isothermal gas-phase system for conversion of methane to methanol over Cu-ZSM-5, *Chem. Commun.* **2014**, 50, 11053-11055.
- [123] Y. Kim, T. Y. Kim, H. Lee and J. Yi, Distinct Activation of Cu-MOR for Direct Oxidation of Methane to Methanol, *Chem. Commun.* **2017**, 53, 4116-4119.
- [124] X. Wang, N. M. Martin, J. Nilsson, S. Carlson, J. Gustafson, M. Skoglundh and P.-A. Carlsson, Copper-Modified Zeolites and Silica for Conversion of Methane to Methanol, *Catalysts* **2018**, 8, 545.
- [125] V. L. Sushkevich, D. Palagin, M. Ranocchiari and J. A. van Bokhoven, Selective Anaerobic Oxidation of Methane Enables Direct Synthesis of Methanol, *Science* **2017**, 356, 523-527.
- [126] V. L. Sushkevich, D. Palagin and J. A. van Bokhoven, The Effect of the Active-Site Structure on the Activity of Copper Mordenite in the Aerobic and Anaerobic Conversion of Methane into Methanol, *Angew. Chem. Int. Ed.* **2018**, 57, 8906-8910.
- [127] Y. K. Chow, N. F. Dummer, J. H. Carter, R. J. Meyer, R. D. Armstrong, C. Williams, G. Shaw, S. Yacob, M. M. Bhasin, D. J. Willock, S. H. Taylor and G. J. Hutchings, A Kinetic Study of Methane Partial Oxidation over Fe-ZSM-5 Using N₂O as an Oxidant, *ChemPhysChem* **2018**, 19, 402-411.
- [128] V. I. Sobolev, K. A. Dubkov, O. V. Panna and G. I. Panov, Selective oxidation of methane to methanol on a FeZSM-5 surface, *Catal. Today* **1995**, 24, 251-252.
- [129] E. V. Starokon, M. V. Parfenov, S. S. Arzumanov, L. V. Pirutko, A. G. Stepanov and G. I. Panov, Oxidation of methane to methanol on the surface of FeZSM-5 zeolite, *J. Catal.* **2013**, 300, 47-54.
- [130] W.-L. Yang, S.-D. Zhang and M.-Y. Zhang, Theoretical study of the natural active structure of the Fe-SSZ-13 zeolite and its reactivity toward the methane to methanol oxidation reaction, *Chem. Phys. Lett.* **2023**, 819, 140440.
- [131] T. Yu, Z. Li, W. Jones, Y. Liu, Q. He, W. Song, P. Du, B. Yang, H. An, D. M. Farmer, C. Qiu, A. Wang, B. M. Weckhuysen, A. M. Beale and W. Luo, Identifying key mononuclear Fe species for low-temperature methane oxidation, *Chem. Sci.* **2021**, 12, 3152-3160.
- [132] J. Shan, W. Huang, L. Nguyen, Y. Yu, S. Zhang, Y. Li, A. I. Frenkel and F. Tao, Conversion of Methane to Methanol with a Bent Mono(μ -oxo)dinickel Anchored on the Internal Surfaces of Micropores, *Langmuir* **2014**, 30, 8558-8569.
- [133] N. V. Beznis, A. N. C. van Laak, B. M. Weckhuysen and J. H. Bitter, Oxidation of methane to methanol and formaldehyde over Co-ZSM-5 molecular sieves: Tuning the reactivity and selectivity by alkaline and acid treatments of the zeolite ZSM-5 agglomerates, *Micropor. Mesopor. Mat.* **2011**, 138, 176-183.
- [134] M. C. Kung, S. S. Y. Lin and H. H. Kung, In situ Infrared Spectroscopic Study of CH₄ Oxidation Over Co-ZSM-5, *Top. Catal.* **2012**, 55, 108-115.
- [135] P. Tomkins, A. Mansouri, S. E. Bozbag, F. Krumeich, M. B. Park, E. M. Alayon, M. Ranocchiari and J. A. van Bokhoven, Isothermal Cyclic Conversion of Methane into Methanol over Copper-Exchanged Zeolite at Low Temperature, *Angew. Chem. Int. Ed.* **2016**, 55, 5467-5471.
- [136] V. L. Sushkevich and J. A. van Bokhoven, Methane-to-Methanol: Activity Descriptors in Copper-Exchanged Zeolites for the Rational Design of Materials, *ACS Catal.* **2019**, 9, 6293-6304.

- [137] G. Brezicki, J. D. Kammert, T. B. Gunnoe, C. Paolucci and R. J. Davis, Insights into the Speciation of Cu in the Cu-H-Mordenite Catalyst for the Oxidation of Methane to Methanol, *ACS Catal.* **2019**, 9, 5308-5319.
- [138] J. Zheng, I. Lee, E. Khramenkova, M. Wang, B. Peng, O. Y. Gutierrez, J. L. Fulton, D. M. Camaioni, R. Khare, A. Jentys, G. L. Haller, E. A. Pidko, M. Sanchez-Sanchez and J. A. Lercher, Importance of Methane Chemical Potential for Its Conversion to Methanol on Cu-Exchanged Mordenite, *Chem. Eur. J.* **2020**, 26, 7563-7567.
- [139] V. L. Sushkevich, A. V. Smirnov and J. A. van Bokhoven, Autoreduction of Copper in Zeolites: Role of Topology, Si/Al Ratio, and Copper Loading, *J. Phys. Chem. C* **2019**, 123, 9926-9934.
- [140] D. K. Pappas, E. Borfecchia, M. Dyballa, K. A. Lomachenko, A. Martini, G. Berlier, B. Arstad, C. Lamberti, S. Bordiga, U. Olsbye, S. Svelle and P. Beato, Understanding and Optimizing the Performance of Cu-FER for The Direct CH₄ to CH₃OH Conversion, *ChemCatChem* **2019**, 11, 621-627.
- [141] D. K. Pappas, K. Kvande, M. Kalyva, M. Dyballa, K. A. Lomachenko, B. Arstad, E. Borfecchia, S. Bordiga, U. Olsbye, P. Beato and S. Svelle, Influence of Cu-speciation in mordenite on direct methane to methanol conversion: Multi-Technique characterization and comparison with NH₃ selective catalytic reduction of NO_x, *Catal. Today* **2021**, 369, 105-111.
- [142] K. A. Lomachenko, A. Martini, D. K. Pappas, C. Negri, M. Dyballa, G. Berlier, S. Bordiga, C. Lamberti, U. Olsbye, S. Svelle, P. Beato and E. Borfecchia, The impact of reaction conditions and material composition on the stepwise methane to methanol conversion over Cu-MOR: an operando XAS study, *Catal. Today* **2019**, 336, 99-108.
- [143] A. Martini, M. Signorile, C. Negri, K. Kvande, K. A. Lomachenko, S. Svelle, P. Beato, G. Berlier, E. Borfecchia and S. Bordiga, EXAFS wavelet transform analysis of Cu-MOR zeolites for the direct methane to methanol conversion, *Phys. Chem. Chem. Phys.* **2020**, 22, 18950-18963.
- [144] D. Pappas, E. Borfecchia, K. Lomachenko, A. Lazzarini, E. Gutterød, M. Dyballa, A. Martini, G. Berlier, S. Bordiga, C. Lamberti, B. Arstad, U. Olsbye, P. Beato and S. Svelle, Cu-Exchanged Ferrierite Zeolite for the Direct CH₄ to CH₃OH Conversion: Insights on Cu Speciation from X-Ray Absorption Spectroscopy, *Top. Catal.* **2019**, 62, 712-723.
- [145] S. L. Scott, Bioinspired methane oxidation in a zeolite, *Science* **2021**, 373, 277-278.
- [146] B. E. R. Snyder, P. Vanelderen, R. A. Schoonheydt, B. F. Sels and E. I. Solomon, Second-Sphere Effects on Methane Hydroxylation in Cu-Zeolites, *J. Am. Chem. Soc.* **2018**, 140, 9236-9243.
- [147] M. H. Mahyuddin, A. Staykov, Y. Shiota, M. Miyanishi and K. Yoshizawa, Roles of Zeolite Confinement and Cu–O–Cu Angle on the Direct Conversion of Methane to Methanol by [Cu₂(μ-O)]²⁺-Exchanged AEI, CHA, AFX, and MFI Zeolites, *ACS Catal.* **2017**, 7, 3741-3751.
- [148] J. Zhu, V. L. Sushkevich, A. J. Knorpp, M. A. Newton, S. C. M. Mizuno, T. Wakihara, T. Okubo, Z. Liu and J. A. van Bokhoven, Cu-Erionite Zeolite Achieves High Yield in Direct Oxidation of Methane to Methanol by Isothermal Chemical Looping, *Chem. Mater.* **2020**, 32, 1448-1453.

- [149] V. L. Sushkevich, M. Artsiusheuski, D. Klose, G. Jeschke and J. A. van Bokhoven, Identification of Kinetic and Spectroscopic Signatures of Copper Sites for Direct Oxidation of Methane to Methanol, *Angew. Chem., Int. Ed.* **2021**, 60, 15944-15953.
- [150] D. T. Bregante, L. N. Wilcox, C. Liu, C. Paolucci, R. Gounder and D. W. Flaherty, Dioxygen Activation Kinetics over Distinct Cu Site Types in Cu-Chabazite Zeolites, *ACS Catal.* **2021**, 11, 11873-11884.
- [151] M. H. Groothaert, J. A. van Bokhoven, A. A. Battiston, B. M. Weckhuysen and R. A. Schoonheydt, Bis (μ -oxo) Dicopper in Cu-ZSM-5 and its Role in the Decomposition of NO: A Combined *In Situ* XAFS, UV-Vis-Near-IR, and Kinetic Study, *J. Am. Chem. Soc.* **2003**, 125, 7629-7640.
- [152] K. Fujisawa, M. Tanaka, Y. Moro-oka and N. Kitajima, A Monomeric Side-On Superoxocopper(II) Complex: $\text{Cu}(\text{O}_2)(\text{HB}(3\text{-tBu-5-iPrpz})_3)$, *J. Am. Chem. Soc.* **1994**, 116, 12079-12080.
- [153] E. I. Solomon, D. E. Heppner, E. M. Johnston, J. W. Ginsbach, J. Cirera, M. Qayyum, M. T. Kieber-Emmons, C. H. Kjaergaard, R. G. Hadt and L. Tian, Copper Active Sites in Biology, *Chem. Rev.* **2014**, 114, 3659-3853.
- [154] A. R. Kulkarni, Z.-J. Zhao, S. Siahrostami, J. K. Nørskov and F. Studt, Monocopper Active Site for Partial Methane Oxidation in Cu-Exchanged 8MR Zeolites, *ACS Catal.* **2016**, 6, 6531-6536.
- [155] C. Paolucci, A. A. Parekh, I. Khurana, J. R. Di Iorio, H. Li, J. D. Albarracin Caballero, A. J. Shih, T. Anggara, W. N. Delgass, J. T. Miller, F. H. Ribeiro, R. Gounder and W. F. Schneider, Catalysis in a Cage: Condition-Dependent Speciation and Dynamics of Exchanged Cu Cations in SSZ-13 Zeolites, *J. Am. Chem. Soc.* **2016**, 138, 6028-6048.
- [156] A. Martini, E. Borfecchia, K. A. Lomachenko, I. A. Pankin, C. Negri, G. Berlier, P. Beato, H. Falsig, S. Bordiga and C. Lamberti, Composition-Driven Cu-Speciation and Reducibility in Cu-CHA Zeolite Catalysts: a Multivariate XAS/FTIR Approach to Complexity, *Chem. Sci.* **2017**, 8, 6836-6851.
- [157] J. H. Kwak, H. Y. Zhu, J. H. Lee, C. H. F. Peden and J. Szanyi, Two Different Cationic Positions in Cu-SSZ-13?, *Chem. Commun.* **2012**, 48, 4758-4760.
- [158] S. Grundner, M. A. C. Markovits, G. Li, M. Tromp, E. A. Pidko, E. J. M. Hensen, A. Jentys, M. Sanchez-Sanchez and J. A. Lercher, Single-site trinuclear copper oxygen clusters in mordenite for selective conversion of methane to methanol, *Nat. Commun.* **2015**, 6, 7546.
- [159] G. Li, P. Vassilev, M. Sanchez-Sanchez, J. A. Lercher, E. J. M. Hensen and E. A. Pidko, Stability and reactivity of copper oxo-clusters in ZSM-5 zeolite for selective methane oxidation to methanol, *J. Catal.* **2016**, 338, 305-312.
- [160] M. H. Mahyuddin, T. Tanaka, Y. Shiota, A. Staykov and K. Yoshizawa, Methane Partial Oxidation over $[\text{Cu}_2(\mu\text{-O})]^{2+}$ and $[\text{Cu}_3(\mu\text{-O})_3]^{2+}$ Active Species in Large-Pore Zeolites, *ACS Catal.* **2018**, 8, 1500-1509.
- [161] T. Ikuno, S. Grundner, A. Jentys, G. Li, E. Pidko, J. Fulton, M. Sanchez-Sanchez and J. A. Lercher, Formation of Active Cu-oxo Clusters for Methane Oxidation in Cu-Exchanged Mordenite, *J. Phys. Chem. C* **2019**, 123, 8759-8769.
- [162] I. Lee, M.-S. Lee, L. Tao, T. Ikuno, R. Khare, A. Jentys, T. Huthwelker, C. N. Borca, A. Kalinko and O. Y. Gutiérrez, Activity of Cu-Al-Oxo Extra-Framework Clusters for Selective Methane Oxidation on Cu-Exchanged Zeolites, *JACS Au* **2021**, 1, 1412-1421.

- [163] E. V. Khramenkova, M. G. Medvedev, G. Li and E. A. Pidko, Unraveling the Nature of Extraframework Catalytic Ensembles in Zeolites: Flexibility and Dynamics of the Copper-Oxo Trimers in Mordenite, *J. Phys. Chem. Lett.* **2021**, 12, 10906-10913.
- [164] D. Palagin, A. J. Knorpp, A. B. Pinar, M. Ranocchiari and J. A. van Bokhoven, Assessing the Relative Stability of Copper Oxide Clusters as Active Sites of a CuMOR Zeolite for Methane to Methanol Conversion: Size Matters?, *Nanoscale* **2017**, 9, 1144-1153.
- [165] A. A. Verma, S. A. Bates, T. Anggara, C. Paolucci, A. A. Parekh, K. Kamasamudram, A. Yezerets, J. T. Miller, W. N. Delgass, W. F. Schneider and F. H. Ribeiro, NO oxidation: A probe reaction on Cu-SSZ-13, *J. Catal.* **2014**, 312, 179-190.
- [166] A. Martini, E. Alladio and E. Borfecchia, Determining Cu-Speciation in the Cu-CHA Zeolite Catalyst: The Potential of Multivariate Curve Resolution Analysis of In Situ XAS Data, *Top. Catal.* **2018**, 61, 1396-1407.
- [167] A. J. Knorpp, A. B. Pinar, M. A. Newton, V. L. Sushkevich and J. A. van Bokhoven, Copper-Exchanged Omega (MAZ) Zeolite: Copper-Concentration Dependent Active Sites and its Unprecedented Methane to Methanol Conversion, *ChemCatChem* **2018**, 10, 5593-5596.
- [168] A. J. Knorpp, A. B. Pinar, C. Baerlocher, L. B. McCusker, N. Casati, M. A. Newton, S. Checchia, J. Meyet, D. Palagin and J. A. van Bokhoven, Paired Copper Monomers in Zeolite Omega: The Active Site for Methane-to-Methanol Conversion, *Angew. Chem. Int. Ed.* **2021**, 60, 5854-5858.
- [169] G. Deplano, A. Martini, M. Signorile, E. Borfecchia, V. Crocellà, S. Svelle and S. Bordiga, Copper Pairing in the Mordenite Framework as a Function of the Cu^I/Cu^{II} Speciation, *Angew. Chem. Int. Ed.* **2021**, 60, 25891-25896.
- [170] V. L. Sushkevich, O. V. Safonova, D. Palagin, M. A. Newton and J. A. van Bokhoven, Structure of Copper Sites in Zeolites Examined by Fourier and Wavelet Transform Analysis of EXAFS, *Chem. Sci.* **2020**, 11, 5299-5312.
- [171] I. A. Pankin, A. Martini, K. A. Lomachenko, A. V. Soldatov, S. Bordiga and E. Borfecchia, Identifying Cu-Oxo Species In Cu-Zeolites By XAS: A Theoretical Survey by DFT-Assisted XANES Simulation and EXAFS Wavelet Transform, *Catal. Today* **2020**, 345, 125-135.
- [172] L. Tao, I. Lee, R. Khare, A. Jentys, J. L. Fulton, M. Sanchez-Sanchez and J. A. Lercher, Speciation of Cu-Oxo Clusters in Ferrierite for Selective Oxidation of Methane to Methanol, *Chem. Mater.* **2022**, 34, 4355-4363.
- [173] P. N. R. Vennestrøm, A. Katerinopoulou, R. R. Tiruvalam, A. Kustov, P. G. Moses, P. Concepcion and A. Corma, Migration of Cu Ions in SAPO-34 and Its Impact on Selective Catalytic Reduction of NOx with NH₃, *ACS Catal.* **2013**, 3, 2158-2161.
- [174] P. N. R. Vennestrøm, T. V. W. Janssens, A. Kustov, M. Grill, A. Puig-Molina, L. F. Lundegaard, R. R. Tiruvalam, P. Concepción and A. Corma, Influence of lattice stability on hydrothermal deactivation of Cu-ZSM-5 and Cu-IM-5 zeolites for selective catalytic reduction of NOx by NH₃, *J. Catal.* **2014**, 309, 477-490.
- [175] S. Shwan, M. Skoglundh, L. F. Lundegaard, R. R. Tiruvalam, T. V. W. Janssens, A. Carlsson and P. N. R. Vennestrøm, Solid-State Ion-Exchange of Copper into Zeolites Facilitated by Ammonia at Low Temperature, *ACS Catal.* **2015**, 5, 16-19.
- [176] H. V. Le, S. Parishan, A. Sagaltchik, C. Göbel, C. Schlesiger, W. Malzer, A. Trunschke, R. Schomäcker and A. Thomas, Solid-State Ion-Exchanged

- Cu/Mordenite Catalysts for the Direct Conversion of Methane to Methanol, *ACS Catal.* **2017**, 7, 1403-1412.
- [177] V. L. Sushkevich and J. A. van Bokhoven, Effect of Brønsted acid sites on the direct conversion of methane into methanol over copper-exchanged mordenite, *Catal. Sci. Technol.* **2018**, 8, 4141-4150.
- [178] M. Dybala, K. Thorshaug, D. K. Pappas, E. Borfecchia, K. Kvande, S. Bordiga, G. Berlier, A. Lazzarini, U. Olsbye, P. Beato, S. Svelle and B. Arstad, Zeolite Surface Methoxy Groups as Key Intermediates in the Stepwise Conversion of Methane to Methanol, *ChemCatChem* **2019**, 11, 5022-5026.
- [179] V. L. Sushkevich, J. A. van Bokhoven and R. Verel, Pathways of Methane Transformation over Copper-Exchanged Mordenite as Revealed by In Situ NMR and IR Spectroscopy, *Angew. Chem. Int. Ed.* **2020**, 59, 910-918.
- [180] S. Grundner, W. Luo, M. Sanchez-Sanchez and J. A. Lercher, Synthesis of Single-Site Copper Catalysts for Methane Partial Oxidation, *Chem. Commun.* **2016**, 52, 2553-2556.
- [181] A. M. Beale, I. Lezcano-Gonzalez, W. A. Slawinski and D. S. Wragg, Correlation between Cu ion migration behaviour and deNO_x activity in Cu-SSZ-13 for the standard NH₃-SCR reaction, *Chem. Commun.* **2016**, 52, 6170-6173.
- [182] M. A. Deimund, L. Harrison, J. D. Lunn, Y. Liu, A. Malek, R. Shayib and M. E. Davis, Effect of Heteroatom Concentration in SSZ-13 on the Methanol-to-Olefins Reaction, *ACS Catal.* **2016**, 6, 542-550.
- [183] S. Zhang, L. Pang, Z. Chen, S. Ming, Y. Dong, Q. Liu, P. Liu, W. Cai and T. Li, Cu/SSZ-13 and Cu/SAPO-34 catalysts for deNO_x in diesel exhaust: Current status, challenges, and future perspectives, *Appl. Catal., A* **2020**, 607, 117855.
- [184] J. R. Di Iorio, S. Li, C. B. Jones, C. T. Nimlos, Y. Wang, E. Kunkes, V. Vattipalli, S. Prasad, A. Moini, W. F. Schneider and R. Gounder, Cooperative and Competitive Occlusion of Organic and Inorganic Structure-Directing Agents within Chabazite Zeolites Influences Their Aluminum Arrangement, *J. Am. Chem. Soc.* **2020**, 142, 4807-4819.
- [185] J. R. Di Iorio and R. Gounder, Controlling the Isolation and Pairing of Aluminum in Chabazite Zeolites Using Mixtures of Organic and Inorganic Structure-Directing Agents, *Chem. Mater.* **2016**, 28, 2236-2247.
- [186] V. Pashkova, P. Klein, J. Dedeczek, V. Tokarová and B. Wichterlová, Incorporation of Al at ZSM-5 hydrothermal synthesis. Tuning of Al pairs in the framework, *Microporous and Mesoporous Mater.* **2015**, 202, 138-146.
- [187] L. Chen, H. Falsig, T. V. W. Janssens, J. Jansson, M. Skoglundh and H. Grönbeck, Effect of Al-distribution on oxygen activation over Cu-CHA, *Catal. Sci. Technol.* **2018**, 8, 2131-2136.
- [188] A. B. Pinar, L. Gómez-Hortigüela, L. B. McCusker and J. Pérez-Pariente, Controlling the Aluminum Distribution in the Zeolite Ferrierite via the Organic Structure Directing Agent, *Chem. Mater.* **2013**, 25, 3654-3661.
- [189] Y. Román-Leshkov, M. Moliner and M. E. Davis, Impact of Controlling the Site Distribution of Al Atoms on Catalytic Properties in Ferrierite-Type Zeolites, *J. Phys. Chem. C* **2011**, 115, 1096-1102.
- [190] J. Devos, M. L. Bols, D. Plessers, C. V. Goethem, J. W. Seo, S.-J. Hwang, B. F. Sels and M. Dusselier, Synthesis–Structure–Activity Relations in Fe-CHA for C–H Activation: Control of Al Distribution by Interzeolite Conversion, *Chem. Mater.* **2020**, 32, 273-285.

- [191] D. Plessers, A. J. Heyer, H. M. Rhoda, M. L. Bols, E. I. Solomon, R. A. Schoonheydt and B. F. Sels, Tuning Copper Active Site Composition in Cu-MOR through Co-Cation Modification for Methane Activation, *ACS Catal.* **2023**, 13, 1906-1915.
- [192] J. Meyet, K. Searles, M. A. Newton, M. Wörle, A. P. van Bavel, A. D. Horton, J. A. van Bokhoven and C. Copéret, Monomeric Copper(II) Sites Supported on Alumina Selectively Convert Methane to Methanol, *Angew. Chem. Int. Ed.* **2019**, 58, 9841-9845.
- [193] K. D. Vogiatzis, G. Li, E. J. M. Hensen, L. Gagliardi and E. A. Pidko, Electronic Structure of the $[\text{Cu}_3(\mu\text{-O})_3]^{2+}$ Cluster in Mordenite Zeolite and Its Effects on the Methane to Methanol Oxidation, *J. Phys. Chem. C* **2017**, 121, 22295-22302.
- [194] M. A. Newton, A. J. Knorpp, A. B. Pinar, V. L. Sushkevich, D. Palagin and J. A. van Bokhoven, On the Mechanism Underlying the Direct Conversion of Methane to Methanol by Copper Hosted in Zeolites; Braiding Cu K-Edge XANES and Reactivity Studies, *J. Am. Chem. Soc.* **2018**, 140, 10090-10093.
- [195] E. M. C. Alayon, M. Nachtegaal, A. Bodi, M. Ranocchiari and J. A. van Bokhoven, Bis(μ -oxo) Versus mono(μ -oxo) Dicopper Cores in a Zeolite for Converting Methane to Methanol: an *In Situ* XAS and DFT Investigation, *Phys. Chem. Chem. Phys.* **2015**, 17, 7681-7693.
- [196] E. Borfecchia, K. A. Lomachenko, F. Giordanino, H. Falsig, P. Beato, A. V. Soldatov, S. Bordiga and C. Lamberti, Revisiting the Nature of Cu sites in the Activated Cu-SSZ-13 Catalyst for SCR reaction, *Chem. Sci.* **2015**, 6, 548-563.
- [197] S. C. Larsen, A. Aylor, A. T. Bell and J. A. Reimer, Electron Paramagnetic Resonance Studies of Copper Ion-Exchanged ZSM-5, *J. Phys. Chem.* **1994**, 98, 11533-11540.
- [198] F. X. Llabrés i Xamena, P. Fisicaro, G. Berlier, A. Zecchina, G. T. Palomino, C. Prestipino, S. Bordiga, E. Giamello and C. Lamberti, Thermal Reduction of Cu^{2+} -Mordenite and Re-oxidation upon Interaction with H_2O , O_2 , and NO , *J. Phys. Chem. B* **2003**, 107, 7036-7044.
- [199] V. L. Sushkevich and J. A. van Bokhoven, Revisiting copper reduction in zeolites: the impact of autoreduction and sample synthesis procedure, *Chem. Commun.* **2018**, 54, 7447-7450.
- [200] K. Narsimhan, K. Iyoki, K. Dinh and Y. Roman-Leshkov, Catalytic Oxidation of Methane into Methanol over Copper-Exchanged Zeolites with Oxygen at Low Temperature, *ACS Cent. Sci.* **2016**, 2, 424-429.
- [201] Y. R. Jeong, H. Jung, J. Kang, J. W. Han and E. D. Park, Continuous Synthesis of Methanol from Methane and Steam over Copper-Mordenite, *ACS Catal.* **2021**, 11, 1065-1070.
- [202] R. Xu, N. Liu, C. Dai, Y. Li, J. Zhang, B. Wu, G. Yu and B. Chen, H_2O -Built Proton Transfer Bridge Enhances Continuous Methane Oxidation to Methanol over Cu-BEA Zeolite, *Angew. Chem. Int. Ed.* **2021**, 60, 16634-16640.
- [203] L. Luo, J. Luo, H. Li, F. Ren, Y. Zhang, A. Liu, W.-X. Li and J. Zeng, Water enables mild oxidation of methane to methanol on gold single-atom catalysts, *Nat. Commun.* **2021**, 12, 1218.
- [204] Z. Liu, E. Huang, I. Orozco, W. Liao, R. M. Palomino, N. Rui, T. Duchon, S. Nemšák, D. C. Grinter, M. Mahapatra, P. Liu, J. A. Rodriguez and S. D. Senanayake, Water-promoted interfacial pathways in methane oxidation to methanol on a CeO_2 - Cu_2O catalyst, *Science* **2020**, 368, 513-517.

- [205] M. Wu, W. Li, C. Zhu, W. Wu, L. Zhang, T. Zheng, Y. Fu and L. Yuan, Single-Step Oxidation of Low-Concentration Methane to Methanol in the Gaseous Phase Using Ceria-Based Iridium-Copper Catalysts, *ChemistrySelect* **2023**, 8, e202204745.
- [206] H. Saito and Y. Sekine, Catalytic conversion of ethane to valuable products through non-oxidative dehydrogenation and dehydroaromatization, *RSC Adv.* **2020**, 10, 21427-21453.
- [207] Y. Gao, L. Neal, D. Ding, W. Wu, C. Baroi, A. M. Gaffney and F. Li, Recent Advances in Intensified Ethylene Production—A Review, *ACS Catal.* **2019**, 9, 8592-8621.
- [208] X. Liu, T. Liang, R. Barbosa, G. Chen, H. Toghiani and Y. Xiang, Ammoxidation of Ethane to Acetonitrile and Ethylene: Reaction Transient Analysis for the Co/HZSM-5 Catalyst, *ACS Omega* **2020**, 5, 1669-1678.
- [209] U. Olsbye, A. Virnovskaia, Ø. Prytz, S. J. Tinnemans and B. M. Weckhuysen, Mechanistic insight in the ethane dehydrogenation reaction over Cr/Al₂O₃ catalysts, *Catal. Lett.* **2005**, 103, 143-148.
- [210] V. Galvita, G. Siddiqi, P. Sun and A. T. Bell, Ethane dehydrogenation on Pt/Mg(Al)O and PtSn/Mg(Al)O catalysts, *J. Catal.* **2010**, 271, 209-219.
- [211] S. Yao, B. Yan, Z. Jiang, Z. Liu, Q. Wu, J. H. Lee and J. G. Chen, Combining CO₂ Reduction with Ethane Oxidative Dehydrogenation by Oxygen-Modification of Molybdenum Carbide, *ACS Catal.* **2018**, 8, 5374-5381.
- [212] M. M. Forde, R. D. Armstrong, C. Hammond, Q. He, R. L. Jenkins, S. A. Kondrat, N. Dimitratos, J. A. Lopez-Sanchez, S. H. Taylor, D. Willock, C. J. Kiely and G. J. Hutchings, Partial Oxidation of Ethane to Oxygenates Using Fe- and Cu-Containing ZSM-5, *J. Am. Chem. Soc.* **2013**, 135, 11087-11099.
- [213] C. Wang, B. Yang, Q. Gu, Y. Han, M. Tian, Y. Su, X. Pan, Y. Kang, C. Huang, H. Liu, X. Liu, L. Li and X. Wang, Near 100% ethene selectivity achieved by tailoring dual active sites to isolate dehydrogenation and oxidation, *Nat. Commun.* **2021**, 12, 5447.
- [214] D. J. Xiao, E. D. Bloch, J. A. Mason, W. L. Queen, M. R. Hudson, N. Planas, J. Borycz, A. L. Dzubak, P. Verma, K. Lee, F. Bonino, V. Crocellà, J. Yano, S. Bordiga, D. G. Truhlar, L. Gagliardi, C. M. Brown and J. R. Long, Oxidation of ethane to ethanol by N₂O in a metal-organic framework with coordinatively unsaturated iron(II) sites, *Nat. Chem.* **2014**, 6, 590-595.
- [215] T. V. W. Janssens, H. Falsig, L. F. Lundegaard, P. N. R. Vennestrøm, S. B. Rasmussen, P. G. Moses, F. Giordanino, E. Borfecchia, K. A. Lomachenko, C. Lamberti, S. Bordiga, A. Godiksen, S. Mossin and P. Beato, A Consistent Reaction Scheme for the Selective Catalytic Reduction of Nitrogen Oxides with Ammonia, *ACS Catal.* **2015**, 5, 2832-2845.
- [216] M. M. Mertens, *Synthesis and use of AEI Structure-type Molecular Sieves*, WO/2009/117186, ExxonMobil Chemical Patents Inc, USA, **2009**.
- [217] S. Prodingler, M. F. K. Verstreken and R. F. Lobo, Selective and Efficient Production of Biomass Derived Vinylfurans, *ACS Sustainable Chem. Eng.* **2020**, 8, 11930-11939.
- [218] P. Llewellyn, F. R. Reinoso, J. Rouquerol and N. Seaton, Characterization of Porous Solids VII., in *Studies in Surface Science and Catalysis; Elsevier* **2006**, 160, 748.

- [219] G. Deplano, M. Signorile, V. Crocellà, N. G. Porcaro, C. Atzori, B. G. Solemsli, S. Svelle and S. Bordiga, Titration of Cu(I) Sites in Cu-ZSM-5 by Volumetric CO Adsorption, *ACS Appl. Mater. Interfaces* **2022**, 14, 21059-21068.
- [220] K. Kvande, D. K. Pappas, M. Dyballa, C. Buono, M. Signorile, E. Borfecchia, K. A. Lomachenko, B. Arstad, S. Bordiga, G. Berlier, U. Olsbye, P. Beato and S. Svelle, Comparing the Nature of Active Sites in Cu-loaded SAPO-34 and SSZ-13 for the Direct Conversion of Methane to Methanol, *Catalysts* **2020**, 10, 191.
- [221] P. M. Abdala, O. V. Safonova, G. Wiker, W. van Beek, H. Emerich, J. A. van Bokhoven, J. Sa, J. Szlachetko and M. Nachtegaal, Scientific Opportunities for Heterogeneous Catalysis Research at the SuperXAS and SNBL Beam Lines, *Chimia* **2012**, 66, 699-705.
- [222] W. van Beek, O. V. Safonova, G. Wiker and H. Emerich, SNBL, a dedicated beamline for combined in situ X-ray diffraction, X-ray absorption and Raman scattering experiments, *Phase Transitions* **2011**, 84, 726-732.
- [223] B. Ravel and M. Newville, ATHENA, ARTEMIS, HEPHAESTUS: data analysis for X-ray absorption spectroscopy using IFEFFIT, *J. Synchrotron Radiat.* **2005**, 12, 537-541.
- [224] J. E. Penner-Hahn, X-ray absorption spectroscopy in coordination chemistry, *Coord. Chem. Rev.* **1999**, 190, 1101-1123.
- [225] S. Bordiga, E. Groppo, G. Agostini, J. A. van Bokhoven and C. Lamberti, Reactivity of Surface Species in Heterogeneous Catalysts Probed by In Situ X-ray Absorption Techniques, *Chem. Rev.* **2013**, 113, 1736-1850.
- [226] C. Ruckebusch, *Resolving spectral mixtures: with applications from ultrafast time-resolved spectroscopy to super-resolution imaging*, Elsevier, **2016**.
- [227] C. Ruckebusch and L. Blanchet, Multivariate curve resolution: a review of advanced and tailored applications and challenges, *Anal. Chim. Acta* **2013**, 765, 28-36.
- [228] A. de Juan and R. Tauler, Chemometrics applied to unravel multicomponent processes and mixtures: Revisiting latest trends in multivariate resolution, *Anal. Chim. Acta* **2003**, 500, 195-210.
- [229] W. Windig and J. Guilment, Interactive self-modeling mixture analysis, *Anal. Chem.* **1991**, 63, 1425-1432.
- [230] J. Jaumot, R. Gargallo, A. De Juan and R. Tauler, A graphical user-friendly interface for MCR-ALS: a new tool for multivariate curve resolution in MATLAB, *Chemom. Intell. Lab. Syst.* **2005**, 76, 101-110.
- [231] G. Leofanti, A. Marsella, B. Cremaschi, M. Garilli, A. Zecchina, G. Spoto, S. Bordiga, P. Fisticaro, G. Berlier, C. Prestipino, G. Casali and C. Lamberti, Alumina-supported copper chloride 3. Effect of exposure to ethylene, *J. Catal.* **2001**, 202, 279-295.
- [232] F. Giordanino, P. N. R. Vennestrom, L. F. Lundegaard, F. N. Stappen, S. Mossin, P. Beato, S. Bordiga and C. Lamberti, Characterization of Cu-Exchanged SSZ-13: a Comparative FTIR, UV-Vis, and EPR Study with Cu-ZSM-5 and Cu-beta with Similar Si/Al and Cu/Al Ratios, *Dalton Trans.* **2013**, 42, 12741-12761.
- [233] P. Chen, D. E. Root, C. Campochiaro, K. Fujisawa and E. I. Solomon, Spectroscopic and Electronic Structure Studies of the Diamagnetic Side-On CuII-Superoxo Complex Cu(O2)[HB(3-R-5-iPrpz)3]: Antiferromagnetic Coupling versus Covalent Delocalization, *J. Am. Chem. Soc.* **2003**, 125, 466-474.

- [234] S. Bordiga, C. Lamberti, F. Bonino, A. Travert and F. Thibault-Starzyk, Probing zeolites by vibrational spectroscopies, *Chem. Soc. Rev.* **2015**, 44, 7262-7341.
- [235] D. Barthomeuf, Framework induced basicity in zeolites, *Microporous and Mesoporous Mater.* **2003**, 66, 1-14.
- [236] G. A. V. Martins, G. Berlier, S. Coluccia, H. O. Pastore, G. B. Superti, G. Gatti and L. Marchese, Revisiting the Nature of the Acidity in Chabazite-Related Silicoaluminophosphates: Combined FTIR and ²⁹Si MAS NMR Study, *J. Phys. Chem. C* **2007**, 111, 330-339.
- [237] H.-K. Min, M. B. Park and S. B. Hong, Methanol-to-olefin conversion over H-MCM-22 and H-ITQ-2 zeolites, *J. Catal.* **2010**, 271, 186-194.
- [238] S. Svelle, M. Visur, U. Olsbye, Saepurahman and M. Bjørgen, Mechanistic Aspects of the Zeolite Catalyzed Methylation of Alkenes and Aromatics with Methanol: A Review, *Top. Catal.* **2011**, 54, 897.
- [239] S. Wang, Z. Wei, Y. Chen, Z. Qin, H. Ma, M. Dong, W. Fan and J. Wang, Methanol to Olefins over H-MCM-22 Zeolite: Theoretical Study on the Catalytic Roles of Various Pores, *ACS Catal.* **2015**, 5, 1131-1144.
- [240] K. Frolich, R. Bulánek and E. Frýdová, Interaction of CO probe molecules with Cu(+) in MCM-22 zeolite, *Microporous Mesoporous Mater.* **2014**, 186, 37-45.
- [241] L. M. Kustov, V. B. Kazanskii, S. Beran, L. Kubelkova and P. Jiru, Adsorption of carbon monoxide on ZSM-5 zeolites: infrared spectroscopic study and quantum-chemical calculations, *J. Phys. Chem.* **1987**, 91, 5247-5251.
- [242] A. Auroux, *Acidity and basicity: determination by adsorption microcalorimetry in Molecular Sieves*, ed. H.G. Karge and J. Weitkamp, Springer-Verlag, **2006**, 45-152.
- [243] D. J. Parrillo and R. J. Gorte, Characterization of acidity in H-ZSM-5, H-ZSM-12, H-Mordenite, and H-Y using microcalorimetry, *J. Phys. Chem.* **1993**, 97, 8786-8792.
- [244] G. Busca, L. Lietti, G. Ramis and F. Berti, Chemical and mechanistic aspects of the selective catalytic reduction of NO_x by ammonia over oxide catalysts: A review, *Appl. Catal., B* **1998**, 18, 1-36.
- [245] F. Giordanino, E. Borfecchia, K. A. Lomachenko, A. Lazzarini, G. Agostini, E. Gallo, A. V. Soldatov, P. Beato, S. Bordiga and C. Lamberti, Interaction of NH₃ with Cu-SSZ-13 Catalyst: A Complementary FTIR, XANES, and XES Study, *J. Phys. Chem. Letters* **2014**, 5, 1552-1559.
- [246] R. Arrigo, S. Wrabetz, M. E. Schuster, D. Wang, A. Villa, D. Rosenthal, F. Girsgdies, G. Weinberg, L. Prati, R. Schlögl and D. S. Su, Tailoring the morphology of Pd nanoparticles on CNTs by nitrogen and oxygen functionalization, *Phys. Chem. Chem. Phys.* **2012**, 14, 10523-10532.
- [247] J. Chen, G. Peng, T. Liang, W. Zhang, W. Zheng, H. Zhao, L. Guo and X. Wu, Catalytic Performances of Cu/MCM-22 Zeolites with Different Cu Loadings in NH₃-SCR, *Nanomaterials* **2020**, 10, 2079-4991.
- [248] E. Borfecchia, C. Negri, K. A. Lomachenko, C. Lamberti, T. V. W. Janssens and G. Berlier, Temperature-dependent dynamics of NH₃-derived Cu species in the Cu-CHA SCR catalyst, *React. Chem. Eng.* **2019**, 4, 1067-1080.
- [249] C. H. Giles, D. Smith and A. Huitson, A general treatment and classification of the solute adsorption isotherm. I. Theoretical, *J. Colloid Interface Sci.* **1974**, 47, 755-765.

- [250] V. J. Inglezakis, S. G. Pouloupoulos and H. Kazemian, Insights into the S-shaped sorption isotherms and their dimensionless forms, *Microporous Mesoporous Mater.* **2018**, 272, 166-176.
- [251] G. Limousin, J. P. Gaudet, L. Charlet, S. Szenknect, V. Barthès and M. Krimissa, Sorption isotherms: A review on physical bases, modeling and measurement, *Appl. Geochem.* **2007**, 22, 249-275.
- [252] Z. N. Lashchinskaya, A. A. Gabrienko and A. G. Stepanov, Propene transformation on Cu-modified ZSM-5 zeolite: Aromatization and oxidation, *Microporous and Mesoporous Mater.* **2023**, 350, 112448.
- [253] E. Borfecchia, D. K. Pappas, M. Dyballa, K. A. Lomachenko, C. Negri, M. Signorile and G. Berlier, Evolution of Active Sites During Selective Oxidation of Methane to Methanol over Cu-CHA and Cu-MOR Zeolites as Monitored by Operando XAS, *Catal. Today* **2019**, 333, 17-27.
- [254] A. Voronov, A. Urakawa, W. van Beek, N. E. Tsakoumis, H. Emerich and M. Ronning, Multivariate curve resolution applied to in situ X-ray absorption spectroscopy data: An efficient tool for data processing and analysis, *Anal. Chim. Acta* **2014**, 840, 20-27.
- [255] R. Haase, T. Beschnitt, U. Flörke and S. Herres-Pawlis, Bidentate guanidine ligands with ethylene spacer in copper-dioxygen chemistry: Structural characterization of bis(μ -hydroxo) dicopper complexes, *Inorg. Chim. Acta* **2011**, 374, 546-557.
- [256] M. R. Halvagar, P. V. Solntsev, H. Lim, B. Hedman, K. O. Hodgson, E. I. Solomon, C. J. Cramer and W. B. Tolman, Hydroxo-Bridged Dicopper(II,III) and -(III,III) Complexes: Models for Putative Intermediates in Oxidation Catalysis, *J. Am. Chem. Soc.* **2014**, 136, 7269-7272.
- [257] A. Martini and E. Borfecchia, Spectral Decomposition of X-ray Absorption Spectroscopy Datasets: Methods and Applications, *Crystals* **2020**, 10, 664.
- [258] C. Buono, A. Martini, I. A. Pankin, D. K. Pappas, C. Negri, K. Kvande, K. A. Lomachenko and E. Borfecchia, Local structure of Cu(I) ions in the MOR zeolite: A DFT-assisted XAS study, *Radiat. Phys. Chem.* **2020**, 175, 108111.
- [259] V. M. Rakić, R. V. Hercigonja and V. T. Dondur, CO interaction with zeolites studied by TPD and FTIR: transition-metal ion-exchanged FAU-type zeolites, *Microporous and Mesoporous Mater.* **1999**, 27, 27-39.
- [260] P. J. Smeets, R. G. Hadt, J. S. Woertink, P. Vanelderen, R. A. Schoonheydt, B. F. Sels and E. I. Solomon, Oxygen Precursor to the Reactive Intermediate in Methanol Synthesis by Cu-ZSM-5, *J. Am. Chem. Soc.* **2010**, 132, 14736-14738.
- [261] J. Hunt, A. Ferrari, A. Lita, M. Crosswhite, B. Ashley and A. E. Stiegman, Microwave-Specific Enhancement of the Carbon–Carbon Dioxide (Boudouard) Reaction, *J. Phys. Chem. C* **2013**, 117, 26871-26880.
- [262] C. Negri, T. Selleri, E. Borfecchia, A. Martini, K. A. Lomachenko, T. V. W. Janssens, M. Cutini, S. Bordiga and G. Berlier, Structure and Reactivity of Oxygen-Bridged Diamino Dicopper(II) Complexes in Cu-Ion-Exchanged Chabazite Catalyst for NH₃-Mediated Selective Catalytic Reduction, *J. Am. Chem. Soc.* **2020**, 142, 15884-15896.
- [263] P. Da Costa, B. Modén, G. D. Meitzner, D. K. Lee and E. Iglesia, Spectroscopic and chemical characterization of active and inactive Cu species in NO decomposition catalysts based on Cu-ZSM5, *Phys. Chem. Chem. Phys.* **2002**, 4, 4590-4601.

- [264] R. Villamaina, U. Iacobone, I. Nova, M. P. Ruggeri, J. Collier, D. Thompsett and E. Tronconi, Low-T CO Oxidation over Cu-CHA Catalysts in Presence of NH₃: Probing the Mobility of CuII Ions and the Role of Multinuclear CuII Species, *ChemCatChem* **2020**, 12, 3843-3848.
- [265] U. Iacobone, I. Nova, E. Tronconi, R. Villamaina, M. P. Ruggeri, J. Collier and D. Thompsett, Appraising Multinuclear Cu²⁺ Structure Formation in Cu-CHA SCR Catalysts via Low-T Dry CO Oxidation with Modulated NH₃ Solvation, *ChemistryOpen* **2022**, 11, e202200186.
- [266] K.-H. Steinberg, U. Mroczek and F. Roessner, Aromatization of ethane on platinum containing ZSM-5 zeolites, *Appl. Catal.* **1990**, 66, 37-44.
- [267] J. A. Biscardi and E. Iglesia, Reaction Pathways and Rate-Determining Steps in Reactions of Alkanes on H-ZSM5 and Zn/H-ZSM5 Catalysts, *J. Catal.* **1999**, 182, 117-128.
- [268] V. B. Kazansky, I. R. Subbotina, N. Rane, R. A. van Santen and E. J. M. Hensen, On two alternative mechanisms of ethane activation over ZSM-5 zeolite modified by Zn²⁺ and Ga¹⁺ cations, *Phys. Chem. Chem. Phys.* **2005**, 7, 3088-3092.
- [269] M. B. Park, S. H. Ahn, A. Mansouri, M. Ranocchiari and J. A. van Bokhoven, Comparative Study of Diverse Copper Zeolites for the Conversion of Methane into Methanol, *ChemCatChem* **2017**, 9, 3705-3713.
- [270] G. Spoto, S. Bordiga, G. Ricchiardi, D. Scarano, A. Zecchina and E. Borello, IR Study of Ethene and Propene Oligomerization on H-ZSM-5: Hydrogen-bonded Precursor Formation, Initiation and Propagation Mechanisms and Structure of the Entrapped Oligomers, *J. Chem. Soc. Faraday trans.* **1994**, 90, 2827-2835.
- [271] M. Boronat, C. Martínez-Sánchez, D. Law and A. Corma, Enzyme-like Specificity in Zeolites: A Unique Site Position in Mordenite for Selective Carbonylation of Methanol and Dimethyl Ether with CO, *J. Am. Chem. Soc.* **2008**, 130, 16316-16323.
- [272] E. J. M. Hensen, E. A. Pidko, N. Rane and R. A. van Santen, Water-Promoted Hydrocarbon Activation Catalyzed by Binuclear Gallium Sites in ZSM-5 Zeolite, *Angew. Chem. Int. Ed.* **2007**, 46, 7273-7276.
- [273] V. L. Sushkevich and J. A. van Bokhoven, Kinetic study and effect of water on methane oxidation to methanol over copper-exchanged mordenite, **2020**, 10, 382-390.
- [274] F. Göttl, S. Bhandari and M. Mavrikakis, Thermodynamics Perspective on the Stepwise Conversion of Methane to Methanol over Cu-Exchanged SSZ-13, *ACS Catal.* **2021**, 11, 7719-7734.





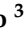

APPENDIX



Paper I

Article

Comparing the Nature of Active Sites in Cu-loaded SAPO-34 and SSZ-13 for the Direct Conversion of Methane to Methanol

Karoline Kvande ^{1,*}, Dimitrios K. Pappas ¹, Michael Dybala ¹, Carlo Buono ¹, Matteo Signorile ², Elisa Borfecchia ², Kirill A. Lomachenko ³, Bjørnar Arstad ⁴, Silvia Bordiga ², Gloria Berlier ², Unni Olsbye ¹, Pablo Beato ⁵ and Stian Svelle ¹

¹ Center for Materials Science and Nanotechnology (SMN), Department of Chemistry, University of Oslo, 1033 Blindern, 0315 Oslo, Norway; dimitrios.pappas@smn.uio.no (D.K.P.); michael.dybala@itc.uni-stuttgart.de (M.D.); carlo.buono@smn.uio.no (C.B.); unni.olsbye@kjemi.uio.no (U.O.); stian.svelle@kjemi.uio.no (S.S.)

² Department of Chemistry, NIS Center and INSTM Reference Center, University of Turin, via P. Giuria 7, 10125 Turin, Italy; matteo.signorile@unito.it (M.S.); elisa.borfecchia@unito.it (E.B.); silvia.bordiga@unito.it (S.B.); gloria.berlier@unito.it (G.B.)

³ European Synchrotron Radiation Facility, 71 avenue des Martyrs, CS 40220, CEDEX 9, 38043 Grenoble, France; kirill.lomachenko@esrf.fr

⁴ SINTEF Industry, Department of Process Technology, Forskningsveien 1, 0373 Oslo, Norway; bjornar.arstad@sintef.no

⁵ Haldor Topsøe A/S, Haldor Topsøes Allé 1, DK-2800 Kgs. Lyngby, Denmark; pabb@topsoe.com

* Correspondence: karoline.kvande@smn.uio.no; Tel.: +47-228-55-535

Received: 20 December 2019; Accepted: 3 February 2020; Published: 5 February 2020



Abstract: On our route towards a more sustainable future, the use of stranded and underutilized natural gas to produce chemicals would be a great aid in mitigating climate change, due to the reduced CO₂ emissions in comparison to using petroleum. In this study, we investigate the performance of Cu-exchanged SSZ-13 and SAPO-34 microporous materials in the stepwise, direct conversion of methane to methanol. With the use of X-ray absorption spectroscopy, infrared (in combination with CO adsorption) and Raman spectroscopy, we compared the structure–activity relationships for the two materials. We found that SSZ-13 performed significantly better than SAPO-34 at the standard conditions. From CH₄-TPR, it is evident that SAPO-34 requires a higher temperature for CH₄ oxidation, and by changing the CH₄ loading temperature from 200 to 300 °C, the yield (μmol/g) of SAPO-34 was increased tenfold. As observed from spectroscopy, both three- and four-fold coordinated Cu-species were formed after O₂-activation; among them, the active species for methane activation. The Cu speciation in SAPO-34 is distinct from that in SSZ-13. These deviations can be attributed to several factors, including the different framework polarities, and the amount and distribution of ion exchange sites.

Keywords: methane; methanol; zeolite; chabazite; spectroscopy; TPR

1. Introduction

Methane has become increasingly abundant as a carbon resource in recent years, and can be found in numerous sources [1]. The utilization of methane for chemicals, however, is rather complicated, due to the high stability of the molecule. The main method for converting methane in industry today is with the steam reforming reaction to produce synthesis gas. Synthesis gas can further be converted into valuable products, such as olefins, alcohols and ethers [2,3]. Nevertheless, the production of

this intermediate gas requires large facilities, due to the economy of scale, and transportation from remote areas is costly. These restrictions lead to the flaring of large amounts of associated petroleum gas. Flaring of methane causes more than 300 million tons of CO₂ to be released into the atmosphere every year. The World Bank has set in motion a “zero routine flaring initiative” to eliminate all routine flaring by the end of 2030 [4]. It is therefore of high interest to find a direct route for converting methane into liquid products on-site for the utilization of such stranded gas. Some promising liquids for further utilization are methanol and dimethyl ether (DME). Methanol may be used directly as a gasoline additive and for electric power generation; it is also an important starting material in the chemical industry for the production of highly demanded products, such as plastic, pharmaceuticals and plywood [5]. DME is usually made from methanol dehydration, and is an important compound for the future. DME has been extensively investigated the last decades as a more sustainable alternative to regular diesel fuel and LPG (both products from oil refining). This is because the properties of DME are quite similar to those of diesel and LPG, and therefore, only a few modifications are necessary to the already existing infrastructure [6,7]. One of the most promising routes currently being explored by the scientific community is the direct conversion of methane to methanol (DMTM). Many paths have been proposed and tested. The main problem, however, is the challenge of overcoming the over-oxidation of methanol to CO_x [3].

In nature, methane monooxygenase (MMO) enzymes convert methane directly into methanol under ambient conditions over active Fe or Cu metal sites [8]. Taking inspiration from these enzymes, metal-exchanged zeolites have been tested extensively for DMTM in a stepwise, stoichiometric reaction process. It has been demonstrated that a wide variety of zeolites (e.g., MOR [9–13], CHA [14,15], MFI [16,17]) are able to form stable and unique metal-oxo sites. In 2005, Groothaert et al. reported a stepwise reaction procedure working with Cu-ZSM-5 and Cu-MOR zeolites activated in O₂ for the direct conversion of methane to methanol [16]. The reaction procedure usually consists of three steps. First, an activation step at elevated temperatures (around 500 °C) is performed with an oxidant (e.g., N₂O, O₂) to create the metal-oxo sites. Subsequently, the temperature is lowered, before the methane is reacted over the active sites. Last, methanol is extracted by sending steam through the reactor isothermally, or by using a polar liquid solvent at room temperature (RT). The highest productivity achieved at atmospheric pressure thus far is 0.47 mol_{MeOH}/mol_{Cu}, for a Cu-MOR zeolite [18,19]. If a dinuclear active site is assumed, the theoretical limit is 0.5. It has been shown that there are a number of factors that influence the productivity and yield of methanol in the reaction, with some of the more important being the process parameters as well as the Cu speciation in the zeolite and the subsequent reducibility [14,19–24].

The high-silica, chabazite zeolite, SSZ-13, has been tested extensively for the reaction. However, the literature is scarce on the isostructural zeolite material SAPO-34. To the best of our knowledge, only Wulfers et al. have tested this material in the stepwise DMTM conversion [15]. Since SAPO-34 is an industrial scale catalyst for the conversion of methanol to olefins (MTO) [25], and is widely investigated as a Cu-loaded catalyst in NH₃-assisted selective catalytic reduction (NH₃-SCR) of NO_x [26], it became clear that a more extensive, comparative study on the reactivity of these materials in the DMTM-conversion would be of high interest.

The CHA framework consists of double six-membered rings (D6R) stacked in an ABC-sequence and interconnected with four membered rings (4MR). The resulting cages can be considered catalytic converters, which are interconnected with eight-membered ring (8MR) windows (Figure 1a). CHA is an ideal framework to work with, as the framework only has one crystallographically unique T-site [27,28]. Four different ion exchange sites have been determined in the CHA framework. Three of them point towards the centre of the 8MR-window, while one is in a more constrained position pointing into the D6R (Figure 1b) [29].

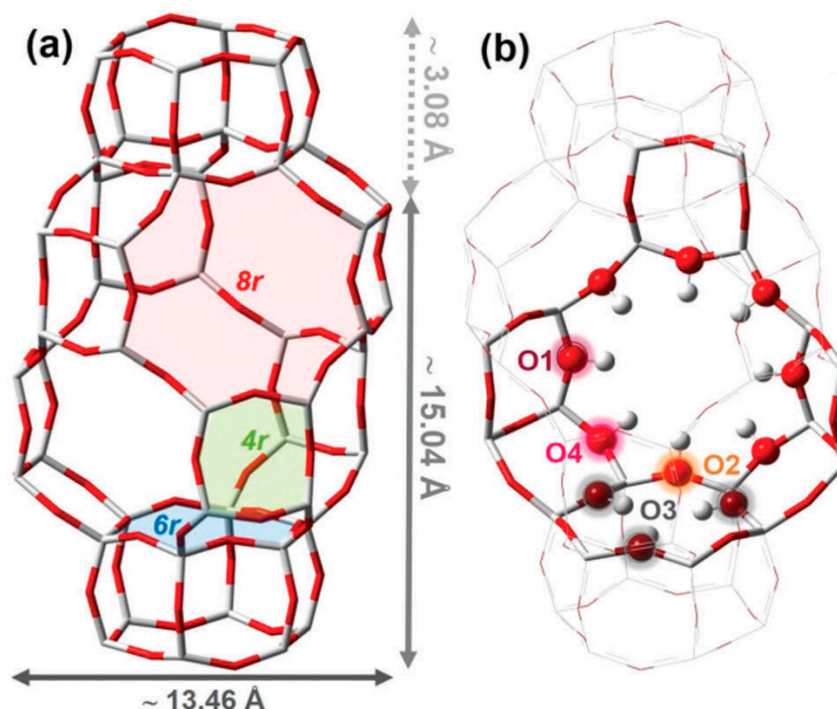


Figure 1. Representation of the CHA framework. The coloured areas in (a) marks the three different ring types (4MR, D6R and 8MR) surrounding the cages. (b) illustrates the four different O-sites in the framework. Colour code: grey: Si (SSZ-13) or alternating Al and P (SAPO-34), red: O, orange: Al (SSZ-13) or Si (SAPO-34). Adapted from Borfecchia et al. [29].

In SSZ-13, the amount of ion exchange sites (i.e., Brønsted acid sites) is determined by the Al-content. Conversely, the ion exchange sites in SAPO-34 are correlated to the amount of Si in the framework. In SAPO-34, Si incorporation may follow different substitution mechanisms (SM). There are two main mechanisms, where one leads to the formation of one Brønsted acid site per Si (SM2), while the other leads to a Si-rich patch (SM3) [30]. The two mechanisms are illustrated in Figure 2. Due to the different paths, the amount of Si in the framework will most likely not correlate directly to the amount of ion exchange sites. Whether the Si mostly follows the SM2, SM3, or a combination of these depends on the synthesis procedure [31].

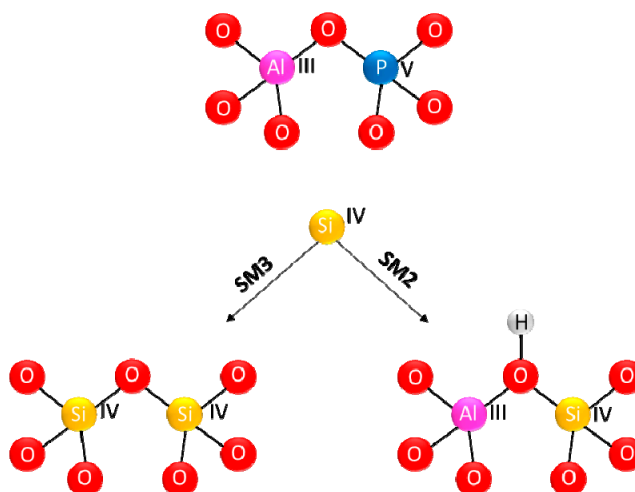


Figure 2. Scheme of the SM2 and SM3 mechanisms for Si substitution into the SAPO-34 framework. O is presented in red, Al in purple, Si in yellow, and P in blue.

Pappas et al. reported a thorough investigation of Cu-exchanged SSZ-13 for the DMTM reaction [14]. They combined characterization data from several spectroscopic techniques, together with a detailed study of the process conditions to pinpoint structure-activity relations [14]. A set of parameters were found to represent the optimal conditions for the conversion of methane (8 h in O₂ (500 °C), 6 h in CH₄ (200 °C), H₂O-assisted extraction (200 °C)).

In the current work, two Cu-SAPO-34 samples, with low and high Cu loading, were tested for the direct conversion of methane to methanol. When investigating the DMTM conversion, methanol and DME should both be regarded as important products, and therefore, the reported methanol activity in this study is given as the sum of methanol and DME observed in the extraction feed (MeOH = CH₃OH + 2 × (CH₃-O-CH₃)). Due to practical reasons, the standard experiments performed in this study had a shortened CH₄-loading time of 3 h. All other parameters were kept equal to the optimal conditions reached by Pappas et al. [14]. These results were then compared to a high loaded Cu-SSZ-13 material. Furthermore, IR, Raman and XAS spectroscopies, as well as CH₄-TPR have been employed to obtain a deeper understanding of the differences between the two isostructural CHA-zeolites, with respect to the nature of the Cu-sites and the effect of framework acidity.

2. Results and Discussion

2.1. Physicochemical Characterization

The Cu exchanged samples were prepared from the H-form of the materials. The introduction of Cu was performed with Liquid Ion Exchange (LIE), as described in the experimental section. In SAPO-34, it was not feasible to reach a high degree of Cu incorporation, and the highest amount of Cu obtained was 1.58 wt% (Cu/Si=0.25). This amount was reached after three consecutive exchanges according to a method reported by Vennestrøm et al. [32]. The calcining step between each exchange should help the migration of Cu ions from the surface into the crystal.

Nomenclature and physicochemical characterization data, such as compositional information, N₂-physisorption data, and water content are reported in Table S1 in the supporting information (SI). Scanning Electron Microscopy (SEM) (Figure S1) and X-ray Diffraction (XRD) (Figures S2 and S3) analyses were performed for all the (Cu-)SAPO-34 samples and the results are reported in the SI. SEM-images and XRD pattern of (Cu-)SSZ-13 have been reported previously [14]. No extra CuO phase is observed in the materials, indicating that they are free of any large CuO agglomerates and that the Cu exchange took place properly.

2.2. Direct Methane to Methanol Conversion

The exchanged Cu-SAPO-34 and SSZ-13 materials were investigated for the direct conversion of methane to methanol. The test procedure is described in the experimental section (Test #1). The protocol is based on optimal conditions reported in a previous study by Pappas et al. [14] on Cu-SSZ-13 materials for the same reaction. The results are reported in Figure 3. On the left, the total yield of methanol (mol_{MeOH}/g_{zeolite}) is shown as a function of the Cu-content. The right panel shows the productivity, where the total amount of methanol is normalized to the Cu-content. Minor fractions of CO/CO₂ were observed in the effluent during methane loading and H₂O-assisted extraction. However, the yield of the CO_x species has not been reported in this study due to high uncertainties in the obtained CO_x values. From the results reported in Figure 3, it is evident that the Cu-loaded SSZ-13 outperforms the Cu-SAPO-34 materials in the reaction. This is in line with previous results obtained for the DMTM conversion over Cu-SSZ-13 and SAPO-34, reported by Wulfers et al. [29]. Another interesting observation is that a higher loading of Cu in SAPO-34 does not increase the yield of methanol. Indeed, a slightly higher productivity is seen for the low loaded sample, as observed in the right panel of Figure 3. These results indicate that it is only a small fraction of the exchanged Cu in SAPO-34 that contributes as active sites for methane conversion, and that an increase in Cu-content does not lead to an increased amount of these active sites. A blind test was performed on both Cu-free SAPO-34

and SSZ-13 under the same reaction conditions, and no methanol was detected in the effluent. This confirms that the small amount of methanol observed for Cu-SAPO-34 in the tests is significant.

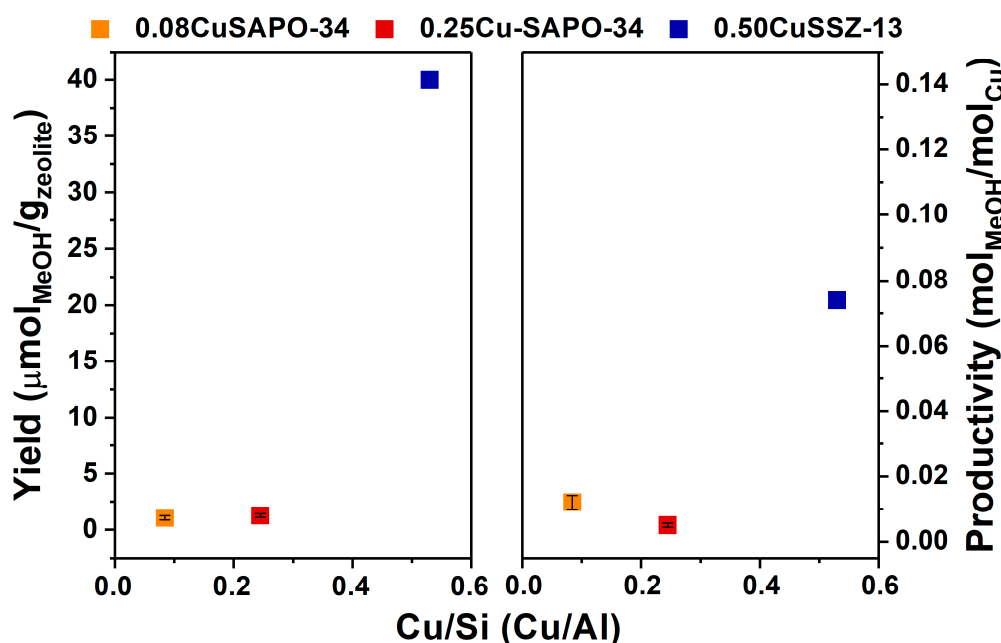


Figure 3. Representation of the performance of 0.08CuSAPO-34 (orange), 0.25CuSAPO-34 (red) and 0.50CuSSZ-13 (blue) at identical reaction conditions (Table 1). The panel on the left shows CH₃OH yield per gram of zeolite. The panel on the right gives the CH₃OH yield normalized to the Cu content (molCH₃OH/molCu). The estimated error from DMTM conversion over Cu-SAPO-34 is shown as black error bars inside the squares.

Due to the structural similarities between the materials, the difference in performance was unexpected. A deeper investigation with various spectroscopic techniques (IR, Raman and in situ XAS) was therefore performed, with the aim of elucidating the Cu-speciation of the materials.

2.3. Utilizing Spectroscopy to Investigate the Cu-Speciation

2.3.1. Investigating the Cu(II)_xO_y Sites with Raman Spectroscopy

Resonance Raman (rRaman) spectra of activated, sealed capillaries were collected with a blue laser (488 nm) at RT. The resulting spectra of hydrated and activated 0.25Cu-SAPO-34 (red) and 0.50Cu-SSZ-13 (blue) are shown in Figure 4. It is clear from the figure that a new set of bands arise in the spectra when the material has been activated at high temperatures in static air. These bands are correlated to Cu(II)_xO_y species that are resonantly enhanced by the blue laser. Frequencies and reasonable assignments are summarized in Table S2. The assignment of the Cu(II)_xO_y-species in the Cu-SSZ-13 material has been made previously [14]. For SAPO 34, the assignments presented below are based on previous observations on Cu-SSZ-13, Cu-ZSM-5 and other compounds [14,17]. The band at 812 cm⁻¹, together with the shoulders found at 524 and 587 cm⁻¹ have been assigned to a three-fold coordinated dicopper species [Cu(trans-μ-1,2-O₂)Cu]²⁺, which is based on bands appearing at similar positions in Cu-loaded SSZ-13 (830, 510 and 580 cm⁻¹), observed by Pappas et al. and Ipek et al. [14,33]. It is worth noting that the resonance enhancement of this dicopper-species is very clear in Cu-SSZ-13, while in Cu-SAPO-34, the features are only observed as minor contributions. The strongest band in Cu-SAPO-34, at 549 cm⁻¹ is assigned to the symmetric vibration of Cu-O in a side-on superoxo Cu(II) species. The corresponding ν(O-O) mode of the same species is observed at 1006 cm⁻¹. These bands are assigned by analogy with the rRaman results by Solomon and co-workers, reporting signals at 554 and 1043 cm⁻¹ for Cu-superoxo species in homogeneous model compounds [34]. Pappas et al.

also found bands indicating the presence of side-on superoxo Cu(II) and mono- μ -oxo dicopper(II) Cu(II) and mono- μ -oxo dicopper(II) ($[\text{Cu}-(\mu\text{-O})-\text{Cu}]^{2+}$) in Cu-SSZ-13 [14]. No bands corresponding to these species were found to be present in Cu-SAPO-34. The assignment of the observed bands indicates that there are significant differences between SSZ-13 and SAPO-34 with respect to the types of $\text{Cu}(\text{II})_x\text{O}_y$ complexes formed in the materials, even though they possess the same CHA framework topology. Pappas et al. have suggested that three-fold coordinated Cu(II) sites may be the most favourable geometric sites for methane conversion, which is the most pronounced species appearing in SSZ-13 (trans- μ -oxo dicopper(II)) [14]. The more pronounced species appearing in Cu-SAPO-34 is a monomeric site with a four-fold coordination (side-on superoxo Cu(II)), and these sites are assumed to be less active for CH_4 -activation [14].

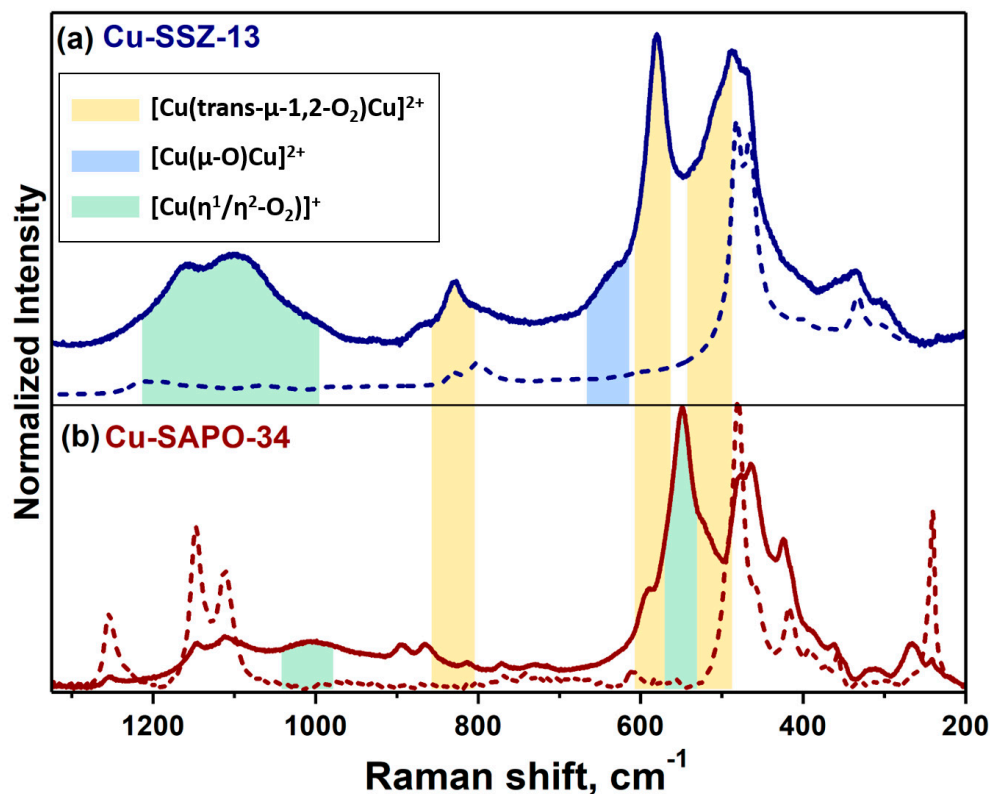


Figure 4. Raman spectra of (a) hydrated (dashed blue) and activated (solid blue) 0.50CuSSZ-13, and (b) hydrated (dashed red) and activated (solid red) 0.25CuSAPO-34. The contributions from different $\text{Cu}(\text{II})_x\text{O}_y$ moieties are marked. Yellow shading: $[\text{Cu}(\text{trans-}\mu\text{-1,2-O}_2)\text{Cu}]^{2+}$, blue shading: $[\text{Cu}(\mu\text{-O})\text{Cu}]^{2+}$ and green shading: $[\text{Cu}(\eta^1/\eta^2\text{-O}_2)]^+$.

2.3.2. IR Spectroscopy Measurements of Adsorbed CO

2.3.2. IR Spectroscopy Measurements of Adsorbed CO

By dosing CO on the Cu-samples, it is possible to selectively follow the interaction of CO with distinct Cu(I) sites in the sample. Importantly, by probing at RT, the CO interaction with Brønsted acid sites is not detectable [35,36]. Figure 3 shows the evolution of the mono- and dicarbonyl species on Cu. Already at small doses of CO, there is a band evolving at 2153 cm^{-1} . This band is due to the vibration of monocarbonyl adducts ($\text{Cu}(\text{I})\text{-CO}$) [35–37]. Since the spectra have been normalized to the framework vibration overtone mode (1868 cm^{-1} (SSZ-13) and 1853 cm^{-1} (SAPO-34)), weighted on the Cu-content and background subtracted, the intensities of the bands can be directly compared for the samples with different Cu-loading. Interestingly, it can be observed that the 0.08CuSAPO-34 has a higher intensity of the band at 2153 cm^{-1} , which could be caused by a higher fraction of Cu(I) sites that are accessible by CO. It may also be the case that some of the Cu-sites in the high-loaded SAPO-34 and/or SSZ-13 samples are more resistant to self-reduction and therefore remain as Cu(II) [19].

As the amount of CO increases, the bands at 2176 cm^{-1} and 2148 cm^{-1} develop. These bands are assigned to the symmetric and antisymmetric stretching vibration of dicarbonyl adducts

As the amount of CO increases, the bands at 2176 cm^{-1} and 2148 cm^{-1} develop. These bands are assigned to the symmetric and antisymmetric stretching vibration of dicarbonyl adducts (Cu(I)(CO)_2) [35–37]. It is clear that these species are more easily formed in 0.50CuSSZ-13, as seen from the higher intensity increase of these bands. The larger amount of dicarbonyl adducts indicates that 0.50CuSSZ-13 has more freely coordinated Cu(I) species, where the Cu has only two or three oxygen framework neighbours. These findings support what is already observed from Raman spectroscopy.

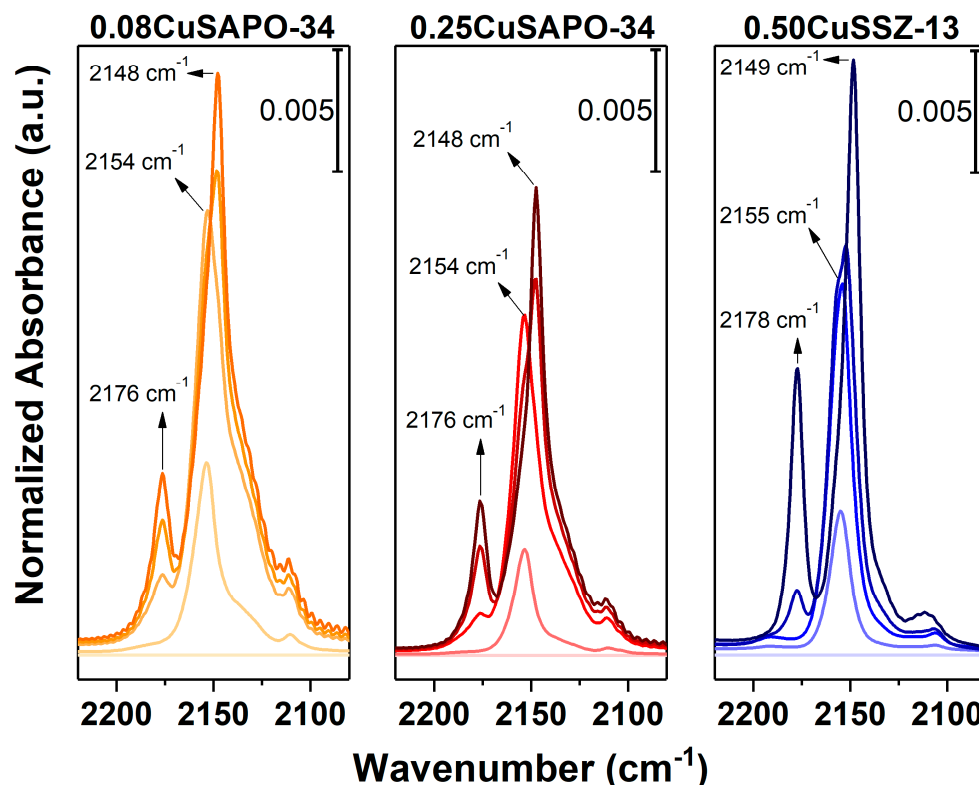


Figure 5. FT-IR spectra of adsorbed CO at RT on 0.08CuSAPO-34 (orange), 0.25CuSAPO-34 (red) and 0.50CuSSZ-13 (blue). The CO pressure was increased from $20\ \mu\text{bar}$ to $20\ \text{mbar}$. The materials were activated for 1 h at $150\text{ }^\circ\text{C}$, $300\text{ }^\circ\text{C}$ and $450\text{ }^\circ\text{C}$. The spectra are background subtracted and normalized to the framework overtones as well as to the Cu content ($\mu\text{mol/g}$).

2.3.3. IR Spectroscopy Measurements During Heating in O_2

Pappas et al. observed evidence that $[\text{Cu(II)OH}]^+$ sites exist in SSZ-13, and that they act as precursors to form the active sites for the DMTM conversion [14]. When heating Cu-SSZ-13 in an O_2 -atmosphere while collecting IR spectra, a band at 3650 cm^{-1} is clearly observed, and the intensity of this band decreases with the increasing temperature. This band has previously been assigned to be the fingerprint for $\text{Z}[\text{Cu(II)OH}]$ vibration [36,38,39], supporting the existence of these species and suggesting that they are likely to be precursors for other species. We therefore chose to perform the same treatment on 0.25CuSAPO-34, to see if these species exist in Cu-SAPO-34. However, as can be observed in Figure 6, it is clear that no such band exists in this sample. The only features that can be observed in the spectra are two bands at 3622 and 3594 cm^{-1} , which are related to the $\nu(\text{O-H})$ mode of Brønsted acid sites [38,40,41].

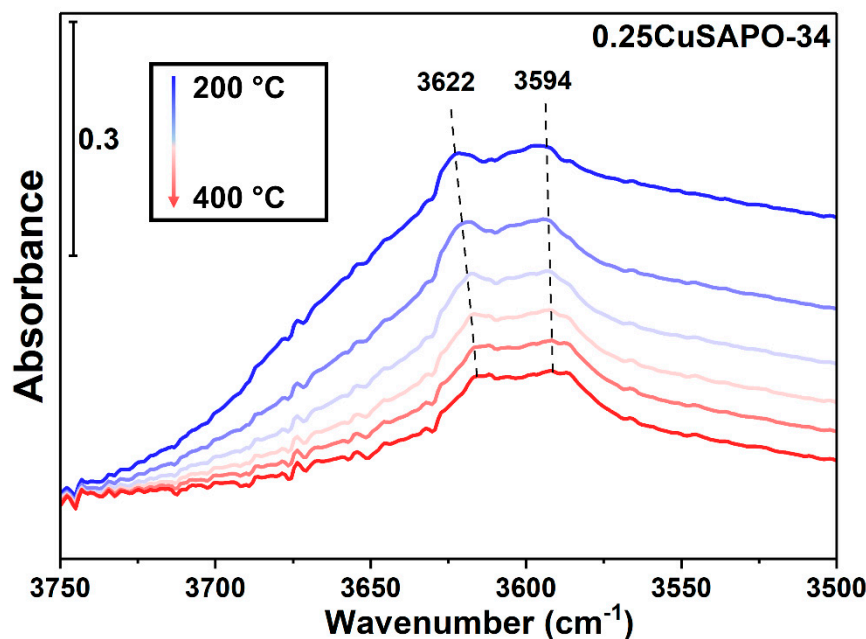


Figure 6. Spectra of O_2 -activated 0.25CuSAPO-34. The temperature increases gradually from 200 °C (blue) to 400 °C (red). The dashed lines represent two peaks related to the Brønsted acid sites of the material. No band is observed at 3650 cm^{-1} (fingerprint region of $Z[\text{Cu(II)OH}]$ vibrations).

2.3.4. In Situ X-ray Absorption Spectroscopy

To investigate the oxidation state and average coordination of the Cu species, in situ X-ray absorption spectroscopy (XAS) measurements at the Cu K-edge were performed on the highest Cu-loaded SAPO-34 (0.25CuSAPO-34). The obtained spectra were compared with XAS spectra of 0.50CuSSZ-13 collected under similar conditions, see Figure 7. The spectra were collected after pre-treatment in He at 500 °C (dashed lines) and then after further exposure to O_2 for 2–3 h (solid lines).

He activation of the materials results in a peak at 8983 eV, corresponding to the characteristic $1s \rightarrow 4p$ transitions of Cu(I) ions [14,38,42–44]. The spectrum of the He-activated material shows a highly developed Cu(I) state in Cu-SAPO-34, indicating that the Cu in the material undergoes “self-reduction” to a large extent [14,38]. The higher intensity of the peak at 8983 eV could indicate that the degree of self-reduction of Cu-SAPO-34 is even higher than for Cu-SSZ-13, however, it could also be due to a different coordination of Cu(I)-states in the two materials. Under the latter assumption, one would expect a higher fraction of linear or quasi-linear Cu(I) species in Cu-SAPO-34, while Cu(I) ions with higher coordination and/or lower O-Cu-O bond angles would be expected after He-activation in Cu-SSZ-13 [45]. Moreover, it has also previously been suggested that SAPO-34 has a higher reducibility than SSZ-13, as seen by H_2 -TPR experiments by Gao et al. [46]. A higher reducibility of SAPO-34 also supports the higher intensity observed for monocarbonyl adducts adsorbed on the low loaded SAPO-34 material compared to SSZ-13.

After the material is contacted with O_2 , a high fraction of Cu(I) is oxidized to Cu(II), as seen by the decrease of the peak at 8983 eV. The change to Cu(II) is further supported by the increase of the dipole-forbidden $1s \rightarrow 3d$ transition of Cu(II) ions, appearing in the pre-edge region at 8977 eV (inset in Figure 7a) [38,39,41,47]. In Cu-SAPO-34, it can be observed that some of the Cu remains as Cu(I) after exposure to O_2 . This can be seen from the remaining peak at 8983 eV. It is also evident that the average coordination number of both samples is higher in the O_2 -activated state compared to the He-activated state, evidenced by a higher white line (WL) intensity [14,38]. The overall shape of the XANES and EXAFS spectra after O_2 -activation of the two compounds is very similar, suggesting similar Cu environment. Nonetheless, some difference is observed in the WL, which appears to be slightly higher and with a somewhat different shape for Cu-SSZ-13 than for Cu-SAPO-34. This observation is

further supported by the higher intensity of the first shell of the EXAFS spectra (Figure 7). This EXAFS feature is linked with Cu–O single scattering (ss) paths involving framework (O_{fw}) and possibly extra framework (O_{ef}) oxygen atoms in the first coordination shell of Cu ions [14]. As evidenced from the dipole-forbidden $1s \rightarrow 3d$ transition in the pre-edge region, there is more Cu(II) present in SSZ-13 than in SAPO-34 after O_2 -activation. More Cu in a higher oxidation state is usually linked with a higher coordination number to O atomic neighbours in the first shell, which consequently explains the observed difference in the shape and intensity of the XANES WL as well as the higher first shell intensity of the FT-EXAFS spectra for SSZ-13 and SAPO-34 recorded after O_2 -activation.

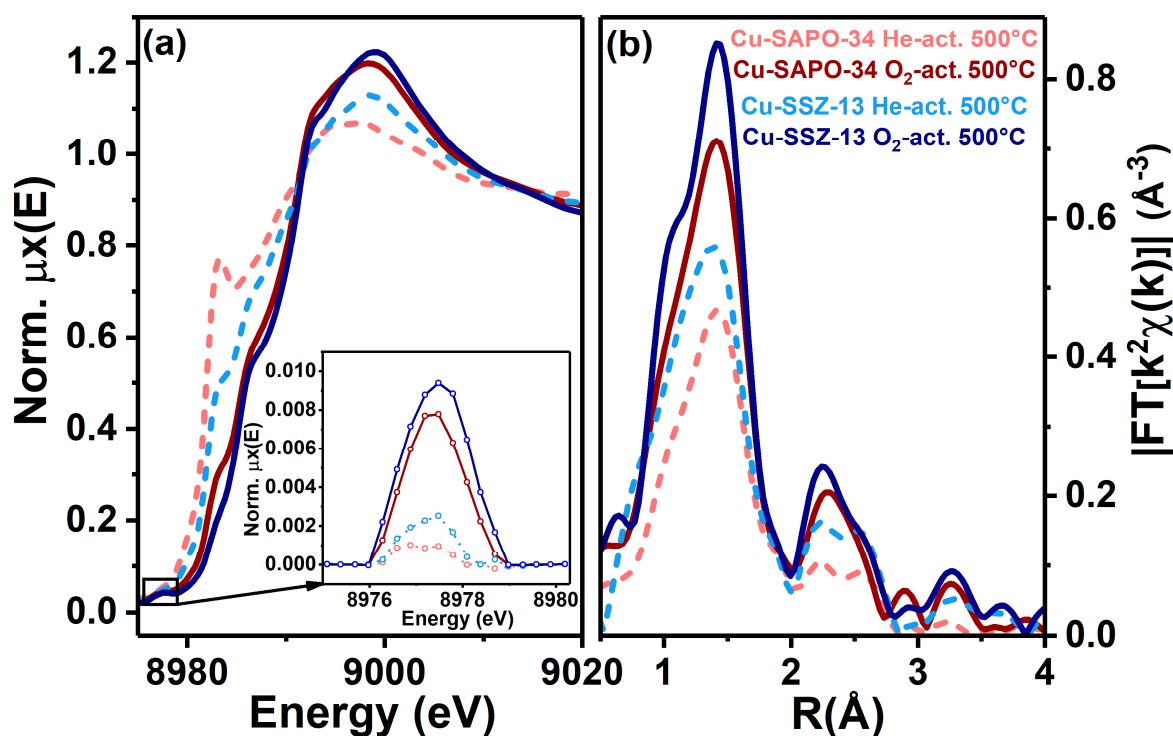


Figure 7. XANES (a) and FT-EXAFS (b) spectra of 0.25CuSAPO-34 (red) and 0.50CuSSZ-13 (blue) after He-activation at 500 °C (light coloured, dotted lines) and after consecutive O_2 -activation for 1 h (dark coloured, solid lines). The inset in (a) is an enhancement of the dipole-forbidden $1s \rightarrow 3d$ transition in the pre-edge region.

2.4. Comparing the CH_4 Consumption

Based on the Raman and IR spectroscopies, we suggest that more highly coordinated Cu-species are hosted in SAPO-34. If this is combined with the knowledge that SAPO-34 has a more restricted placement of Si in the framework, which leads to fewer acid sites in close proximity, it can be suggested that more of the Cu in SAPO-34 exists as monomeric isolated Cu-sites, compared to SSZ-13. Recently, van Bokhoven and coworkers performed CH_4 -TPR on various zeolites, as well as monitored, with XANES, the Cu(I) formation in MOR zeolites with different Cu-loadings and were able to show that more isolated Cu-sites need a higher temperature to be reduced [20,21]. Based on these observations, we similarly performed CH_4 -TPR on the SAPO-34 and SSZ-13 samples investigated in this work. The consumption of CH_4 is shown in Figure 8, while the total oxidation to CO_2 is reported in Figure S4. It is clear from the results that the CH_4 -consumption starts at a substantially lower temperature in 0.50CuSSZ-13 (ca. 200 °C) than in 0.08CuSAPO-34 and 0.25CuSAPO-34 (ca. 280 and 300 °C, respectively).

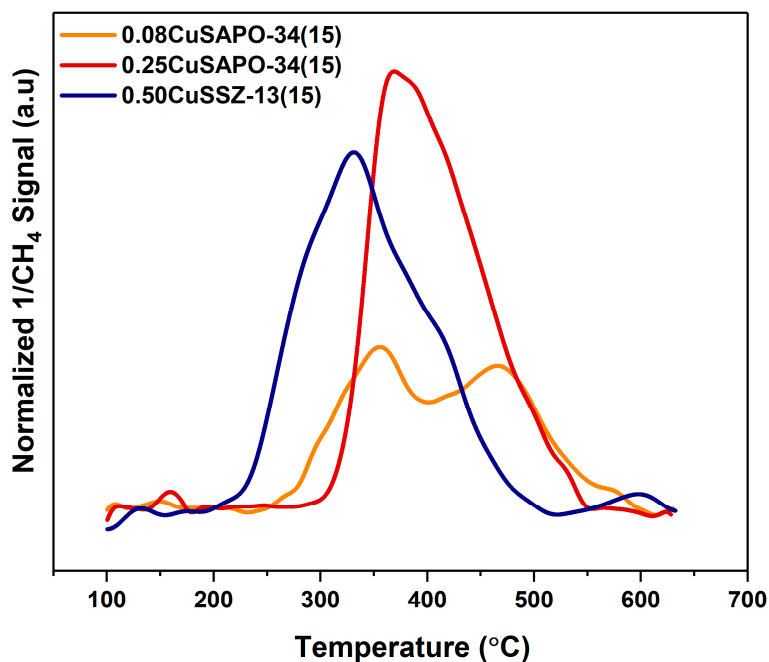


Figure 8. Inversed CH_4 consumption of 0.50CuSSZ-13 (blue), 0.08CuSAPO-34 (orange) and 0.25CuSAPO-34 (red) measured by an online MS during flow of CH_4 while heating from 100 to 650 °C (ramp: 5 °C/min). The materials were activated at 500 °C in O_2 for 8 h prior to the CH_4 -TPR experiment. The graphs have been normalized to the sample weight.

2.5. Optimization of the Test Parameters

Based on the differences in CH_4 -oxidation temperature observed in the TPR profiles, we changed the test parameters by increasing the CH_4 -loading temperature from 200 to 300 °C for the two SAPO-34 materials (Test #2 reported in Table 1). The performances thus obtained are plotted in Figure 9 together with the previous results for clarity. Interestingly, after increasing the CH_4 -loading temperature, we observe a tenfold increase in the CH_3OH -yield over 0.08CuSAPO-34 and 0.25CuSAPO-34, while the CH_3OH -yield from 0.50CuSSZ-13 decreases significantly, indicating a loss in selectivity, as also suggested from CO_2 production observed with CH_4 -TPR experiments (Figure S4). When normalizing the yield to the Cu-content, 0.08CuSAPO-34 reaches even a higher productivity than that observed for 0.50CuSSZ-13 at a 200 °C CH_4 -loading temperature. The parent materials, H-SAPO-34 and H-SSZ-13, were also tested with a 300 °C CH_4 -loading temperature. Both parent samples had a productivity of less than 2 $\mu\text{mol/g}$, proving that the productivity of the materials derive from the O_2 -activated Cu-species.

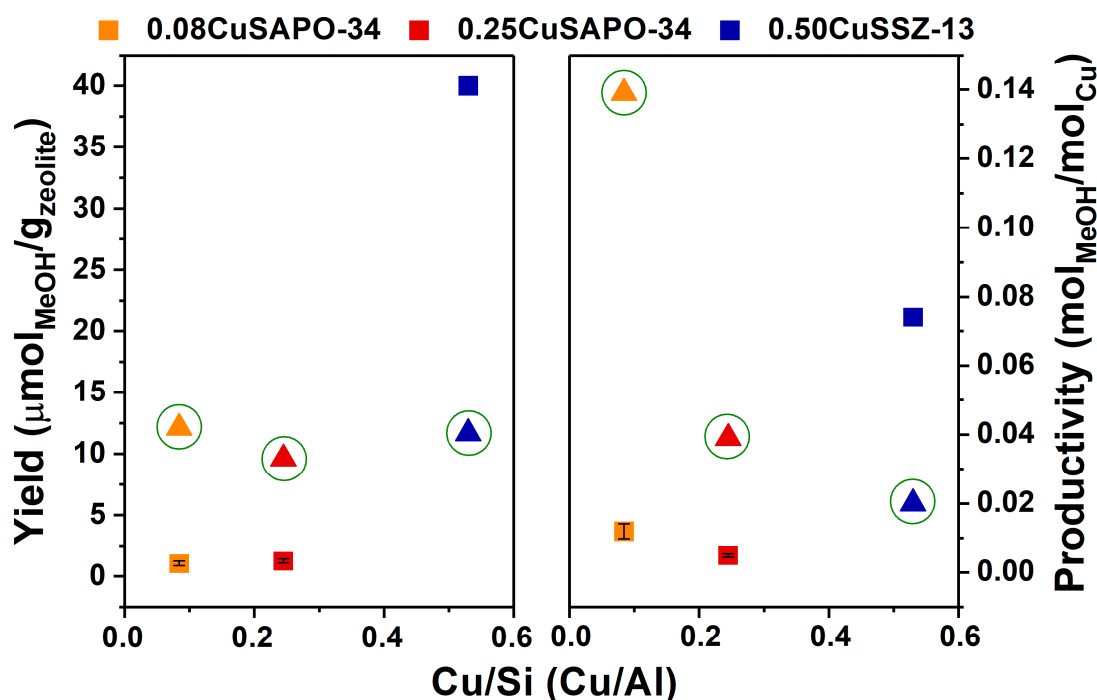


Figure 9. Comparison of the standard test conditions (Test #1-represented by squares) to the high temperature CH_4 -loading test conditions (Test #2-represented by green circled triangles). The panel on the left shows CH_3OH yield per gram of zeolite. The panel on the right gives the CH_3OH yield normalized to the Cu content ($\text{mol}_{\text{CH}_3\text{OH}}/\text{mol}_{\text{Cu}}$). Colours: 0.08CuSAPO-34 (orange), 0.25CuSAPO-34 (red) and 0.50CuSSZ-13 (blue). The estimated error from DMTM conversion over the Cu-SAPO-34 materials in Test #1 is shown as black error bars inside the squares.

3. Materials and Methods

3.1. Material Synthesis

The synthesis and ion exchange procedure for the SSZ-13 zeolite ($\text{Si}/\text{Al}=15$) is reported in a previous article [14], while the synthesis procedures performed on (Cu-)SAPO-34 ($(\text{Al}+\text{P})/\text{Si}=15$) is described below.

The parent SAPO-34 was synthesized according the synthesis route reported by Mertens [48]. The final gel had a molar ratio of 0.3 $\text{SiO}_2/1 \text{ Al}_2\text{O}_3/1 \text{ P}_2\text{O}_5/1 \text{ TEOH}/35 \text{ H}_2\text{O}$. First, orthophosphoric acid, (85 %, Merck), tetraethyl ammonium hydroxide (TEAOH, 35 %, Sigma-Aldrich) and deionised water were mixed. The mixture was then heated to 30 °C, after which silica (ludox-AS-40, 40 % SiO_2 , DuPont) and alumina (Pural SB, 76% Al_2O_3 , SASOL) were added under continuous stirring, before aging at 30 °C for 2 h. Thereafter, the aged gel was transferred into Teflon lined autoclaves, and heated to 165 °C, and kept there for 72 h with rotation. The heating rate was 5 °C/h. Last, the reaction was stopped by quenching, and the obtained powder was washed well with deionised water before drying over night at 95 °C. The proton form of SAPO-34 was obtained by calcining the material in static air at 600 °C for 15 h. The heating rate was 2 °C/min, starting from room temperature (RT). Liquid ion exchange (LIE) was performed to incorporate Cu. For the low loaded material ($\text{Cu}/\text{Si}=0.08$), a 0.02 M CuAc_2 -solution was prepared and stirred with the material (60 mL solution/g of zeolite) at RT for 24 h. The pH of the solution was kept in the 5.5–6 range. After stirring, the material was washed and centrifuged three times. The high loaded material was prepared in the same way, but the process was repeated three times, with a calcining step between each round (600 °C, 15 h, 2 °C/min). The CuAc_2 solution used in the first round was 0.02 M. For the second and third round, a CuAc_2 -solution resulting in a Cu/Si ratio of 0.5 was used (0.008 M).

3.2. Characterization

Powder X-ray diffraction patterns of the materials, before and after Cu-incorporation were obtained on a Bruker D8 Discover Diffractometer with a Cu K α radiation ($\lambda = 1.5406 \text{ \AA}$).

Thermogravimetric analysis was used to find the dry weight of the Cu-exchanged materials. For all measurements, a small platinum crucible, filled with a small amount of sample (around 25 mg), was placed inside a Stanton Redcroft furnace. The samples were heated to 300 °C with a heating rate of 2 °C/min. The material was kept at 300 °C for 30 min and then slowly cooled to RT.

Specific surface area and pore volume were measured by N₂-adsorption experiments, performed at −196 °C on approximately 40 mg of sample, by estimating the BET isotherm. The data were collected on a BelSorp MINI instrument. The materials were first pre-treated in vacuum (1 h at 80 °C, and 2 h at 300 °C). The p/p_0 range used for the BET surface area was 0.0–0.1.

Scanning electron microscopy (SEM) was used to investigate the crystal morphology. The images were collected on a Hitachi SU8230 in deceleration mode. Energy dispersive X-ray (EDX) was used to obtain the elemental composition of the materials (e.g., Cu/Si and (Al+P)/Si). A small amount of powder was pressed (5 tons) into a self-supporting wafer, and placed on a carbon tape on top of a carbon holder, prior to the EDX-measurements.

CO-adsorption at RT was characterized by IR spectroscopy on 0.08CuSAPO-34, 0.25CuSAPO-34 and 0.50CuSSZ-13, in order to investigate the interaction of CO adsorbed on the Cu-sites. Each material was pressed into a self-supporting wafer (11.3 mg/cm²) and placed inside a gold envelope. The material was pre-treated in a vacuum for 1 h at 150 °C, 1 h at 300 °C and 1 h at 450 °C. After cooling, small amounts of CO were dosed repeatedly into the cell at RT, until reaching about a CO equilibrium pressure of 20 mbar. A spectrum was recorded after each dosing.

Raman spectroscopy measurements were used to investigate Cu–O and O–O vibrations in the Cu exchanged SAPO-34 and SSZ-13 materials. The samples were investigated at RT, both as-synthesized (hydrated), as well as in sealed capillaries after activation in static air atmosphere. For measuring the activated samples, boron-silicate glass capillaries (0.5 mm diameter and 0.01 mm wall thickness) containing the studied materials were heated to 550 °C, with a 3 °C/min ramp and kept overnight (14 h) at the same temperature. The capillaries were then sealed with a flame gun while hot, and then slowly cooled to RT. The spectra were collected with a blue laser (488 nm) and recorded with a Horiba LabRamanHR microscope, equipped with a Coherent Sapphire laser. The signal was dispersed over a 1800 lines/mm grating on a thermoelectrically cooled CCD detector. The excitation beam was focused on the sample with a 50x objective lens.

In situ X-ray absorption spectroscopy (XAS) experiments were performed at the BM23 beamline of the European Synchrotron Radiation Facility (ESRF) in Grenoble. The measurements were performed in a Microtomo reactor cell designed by the ESRF Sample Environment group [49], integrated in a dedicated gas flow setup. Before starting the measurements, the samples were transformed into self-supporting pellets (ca. 85 mg/cm²) This leads to edge jumps in the 0.4–0.9 region and total absorption $\mu x = 2.5$. The in situ procedure applied was as described previously by Pappas et al. [14], where the samples were heated in He from RT to 500 °C with a heating ramp of 5 °C/min and a flow rate of 100 mL/min. After activation, an O₂ flow (100 mL/min) was introduced for 180 min. With the use of a liquid N₂-cooled flat Si(111) double-crystal monochromator, the Cu K-edge spectra were collected in transmission mode. Ionization chambers filled with Ar and He were used to detect the incident (I_0) and transmitted ($I_{1,2}$) X-ray intensities. The third ionization chamber (I_2) was used to collect the XANES spectrum of a Cu metal foil simultaneously with the samples. [50] After the samples had been stabilised at constant temperature in static conditions, high quality EXAFS scans were collected. These were acquired in the 8800–9955 eV range with an energy step of 5 eV in the pre-edge region, 0.3 eV in the XANES region and a constant k step of $\Delta k = 0.035 \text{ \AA}^{-1}$ in the EXAFS region. With an integration time of 1 s/point, the resulting acquisition of the whole spectrum was 17 min/scan. For analysis, all XAS spectra were normalized to unity edge jump, and thereafter aligned in energy by applying the Athena software from the Demeter package [51]. To characterize the static states, three/four consecutive XAS

scans were collected, and after checking for signal reproducibility, the scans were averaged to the corresponding $\mu\chi(E)$ curves. The $\chi(k)$ EXAFS functions were extracted using the Athena program, and by transforming the $k^2 \chi(k)$ functions in the range of 2.4–13.0 \AA^{-1} , the Fourier-Transform (FT) EXAFS spectra were obtained.

CH_4 -TPR experiments were performed using a U-shaped fixed bed reactor. The effluent was monitored with an online Pfeiffer MS. About 100 mg of material was used for the measurements. The flows of CH_4 (100%), He (100%) and O_2 (100%) were controlled by needle valve/rotameter controllers and fed stepwise to the reactor with the use of stop- and 4-way valves. The total gas flow was always 15 mL/min. The reaction protocol consisted of heating the material at 500 °C in O_2 (8 h), before the reactor was cooled to 100 °C, and flushed with He for 1 h. Then CH_4 was introduced, while the temperature was ramped (5 °C/min) to 650 °C.

3.3. Performance Tests

The direct conversion of methane to methanol over the materials was tested with a purpose-designed setup. Before exposing the material to the test conditions, the samples were crushed and sieved with a sieve fraction of 250–425 μm . 100 mg of the sample was transferred to a straight quartz tube (i.d.=6 mm) containing a porous plug. The reactor was connected to the gas lines inside a tubular oven. The reaction temperature was monitored by inserting a thermocouple placed inside a quartz sheath at the top of the reactor bed. The flow of CH_4 (100 %), He (100 %), O_2 (100 %) and a Ne/He mixture (10 % Ne in He) was controlled by MFCs and fed stepwise to the reactor with the use of stop- and 4-way valves. To obtain approximately 10 % water in the Ne/He-stream passing through the reactor, the mixture was bubbled through a saturator immersed in an oil bath heated to 45 °C (water vapour pressure \approx 9.6 kPa).

The standard reaction procedure (test #1) consisted of dehydrating the material at 150 °C in He (15 mL/min), before a flow of pure O_2 was introduced, and the temperature increased to 500 °C with a heating rate of 5 °C/min. The material was kept at 500 °C in O_2 (15 mL/min) for 8 h. Then, the temperature was decreased (5 °C/min) to 200 °C, and CH_4 (15 mL/min) was purged for 3 h. Finally, a 10 % H_2O -saturated Ne/He stream (14.9 mL/min) was introduced to extract the selectively oxidized products out of the pores. The detected products were methanol, dimethyl ether (counted as two methanol molecules) and some CO_x species. The reaction conditions are summarized in Table 1 below.

Table 1. Test conditions applied for the DMTM conversion.

	He Activation (°C) (Time(min))	O_2 Activation (°C) (Time(min))	CH_4 Loading (°C) (Time(min))	H_2O -Assisted CH_3OH ext. (°C) (Time(min))
Test #1	150 (~120)	500 (480)	200 (180)	200 (~120)
Test #2	150 (~120)	500 (480)	300 (180)	200 (~120)

The effluent from Test #1 (Table 1) were analysed with a Hewlett Packard 6890/6972 GC-MS. This was equipped with a Supel-Q PLOT capillary column and the carrier gas was He. Analysis was conducted isothermally at 125 °C and the analysis time was 3.5 min. Samples were injected every 4 min and repeated 30 times during extraction. Combined, the chromatography and mass selective detector allow separation and accurate analysis of all relevant components in the effluent. For Test #2 (Table 1), an online Pfeiffer MS was used to analyse the effluent.

4. Conclusions

To summarize, it has been observed that there are large differences in the Cu speciation of the two CHA topology materials - SAPO-34 and SSZ-13 - as observed from XAS, Raman and IR spectroscopies. These differences are due to several important factors. The polarity of the framework, induced by the different framework components, is likely to have a large impact on the location and coordination of the Cu-species. In addition, the multiple Si substitution mechanisms in SAPO-34 affect the amount and distribution of ion exchange sites, leading to fewer Cu-sites in close proximity in SAPO-34 than in SSZ-13. With CH₄-TPR experiments, we supported the hypothesis that SAPO-34 has more isolated Cu-sites, by observing that a higher temperature was needed to oxidize CH₄. By changing the CH₄-loading temperature from 200 to 300 °C we observed more than a tenfold increase in methanol yield from 1 to 12 µmol/g for 0.08CuSAPO-34. These results show that the framework polarity and acid site proximity play an important role for the Cu-speciation. Furthermore, it is evident that the redox properties of the materials are strongly influenced by the Cu-speciation. These results indicate that CH₄-TPR can function as a possible descriptor for the reducibility of the Cu-sites in zeolites, and we suggest that CH₄-TPR will be an important tool in future work for tuning metal-loaded zeolites under different reaction conditions and finding the best suited process for direct conversion of methane to methanol.

Supplementary Materials: The following are available online at <http://www.mdpi.com/2073-4344/10/2/191/s1>, Figure S1: SEM images, Figure S2: PXRD patterns of SAPO-34, Figure S3: PXRD patterns of Cu-SAPO-34, Figure S4: CO₂ production from CH₄-TPR. Table S1: physicochemical characterization, Table S2: Raman spectroscopy assignments.

Author Contributions: Testing, Cu-exchange, standard characterization, K.K., D.K.P., M.D.; spectroscopy measurements and writing of original draft, K.K.; Collection of XAS data, K.A.L.; Analysis of XAS data, E.B.; Data analysis and interpretation, K.K., C.B., S.B., G.B., B.A., M.S., D.K.P., M.D., E.B.; Review and editing, M.S., E.B., K.A.L., S.B., B.A., S.S.; Supervision and funding acquisition, P.B., U.O., S.S. All authors have read and agreed to the published version of the manuscript.

Funding: This publication forms a part of the iCSI (industrial Catalysis Science and Innovation) Centre for Research-based Innovation, which receives financial support from the Research Council of Norway under contract no. 237922. A.L. and C.B. acknowledges the Research Council of Norway for financial support (FRINATEK Toppforsk Grant no. 250795 CONFINE).

Acknowledgments: Anna Lind, SINTEF, is acknowledged for preparing the as-synthesized SAPO-34 material. Andrea Lazzarini (A.L.) is acknowledged for support in the collection of IR spectra.

Conflicts of Interest: The authors declare no conflict of interest.

References

1. Schwach, P.; Pan, X.; Bao, X. Direct Conversion of Methane to Value-Added Chemicals over Heterogeneous Catalysts: Challenges and Prospects. *Chem. Rev.* **2017**, *117*, 8497–8520. [[CrossRef](#)] [[PubMed](#)]
2. Park, M.B.; Park, E.D.; Ahn, W.-S. Recent Progress in Direct Conversion of Methane to Methanol Over Copper-Exchanged Zeolites. *Front. Chem.* **2019**, *7*, 1–7. [[CrossRef](#)] [[PubMed](#)]
3. McFarland, E. Unconventional Chemistry for Unconventional Natural Gas. *Science* **2012**, *338*, 340. [[CrossRef](#)] [[PubMed](#)]
4. Zero Routine Flaring by 2030. Available online: <http://www.worldbank.org/en/programs/zero-routine-flaring-by-2030#1> (accessed on 8 January 2019).
5. The Many Uses of Methanol—From Clothing to Fuel. Available online: <https://www.mgc.co.jp/eng/rd/technology/methanol.html> (accessed on 31 January 2020).
6. Fleisch, T.H.; Basu, A.; Sills, R.A. Introduction and advancement of a new clean global fuel: The status of DME developments in China and beyond. *J. Nat. Gas Sci. Eng.* **2012**, *9*, 94–107. [[CrossRef](#)]
7. Semelsberger, T.A.; Borup, R.L.; Greene, H.L. Dimethyl ether (DME) as an alternative fuel. *J. Power Sources* **2006**, *156*, 497–511. [[CrossRef](#)]
8. Bjorck, C.E.; Dobson, P.D.; Pandhal, J. Biotechnological conversion of methane to methanol: Evaluation of progress and potential. *Environ. Sci.* **2018**, *5*, 1–38. [[CrossRef](#)]

9. Sushkevich, V.L.; Palagin, D.; Ranocchiari, M.; van Bokhoven, J.A. Selective Anaerobic Oxidation of Methane Enables Direct Synthesis of Methanol. *Science* **2017**, *356*, 523–527. [[CrossRef](#)] [[PubMed](#)]
10. Alayon, E.M.; Nachttegaal, M.; Ranocchiari, M.; van Bokhoven, J.A. Catalytic conversion of methane to methanol over Cu-mordenite. *Chem. Commun.* **2012**, *48*, 404–406. [[CrossRef](#)] [[PubMed](#)]
11. Grundner, S.; Markovits, M.A.; Li, G.; Tromp, M.; Pidko, E.A.; Hensen, E.J.; Jentys, A.; Sanchez-Sanchez, M.; Lercher, J.A. Single-site trinuclear copper oxygen clusters in mordenite for selective conversion of methane to methanol. *Nat. Commun.* **2015**, *6*, 7546. [[CrossRef](#)] [[PubMed](#)]
12. Grundner, S.; Luo, W.; Sanchez-Sanchez, M.; Lercher, J.A. Synthesis of Single-Site Copper Catalysts for Methane Partial Oxidation. *Chem. Commun.* **2016**, *52*, 2553–2556. [[CrossRef](#)] [[PubMed](#)]
13. Tomkins, P.; Mansouri, A.; Bozbag, S.E.; Krumeich, F.; Park, M.B.; Alayon, E.M.; Ranocchiari, M.; van Bokhoven, J.A. Isothermal Cyclic Conversion of Methane into Methanol over Copper-Exchanged Zeolite at Low Temperature. *Angew. Chem. Int. Ed.* **2016**, *55*, 5467–5471. [[CrossRef](#)]
14. Pappas, D.K.; Borfecchia, E.; Dyballa, M.; Pankin, I.A.; Lomachenko, K.A.; Martini, A.; Signorile, M.; Teketel, S.; Arstad, B.; Berlier, G.; et al. Methane to Methanol: Structure-Activity Relationships for Cu-CHA. *J. Am. Chem. Soc.* **2017**, *139*, 14961–14975. [[CrossRef](#)]
15. Wulfers, M.J.; Teketel, S.; Ipek, B.; Lobo, R.F. Conversion of methane to methanol on copper-containing small-pore zeolites and zeotypes. *Chem. Commun.* **2015**, *51*, 4447–4450. [[CrossRef](#)] [[PubMed](#)]
16. Groothaert, M.H.; Smeets, P.J.; Sels, B.F.; Jacobs, P.A.; Schoonheydt, R.A. Selective oxidation of methane by the bis(μ -oxo)dicopper core stabilized on ZSM-5 and mordenite zeolites. *J. Am. Chem. Soc.* **2005**, *127*, 1394–1395. [[CrossRef](#)] [[PubMed](#)]
17. Woertink, J.S.; Smeets, P.J.; Groothaert, M.H.; Vance, M.A.; Sels, B.F.; Schoonheydt, R.A.; Solomon, E.I. A $[\text{Cu}_2\text{O}]^{2+}$ Core in Cu-ZSM-5, the Active Site in the Oxidation of Methane to Methanol. *Proc. Natl. Acad. Sci. USA* **2009**, *106*, 18908–18913. [[CrossRef](#)] [[PubMed](#)]
18. Dyballa, M.; Pappas, D.K.; Kvande, K.; Borfecchia, E.; Arstad, B.; Beato, P.; Olsbye, U.; Svelle, S. On How Copper Mordenite Properties Govern the Framework Stability and Activity in the Methane-to-Methanol Conversion. *ACS Catal.* **2019**, *9*, 365–375. [[CrossRef](#)]
19. Pappas, D.K.; Martini, A.; Dyballa, M.; Kvande, K.; Teketel, S.; Lomachenko, K.A.; Baran, R.; Glatzel, P.; Arstad, B.; Berlier, G.; et al. The Nuclearity of the Active Site for Methane to Methanol Conversion in Cu-Mordenite: A Quantitative Assessment. *J. Am. Chem. Soc.* **2018**, *140*, 15270–15278. [[CrossRef](#)]
20. Sushkevich, V.L.; Smirnov, A.V.; van Bokhoven, J.A. Autoreduction of Copper in Zeolites: Role of Topology, Si/Al Ratio, and Copper Loading. *J. Phys. Chem. C* **2019**, *123*, 9926–9934. [[CrossRef](#)]
21. Sushkevich, V.L.; van Bokhoven, J.A. Methane-to-Methanol: Activity Descriptors in Copper-Exchanged Zeolites for the Rational Design of Materials. *ACS Catal.* **2019**, *9*, 6293–6304. [[CrossRef](#)]
22. Ravi, M.; Sushkevich, V.L.; Knorpp, A.J.; Newton, M.A.; Palagin, D.; Pinar, A.B.; Ranocchiari, M.; van Bokhoven, J.A. Misconceptions and challenges in methane-to-methanol over transition-metal-exchanged zeolites. *Nat. Catal.* **2019**, *2*, 485–494. [[CrossRef](#)]
23. Lomachenko, K.A.; Martini, A.; Pappas, D.K.; Negri, C.; Dyballa, M.; Berlier, G.; Bordiga, S.; Lamberti, C.; Olsbye, U.; Svelle, S.; et al. The impact of reaction conditions and material composition on the stepwise methane to methanol conversion over Cu-MOR: An operando XAS study. *Catal. Today* **2019**, *336*, 99–108. [[CrossRef](#)]
24. Borfecchia, E.; Pappas, D.K.; Dyballa, M.; Lomachenko, K.A.; Negri, C.; Signorile, M.; Berlier, G. Evolution of active sites during selective oxidation of methane to methanol over Cu-CHA and Cu-MOR zeolites as monitored by operando XAS. *Catal. Today* **2019**, *333*, 17–27. [[CrossRef](#)]
25. Olsbye, U.; Svelle, S.; Bjørgen, M.; Beato, P.; Janssens, T.V.W.; Joensen, F.; Bordiga, S.; Lillerud, K.P. Conversion of Methanol to Hydrocarbons: How Zeolite Cavity and Pore Size Controls Product Selectivity. *Angew. Chem. Int. Ed.* **2012**, *51*, 5810–5831. [[CrossRef](#)]
26. Cortés-Reyes, M.; Finocchio, E.; Herrera, C.; Larrubia, M.A.; Alemany, L.J.; Busca, G. A study of Cu-SAPO-34 catalysts for SCR of NO_x by ammonia. *Microporous Mesoporous Mater.* **2017**, *241*, 258–265. [[CrossRef](#)]
27. Deka, U.; Juhin, A.; Eilertsen, E.A.; Emerich, H.; Green, M.A.; Korhonen, S.T.; Weckhuysen, B.M.; Beale, A.M. Confirmation of Isolated Cu²⁺ Ions in SSZ-13 Zeolite as Active Sites in NH₃-Selective Catalytic Reduction. *J. Phys. Chem. C* **2012**, *116*, 4809–4818. [[CrossRef](#)]
28. Fickel, D.W.; Fedeyko, J.M.; Lobo, R.F. Copper Coordination in Cu-SSZ-13 and Cu-SSZ-16 Investigated by Variable-Temperature XRD. *J. Phys. Chem. C* **2010**, *114*, 1633–1640. [[CrossRef](#)]

29. Borfecchia, E.; Beato, P.; Svelle, S.; Olsbye, U.; Lamberti, C.; Bordiga, S. Cu-CHA - a model system for applied selective redox catalysis. *Chem. Soc. Rev.* **2018**, *47*, 8097–8133. [[CrossRef](#)]
30. Pinilla-Herrero, I.; Olsbye, U.; Márquez-Álvarez, C.; Sastre, E. Effect of framework topology of SAPO catalysts on selectivity and deactivation profile in the methanol-to-olefins reaction. *J. Catal.* **2017**, *352*, 191–207. [[CrossRef](#)]
31. Woo, J.; Leistner, K.; Bernin, D.; Ahari, H.; Shost, M.; Zammit, M.; Olsson, L. Effect of various structure directing agents (SDAs) on low-temperature deactivation of Cu/SAPO-34 during NH₃-SCR reaction. *Catal. Sci. Technol.* **2018**, *8*, 3090–3106. [[CrossRef](#)]
32. Vennestrøm, P.N.R.; Katerinopoulou, A.; Tiruvalam, R.R.; Kustov, A.; Moses, P.G.; Concepcion, P.; Corma, A. Migration of Cu Ions in SAPO-34 and Its Impact on Selective Catalytic Reduction of NO_x with NH₃. *ACS Catal.* **2013**, *3*, 2158–2161. [[CrossRef](#)]
33. Ipek, B.; Wulfers, M.J.; Kim, H.; Göttl, F.; Hermans, I.; Smith, J.P.; Booksh, K.S.; Brown, C.M.; Lobo, R.F. Formation of [Cu₂O₂]²⁺ and [Cu₂O]²⁺ toward C–H Bond Activation in Cu-SSZ-13 and Cu-SSZ-39. *ACS Catal.* **2017**, *7*, 4291–4303. [[CrossRef](#)]
34. Chen, P.; Root, D.E.; Campochiaro, C.; Fujisawa, K.; Solomon, E.I. Spectroscopic and Electronic Structure Studies of the Diamagnetic Side-On CuII-Superoxo Complex Cu(O₂)[HB(3-R-5-iPrpz)₃]: Antiferromagnetic Coupling versus Covalent Delocalization. *J. Am. Chem. Soc.* **2003**, *125*, 466–474. [[CrossRef](#)] [[PubMed](#)]
35. Leofanti, G.; Marsella, A.; Cremaschi, B.; Garilli, M.; Zecchina, A.; Spoto, G.; Bordiga, S.; Fiscaro, P.; Berlier, G.; Prestipino, C.; et al. Alumina-supported copper chloride 3. Effect of exposure to ethylene. *J. Catal.* **2001**, *202*, 279–295. [[CrossRef](#)]
36. Giordanino, F.; Vennestrøm, P.N.R.; Lundegaard, L.F.; Stappen, F.N.; Mossin, S.; Beato, P.; Bordiga, S.; Lamberti, C. Characterization of Cu-Exchanged SSZ-13: A Comparative FTIR, UV-Vis, and EPR Study with Cu-ZSM-5 and Cu-beta with Similar Si/Al and Cu/Al Ratios. *Dalton Trans.* **2013**, *42*, 12741–12761. [[CrossRef](#)] [[PubMed](#)]
37. Bordiga, S.; Lamberti, C.; Bonino, F.; Travert, A.; Thibault-Starzyk, F. Probing zeolites by vibrational spectroscopies. *Chem. Soc. Rev.* **2015**, *44*, 7262–7341. [[CrossRef](#)] [[PubMed](#)]
38. Borfecchia, E.; Lomachenko, K.A.; Giordanino, F.; Falsig, H.; Beato, P.; Soldatov, A.V.; Bordiga, S.; Lamberti, C. Revisiting the Nature of Cu sites in the Activated Cu-SSZ-13 Catalyst for SCR reaction. *Chem. Sci.* **2015**, *6*, 548–563. [[CrossRef](#)]
39. Paolucci, C.; Parekh, A.A.; Khurana, I.; Di Iorio, J.R.; Li, H.; Albarracín Caballero, J.D.; Shih, A.J.; Anggara, T.; Delgass, W.N.; Miller, J.T.; et al. Catalysis in a Cage: Condition-Dependent Speciation and Dynamics of Exchanged Cu Cations in SSZ-13 Zeolites. *J. Am. Chem. Soc.* **2016**, *138*, 6028–6048. [[CrossRef](#)]
40. Martins, G.V.A.; Berlier, G.; Bisio, C.; Coluccia, S.; Pastore, H.O.; Marchese, L. Quantification of Brønsted Acid Sites in Microporous Catalysts by a Combined FTIR and NH₃-TPD Study. *J. Phys. Chem. C* **2008**, *112*, 7193–7200. [[CrossRef](#)]
41. Giordanino, F.; Borfecchia, E.; Lomachenko, K.A.; Lazzarini, A.; Agostini, G.; Gallo, E.; Soldatov, A.V.; Beato, P.; Bordiga, S.; Lamberti, C. Interaction of NH₃ with Cu-SSZ-13 Catalyst: A Complementary FTIR, XANES, and XES Study. *J. Phys. Chem. Lett.* **2014**, *5*, 1552–1559. [[CrossRef](#)]
42. Alayon, E.M.C.; Nachtegaal, M.; Bodi, A.; Ranocchiari, M.; van Bokhoven, J.A. Bis(μ-oxo) Versus mono(μ-oxo) Dicopper Cores in a Zeolite for Converting Methane to Methanol: An In Situ XAS and DFT Investigation. *Phys. Chem. Chem. Phys.* **2015**, *17*, 7681–7693. [[CrossRef](#)]
43. Llabrés i Xamena, F.X.; Fiscaro, P.; Berlier, G.; Zecchina, A.; Palomino, G.T.; Prestipino, C.; Bordiga, S.; Giamello, E.; Lamberti, C. Thermal Reduction of Cu²⁺–Mordenite and Re-oxidation upon Interaction with H₂O, O₂, and NO. *J. Phys. Chem. B* **2003**, *107*, 7036–7044. [[CrossRef](#)]
44. Palomino, G.T.; Bordiga, S.; Zecchina, A.; Marra, G.L.; Lamberti, C. XRD, XAS, and IR Characterization of Copper-Exchanged Y Zeolite. *J. Phys. Chem. B* **2000**, *104*, 8641–8651. [[CrossRef](#)]
45. Kaucky, D.; Dědeček, J.I.; Wichterlová, B. Co²⁺ ion siting in pentasil-containing zeolites II. Co²⁺ ion sites and their occupation in ferrierite. A VIS diffuse reflectance spectroscopy study. *Micropor. Mesopor. Mater.* **1999**, *31*, 75–87. [[CrossRef](#)]
46. Gao, F.; Walter, E.D.; Washton, N.M.; Szanyi, J.; Peden, C.H.F. Synthesis and evaluation of Cu/SAPO-34 catalysts for NH₃-SCR 2: Solid-state ion exchange and one-pot synthesis. *Appl. Catal. B* **2015**, *162*, 501–514. [[CrossRef](#)]

47. Alayon, E.M.C.; Nachtegaal, M.; Bodi, A.; van Bokhoven, J.A. Reaction Conditions of Methane-to-Methanol Conversion Affect the Structure of Active Copper Sites. *ACS Catal.* **2014**, *4*, 16–22. [[CrossRef](#)]
48. Mertens, M.M. Synthesis and Use of AEI Structure-Type Molecular Sieves. WO/2009/117186. U.S. Patent 7622417B2, 6 February 2009.
49. Bellet, D.; Gorges, B.; Dallery, A.; Bernard, P.; Pereiro, E.; Baruchel, J. A 1300 K furnace for in situ X-ray microtomography. *J. Appl. Crystallogr.* **2003**, *36*, 366–367. [[CrossRef](#)]
50. Bordiga, S.; Groppo, E.; Agostini, G.; Bokhoven, J.A.V.; Lamberti, C. Reactivity of Surface Species in Heterogeneous Catalysts Probed by In Situ X-ray Absorption Techniques. *Chem. Rev.* **2013**, *113*, 1736–1850. [[CrossRef](#)]
51. Ravel, B.; Newville, M. Athena, Artemis, Hephaestus: Data analysis for X-ray absorption spectroscopy using IFEFFIT. *J. Synchrotron Radiat.* **2005**, *12*, 537–541. [[CrossRef](#)] [[PubMed](#)]



© 2020 by the authors. Licensee MDPI, Basel, Switzerland. This article is an open access article distributed under the terms and conditions of the Creative Commons Attribution (CC BY) license (<http://creativecommons.org/licenses/by/4.0/>).

Supporting Information

Comparing the Nature of the Active Sites in Cu-loaded SAPO-34 and SSZ-13 for the Direct Conversion of Methane to Methanol

Karoline Kvande^{1,*}, Dimitrios K. Pappas¹, Michael Dyballa¹, Carlo Buono¹, Matteo Signorile², Elisa Borfecchia², Kirill A. Lomachenko³, Bjørnar Arstad⁴, Silvia Bordiga², Gloria Berlier², Unni Olsbye¹, Pablo Beato⁵, Stian Svelle¹

¹ Center for Materials Science and Nanotechnology (SMN), Department of Chemistry, University of Oslo, 1033 Blindern, 0315, Oslo, Norway

² Department of Chemistry, NIS Center and INSTM Reference Center, University of Turin, via P. Giuria 7, 10125 Turin, Italy

³ European Synchrotron Radiation Facility, 71 avenue des Martyrs, CS 40220, 38043 Grenoble Cedex 9, France

⁴ SINTEF Industry, Department of Process Technology, Forskningsveien 1, 0373 Oslo, Norway

⁵ Haldor Topsøe A/S, Haldor Topsøes Allé 1, DK-2800 Kgs. Lyngby, Denmark

* Correspondence: karoline.kvande@smn.uio.no (K.K.)

Table of Contents

1	Physico-chemical characterization.....	1
1.1	Elemental and N ₂ -physisorption Measurements.....	1
1.2	Scanning Electron Microscopy (SEM).....	3
1.3	Powder X-ray Diffraction (PXRD).....	3
1.4	CO ₂ production from CH ₄ -TPR.....	5
1.5	Raman Spectroscopy	5
2	References.....	6

1 Physico-chemical characterization

1.1 Elemental and N₂-physisorption Measurements

The results from standard characterization is reported in Table S1. The samples are denoted xCuSSZ-13 and yCuSAPO-34, where x is the Cu/Al ratio and y is the Cu/Si ratio.

Table S1. Elemental composition, such as (Al+P)/Si [Si/Al], Cu/Si [Cu/Al] and Cu content was determined with Energy Dispersive X-ray Spectroscopy (EDX). N₂-adsorption/desorption measurements recorded at -196 °C were used to find the specific surface area (m²/g) and total pore volume (V_T). Thermogravimetric analysis was used to find the water content (%).

Sample	Exchange Method (Cu-salt)	(Al+P)/Si [Si/Al] ^a	Cu/Si [Cu/Al] ^a	Cu ^a ($\mu\text{mol/g}$)	Water content ^b (%)	Specific surface area ^c (m^2/g)	V_T^c (cm^3/g)
0.50Cu SSZ-13	LIE (CuAc ₂)	14.8	0.53	540	18	770	0.334
0.25CuSAPO- 34	LIE (CuAc ₂) (x3) ^d	14.9	0.25	249	18	616	0.294
0.08CuSAPO- 34	LIE (CuAc ₂)	14.9	0.08	87	14	690	0.306

^adetermined by EDX

^bdetermined with TGA

^cdetermined at $p/p_0 = 0.99$

^dThe CuAc₂ solution used in the first round was 0.02 M. For the second and third round, a CuAc₂-solution resulting in a Cu/Si ratio of 0.5 was used (0.008 M).

1.2 Scanning Electron Microscopy (SEM)

Figure S1 shows the SAPO-34 morphology at different distances.

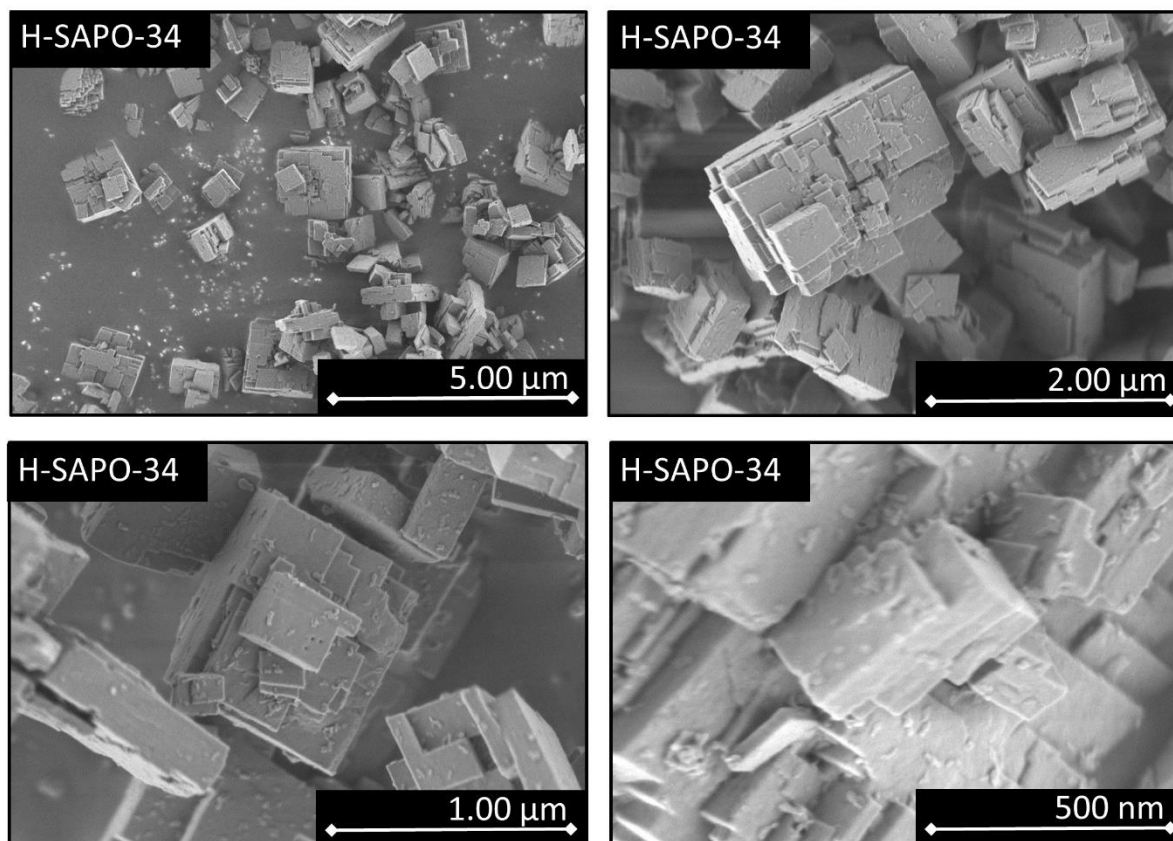


Figure S1. SEM-images of H-SAPO-34 at different distances. The crystals of the copper incorporated SAPO-34 materials were similar to the parent material, and are therefore not included.

1.3 Powder X-ray Diffraction (PXRD)

The PXRD patterns of the template containing and H-form SAPO-34 is reported in Figure S2. In Figure S3, the H-form SAPO-34 pattern is reported together with the Cu exchanged SAPO-34 samples used in this study.

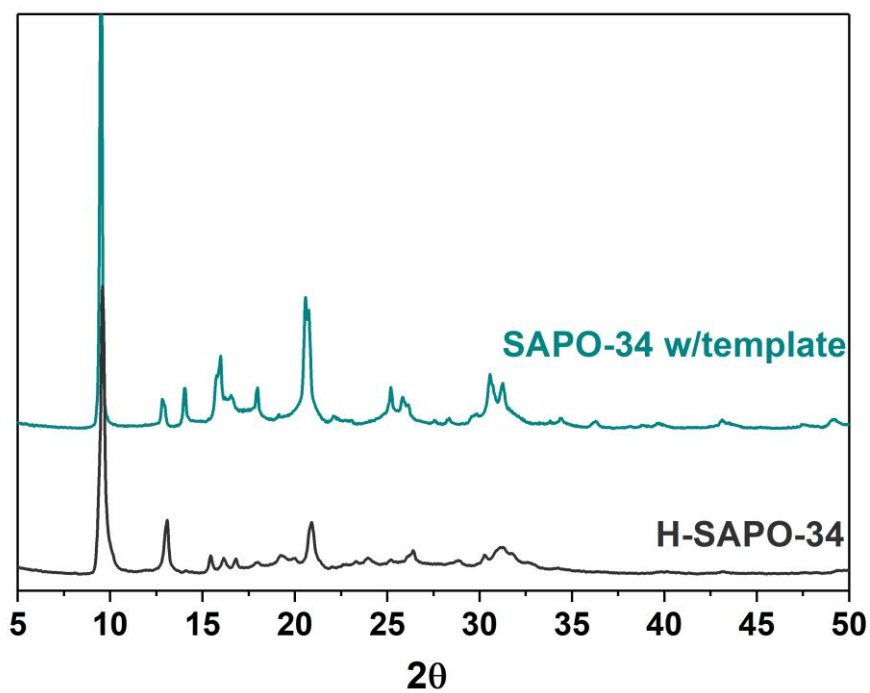


Figure S2. PXRD pattern of the template containing SAPO-34 (turquoise), and the calcined SAPO-34 (black). The patterns are vertically shifted for clarity.

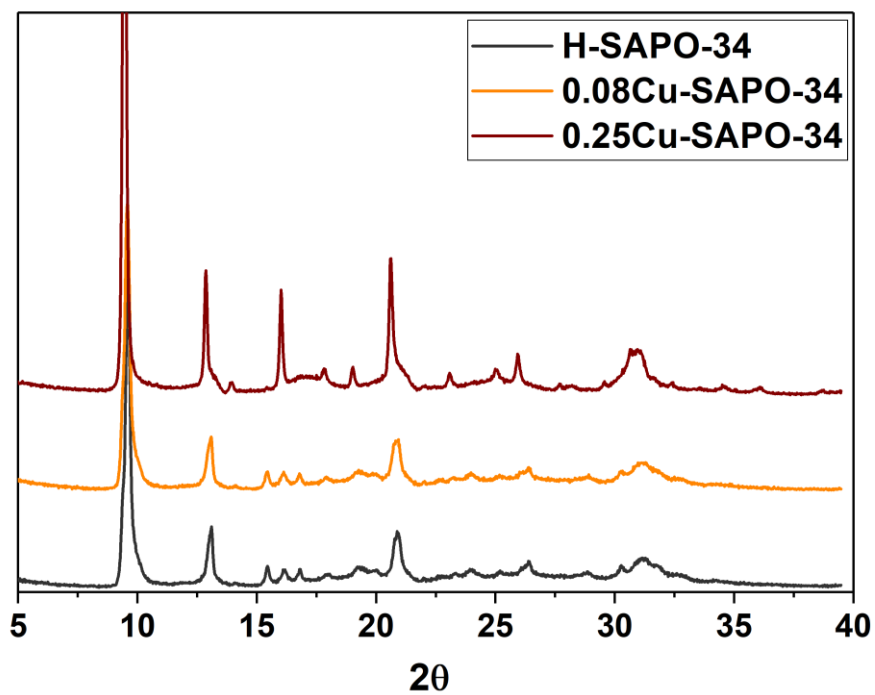


Figure S3. PXRD patterns of the calcined parent material (black) as well as the Cu-exchanged SAPO-34 materials, 0.08CuSAPO-34 (orange) and 0.25CuSAPO-34 (red). The patterns are vertically shifted for clarity.

1.4 CO_2 production from CH_4 -TPR

Figure S4 shows the product detected after fully oxidation of methane over the three Cu-CHA samples tested in this study.

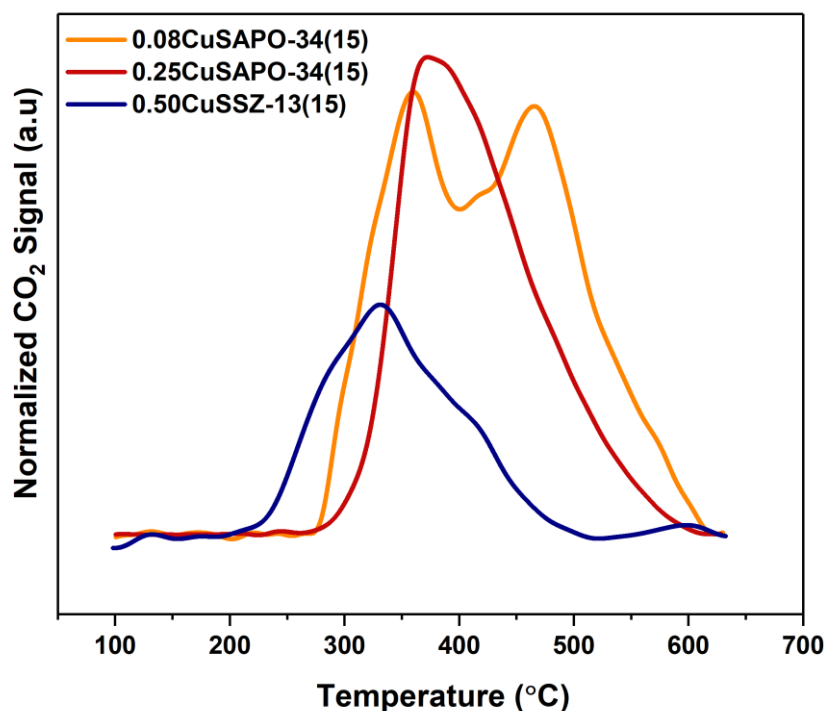


Figure S4. CO_2 production profiles from total oxidation of CH_4 over 0.50CuSSZ-13 (blue), 0.08CuSAPO-34 (orange) and 0.25CuSAPO-34 (red), measured by an online MS during flow of CH_4 while heating from 100 to 650 $^\circ\text{C}$ (ramp: 5 $^\circ\text{C}/\text{min}$). The materials were activated at 500 $^\circ\text{C}$ in O_2 for 8 h prior to the CH_4 -TPR experiment. The profiles have been normalized to the sample weight.

1.5 Raman Spectroscopy

Table S2 is summary of the $\text{Cu}(\text{II})_x\text{O}_y$ species assigned to peaks observed in the Raman spectra.

Table S2. Overview of bands correlating to $\text{Cu}(\text{II})_x\text{O}_y$ species observed in this study, and their comparison to assignments found in literature

SAPO-34	SSZ-13	Coordination	Cu(II) _x O _y -species	Reference
	620	Three-fold	[Cu-(μ-O)-Cu] ²⁺	Ipek et al. [1]
524	510	Three-fold	[Cu(trans-μ-1,2-O ₂)Cu] ²⁺	Pappas et al. [2]
587	580			
812	830			
549		Four-fold	[Cu(η ² -O ₂)] ⁺	Pappas et al. [2]
1006	1100			
	1155	Three-fold	[Cu(η ¹ -O ₂)] ⁺	Woertink et al. [3]

2 References

- Ipek, B.; Wulfers, M. J.; Kim, H.; Göttl, F.; Hermans, I.; Smith, J. P.; Booksh, K. S.; Brown, C. M.; Lobo, R. F., Formation of [Cu₂O₂]²⁺ and [Cu₂O]²⁺ toward C–H Bond Activation in Cu-SSZ-13 and Cu-SSZ-39. *ACS Catal.* **2017**, *7*, 4291-4303. [10.1021/acscatal.6b03005]
- Pappas, D. K.; Borfecchia, E.; Dyballa, M.; Pankin, I. A.; Lomachenko, K. A.; Martini, A.; Signorile, M.; Teketel, S.; Arstad, B.; Berlier, G.; Lamberti, C.; Bordiga, S.; Olsbye, U.; Lillerud, K. P.; Svelle, S.; Beato, P., Methane to Methanol: Structure-Activity Relationships for Cu-CHA. *J. Am. Chem. Soc.* **2017**, *139*, 14961-14975. [10.1021/jacs.7b06472]
- Woertink, J. S.; Smeets, P. J.; Groothaert, M. H.; Vance, M. A.; Sels, B. F.; Schoonheydt, R. A.; Solomon, E. I., A [Cu₂O]²⁺ Core in Cu-ZSM-5, the Active Site in the Oxidation of Methane to Methanol. *Proc. Natl. Acad. Sci. USA* **2009**, *106*, 18908-18913. [10.1073/pnas.0910461106]



Paper II

Microcalorimetry on Cu-MCM-22 reveals structure-activity relationships for the methane-to-methanol reaction

Karoline Kvande^a, Moses Mawanga^b, Sebastian Prodinge^a, Bjørn Gading Solemsli^a, Jia Yang^b, Unni Olsbye^a, Pablo Beato^c, Edd Anders Blekkan^b, and Stian Svelle^{*,a}.

^a Center for Materials Science and Nanotechnology, Department of Chemistry, University of Oslo, 1033 Blindern, 0315 Oslo, Norway

^b Department of Chemical Engineering, Norwegian University of Science and Technology (NTNU), NO-7491, Trondheim, Norway

^c Topsoe A/S, Haldor Topsøes Allé 1, DK-2800 Kgs. Lyngby, Denmark

Corresponding authors:

*stian.svelle@kjemi.uio.no (S.S)

Supporting information for this article is given via a link at the end of the document.

Abstract With a stepwise mechanism for direct methane activation to methanol (MTM) over Cu-zeolites, it is possible to produce methanol with high selectivity. With this study, we apply adsorption/desorption experiments with n-propylamine, NH₃ and CH₄ as powerful techniques to learn more about the acidity and nature of the Cu sites within a hitherto untested material for MTM, namely MCM-22. The Cu-exchanged zeolites have a moderate performance in MTM (~ 0.10 mol_{MeOH}/mol_{Cu}), and upon comparing to the activity of other zeolite frameworks, we use the results found for MCM-22 to search for structure-activity relationships. We show with CO-adsorption FT-IR spectroscopy experiments that there is more than one distinct Cu-site within MCM-22, where one of which is likely linked with inactive Cu species. NH₃ adsorption/desorption experiments disclose that the Brønsted acid sites before Cu exchange are few and heterogeneous in strength, leading to a low number of C-H activating Cu-oxo species.

1. Introduction

As the emissions of fossil carbon and other gases leading to climate change increase, finding improved and more efficient routes for the chemical industry represents a pressing matter. One path would be to utilize more of the natural resources we already are recovering today. One of those under-utilized raw materials is methane. Since gas is expensive to transport from remote areas, finding a path for directly converting methane into a liquid, like methanol, without the need for creating synthesis gas (CO, H₂) would be of great potential for the industry.⁽¹⁾ Several different routes have been suggested over the years, however, one of the more promising was suggested by Groothaert et al. back in 2005.⁽²⁾ They showed that dimeric Cu-oxo species formed in ZSM-5 were able to activate the C-H bond in methane to form methanol. The type of reaction proposed is a cyclic reaction route that involves a high-temperature step in an oxidizer e.g. oxygen at ~ 500 °C forming Cu_xO_y-moieties in the zeolite framework. Methane is then dosed onto the sample at around 200 °C at which point some of the Cu-sites are reduced to Cu⁺ by the formation of methoxy-species. Finally, methanol is extracted by passing steam through the reactor bed. With this method, very high selectivity is achieved because the

stepwise nature of the reaction protocol hinders the gas phase reaction between reactants and products, and hence avoids over-oxidation of the products. Since Groothaert et al., many different Cu-loaded zeolite frameworks have been tested for this reaction, with some of the more promising being MOR,(3-8) CHA,(9,10) FER,(11) FAU,(12) and MAZ.(13) Although many different frameworks have already been tested, there are still unresolved questions regarding the effect of the morphology, acidity, and homogeneity of the ion exchange site on the formation of the active Cu-sites, and hence the material's activity towards methanol. With that in mind, we aimed to investigate MWW, more specifically, MCM-22, a hitherto untested material, for the methane-to-methanol (MTM) reaction. For other reactions, MCM-22 has been tested extensively as a large pore zeolite for methylation reactions.(14,15) MCM-22 has an MWW-type framework with 10-ring pore openings and two independent channels.(16) One channel is a sinusoidal 10-ring channel, while the other consists of layered super cages with 12-ring diameter, interlinked by double 6-rings, and accessible through 10-rings. The channel and cage sizes are not that different from e.g. MOR, FAU, and MAZ zeolites that also have 12-ring pores, and MCM-22 often has properties similar to 12-ring zeolites.(17) However, one main difference is the complexity of the MCM-22 structure, causing the zeolite to have no less than 8 different T-sites, while the others have 4, 1, and 2, respectively. Additionally, MCM-22 has an outer surface that consists of pockets formed by half a super cage. These pockets have been shown to hold some of the catalytic sites of MCM-22.(18)

As the complex structure especially could influence the positioning of the Brønsted acid sites, and by extension the Cu-speciation, it was crucial to assess the acidity of the zeolite, with and without Cu. To that end, NH₃-microcalorimetry, a powerful technique providing information on the heats of adsorption of various acidic sites as well as the adsorption isotherms was applied to study the H- and Cu-MCM-22. Cu-exchanged MCM-22 was synthesized, characterized, and tested for the MTM reaction. Further, CO-adsorption experiments with Fourier transform infrared (FT-IR) and X-ray Absorption spectroscopy was used to assess the nature of the Cu-sites beyond information obtained from basic characterization tools. NH₃- and n-propylamine temperature-programmed desorption (TPD) experiments was then used in comparison to the NH₃-microcalorimetry to investigate the strength and homogeneity of the active sites by comparing Cu- and H-exchanged MCM-22. Lastly, CH₄-calorimetry experiments were attempted to learn more about the C-H activation and adsorption process in that step of the MTM reaction protocol.

2. Results and Discussion

2.1. Material properties of H- and Cu-MCM-22

MCM-22 was synthesized in-house and Cu-exchanged by liquid ion exchange with Cu acetate. To verify that the materials were pure and well exchanged, they were characterized with a suite of different techniques like microwave plasma atomic emission spectroscopy (MP-AES), powder X-ray diffraction (PXRD), scanning electron microscopy (SEM), thermogravimetric analysis (TGA) and N₂-physisorption (For experimental details, see supporting information (SI), section 1.1-1.2). The PXRD pattern of H-MCM-22 was refined against the MWW crystal structure (Figure S1), and the result demonstrated that a pure MCM-22 zeolite crystal structure was retained. In Figure 1 we report the comparison of H-MCM-22 to the Cu-exchanged samples, and no peaks related to larger Cu nanoparticles and agglomerates are observed in the PXRD pattern. The synthesized MCM-22 material had a typical morphology with the crystals growing in the form of small, layered sheets packed together in larger, “rose-like” agglomerates.⁽¹⁹⁾

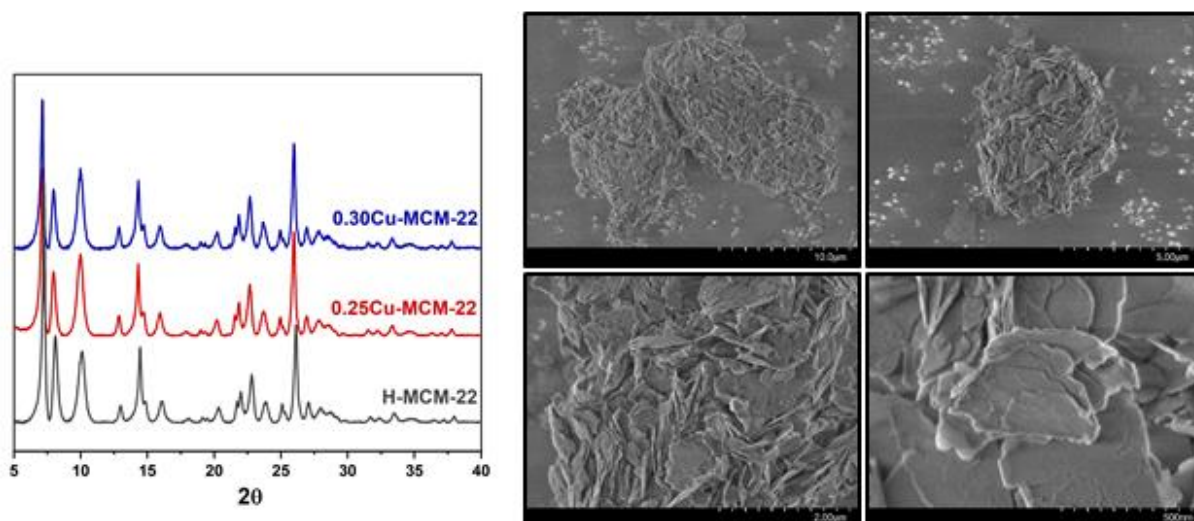


Figure 1. PXRD powder patterns (left panel) of the three MCM-22 samples. The patterns are organized from bottom to top in the order of increasing Cu content. SEM images (right panel) of 0.25Cu-MCM-22. The four images show the crystal agglomerates of 0.30Cu-MCM-22 at different scales.

All physicochemical data are reported in Table 1. For naming the materials, the following code has been applied; xy -MCM-22, where x is the Cu/Al ratio, and y is either H or Cu.

Table 1. Summary of synthesis, characterization, and test results of the different ion-exchanged MCM-22 zeolites discussed herein. The elemental composition was obtained with MP-AES and is reported as Si/Al, Cu/Al, Cu ($\mu\text{mol/g}$), and Cu wt%.

Sample name	Exchange conditions ^a	Elemental analysis			Specific surface area (m^2/g) ^b	Water content (%) ^c	MTM test results		
		Si/Al	Cu/Al	Cu wt.%			Yield ($\mu\text{mol/g}$)	Productivity ($\text{mol}_{\text{MeOH}}/\text{mol}_{\text{Cu}}$)	Selectivity (%)
H-MCM-22	-	15.0	-	-	540	10	-	-	-
0.25Cu-MCM-22	LIE, 0.01	15.2	0.25	1.67	-	10	20	0.08	77
0.30Cu-MCM-22	LIE, 0.02	15.2	0.30	1.98	-	10	27	0.09	76

^aBoth the exchange method and molarity of the exchange solution are indicated here. ^bSpecific surface area is obtained by N_2 -physisorption experiments. ^cWater content obtained by TGA.

2.2. Performance in the methane-to-methanol reaction

The Cu-exchanged MCM-22 materials were, to the best of our knowledge, evaluated herein as hitherto untested materials for the MTM reaction. The reaction protocol is based on an optimized protocol by Pappas et al. on Cu-CHA.(9) The materials are first activated at 500 °C in O_2 (500 °C), cooled to 200 °C, flushed with He (45 min) and exposed to CH_4 (3 h). Then the sample is again flushed with He (45 min), before steam (10 % H_2O in He), at the same temperature, is passed over the material to extract the products. The results from the tests are reported in Table 1. The production of total methanol is given per weight of the sample (yield, $\mu\text{mol/g}$) and per Cu content (productivity, $\text{mol}_{\text{MeOH}}/\text{mol}_{\text{Cu}}$). Selectivity is given in % and reports the amount of total methanol obtained compared to the total effluent measured during the desorption with steam, where the byproduct of the reaction is CO_2 . The yield shows that the sample with the highest Cu content also has the highest methanol activity (27 vs 20 $\mu\text{mol/g}$), however, when comparing the normalized productivity, the samples are much more similar (0.09 vs 0.08). When comparing the values obtained herein to other tested Cu-zeolites for methane to methanol, the values are lower than what is reported when using the same reaction protocol and setup. Depending on the framework, exchange method, Si/Al, and Cu/Al ratio, the productivities previously obtained for Cu-zeolites are in the range of about 0.10 – 0.47.(9,11,20) The selectivity was about 75 % for both samples, which is also in the lower region of what is typically observed with this reaction protocol over other Cu-zeolites.(9,11,20)

Previously, MCM-22 has been shown to be quite active for the methanol-to-olefin (MTO) reaction by exhibiting a high selectivity towards propene.(21) In the MTO mechanism, there are generally two pathways suggested for methylation, a concerted and a stepwise route.(22) The latter leads to the formation of a methoxy intermediate, however, due to the complex channel structure of MCM-22 it is still debatable which of the mechanisms is dominant in this material.(23) A stepwise mechanism could indicate that the material can form and stabilize methoxy species at least on Brønsted sites, which do suggest that the material should be a candidate for the MTM reaction. Since our material characterization presented above

indicate that the materials have been properly synthesized and exchanged with Cu, it became obvious that more investigations were needed to understand the reason for the low methanol production of these materials.

2.3. Employing XAS and FT-IR spectroscopy to study the nature of the Cu-sites

2.3.1. Investigating the oxidized state of Cu after activation

It has previously been shown that a pure Cu^{2+} state is important before methane loading to get the highest MTM performance possible. It was therefore essential to investigate the oxygen-activated state of the Cu-exchanged materials with XAS. In Figure 2, we report the results obtained over activated samples sealed in capillaries. Both the XANES and EXAFS correspond well with an almost pure Cu^{2+} state, as there is no evidence for the spectral features of Cu^+ . A detailed description of the relevant features is reported in SI, section 2.

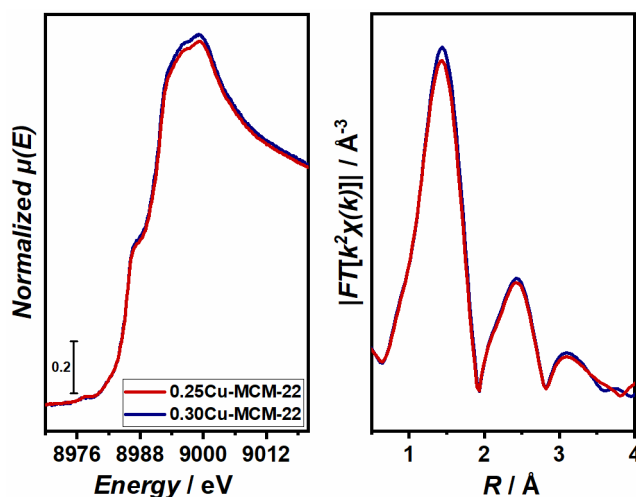


Figure 2. XANES (left panel) and FT-EXAFS (right panel) spectra of the two Cu-exchanged MCM-22 samples, 0.30Cu-MCM-22 (blue) and 0.25Cu-MCM-22 (red). The spectra are obtained at RT on capillaries activated at 500 °C in air overnight and sealed at high temperature.

The spectral features of the two samples investigated are very similar. A slightly higher white line and first shell peak is observed in the XANES and FT-EXAFS spectra for 0.30Cu-MCM-22. This could indicate a marginally higher coordination number around the Cu atoms as well as more uniform bond lengths in this sample. Such trends have previously been suggested to be correlated with higher methanol productivity, however, the difference is so small herein that such a correlation should not be ascertained without a deeper investigation.(24)

2.3.2. CO-adsorption on Cu^+ sites with FT-IR spectroscopy

To understand more about the effect of zeolite structure on the Cu speciation, the samples were first treated by activating in vacuum to induce “self-reduction” of the Cu-sites to Cu^+ ,(25,26) and then probed with CO at RT during FT-IR spectroscopy measurements. This has shown to be a helpful tool in studying the Cu sites of zeolites.(11,27,28) At room temperature, it is only Cu^+ -carbonyl species that are stable enough to be observed in an FT-IR spectrum. In **Figure 3** we show the region of interest ($2250\text{-}2080\text{ cm}^{-1}$) from the experiments. 0.25Cu-MCM-22 can

be seen in **Figure 3** (a), while 0.30Cu-MCM-22 is shown in **Figure 3** (b). 0.30Cu-MCM-22 is the sample with the highest Cu-loading, and slightly higher productivity. Looking at both samples, it is clear that as CO is dosed initially, two bands appear at 2158 and 2151 cm^{-1} . While it is usually only observed one band for Cu^+ -monocarbonyl species in Cu-zeolites, for Cu-loaded MCM-22, two distinct bands are growing.(11,27-29) This has also been seen for Cu-BEA zeolites.(29) The two distinct bands indicate that in MCM-22 there are at least two structurally different Cu-sites, which is coherent with the sample having at least three major positions for Cu to be positioned, namely the sinusoidal 10-ring channel, within the supercage, or on the external surface in the supercage half-cups. Interestingly, at low CO coverage, in 0.30Cu-MCM-22, there seems to be more CO interacting with the Cu species giving rise to the high wavenumber band (2158 cm^{-1}) relative to the band at 2151 cm^{-1} , while in 0.25Cu-MCM-22, the intensities of these bands are more similar. When the CO dosage increases to almost full monolayer coverage (marked by the grey area in **Figure 3**), the opposite trend is observed for the two samples. The fact that the sample with the lowest Cu/Al ratio has a higher band intensity of the high-frequency band at monolayer coverage has also been observed previously by Frolich *et al.*(30) They correlate the high-frequency band to a trigonal planar Cu^+ species coordinated to two framework oxygen and one CO molecule. The low-frequency band, however, is a bit more uncertain, but they suggest it be linked to a higher coordinated Cu species. The authors also observe this band diminish as the temperature is increased, suggesting that the Cu^+ species shift to a trigonal planar configuration. The authors indicate that the low-frequency band is in a more constrained position, possibly at the double 6-ring at the bottom of the supercage, while the high-frequency band is coming from a species situated at the center of the supercage. Interestingly, it has been shown for CHA zeolites that Cu situated in the double 6-ring could lead to inactive Cu-sites for the MTM reaction, where the amount of Cu situated in the double 6-ring depends on the Si/Al and Cu/Al ratio.(9,31) If the low-frequency band is linked to Cu in double 6-rings and this leads to inactive Cu also in MCM-22, this could help explain why the Cu-MCM-22 samples presented here have such a low C-H activation capacity.

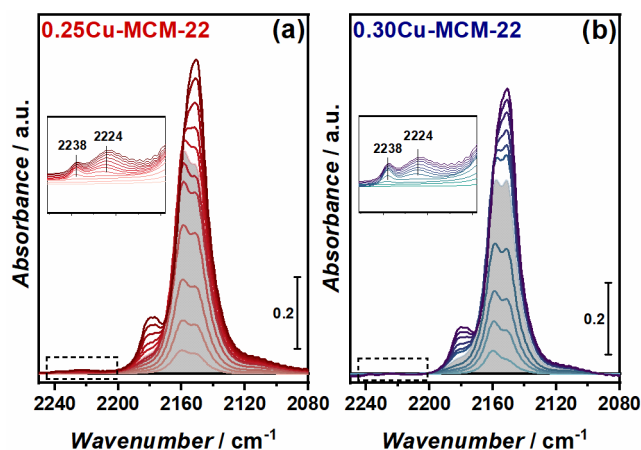


Figure 3. FT-IR spectra of the -CO stretch region after exposure to CO of the two Cu-exchanged MCM-22 samples, 0.30Cu-MCM-22 (blue) and 0.25Cu-MCM-22 (red). The spectra are collected at RT after stabilization of the equilibrium pressure at incremental doses of CO from $\sim 50 \mu\text{bar}$ to 8 mbar. The samples were pre-treated in vacuum at 450 $^{\circ}\text{C}$ (1.5 h). The spectra are background subtracted by dividing on the pre-treated spectra and normalized to the framework overtone, as well as Cu-content. The insets give a closer view of the marked area where the CO vibrations on Al^{3+} are found.

As the CO dosage is increased beyond monolayer coverage, three new bands start appearing corresponding to the symmetric and asymmetric stretches of dicarbonyl species interacting with Cu^+ . The symmetric stretch is observed as two separate bands, corresponding to the two structurally different sites at 2180 and 2176 cm^{-1} . The asymmetric stretch, however, is observed as a small downward shift and merging of the monocarbonyl bands into a more single narrow band at about 2151 cm^{-1} . Few differences are observed for the two samples as the dicarbonyl species are formed suggesting that the availability for dicarbonyl formation is about the same in the two Cu-exchanged samples.

In addition to the typical bands appearing for CO interacting with Cu^+ , there are also two smaller bands appearing at slightly higher wavenumbers (2238 and 2224 cm^{-1}). These bands are positioned at typical energies for CO interacting with extra-framework Al^{3+} (EFAl) sites.(32,33) The observation of these bands suggests that there are some extra-framework Al in the zeolite, which reduce the amount of Brønsted sites able to form in the sample. This could have at least two potential implications on the MTM reaction. First, fewer Brønsted sites could minimize the amount of Cu exchanged in the samples. Indeed, LIE with both 0.01 and 0.02 M $\text{Cu}(\text{OAc})_2$ solution led to very similar amounts of Cu exchanged. Although other methods to increase the Cu exchange was not attempted as higher loadings often lead to Cu clusters and nanoparticles, the similarity between the two materials obtained with different LIE solutions suggests that we have reached a maximum of Cu exchange sites. Secondly, it has been shown that the presence of Brønsted sites is important for stabilizing methoxy intermediates, and if the accessibility to the remaining sites is somewhat blocked by the EFAl, this could both minimize the availability for Cu exchange but also reduce the stabilizing effect of Brønsted acid sites. Based on this, we found it interesting to further investigate the effect of acid site distribution in the MCM-22 framework and by extension its effect on the Cu siting to unravel more about the influence these parameters have on the MTM reaction.

2.4. NH_3 -adsorption microcalorimetry

To study the changes in acidic properties of MCM-22 before and after Cu exchange, NH_3 -adsorption microcalorimetry experiments were performed. NH_3 was initially chosen as the probe molecule since both Brønsted and Lewis acid sites should adsorb the NH_3 molecule. The heat evolved during adsorption should give some insight into the strength of the adsorption site as well as the heterogeneity of the acid sites. The results are reported in Figure 4. In the top panel, we show the differential heat of adsorption (ΔH_{ads}) vs the amount of adsorbed NH_3 , obtained for H-MCM-22 (a), 0.25Cu-MCM-22 (b), and 0.30Cu-MCM-22 (c). Both a primary (solid squares) and a secondary (open triangles) adsorption experiment were performed for all three samples. If we first look at the differential heat of adsorption measured for the Cu-free sample, there are three regions of interest marked with alternating light and dark grey colors. Initially, at very low coverage, there is a strong heat of adsorption (> 160 kJ/mol), which decreases sharply as the coverage increases. This is typically related to strong Lewis acid sites.(34) The second region of interest is a narrow area around $-(150 - 120)$ kJ/mol that should be correlated to a set of homogeneous acid sites like the Brønsted acid sites.(34) The Al concentration of the H-MCM-22 applied herein is about 1.1 mmol/g, and as the second region diminishes already at about 0.25 mmol/g of adsorbed NH_3 , it is evident that the amount of homogeneously strong Brønsted acid sites is lower in this sample, compared to what would be expected from a zeolite with similar Al content. Indeed, this area has previously been reported

to be stable up to at least 0.8 mmol/g in an H-MOR with similar Al content (1.1 mmol/g) as our samples.(35) After the high enthalpy area, we enter the third region, where the heat of adsorption decreases gradually with coverage until the enthalpy for condensation of NH₃ is reached ($\Delta H_c = -23.4$ kJ/mol). This is linked with a set of heterogeneous acid sites,(34) indicating that a large portion of the total amount of Al in the sample is either present as EFAl, as indicated already by FT-IR spectroscopy, or more Brønsted sites with lower heat of adsorption possibly due to lower accessibility.

If we shift our focus onto the Cu-exchanged samples, a few interesting changes are noteworthy. The first and second region of strongly adsorbing sites and Brønsted acid sites seem to be non-existing. However, a broader region of heterogeneous sites is observed in a region of intermediate strength with $\Delta H_{ads} \approx - (120 - 80)$ kJ/mol. This region is observed up to about 0.6 mmol/g of adsorbed NH₃ for 0.25Cu-MCM-22 and almost 0.7 mmol/g for 0.30Cu-MCM-22. The “spikes” or heat fluctuations observed in this region can be speculated to be due to the oxidation of NH₃ from a reaction with the pre-oxidized Cu species. This would release additional heat, and influence the heat of adsorption measured.(36) Such fluctuations have also been observed previously on a different system by Arrigo et al.(37) The oxidation of NH₃ would also lead to some of the Cu-sites being reduced to Cu⁺. Giordanino et al. propose a possible reaction pathway at low temperatures (120 °C) that involves the oxidation of two NH₃ molecules to N₂ and H⁺, and this reaction provides the electrons needed for the reduction of Cu²⁺ to Cu⁺.(38) They further suggest that the reduced Cu sites could interact with NH₃ molecules to form mobile, linear diammine Cu⁺ complexes. The formation of Cu⁺ and the mobility of diammine Cu⁺ complexes would introduce structural rearrangements, which again could influence the differential heats measured during adsorption.

Since the strong Lewis and Brønsted site enthalpy region is non-existing in the Cu-exchanged samples, we conjecture that Cu is exchanged first with the strongest Brønsted sites, as well as a few strong Lewis sites. This is also supported by NH₃-TPD experiments by Chen et al., indicating that the strongest Brønsted sites are consumed in favor of a Cu site of intermediate strength.(39) As discussed above, the number of strong Brønsted acid sites observed herein was found to be much less than e.g. in a MOR with a similar Si/Al ratio. Given the high methanol productivity observed over Cu-MOR zeolites,(24) we conjecture that adequately strong Brønsted sites are needed to form the active Cu-oxo species for MTM. The less strong acid sites likely lead to Cu-species that are either less active or inactive for methanol production. It could be that the Cu species are situated in less accessible positions like the sinusoidal 10-ring, or that the Cu is positioned in the double 6-ring at the bottom of the supercages as conjectured from the FT-IR spectroscopy results. A third possibility is that the Cu is positioned on the outer surface in the half “cups” of the supercage and that there is not enough confinement or available Brønsted sites in these positions for the methoxy intermediates to stabilize on the Cu-sites. This hypothesis is supported by previous studies revealing the half cups to be one of the more likely sites for methylation reactions.(18)

In the third region, below $- 80$ kJ/mol, another interesting phenomenon appears for the NH₃ adsorption over Cu-loaded MCM-22. In the H-form, the sample reaches the NH₃ enthalpy of condensation at about the same amount of NH₃ adsorbed (1.4 mmol/g) as there is Al in the sample (1.1 mmol/g). However, for the Cu exchanged samples, the adsorption continues in this low enthalpy region for up to as much as twice the Al content, reaching an adsorption of 2.3 mmol/g and 2.4 mmol/g for 0.30Cu-MCM-22 and 0.25Cu-MCM-22, respectively. If we expect some NH₃ to still be adsorbed on the remaining Brønsted sites, as observed to still be present in Cu-sample from the OH-region of the FT-IR spectra (Figure S2), the higher amount of NH₃

adsorbed suggests that about three to four NH_3 molecules are adsorbed per Cu site at our adsorption conditions (80°C). This high NH_3 to Cu ratio cannot be explained by the formation of linear Cu^+ complexes ($\text{Z}[\text{Cu}(\text{NH}_3)_2]^+$) alone, and we, therefore, conjecture that a combination of this and a four coordinated Cu^{2+} complex (e.g. $\text{Z}_2[\text{Cu}(\text{NH}_3)_4]^{2+}$) are forming. This is supported in a thermodynamic study over Cu-SSZ-13 by Paolucci et al., where they find that the tetraammine complex, in addition to $\text{Z}[\text{Cu}(\text{NH}_3)_2]^+$, is the most stable species ($\Delta G \approx -90$ kJ/mol) formed at 80°C in an NH_3 atmosphere.(31) Also other forms of the tetraammine complex could exist, where some of the NH_3 ligands are switched out with oxygen-derived species like $-\text{OH}$ groups.(40)

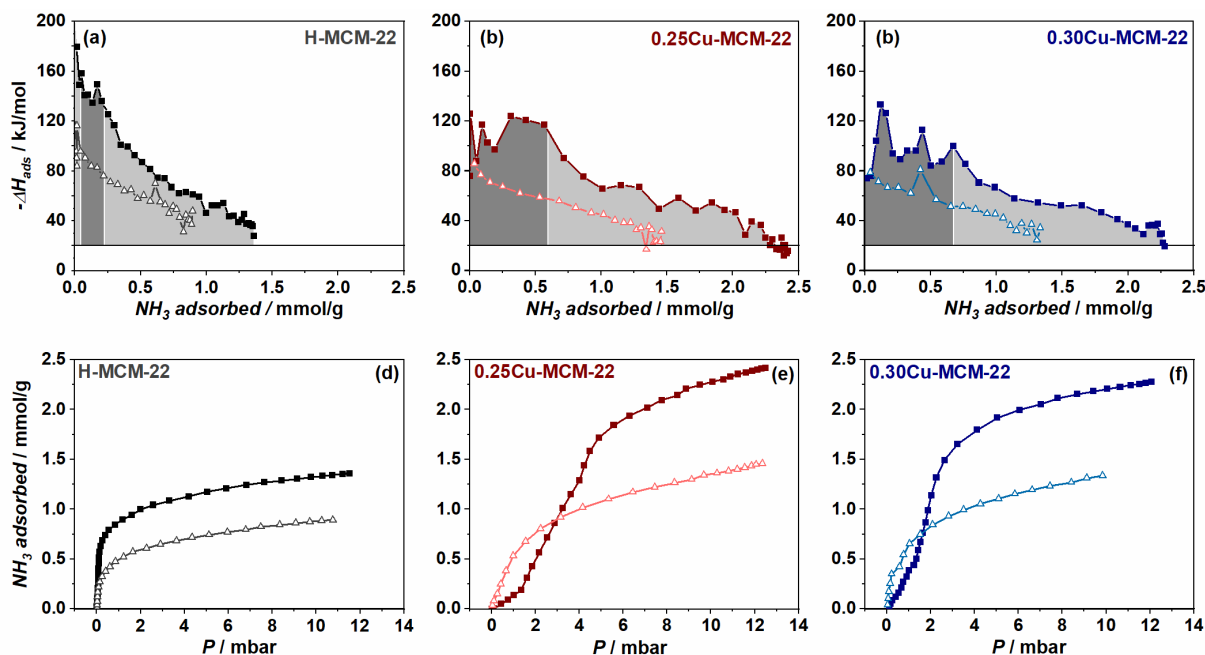


Figure 4. Differential heats of adsorption (a-c) and adsorption isotherms (d-f) for NH_3 on the three MCM-22 samples (a-c). Both primary (dark color, filled symbol) and secondary (light color, open symbol) heat of adsorption curves adsorption isotherms are reported. The differential heats of adsorption (kJ/mol) are plotted against the NH_3 adsorbed in $\mu\text{mol/g}$. The sharp horizontal line is representing the enthalpy for NH_3 condensation. The adsorption isotherms are given as adsorbed NH_3 in $\mu\text{mol/g}$ per absolute pressure (mbar).

In the bottom panel of Figure 4 (d-f), we have reported the ammonia adsorption isotherms, where the coverage of adsorbed ammonia is plotted against the pressure. Both the primary and secondary adsorption are plotted. If we first view the adsorption isotherm for H-MCM-22 (d), the shape suggests that the adsorption follows a typical Langmuir isotherm or an L-shaped isotherm based on the classification by Giles et al.(41) The secondary adsorption has the same shape, however reaching the plateau indicating saturation at less ammonia adsorbed than for the primary. The difference between the primary and secondary adsorption isotherm gives the number of irreversible adsorption sites at 80°C , which is an indication of the density of strong acid sites in the sample, such as Brønsted acid sites and strong Lewis acid sites. The subtracted isotherms for H-MCM-22, 0.25Cu-MCM-22, and 0.30Cu-MCM-22 are plotted in Figure S3. For the Cu-exchanged samples, the primary adsorption isotherm has a peculiar S-shape. An S-shaped isotherm is usually consistent with a scenario where there are two or more competing mechanisms at play during the adsorption.(42) For the two Cu-exchanged samples herein, we conjecture two feasible scenarios. Since NH_3 adsorbs on both H-sites and Cu-sites, and we have seen two distinct Cu-sites from CO-adsorption with FT-IR, the S-shape may come

from a varying site selectivity depending on the coverage.(42) Another scenario arrives from the above observation that NH_3 forms Cu complexes. The slow initial adsorption would then be due to the initial binding and complexation of NH_3 at the strongly adsorbing Cu-sites.(43) Then, as the level of adsorbate increases and the negative effect caused by complex formation subsides, faster adsorption is observed at higher pressures, where also the Brønsted sites are covered. Interestingly, it seems like the negative effect is no longer present for the second isotherm, and the shape is much more similar to the H-MCM-22 sample. Even so, the adsorption amount is still much higher in the Cu samples, which indicates that it is likely both the NH_3 adsorbed to Brønsted sites as well as some of the NH_3 ligands coordinated to Cu that are desorbed during outgassing. Which of the two scenarios explained is occurring would need further investigations beyond the scope of this study, although, it cannot be ruled out that it is a combination of the two.

2.5. The effect of Cu on framework acidity

To further support our findings from NH_3 -calorimetry, we also performed n-propylamine TPD experiments on the three samples. n-Propylamine can be used to solely titrate the Brønsted acid sites of a zeolite due to an acid-catalyzed Hoffmann elimination of chemisorbed n-propylamine that releases propene ($\text{C}_3=$) and NH_3 . The column named “ $\text{C}_3=$ ” in Table 2 gives the total amount of desorbed propene from the reaction. With the total Al in H- and Cu-MCM-22 being about 1.0-1.1 mmol/g, and the quantity of propene observed only 0.46-0.66 mmol/g, we surmise that a large fraction of Al in the samples has to be extra-framework Al^{3+} sites. This is also in line with our microcalorimetry results presented above. The amount of propene desorbed is slightly decreasing from 0.66 mmol/g for the H-MCM-22, as Cu-content increases. Specifically 0.15 and 0.20 mmol/g reduction for 0.25 and 0.30Cu-MCM-22, respectively. This is consistent with Cu exchanging some of the H-sites, however, given that the Cu concentration of the two samples is 0.26 and 0.31 mmol/g, we do speculate that Cu also exchanges some strong EFAl sites like the strongly adsorbing Lewis acid sites observed in the first region of the NH_3 microcalorimetry results (Figure 4). Additionally, some propene could be confined within the zeolite framework or was subjected to undesired side reactions as we have observed to be possible over Cu-zeolites for another study in our lab, and also recently reported by Lashchinskaya et al.(44)

Table 2. Density of acid sites obtained by n-propylamine TPD and NH₃-TPD together with the irreversible NH₃ adsorbed measured with calorimetry. The Al and Cu content is also reported for comparison.

Sample name	Al	Cu	Acid site concentration from n-propylamine TPD	Acid site concentration from NH ₃ TPD	Irreversible NH ₃ adsorption from calorimetry
	concentration (mmol/g)	concentration (mmol/g)	C ₃₌ (mmol/g)	NH ₃ (mmol/g)	NH ₃ (mmol/g)
H-MCM-22	1.07	-	0.66	0.57	0.44
0.25Cu-MCM-22	1.03	0.26	0.51	0.64	0.82
0.30Cu-MCM-22	1.03	0.31	0.46	0.76	0.84

NH₃ TPD was also employed as NH₃ can titrate both the Lewis and Brønsted acid sites in the samples and should be comparable to the results from the microcalorimetry experiment (last two columns of Table 2). The NH₃ desorption (TPD) and adsorption (microcalorimetry) values reported are in the range of 0.57 – 0.76 and 0.44 – 0.84 mmol/g, respectively. The values are a bit low considering the Al content (~1.1 mmol/g), although in the same range and following the same trend as the values obtained from measuring the irreversible NH₃ adsorption with NH₃ calorimetry. The amount of NH₃ desorbed during the TPD experiments indicates that the total density of acid sites (Brønsted and Lewis) increases with increasing Cu content. As one Cu-site (Lewis site) would substitute either one or two Brønsted sites, there has to be something extra that contributes to the increased acid density. We surmise that the increased irreversibly adsorbed NH₃ in the Cu-zeolites compared to the H-form is coherent with Cu-sites forming Cu-ammine complexes that are strongly adsorbing, as described above. We also observe that more NH₃ is measured with NH₃ calorimetry compared to TPD. We attribute this to a higher quantity of more weakly adsorbed sites and possibly more Cu-ammine complexes remaining after outgassing at 80 °C (between the primary and secondary adsorption), compared to the amount remaining after flushing at 170 °C in He before the TPD experiment.

Lastly, it is also of interest to point out the peak desorption temperatures during the NH₃-TPD experiments. As reported in Figure 5, the H-MCM-22 sample has a broad peak (maximum at 350 °C) assigned to Brønsted acid sites. Note, the broad nature of the peak is in line with the heterogeneity of acid site strengths first observed with NH₃ calorimetry on the H-form. The two Cu exchanged samples, however, have three major peaks, specifically at 275, 350, and 450 °C. This is similar to what has been observed on a set of Cu-loaded MCM-22 materials previously by Chen et al.(39) The peak at 350 °C reduces with increasing Cu-loading, supporting that this desorption temperature is linked with Brønsted acid sites. Based on the discussion above, we infer that the other two peaks come from NH₃ molecules being desorbed from the Z[Cu(NH₃)₂]⁺ and Z₂[Cu(NH₃)₄]²⁺ complexes residing after adsorption. According to the phase diagram reported by Paolucci et al. on Cu-SSZ-13,(31) and *in situ* XAS TPD experiments by Borfecchia et al.,(40) we surmise that the low-temperature peak is from NH₃ desorbing from tetraammine derived complexes. This peak is stronger in the 0.30Cu-MCM-22, which indicates that a higher concentration of Cu leads to more sites available for tetraammine complexation. As this requires more space, we could presume that this site is more easily accessible than the site forming

diammine complexes. The broad high-temperature peak is likely to come from Cu sites with different strengths, however stronger than Brønsted acid sites. This correlates well with species desorbing from both the diamine and tetraammine complexes.(31)

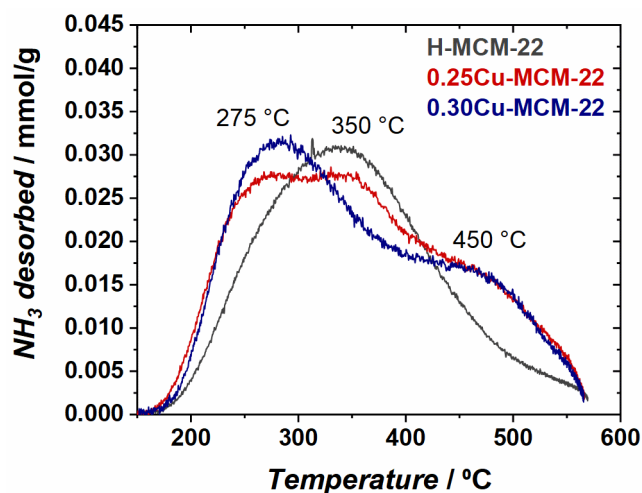


Figure 5. NH₃-TPD profiles of H-MCM-22, 0.25Cu-MCM-22 and 0.30Cu-MCM-22.

2.6. Preliminary microcalorimetry experiments with CH₄

Thus far, the results reported herein indicate that Cu introduces some stronger adsorption sites to the zeolite, and we could hypothesize that it is the effect of these in addition to the redox capability that leads to selective methanol production from methane. As an additional experiment to broaden the scope of microcalorimetry experiments and obtain results that were directly applicable to the MTM reaction, we attempted microcalorimetry experiments with CH₄ at 300 °C to be close to the temperatures for methane activation in the MTM reaction. The results obtained for 0.30Cu-MCM-22 are reported in Figure 6, where (a) gives the adsorption isotherm, and (b) gives the corresponding heat of adsorption measured. The adsorption isotherm appears to be a straight line up to as much as 80 mbar of CH₄, with no apparent adsorption or effect from the partitioning of CH₄ when interacting with the zeolite confinement. Additionally, as observed in Figure 6 (b), where the adsorption heat appears close to – 5 kJ/mol for the entire adsorption experiment, there are no signs of CH₄ oxidation on the Cu sites. In an earlier CH₄ microcalorimetry experiment by Yang et al.,(45) it was shown that the differential heat for CH₄ adsorption lay around 28 - 14 kJ/mol, depending on the H-zeolite. The values were constant with coverage, similar to what we observe herein. However, they observed slightly stronger heats of adsorption, possibly due to the lower temperature of their experiments (– 63.15 °C), which was done to obtain close to complete filling of the pores and cavities, leading to stronger interactions. The CH₄ adsorption experiment reported here gives a picture of how weak the adsorption interaction of CH₄ is with Cu-zeolites at the temperature of CH₄ exposure in MTM, and could perhaps explain why only some types of Cu_xO_y-moieties can activate CH₄ in zeolites.(46) The results also indicate why it is easier to utilize more Cu_xO_y-sites with a higher methane loading pressure (8-37 bar), as previously reported.(7,12,47-49)

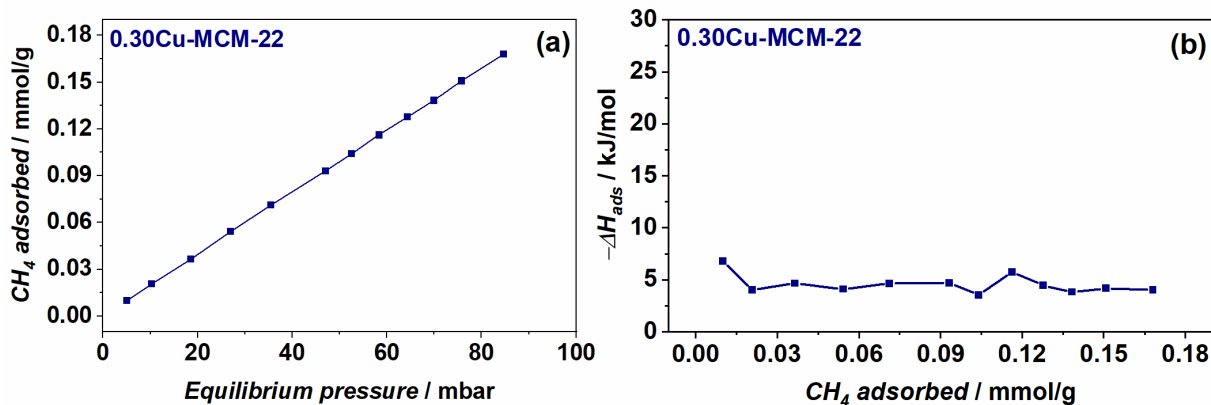


Figure 6. Differential heats of adsorption (a) and adsorption isotherm (b) for CH₄ over 0.30Cu-MCM-22. The adsorption isotherm is given as adsorbed CH₄ in μmol/g per equilibrium pressure (mbar). Differential heats of adsorption (kJ/mol) are plotted against the CH₄ adsorbed in μmol/g.

3. Conclusions

This study investigated Cu-loaded MCM-22 as a hitherto unexplored material for the methane-to-methanol reaction. The results suggested that the material was, indeed, able to form methanol from methane. To understand the impact of this unexplored zeolite structure on the methanol productivity, a deeper study of the material properties was executed. With the help of methods like SEM imaging, PXRD, and XAS on O₂-activated samples, we showed that the Cu-zeolites had no discernible nanoparticles and that the Cu ions were well-distributed and redox-active. This suggested that the more moderate activity towards methanol compared to other zeolite systems was not a result of improper zeolite synthesis or ion exchange. It rather had to be connected with the Cu-speciation, and we, therefore, needed to study the possible implications from the framework topology on the Cu-speciation. To that end, CO-adsorption coupled with FT-IR spectroscopy, NH₃-calorimetry, n-propylamine- and NH₃-TPD experiments were applied as these were methods that gave comparable information about the cationic sites. We show that there are few homogeneously strong Brønsted acid sites in MCM-22 before Cu exchange and that these strong Brønsted sites are likely the sites leading to a Cu-oxo speciation available for C-H activation. CO-adsorption with FT-IR also reveals that there are at least two distinctly different ion exchange sites for Cu, where one is presumably linked with inactive Cu species in a double 6-ring at the bottom of the supercage. Combined, we hypothesize that the complex structure of MCM-22 led to few sites where all the requirements needed for selective C-H activation were present. Among the Cu-sites formed, a significant concentration was either inactive, inaccessible to methane, or unable to stabilize reaction intermediates. Furthermore, as a preliminary study, a CH₄-calorimetry experiment also revealed that CH₄ interaction is very weak (low heat of adsorption), unraveling some of the reasons behind why specific Cu_xO_y-sites are needed to activate CH₄. This study has shown that adequately strong acid sites before Cu-exchange are important to form the active sites for methane activation to methanol. For MCM-22, the lack of such sites is connected with the zeolite topology and forms an additional contribution towards the search for optimal structures in the MTM reaction and for other C-H activation reactions.

4. Experimental details

4.1. Performance measurements

All MTM tests were performed on a purpose-designed setup previously used for the MTM reaction.^(9,11,24,28) 100 mg of sample was weighed, sieved (425 – 250 μm) and placed in a linear quartz tube reactor (i.d. = 6 mm). A thermocouple inside the oven was used to control the temperature. The temperature setpoints were calibrated prior to the experiments by placing a thermocouple inside a quartz sheet touching a reactor bed while following a full protocol. A stepwise protocol was applied for the experiments. The gases were kept separate with the help of different MFCs for each gas, stop- and 4-way valves. The following protocol was applied: The sample was first activated in 15 ml/min O_2 (100%) at 500 $^\circ\text{C}$ (8 h). Then the temperature was lowered (5 $^\circ\text{C}/\text{min}$) to 200 $^\circ\text{C}$, and He (100 %) was sent onto the sample (45 min) to flush the system. Then CH_4 (100 %) was sent onto the sample (3 h), before a second flushing step in He (45 min) was initiated. Finally, a Ne/He (10 %/rest) flow saturated with 10 % water was sent onto the sample (2 h). An online quadrupole mass spectrometer (Ominstar GSD320, Pfeiffer) was connected to the outlet of the reactor to analyze the effluent. The quantitative analysis of the products (MeOH ($m/z = 31$), DME ($m/z = 46$) and CO_2 ($m/z = 44$)) in $\mu\text{mol}/\text{g}$ was obtained with the help of an external calibration bottle with known amounts of the products. The methanol yield is reported herein as $\text{MeOH} + 2\text{xDME}$.

4.2. X-ray absorption spectroscopy (XAS)

X-ray absorption spectroscopy (XAS) experiments were performed at RT on pre-sealed capillaries (i.d. = 1.5 mm, thickness = 0.1 μm) at the Balder beamline at MAX IV in Lund, Sweden. The samples were pretreated in open capillaries at 500 $^\circ\text{C}$ in air overnight and sealed at high temperature before being cooled to RT. A Si(111) double-crystal monochromator was employed, and the monochromator was calibrated against a pre-measured Cu-foil. Cu K-edge spectra of the Cu-exchanged materials were collected in transmission mode, and ionization chambers were used for detection. The EXAFS scans were acquired in the 8795 – 9730 eV range, with an acquisition time of 3 min/scan. 6 scans were accumulated and merged by averaging the $\mu(E)$ curves during analysis for better quality. 2 XANES scans per sample were acquired separately in the 8815 – 9175 eV range, with an acquisition time of 45 s/scan. The XANES scans were also merged for better data quality. For analysis, all XAS spectra were normalized to unity edge jump, and afterwards aligned in energy with the help of Athena software from the Demeter package.⁽⁵⁰⁾ By using the Athena program, the $\chi(k)$ and EXAFS functions were extracted, and the Fourier-Transform (FT) EXAFS spectra were obtained by transforming the $k^2 \chi(k)$ functions in the range of 2.4 – 10.0 \AA^{-1} .

4.3. CO-adsorption coupled with Fourier transform infrared (FT-IR) spectroscopy

CO-adsorption experiments on the Cu-exchanged samples were performed at RT, and measured on a Bruker Vertex 70 instrument, equipped with a Mercury-Cadmium-Telluride (MCT) detector. A thin, self-supporting wafer ($\sim 10 \text{ mg}/\text{cm}^2$) of each sample was prepared and fitted inside a gold envelope. The envelope was placed in a low temperature vacuum cell with KBr windows before being ramped up (5 $^\circ\text{C}/\text{min}$) to 450 $^\circ\text{C}$ and kept for 1.5 h. After being cooled to RT, incremental amounts of CO were dosed onto the sample, while an IR spectrum were collected after every dose, until reaching the equilibrium pressure of about 8 mbar.

4.4. Adsorption Microcalorimetry (NH₃- and CH₄-adsorption)

The adsorption of ammonia was carried out in a stepwise fashion. Small doses of ammonia were introduced to the sample placed in a quartz calorimetric cell maintained at 80 °C. The adsorption microcalorimetry setup comprised of manometric adsorption apparatus (with a dynamic vacuum of 10⁻⁵ mbar) coupled with a Tian-Calvet type heat flow calorimeter (Setaram C80, sensitivity 0.1 μW resolution). The setup measures the adsorption isotherms and enthalpies of adsorption simultaneously using stepwise introduction of the gas to the sample. A capacitance manometer (MKS Baratron 670A, range 0-10 Torr) was used to achieve pressure measurements. Heat flow signal observed upon introduction of gas to the sample was allowed to return to the baseline before introduction of subsequent dose. Integration of the heat flow signal was performed using Calisto v1.066 AKTS-Setaram software.

Prior to each adsorption experiment, the samples were pretreated and activated following the following protocol. Typically, 0.2-0.3 g of sample was placed in the calorimetric cell. The sample was dried in argon at 160 °C for 1-3 hours, followed by a temperature ramp in pure oxygen at 5 °C min⁻¹ to 500 °C. The sample was held at 500 °C for 480 minutes before cooling to 200 °C in oxygen flow. Once at 200 °C the flow was switched back to argon for 60 minutes and later cooled to room temperature and isolated from external atmosphere to avoid exposing the activated sample to atmospheric humidity. The sample containing cell was transferred to the calorimeter, well maintained at 80 °C, and outgassed to a dynamic vacuum of 10⁻⁸ mbar until a stable baseline was achieved. Successive micromolar doses of NH₃ were introduced to the sample until the sample became saturated (i.e., no noticeable changes in the heat flow signal with more doses). Between the primary and secondary adsorption, the sample was outgassed at 80 °C for ~10 h until the heat flow curve returned to baseline.

The same protocol was followed for CH₄ adsorption, except that the adsorption temperature was set to 300 °C.

4.5. Temperature programmed desorption (TPD) experiments

n-Propylamine-temperature programmed desorption (TPD) experiments to study the amount of Brønsted acid sites of both the protonic and Cu-exchanged material were performed on a home-made flow set-up. The effluent from the desorption was detected by an online Pfeiffer Omnistar quadrupole mass spectrometer. About 30 mg of sample was activated in a flow of synthetic air (50 ml/min) for 1 h at 500 °C (ramp rate = 10 °C/min). The sample was then cooled to 170 °C before exposed to N₂ gas flow (50 mL/min) saturated with n-propylamine vapors for 1 h. All excess n-propylamine was flushed from the system with N₂ (66 ml/min, 4 h), before the desorption protocol was initiated (ramping 10 °C/min in 66 ml/min N₂ up to 500 °C). The total amount of propene (m/z = 41) released from the system was quantified using a calibration gas that was sent into the system at the end of the experiment.

NH₃-TPD was performed on ca. 30 mg pelletized protonic and Cu-exchanged zeolite in a comparable manner to the n-propylamine-TPD. After an initial activation step in synthetic air, the sample kept at 170 °C was exposed to 2% NH₃ in N₂ (50 ml/min) for 4h. This was followed by flushing in inert N₂ (66 ml/min) for 4h before heating to 575 °C (10 °C/min) in N₂. The amount of NH₃ released (m/z = 16) was quantified using the calibrant 2% NH₃ in N₂ upon stabilizing at the end of the adsorption step.

Acknowledgment

This publication forms a part of the iCSI (industrial Catalysis Science and Innovation) Centre for Research-based Innovation, which receives financial support from the Research Council of Norway under contract no. 237922. M. Sørensen is acknowledged for his work synthesizing the as-made MCM-22. E. Borfecchia is acknowledged for her valuable insight and support in interpreting the XAS results. We acknowledge MAX IV Laboratory for time on Beamline Balder under Proposal 20190347. Research conducted at MAX IV, a Swedish national user facility, is supported by the Swedish Research council under contract 2018-07152, the Swedish Governmental Agency for Innovation Systems under contract 2018-04969, and Formas under contract 2019-02496. The staff at Balder, M. Ciambezi, J. Just and K. Klementiev, is acknowledged for their help and support during our experiment.

Keywords

C-H activation, MCM-22, Cu, microcalorimetry, TPD

Supporting Information

Insert link here...

References

1. Lunsford, J. H. Catalytic conversion of methane to more useful chemicals and fuels: a challenge for the 21st century. *Catal. Today*. **2000**, 63, 165-174, DOI: [https://doi.org/10.1016/S0920-5861\(00\)00456-9](https://doi.org/10.1016/S0920-5861(00)00456-9)
2. Groothaert, M. H., Smeets, P. J., Sels, B. F., Jacobs, P. A. and Schoonheydt, R. A. Selective oxidation of methane by the bis(μ -oxo)dicopper core stabilized on ZSM-5 and mordenite zeolites. *J. Am. Chem. Soc.* **2005**, 127, 1394-1395, DOI: 10.1021/ja047158u
3. Sushkevich, V. L., Palagin, D., Ranocchiari, M. and van Bokhoven, J. A. Selective Anaerobic Oxidation of Methane Enables Direct Synthesis of Methanol. *Science*. **2017**, 356, 523-527, DOI: 10.1126/science.aam9035
4. Alayon, E. M., Nachtegaal, M., Ranocchiari, M. and van Bokhoven, J. A. Catalytic conversion of methane to methanol over Cu-mordenite. *Chem. Commun.* **2012**, 48, 404-406, DOI: 10.1039/c1cc15840f
5. Grundner, S., Markovits, M. A., Li, G., Tromp, M., Pidko, E. A., Hensen, E. J., Jentys, A., Sanchez-Sanchez, M. and Lercher, J. A. Single-site trinuclear copper oxygen clusters in mordenite for selective conversion of methane to methanol. **2015**, 6, 7546, DOI: 10.1038/ncomms8546
6. Grundner, S., Luo, W., Sanchez-Sanchez, M. and Lercher, J. A. Synthesis of Single-Site Copper Catalysts for Methane Partial Oxidation. *Chem. Commun.* **2016**, 52, 2553-2556, DOI: 10.1039/c5cc08371k
7. Tomkins, P., Mansouri, A., Bozbag, S. E., Krumeich, F., Park, M. B., Alayon, E. M., Ranocchiari, M. and van Bokhoven, J. A. Isothermal Cyclic Conversion of Methane into Methanol over Copper-Exchanged Zeolite at Low Temperature. *Angew. Chem. Int. Ed.* **2016**, 55, 5467-5471, DOI: 10.1002/anie.201511065
8. Proding, S., Kvan, K., Arstad, B., Borfecchia, E., Beato, P. and Svelle, S. Synthesis–Structure–Activity Relationship in Cu-MOR for Partial Methane Oxidation: Al

- Siting via Inorganic Structure-Directing Agents. *ACS Catal.* **2022**, 12, 2166-2177, DOI: 10.1021/acscatal.1c05091
9. Pappas, D. K., Borfecchia, E., Dyballa, M., Pankin, I. A., Lomachenko, K. A., Martini, A., Signorile, M., Teketel, S., Arstad, B., Berlier, G., Lamberti, C., Bordiga, S., Olsbye, U., Lillerud, K. P., Svelle, S. and Beato, P. Methane to Methanol: Structure-Activity Relationships for Cu-CHA. *J. Am. Chem. Soc.* **2017**, 139, 14961-14975, DOI: 10.1021/jacs.7b06472
 10. Wulfers, M. J., Teketel, S., Ipek, B. and Lobo, R. F. Conversion of methane to methanol on copper-containing small-pore zeolites and zeotypes. *Chem. Commun.* **2015**, 51, 4447-4450, DOI: 10.1039/c4cc09645b
 11. Pappas, D. K., Borfecchia, E., Dyballa, M., Lomachenko, K. A., Martini, A., Berlier, G., Arstad, B., Lamberti, C., Bordiga, S., Olsbye, U., Svelle, S. and Beato, P. Understanding and Optimizing the Performance of Cu-FER for The Direct CH₄ to CH₃OH Conversion. *ChemCatChem.* **2019**, 11, 621-627, DOI: 10.1002/cctc.201801542
 12. Sushkevich, V. L. and van Bokhoven, J. A. Methane-to-Methanol: Activity Descriptors in Copper-Exchanged Zeolites for the Rational Design of Materials. *ACS Catal.* **2019**, 9, 6293-6304, DOI: 10.1021/acscatal.9b01534
 13. Knorpp, A. J., Pinar, A. B., Newton, M. A., Sushkevich, V. L. and van Bokhoven, J. A. Copper-Exchanged Omega (MAZ) Zeolite: Copper-Concentration Dependent Active Sites and its Unprecedented Methane to Methanol Conversion. *ChemCatChem.* **2018**, 10, 5593-5596, DOI: 10.1002/cctc.201801809
 14. Ravishankar, R., Bhattacharya, D., Jacob, N. E. and Sivasanker, S. Characterization and catalytic properties of zeolite MCM-22. *Microporous Mater.* **1995**, 4, 83-93, DOI: [https://doi.org/10.1016/0927-6513\(94\)00086-B](https://doi.org/10.1016/0927-6513(94)00086-B)
 15. Bjørgen, M., Akyalcin, S., Olsbye, U., Benard, S., Kolboe, S. and Svelle, S. Methanol to hydrocarbons over large cavity zeolites: Toward a unified description of catalyst deactivation and the reaction mechanism. *J. Catal.* **2010**, 275, 170-180, DOI: <https://doi.org/10.1016/j.jcat.2010.08.001>
 16. Leonowicz, M. E., Lawton, J. A., Lawton, S. L. and Rubin, M. K. MCM-22: A Molecular Sieve with Two Independent Multidimensional Channel Systems. *Science.* **1994**, 264, 1910-1913, DOI: 10.1126/science.264.5167.1910
 17. Souverijns, W., Verrelst, W., Vanbutsele, G., Martens, J. A. and Jacobs, P. A. Micropore structure of zeolite MCM-22 as determined by the decane catalytic test reaction. *J. Chem. Soc., Chem. Commun.* **1994**, 1671-1672, DOI: 10.1039/C39940001671
 18. Lawton, S. L., Leonowicz, M. E., Partridge, R. D., Chu, P. and Rubin, M. K. Twelve-ring pockets on the external surface of MCM-22 crystals. *Microporous Mesoporous Mater.* **1998**, 23, 109-117, DOI: [https://doi.org/10.1016/S1387-1811\(98\)00057-2](https://doi.org/10.1016/S1387-1811(98)00057-2)
 19. Corma, A., Corell, C. and Pérez-Pariente, J. Synthesis and characterization of the MCM-22 zeolite. *Zeolites.* **1995**, 15, 2-8, DOI: [https://doi.org/10.1016/0144-2449\(94\)00013-I](https://doi.org/10.1016/0144-2449(94)00013-I)
 20. Dyballa, M., Pappas, D. K., Kvande, K., Borfecchia, E., Arstad, B., Beato, P., Olsbye, U. and Svelle, S. On How Copper Mordenite Properties Govern the Framework Stability and Activity in the Methane-to-Methanol Conversion. *ACS Catal.* **2019**, 9, 365-375, DOI: 10.1021/acscatal.8b04437
 21. Min, H.-K., Park, M. B. and Hong, S. B. Methanol-to-olefin conversion over H-MCM-22 and H-ITQ-2 zeolites. *J. Catal.* **2010**, 271, 186-194, DOI: <https://doi.org/10.1016/j.jcat.2010.01.012>

22. Svelle, S., Visur, M., Olsbye, U., Saepurahman and Bjørgen, M. Mechanistic Aspects of the Zeolite Catalyzed Methylation of Alkenes and Aromatics with Methanol: A Review. *Top. Catal.* **2011**, 54, 897, DOI: 10.1007/s11244-011-9697-7
23. Wang, S., Wei, Z., Chen, Y., Qin, Z., Ma, H., Dong, M., Fan, W. and Wang, J. Methanol to Olefins over H-MCM-22 Zeolite: Theoretical Study on the Catalytic Roles of Various Pores. *ACS Catal.* **2015**, 5, 1131-1144, DOI: 10.1021/cs501232r
24. Pappas, D. K., Martini, A., Dyballa, M., Kvande, K., Teketel, S., Lomachenko, K. A., Baran, R., Glatzel, P., Arstad, B., Berlier, G., Lamberti, C., Bordiga, S., Olsbye, U., Svelle, S., Beato, P. and Borfecchia, E. The Nuclearity of the Active Site for Methane to Methanol Conversion in Cu-Mordenite: A Quantitative Assessment. *J. Am. Chem. Soc.* **2018**, 140, 15270-15278, DOI: 10.1021/jacs.8b08071
25. Borfecchia, E., Lomachenko, K. A., Giordanino, F., Falsig, H., Beato, P., Soldatov, A. V., Bordiga, S. and Lamberti, C. Revisiting the Nature of Cu sites in the Activated Cu-SSZ-13 Catalyst for SCR reaction. *Chem. Sci.* **2015**, 6, 548-563, DOI: 10.1039/c4sc02907k
26. Llabrés i Xamena, F. X., Fiscaro, P., Berlier, G., Zecchina, A., Palomino, G. T., Prestipino, C., Bordiga, S., Giamello, E. and Lamberti, C. Thermal Reduction of Cu²⁺-Mordenite and Re-oxidation upon Interaction with H₂O, O₂, and NO. *J. Phys. Chem. B.* **2003**, 107, 7036-7044, DOI: 10.1021/jp0275847
27. Pappas, D. K., Kvande, K., Kalyva, M., Dyballa, M., Lomachenko, K. A., Arstad, B., Borfecchia, E., Bordiga, S., Olsbye, U., Beato, P. and Svelle, S. Influence of Cu-speciation in mordenite on direct methane to methanol conversion: Multi-Technique characterization and comparison with NH₃ selective catalytic reduction of NO_x. *Catal. Today.* **2021**, 369, 105-111, DOI: <https://doi.org/10.1016/j.cattod.2020.06.050>
28. Kvande, K., Pappas, D. K., Dyballa, M., Buono, C., Signorile, M., Borfecchia, E., Lomachenko, K. A., Arstad, B., Bordiga, S., Berlier, G., Olsbye, U., Beato, P. and Svelle, S. Comparing the Nature of Active Sites in Cu-loaded SAPO-34 and SSZ-13 for the Direct Conversion of Methane to Methanol. *Catalysts.* **2020**, 10, 191, DOI: doi:10.3390/catal10020191
29. Giordanino, F., Vennestrom, P. N. R., Lundegaard, L. F., Stappen, F. N., Mossin, S., Beato, P., Bordiga, S. and Lamberti, C. Characterization of Cu-Exchanged SSZ-13: a Comparative FTIR, UV-Vis, and EPR Study with Cu-ZSM-5 and Cu-beta with Similar Si/Al and Cu/Al Ratios. *Dalton Trans.* **2013**, 42, 12741-12761, DOI: 10.1039/c3dt50732g
30. Frolich, K., Bulánek, R. and Frýdová, E. Interaction of CO probe molecules with Cu(+) in MCM-22 zeolite. *Microporous Mesoporous Mater.* **2014**, 186, 37-45, DOI: <https://doi.org/10.1016/j.micromeso.2013.11.031>
31. Paolucci, C., Parekh, A. A., Khurana, I., Di Iorio, J. R., Li, H., Albarracin Caballero, J. D., Shih, A. J., Anggara, T., Delgass, W. N., Miller, J. T., Ribeiro, F. H., Gounder, R. and Schneider, W. F. Catalysis in a Cage: Condition-Dependent Speciation and Dynamics of Exchanged Cu Cations in SSZ-13 Zeolites. *J. Am. Chem. Soc.* **2016**, 138, 6028-6048, <http://dx.doi.org/10.1021/jacs.6b02651>
32. Kustov, L. M., Kazanskii, V. B., Beran, S., Kubelkova, L. and Jiru, P. Adsorption of carbon monoxide on ZSM-5 zeolites: infrared spectroscopic study and quantum-chemical calculations. *J. Phys. Chem.* **1987**, 91, 5247-5251, DOI: 10.1021/j100304a023
33. Bordiga, S., Lamberti, C., Bonino, F., Travert, A. and Thibault-Starzyk, F. Probing zeolites by vibrational spectroscopies. *Chem. Soc. Rev.* **2015**, 44, 7262-7341, DOI: 10.1039/C5CS00396B
34. Auroux, A. Acidity and basicity: determination by adsorption microcalorimetry, in: *H.G. Karge, J. Weitkamp (Eds.), Molecular Sieves, Springer-Verlag, Berlin Heidelberg.* **2006**, 6, 45-152,

35. Parrillo, D. J. and Gorte, R. J. Characterization of acidity in H-ZSM-5, H-ZSM-12, H-Mordenite, and H-Y using microcalorimetry. *J. Phys. Chem.* **1993**, 97, 8786-8792, DOI: 10.1021/j100136a023
36. Busca, G., Lietti, L., Ramis, G. and Berti, F. Chemical and mechanistic aspects of the selective catalytic reduction of NO_x by ammonia over oxide catalysts: A review. *Appl. Catal., B.* **1998**, 18, 1-36, DOI: [https://doi.org/10.1016/S0926-3373\(98\)00040-X](https://doi.org/10.1016/S0926-3373(98)00040-X)
37. Arrigo, R., Wrabetz, S., Schuster, M. E., Wang, D., Villa, A., Rosenthal, D., Girschgies, F., Weinberg, G., Prati, L., Schlögl, R. and Su, D. S. Tailoring the morphology of Pd nanoparticles on CNTs by nitrogen and oxygen functionalization. *Phys. Chem. Chem. Phys.* **2012**, 14, 10523-10532, DOI: 10.1039/C2CP40861A
38. Giordanino, F., Borfecchia, E., Lomachenko, K. A., Lazzarini, A., Agostini, G., Gallo, E., Soldatov, A. V., Beato, P., Bordiga, S. and Lamberti, C. Interaction of NH₃ with Cu-SSZ-13 Catalyst: A Complementary FTIR, XANES, and XES Study. *J. Phys. Chem. Letters.* **2014**, 5, 1552-1559, DOI: 10.1021/jz500241m
39. Chen, J., Peng, G., Liang, T., Zhang, W., Zheng, W., Zhao, H., Guo, L. and Wu, X. *Nanomaterials.* **2020**, DOI: 10.3390/nano10112170
40. Borfecchia, E., Negri, C., Lomachenko, K. A., Lamberti, C., Janssens, T. V. W. and Berlier, G. Temperature-dependent dynamics of NH₃-derived Cu species in the Cu-CHA SCR catalyst. *React. Chem. Eng.* **2019**, 4, 1067-1080, DOI: 10.1039/C8RE00322J
41. Giles, C. H., Smith, D. and Huitson, A. A general treatment and classification of the solute adsorption isotherm. I. Theoretical. *J. Colloid Interface Sci.* **1974**, 47, 755-765, DOI: [https://doi.org/10.1016/0021-9797\(74\)90252-5](https://doi.org/10.1016/0021-9797(74)90252-5)
42. Inglezakis, V. J., Pouloupoulos, S. G. and Kazemian, H. Insights into the S-shaped sorption isotherms and their dimensionless forms. *Microporous Mesoporous Mater.* **2018**, 272, 166-176, DOI: <https://doi.org/10.1016/j.micromeso.2018.06.026>
43. Limousin, G., Gaudet, J. P., Charlet, L., Szenknect, S., Barthès, V. and Krimissa, M. Sorption isotherms: A review on physical bases, modeling and measurement. *Appl. Geochem.* **2007**, 22, 249-275, DOI: <https://doi.org/10.1016/j.apgeochem.2006.09.010>
44. Lashchinskaya, Z. N., Gabrienko, A. A. and Stepanov, A. G. Propene transformation on Cu-modified ZSM-5 zeolite: Aromatization and oxidation. *Microporous and Mesoporous Mater.* **2023**, 350, 112448, DOI: <https://doi.org/10.1016/j.micromeso.2023.112448>
45. Yang, L., Trafford, K., Kresnawahjuesa, O., Šepa, J., Gorte, R. J. and White, D. An Examination of Confinement Effects in High-Silica Zeolites. *J. Phys. Chem. B.* **2001**, 105, 1935-1942, DOI: 10.1021/jp002964i
46. Park, M. B., Park, E. D. and Ahn, W.-S. Recent Progress in Direct Conversion of Methane to Methanol Over Copper-Exchanged Zeolites. *Front. Chem.* **2019**, 7, 1-7,
47. Tomkins, P., Ranocchiari, M. and van Bokhoven, J. A. Direct Conversion of Methane to Methanol under Mild Conditions over Cu-Zeolites and Beyond. *Acc. Chem. Res.* **2017**, 50, 418-425, DOI: 10.1021/acs.accounts.6b00534
48. Brezicki, G., Kammert, J. D., Gunnoe, T. B., Paolucci, C. and Davis, R. J. Insights into the Speciation of Cu in the Cu-H-Mordenite Catalyst for the Oxidation of Methane to Methanol. *ACS Catal.* **2019**, 9, 5308-5319, DOI: 10.1021/acscatal.9b00852
49. Zheng, J., Lee, I., Khramenkova, E., Wang, M., Peng, B., Gutierrez, O. Y., Fulton, J. L., Camaioni, D. M., Khare, R., Jentys, A., Haller, G. L., Pidko, E. A., Sanchez-Sanchez, M. and Lercher, J. A. Importance of Methane Chemical Potential for Its Conversion to Methanol on Cu-Exchanged Mordenite. *Chem. Eur. J.* **2020**, 26, 7563-7567, DOI: 10.1002/chem.202000772

50. Ravel, B. and Newville, M. ATHENA, ARTEMIS, HEPHAESTUS: data analysis for X-ray absorption spectroscopy using IFEFFIT. *J. Synchrotron Radiat.* **2005**, 12, 537-541, DOI: doi:10.1107/S0909049505012719

SUPPORTING INFORMATION

Microcalorimetry on Cu-MCM-22 reveals structure-activity relationships for the methane-to-methanol reaction

Karoline Kvande^a, Moses Mawanga^b, Sebastian Prodinge^a, Bjørn Gading Solemsli^a, Jia Yang^b, Unni Olsbye^a, Pablo Beato^c, Edd Anders Blekkan^{*, b}, and Stian Svelle^{*, a}.

^a Center for Materials Science and Nanotechnology, Department of Chemistry, University of Oslo, 1033 Blindern, 0315 Oslo, Norway

^b Department of Chemical Engineering, Norwegian University of Science and Technology (NTNU), NO-7491, Trondheim, Norway

^c Topsoe A/S, Haldor Topsøes Allé 1, DK-2800 Kgs. Lyngby, Denmark

Table of content

1. Experimental section	2
1.1. Material preparation	2
1.2. Standard characterization	2
2. Fitted PXRD pattern of H-MCM-22	3
3. Detailed analysis of the XANES/FT-EXAFS features	3
4. FT-IR spectroscopy	4
5. Subtracted adsorption isotherms	5
References	6

1. Experimental section

1.1. Material preparation

The as-made form of MCM-22 was synthesized according to the method reported by Corma *et al.* [1]. To obtain the H-form (H-MCM-22), the as-made material was mixed 3 times with 1 M NH_4NO_3 solution (stirred for 2 h @ 70 °C between each time). Then the material was washed and centrifuged, before being calcined at 500 °C overnight (16 h). For Cu exchange, two materials were made with different Cu-loading. The H-MCM-22 was mixed with either 0.02 M (to make 0.30Cu-MCM-22) or 0.01 M (to make 0.25Cu-MCM-22) $\text{Cu}(\text{OAc})_2$ -solution (60 ml solution/g of zeolite) and stirred at room temperature (RT) overnight (~25 °C). Afterward, the materials were washed and centrifuged 3 times, before drying at 70 °C. Lastly, the samples were calcined at 500 °C overnight (16h) to remove excess hydrocarbons. 0.25Cu-MCM-22 and 0.30Cu-MCM-22 have a Cu/Al ratio of 0.25 and 0.30 respectively.

1.2. Standard characterization

Microwave Plasma Atomic Emission Spectroscopy (MP-AES) was used for the elemental analysis. Prior to analysis, 1 mL 15 % hydrofluoric acid (HF) was used to dissolve 20 mg of the sample in a Teflon liner for 1 h. The use of hydrofluoric acid requires special precautions (Safety note). A light was centered on the Teflon liner to verify that all solid material were dissolved. 5 wt% H_3BO_3 was added to quench excess fluoride anions. Then the solution was diluted with 50 mL water, and an Agilent 4100 MP-AES instrument was utilized to analyze the solution. To determine the amount of Si, Al, and Cu in $\mu\text{mol/g}$, external calibration curves based on elemental standards were employed.

With Thermogravimetric Analysis (TGA), the water content (in %) of the samples was measured. A Netzsch STA 449F Jupiter system was employed for weight measurements. 10-15 mg of the materials were added to Pt crucibles and heated to 300 °C with a ramp of 2 °C/min. The protocol was performed in a flow of synthetic air (20 ml/min O_2 and 40 ml/min N_2).

Scanning Electron Microscopy (SEM) images were obtained using a Hitachi SU8230 microscope. The acceleration voltage was set to 2 kV and the emission current to 10 μA .

Powder X-ray Diffraction (PXRD) patterns of all materials were obtained with a Bruker D8 Discovery diffractometer with Cu $K\alpha$ radiation ($\lambda = 1.5418 \text{ \AA}$). The materials were measured on full plate sample holders and analyzed with $\theta = 2-40^\circ$ on a timescale = 8. The H-MCM-22 material was refined against an MWW.CIF file obtained from the IZA database [2]. The refinement was performed with BIOVIA Materials Studio.

N_2 -physisorption isotherms were measured to obtain the specific surface area of the H-form material. Prior to measurement, the sample was pretreated in vacuum at 300 °C for 10 h. A BELSorp Maxi volumetric gas adsorption instrument (MicroTrac MRB) was used to measure the sample at -196 °C. To obtain the specific surface area, the Brunauer-Emmett-Teller (BET) approximation was used in a p/p_0 range relevant for microporous materials as defined by Llewellyn *et al.* [3].

2. Fitted PXRD pattern of H-MCM-22

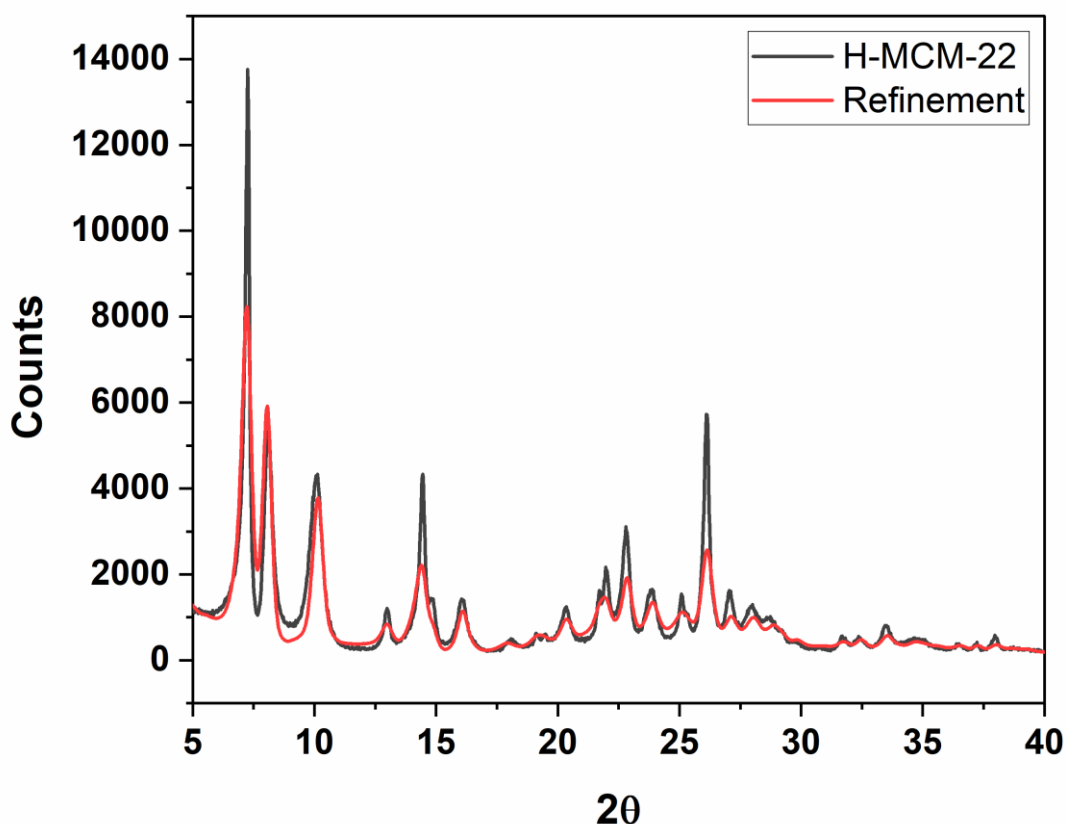


Figure S1. Fitting for the experimental H-MCM-22 PXRD pattern against the MWW structure.

3. Detailed analysis of the XANES/FT-EXAFS features

The Cu K-edge XANES spectra reported in Figure 2 (main text) show very typical spectroscopic fingerprints of a pure Cu^{2+} state within the zeolite. This observation is based on a number of Cu K-edge studies in previous Cu-zeolites [4-10]. The feature observed on the rising edge at 8985 – 8990 eV is from the $1s \rightarrow 4p$ transition of three/four-fold coordinated Cu^{2+} sites. At 8977 eV, a small peak is observed on the pre-edge, arising from the dipole-forbidden $1s \rightarrow 3d$ transition in $d^9 \text{Cu}^{2+}$ ions, confirming that the $1s \rightarrow 4p$ transition stems from Cu^{2+} . Additionally, there is no clear feature at 8983 eV, which would be from the $1s \rightarrow 4p$ transition of linear Cu^+ species.

The k^2 -weighted, phase uncorrected, Fourier transform of the EXAFS spectral region (FT-EXAFS) of the two samples is reported in the left panel of Figure 2 (main text). There, the spectral resolution gives three well-defined maxima from the three first shells in the R-space. The shape and position of the peaks are similar to those observed by Pappas et al. for Cu-CHA [6], and by following their assignment, we can suggest that the first shell corresponds to Cu – O single scattering (SS) paths with two framework oxygen and one extra-framework oxygen. Then, the second peak is likely coming from second shell interactions with framework (T-sites)

or Cu–Cu scattering in Cu_xO_y species. The third peak in the R-space is suggested to stem from Cu–Cu scattering in Cu_xO_y moieties with longer distance between the Cu species.

4. FT-IR spectroscopy

Figure S2 shows the OH stretch region of H-MCM-22 and 0.30Cu-MCM-22. The band at 3749 cm^{-1} is from silanols (Si-OH), while the band at 3621 cm^{-1} is from the O-H stretch vibration at Brønsted acid sites. After Cu-exchange, the latter band has clearly diminished indicating the exchange of Cu onto the sample. Nonetheless, there is still a significant amount of Brønsted acid sites left in the material.

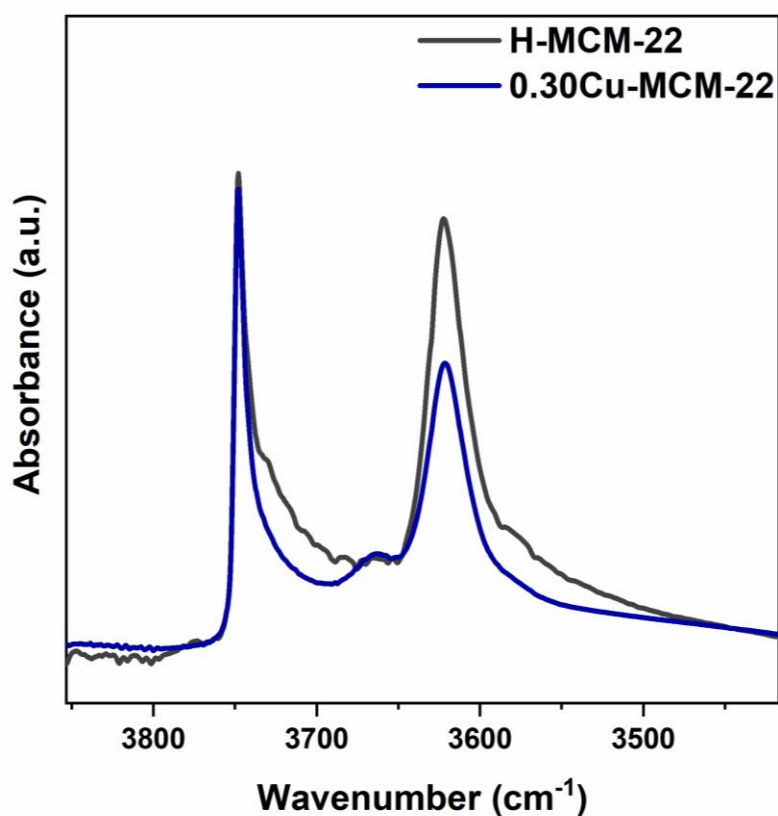


Figure S2. FT-IR spectra from the OH-stretch region of vacuum activated (@ 450 °C) H-MCM-22 and 0.30Cu-MCM-22.

5. Subtracted adsorption isotherms

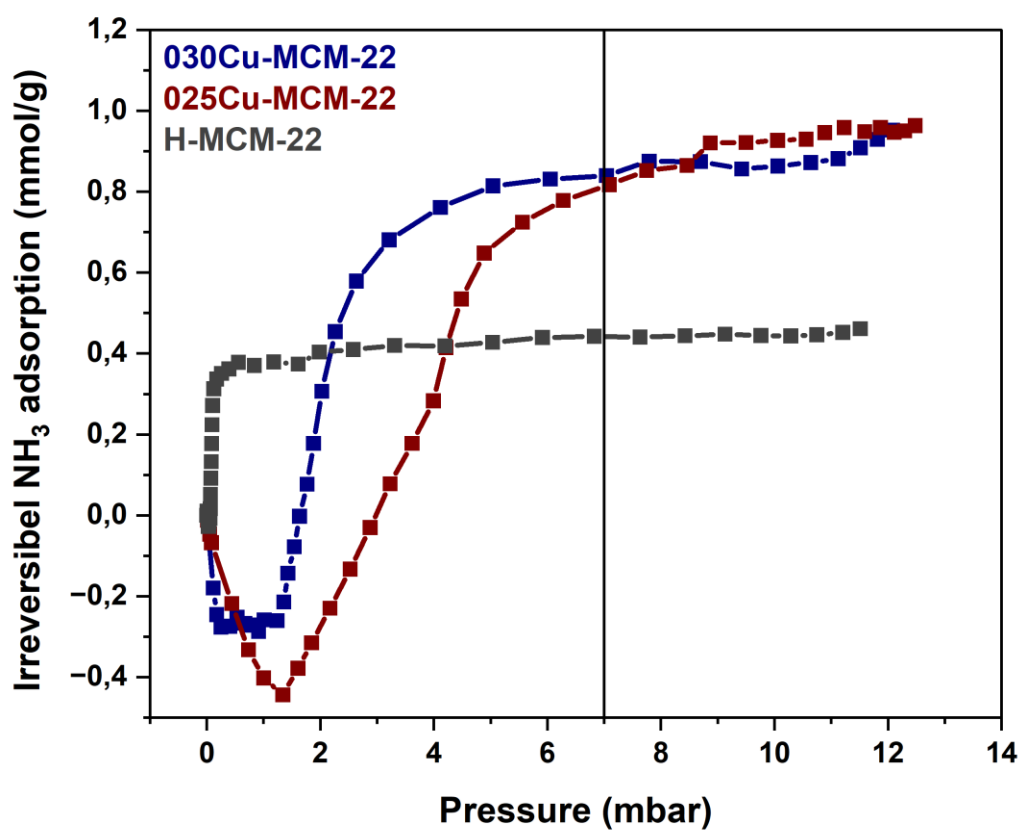


Figure S3. Subtracted (primary minus secondary) adsorption isotherms of the three investigated MCM-22 zeolites.

References

- [1] A. Corma, C. Corell and J. Pérez-Pariente, *Zeolites* **1995**, 15, 2-8.
- [2] C. Baerlocher and L. B. McCusker, *Database of Zeolite Structures*: <http://www.iza-structure.org/databases/>.
- [3] P. Llewellyn, F. R. Reinoso, J. Rouquerol and N. Seaton, in *Studies in Surface Science and Catalysis*; Elsevier **2006**, 160, 748.
- [4] S. Grundner, M. A. Markovits, G. Li, M. Tromp, E. A. Pidko, E. J. Hensen, A. Jentys, M. Sanchez-Sanchez and J. A. Lercher, *Nat. Commun.* **2015**, 6, 7546-7554.
- [5] E. M. C. Alayon, M. Nachttegaal, A. Bodi, M. Ranocchiari and J. A. van Bokhoven, *Phys. Chem. Chem. Phys.* **2015**, 17, 7681-7693.
- [6] D. K. Pappas, E. Borfecchia, M. Dybala, I. A. Pankin, K. A. Lomachenko, A. Martini, M. Signorile, S. Teketel, B. Arstad, G. Berlier, C. Lamberti, S. Bordiga, U. Olsbye, K. P. Lillerud, S. Svelle and P. Beato, *J. Am. Chem. Soc.* **2017**, 139, 14961-14975.
- [7] C. Paolucci, A. A. Parekh, I. Khurana, J. R. Di Iorio, H. Li, J. D. Albarracin Caballero, A. J. Shih, T. Anggara, W. N. Delgass, J. T. Miller, F. H. Ribeiro, R. Gounder and W. F. Schneider, *J. Am. Chem. Soc.* **2016**, 138, 6028-6048.
- [8] F. Giordanino, E. Borfecchia, K. A. Lomachenko, A. Lazzarini, G. Agostini, E. Gallo, A. V. Soldatov, P. Beato, S. Bordiga and C. Lamberti, *J. Phys. Chem. Letters* **2014**, 5, 1552-1559.
- [9] E. Borfecchia, K. A. Lomachenko, F. Giordanino, H. Falsig, P. Beato, A. V. Soldatov, S. Bordiga and C. Lamberti, *Chem. Sci.* **2015**, 6, 548-563.
- [10] M. H. Groothaert, J. A. van Bokhoven, A. A. Battiston, B. M. Weckhuysen and R. A. Schoonheydt, *J. Am. Chem. Soc.* **2003**, 125, 7629-7640.



Paper III



Copper-zeolites Prepared by Solid-state Ion Exchange - Characterization and Evaluation for the Direct Conversion of Methane to Methanol

Karoline Kvande¹ · Sebastian Prodinge¹ · Fabian Schlimpen² · Pablo Beato³ · Patrick Pale² · Stefan Chassaing² · Stian Svelle¹

Accepted: 5 December 2022
© The Author(s) 2022

Abstract

Direct conversion of methane to methanol (MTM) over Cu-zeolites is a so-called “dream reaction” for the chemical industry. There is still a lot that can be done in order to optimize the reaction by e.g. achieving a deeper understanding of the reaction mechanism and the nature of the Cu-sites. In this study, we investigated a solid-state ion exchange method to incorporate Cu^I ions into zeolites (MOR, BEA, ZSM-5 and FAU), as a more scalable technique. The solid-state ion exchange led to a Cu/Al ration of about 0.8, however with a heterogeneous distribution of Cu. Regardless, Fourier transform-infrared spectroscopy still revealed that most Brønsted acid sites were exchanged in all four samples. Further, CH₄-temperature programmed reaction experiments showed that some Cu-sites formed were reactive towards CH₄, with Cu^I-MOR and Cu^I-FAU having the largest CH₄ consumption. Ultimately, the Cu^I-zeolites were tested in the MTM reaction and proved capable of producing methanol, even without the presence of Brønsted sites. A MOR with lower Cu/Al ratio (0.30) was also tested for comparison, and as this sample obtained a much higher productivity than the Cu^I-MOR with high Cu-loading (0.10 vs. 0.03 mol_{MeOH}/mol_{Cu}), it was demonstrated that some fine-tuning is necessary to obtain the active Cu sites for methane activation.

Keywords Methane activation · Solid-state ion exchange · Cu^I–zeolites

1 Introduction

A lot of research effort has been dedicated over the last decades to find a small-scale conversion route for underutilized methane, due to its potential impact on climate change mitigations. The direct conversion of methane to methanol (MTM) is one of the highly explored research areas related

to this. Several different reaction routes have been proposed for this, although one of the more promising ones is a stepwise cyclic conversion route over metal-loaded zeolites, and especially Cu-zeolites. This is because the stepwise cyclic conversion route facilitates for the separation of product and oxidant to prevent over-oxidation [1–3]. This method includes a high temperature (~500°C) oxidation step of the Cu-zeolite in O₂ before the temperature is reduced to 200 °C and the resulting material is then reacted with CH₄. This reduces some of the Cu-oxo sites (mono- and dimeric Cu moieties) formed after O₂-activation, and methoxy intermediates are formed on these sites. Finally, steam is required to extract methanol from the zeolite pores. On the quest of optimizing the reaction, a large array of Cu-zeolites have been investigated. Among the most investigated are MOR [4–6], CHA [7, 8], and ZSM-5 [9, 10]. MOR has been found to be one of the most active zeolites with methanol productivities close to 0.5 mol_{MeOH}/mol_{Cu} [11, 12]. This is often viewed to be the highest obtainable productivity, given a Cu

Karoline Kvande
karoline.kvande@smn.uio.no

- ¹ Center for Materials Science and Nanotechnology (SMN), Department of Chemistry, University of Oslo, 1033 Blindern, 0315 Oslo, Norway
- ² Laboratoire de Synthèse, Réactivité Organiques et Catalyse (LASYROC), Institut de Chimie, CNRS-UMR7177, Université de Strasbourg, 4 rue Blaise Pascal, 67070 Strasbourg, France
- ³ Topsoe A/S, Haldor Topsøes Allé 1, DK-2800 Kgs. Lyngby, Denmark

to methanol ratio of two-to-one [13, 14]. This ratio is based on the active site being a dicopper active site (Cu-O-Cu or Cu-O-O-Cu), or the combination of two monomeric sites (Cu-OH) [11, 15]. It has been found that both the zeolite framework and placement of Cu have large impacts on the formation of the active sites and as a consequence, the activity towards methanol formation [12]. Therefore, finding new materials and synthesis methods is still very important in the attempts to optimize the MTM process. In literature, the Cu loading into zeolites is mostly performed *via* liquid ion exchange or incipient wetness methods with Cu^{II} salts, both giving well-dispersed Cu-zeolites, however only in lab scale quantities [4, 16]. For industrial application, it would be much more beneficial to use a simpler exchange method like solid-state ion exchange (SSIE). SSIE is also relevant for the selective catalytic reduction of NO_x with NH₃, and to that end, Vennestrøm and Shwan et al. have previously investigated a novel method to perform SSIE with CuO/Cu₂O in an atmosphere of NO/NH₃ [17, 18]. Therein, they suggest that the Cu-oxo species are formed at low temperatures due to the formation of mobile [Cu(NH₃)₂]⁺ complexes.

In this study, we have prepared Cu^I exchanged zeolites *via* SSIE with Cu^ICl (Cu^I-BEA, -FAU, -MOR and -ZSM-5) and tested the materials in the methane to methanol reaction. Le et al. have previously shown that SSIE with Cu^{II}(acac)₂ instead of Cu^ICl over mordenites lead to a higher yield of methanol [19]. However, when exchanging Cu^I ions instead of Cu^{II} ions into the zeolites, it is theoretically possible to obtain a Cu/Al=1, thus maximizing the possible Cu-oxo sites. A similar protocol using SSIE with Cu^ICl to exchange H-mordenites for the MTM reaction was previously applied by Bozbag et al., however, they did not explore the possibility of fully exchanging the materials, and used Cu/Al ratios around 0.35 [20]. The SSIE method discussed in this study have also been used to synthesise Cu^I-exchanged FAU zeolites that have been investigated as a catalyst for C–C bond Glaser-type homocoupling reactions by Kuhn et al. [21]. Furthermore, the Cu^I-FAU zeolite has been shown to be applicable as a catalyst in several other types of organic synthesis [22–26]. This truly shows the adversity of Cu-sites in zeolites. To fully study the effect of this SSIE synthesis method for the MTM reaction, the samples were subjected to elemental analysis, and investigated with CO-adsorption coupled with Fourier Transform-Infrared (FT-IR) spectroscopy to understand if the increased amount of Cu led to changes in the Cu speciation. Furthermore, CH₄-TPR experiments, shown to be a helpful tool in optimizing the MTM reaction both in terms of setting the reaction parameters as well as understanding material properties, were performed [27, 28]. Finally, the samples were tested in the methane to methanol reaction and compared to previously obtained

results with the same reaction protocol in order to assess their performance. The target with this investigation is to understand whether it is possible to form methanol from methane when most Brønsted sites are exchanged with Cu, or if this alters the properties of the Cu-sites to an extent where C-H activation is no longer possible. Further, we also aim to clarify the importance of minimizing the formation of Cu agglomerates and nanoparticles to obtain a high methanol productivity.

2 Methods

2.1 Solid-state Cu-exchange

The four zeolite materials used as starting material in this study were commercially available and received in the NH₄-form. The four zeolite frameworks were FAU (USY) zeolite (Zeolyst International (CBV500), Si/Al=2.9), MOR zeolite (CBV21A, Si/Al=10.3), BEA zeolite (Zeolchem International (ZEOCAT PB/H), Si/Al=12.5–17.5) and ZSM-5 zeolite (Zeolyst International (CBV5020), Si/Al=25). The H-form was obtained by calcining the NH₄-form for 12 h at 550 °C in static air. To obtain the expected Cu^I-exchanged forms of the samples, a solid-state ion exchange was performed by mixing 1 g of dry zeolite with a calculated amount of CuCl (Aldrich, >99% purity, melting point: 430 °C) to obtain a specific Cu/Al ratio, where the Cu exchange degree was about 80%. The samples were named Cu^I-FAU, Cu^I-MOR, Cu^I-BEA, and Cu^I-ZSM-5. All samples were made with an intended Cu/Al ratio ≈ 0.8. One Cu-MOR was made with a lower Cu/Al ratio (~0.30) for comparison. This was named 0.30Cu^I-MOR. To limit the exposure to moisture, the mixture was rapidly ground with a mortar and pestle before being loaded into a tubular reactor and connected to a flow setup. The powder mixture was heated to 350 °C (1 °C/min) and held isothermally for 3 d. N₂ was used as a purging gas (40 ml/min) to remove the gaseous HCl formed during the reaction.

2.2 Standard characterization

Microwave Plasma Atomic Emission Spectroscopy (MP-AES) was used for elemental analysis of the sample. Before analysis, 20 mg of sample was dissolved in 1 mL 15% hydrofluoric acid (HF) in a Teflon liner for 1 h. Safety note: The use of hydrofluoric acid requires special precautions. To verify that all of the solid material was dissolved, a light was shone through the thin wall of the Teflon liner. After quenching excess fluoride anions by adding an appropriate amount of 5 wt% H₃BO₃, the solution was diluted with distilled water (50 mL). An Agilent 4100 MP-AES instrument

was used to analyze the solution, and the amount of Si, Al and Cu in $\mu\text{mol/g}$ was quantified with external calibration curves based on commercial elemental standards.

Scanning Electron Microscopy (SEM) combined with backscattered electron (BSE) imaging was used to investigate the samples for Cu nanoparticles before and after activity testing. A Hitachi SU8230 microscope was used to obtain the images using an acceleration voltage of 1 kV and a 10 μA current. On the same instrument, Energy Dispersive X-ray (EDX) was used as a secondary elemental analysis to determine the ratio of Cl in the sample in relation to the Cu content before and after testing. The distribution of Cu on the sample was investigated with EDX mapping.

Thermogravimetric Analysis (TGA) was used to measure the water content (in %) of the samples. For this, a Netzsch STA 449 F Jupiter system was applied to measure the sample weight. The materials were heated to 300 °C with a ramp rate of 2 °C/min in a flow of synthetic air (20 ml/min O₂ and 40 ml/min N₂).

X-ray Diffraction (XRD) patterns of the tested materials were obtained using a Bruker D8 Discovery diffractometer with a Cu K α radiation ($\lambda = 1.5418 \text{ \AA}$). The materials were grinded, and evenly dispersed to make a flat surface on a glass plate sample holder. The experiments were run in a 2 θ range of 2–50° with a step size of 0.02 °/s at ambient conditions.

N₂-physisorption isotherms was used to determine the specific surface area of the samples. The measurements were conducted on a BELSorp Maxi volumetric gas adsorption instrument (MicroTrac MRB) at –196 °C. The samples were pretreated by evacuation at 300 °C for 10 h. The specific surface areas were calculated by using the BET approximation in a p/p_0 range relevant for microporous materials as defined by Llewellyn et al. [29].

2.3 CO-adsorption with Fourier transform-infrared (FT-IR) spectroscopy

For the CO-adsorption FT-IR experiments, the samples were pressed (2–3 tons) into thin wafers ($\sim 11.3 \text{ mg/cm}^2$) and carefully placed into gold envelopes. Then the gold envelope was placed into a T-shaped cell with KBr windows. The cell was connected to vacuum and pretreated at 450 °C for 90 min after a ramp of 5 °C/min from room temperature (RT). After cooling back down to RT, the setup was placed into a Bruker Vertex 80 FT-IR instrument and incremental doses of CO was sent onto the sample until reaching an equilibrium pressure of $\sim 8 \text{ mbar}$. A spectrum was collected after each dose.

2.4 Activity measurements in the methane to methanol reaction

All samples were tested in the methane to methanol reaction. 100 mg of sample (sieve fraction: 425–250 μm) were loaded into a linear quartz reactor (i.d. = 6 mm) and then connected to a gas manifold controlled by Mass Flow Controllers (MFC). The gas feeds were sent stepwise onto the sample, controlled by stop- and 4-way valves. Water was connected to the gas line through a bubbler immersed in an oil bath kept at 45 °C. All gas lines were heated to $\sim 140 \text{ °C}$ to avoid any condensation in the lines. The effluent was analyzed with an online Pfeiffer Mass Spectrometer after the reactor. All gas flows were adjusted to 15 mL/min, using a flow meter. In a flow of 100 O₂, the sample was heated to 500 °C (5 °C/min) and kept there for 8 h. Then the temperature was reduced to 200 °C, and 100 He was used to flush out excess O₂ for 1 h. After that, a flow with 100 CH₄, was sent onto the sample for 3 h. Another round with He flush for 1 h was performed, before a 10 H₂O saturated 10 Ne/He stream was sent onto the sample for 2 h. The mass fragments of MeOH ($m/z = 31$), DME ($m/z = 46$) and CO₂ ($m/z = 44$) was quantified using calibration curves from obtained using a calibration gas mixture with known amounts of all the components. To obtain the accurate yield, the sample weight was corrected by withdrawing the water content of the samples (measured with TGA). The total yield ($\mu\text{mol/g}_{\text{zeolite}}$) of MeOH is given as the amount of MeOH + 2 \sim DME. In the text this will be referred to as *total amount of methanol*.

2.5 CH₄-Temperature programmed reaction (TPR)

For the CH₄-TPR experiments, the same setup as for testing was used. After pretreating the samples in O₂ in the same manner as above, the temperature was lowered to 105 °C, and He was sent onto the sample to flush away all excess O₂ for 1 h. Then 15 mL/min 5% CH₄/He was sent onto the sample for 20 min isothermally, before a ramp up to 550 °C with 5 °C/min was started. The temperature was recorded simultaneously with a thermocouple placed in a thin quartz sheet on top of the sample bed. The output of the reactor was analyzed with an online MS.

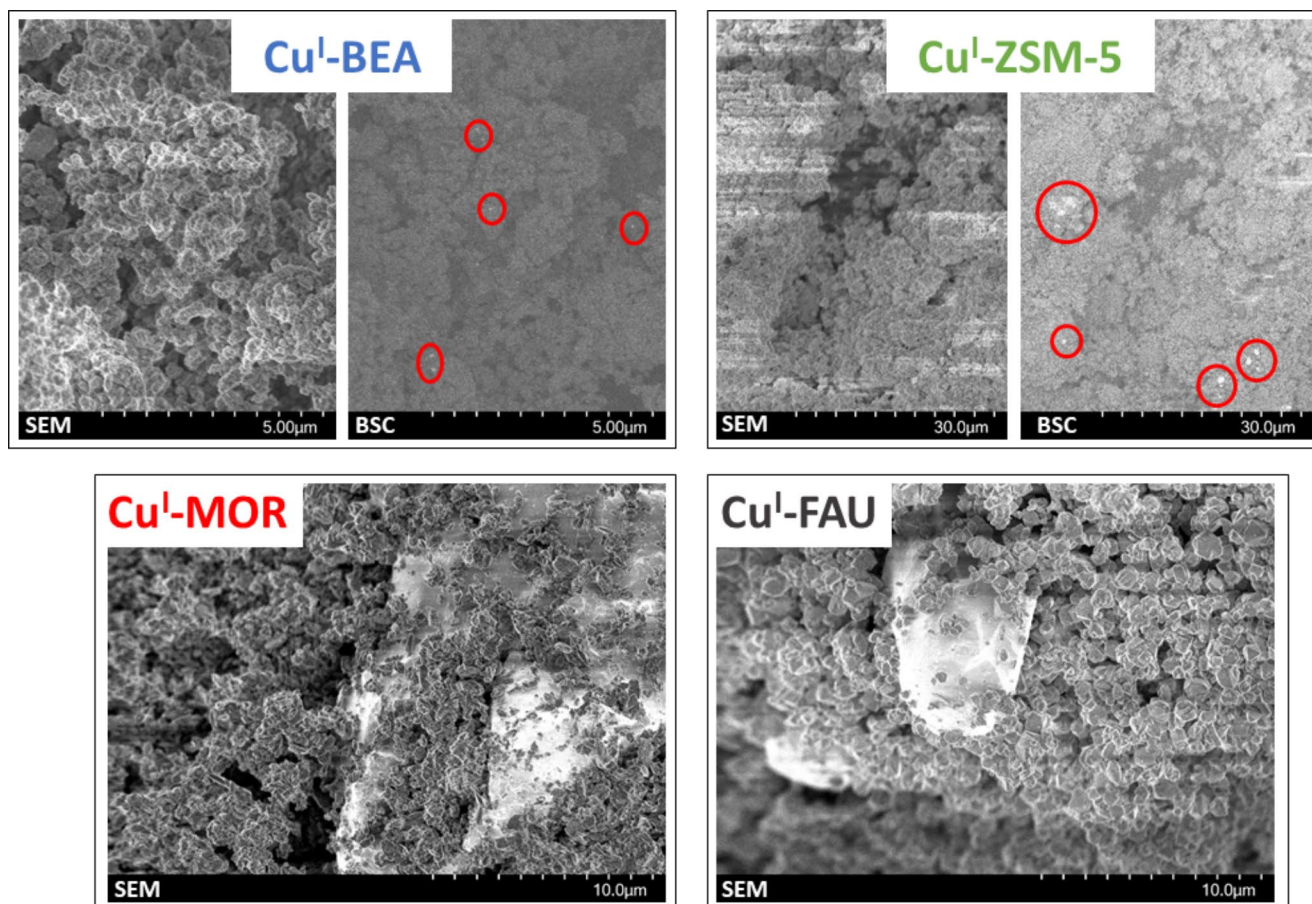
3 Results and Discussion

3.1 Basic characterization by MP-AES, EDX, SEM, XRD and N₂-physisorption

Solid state ion exchange (SSIE) is industrially a much simpler synthesis process than various solution-based exchange procedures. Furthermore, by performing the SSIE with Cu^I

Table 1 Chemical composition of the materials obtained with Microwave Plasma Atomic Emission Spectroscopy (MP-AES).

Sample name	Si/Al	Cu/Al	Al wt%	Al (mmol/g)	Cu wt%	Cu (mmol/g)
Cu ^I -ZSM-5	18.4	0.78	2.3	0.86	4.2	0.67
Cu ^I -BEA	35.7	2.0	1.2	0.45	5.9	0.92
Cu ^I -MOR	12.0	0.89	3.5	1.3	7.2	1.1
Cu ^I -USY	2.9	0.74	12	4.3	20	3.2
0.30Cu ^I -MOR	11.8	0.31	3.5	1.3	2.5	0.40

**Fig. 1** SEM and Backscatter (BSC) images of the materials. The top row shows the presence of nanoparticles observed with Backscattering imaging (bright spots in the red circles). Bottom row shows larger agglomerates visible in regular SEM images

salts, it would be possible to obtain a higher exchange degree of Cu in the zeolite, possibly leading to a larger concentration of copper in close proximity. Their close proximity could make the formation of active sites for C-H activation more feasible. To investigate the resulting Cu-zeolites after SSIE, MP-AES and EDX was used for elemental analysis, N₂-physisorption was applied to determine the specific surface area, and SEM and backscattered images was used to search for Cu outside the frameworks. A more extensive characterization on the effect of the SSIE has been performed on the Cu^I-exchanged FAU sample previously by Kuhn et al. [21]. For three of the zeolites, the SSIE yielded Cu-loaded zeolites with a molar Cu/Al ratio \approx 0.8. Cu^I-BEA ended up over-exchanged with a Cu/Al = 2, due to the much

lower Al content than indicated by the manufacturer in this sample. A full report on the elemental analysis from MP-AES is presented in Table 1.

Figure 1 depicts the SEM and backscattered electron images obtained for the four samples. In Cu^I-BEA and Cu^I-ZSM-5, Cu nanoparticles can be observed as bright spots in the backscattered electron images, as pointed out by the red circles. In the regular SEM images of Cu^I-MOR and Cu^I-FAU, even larger agglomerates of Cu are observed. This was also corroborated with EDX mapping, which showed big agglomerates of Cu outside the framework (Fig. S1). These images indicate a very heterogeneous distribution of Cu in the materials and demonstrates the possible drawback of SSIE as exchange procedure.

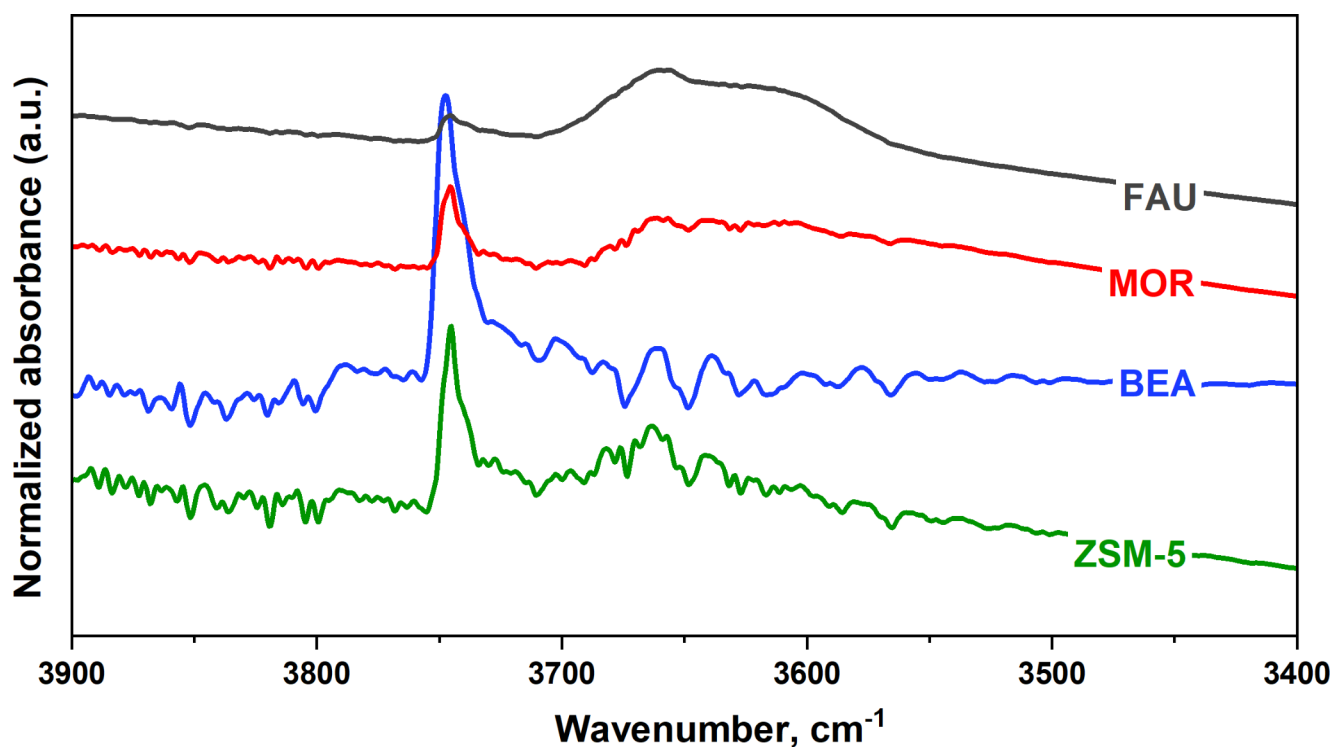


Fig. 2 FT-IR spectra showing the $\nu(\text{OH})$ stretching region of the four Cu^{I} -zeolites after pretreatment in vacuum at $450\text{ }^{\circ}\text{C}$

In addition to the heterogeneous distribution of Cu, elemental analysis with EDX revealed that a significant fraction of Cl was found in all samples as a remnant from the SSIE.

The specific surface area of all samples were obtained using N_2 -physisorption, and compared to the specific surface area of the H-form (Table S1). It is apparent that there is a reduction in surface area ($>10\%$) for most of the samples after the Cu exchange. This loss in surface area could indicate that the formation of nanoparticles and the large excess of Cu contributes to a partial pore blockage for reactants. This is substantiated by the specific surface area of the MOR sample with a smaller Cu/Al ratio, 0.30Cu^{I} -MOR being much higher than for the higher Cu-loaded Cu^{I} -MOR sample.

XRD of the as-synthesized FAU has previously shown that the framework is intact after the Cu exchange and HCl release [21]. Herein, we have measured the XRD pattern of the tested samples. The patterns are presented in Fig. S2. The patterns obtained indicate that 0.30Cu^{I} -MOR, Cu^{I} -MOR, Cu^{I} -ZSM-5 and Cu^{I} -FAU has kept the structural integrity after testing. However, it should be noted that impurities of both CuCl_2 and CuO was present in the highly exchanged samples, as evidenced by some additional peaks at $2\theta = 16$, 32 and 40° .

The basic characterization of the solid-state ion exchanged materials reveal that there is a heterogeneous distribution of Cu in the samples and possible pore blockage

by larger agglomerates present around the pores. Therefore, even though the exchange led to a Cu/Al ratio of 0.8, it is not likely that all the Cu present in the samples will contribute to C-H bond activation.

3.2 CO-adsorption with FT-IR spectroscopy

The effects of the very high exchange degree achieved for the four zeolites (Cu/Al ratio of 0.8) on Cu speciation were studied using FT-IR spectroscopy. Figure 2 depicts the $\nu(\text{OH})$ stretching region of the spectra at RT after pretreatment at $450\text{ }^{\circ}\text{C}$ in vacuum. O-H stretching bands connected to Brønsted sites ($\text{Si}(-\text{OH})\text{Al}$) should be found in the region between 3700 and 3550 cm^{-1} . The lack of bands in this region indicates that all Brønsted sites are covered by Cu, except a broad band in the Cu^{I} -FAU sample. A comparison between the parent MOR and the Cu-exchanged MOR for this region can be found in the SI (Fig. S3). The bands at $\sim 3750\text{ cm}^{-1}$ are related to silanols ($\text{Si}-\text{OH}$) in the samples. The non-existing Brønsted site vibrations should be noted, as it has been previously suggested that Brønsted sites are necessary to produce methanol, as shown with the help of FT-IR and NMR spectroscopy by Dyballa et al. as well as Sushkevich et al. [30, 31]. The effect of the lacking Brønsted sites on the performance of the materials will be discussed in-depth later in this paper.

Dosing CO at RT onto the pretreated materials can determine if the high Cu/Al ratio has an impact on the nature of

the Cu-sites and their accessibility. CO will only form stable adducts with Cu^I ions and not Cu^{II} ions at RT. Therefore, ideal conditions would be to ensure that all Cu ions in available, redox active sites, are oxidation state 1+, and hence able to react with CO. To do so, the Cu^I-exchanged samples were pretreated at 450 °C under vacuum prior to the CO-adsorption measurements, as this has been shown to induce “self-reduction” of Cu^{II} to Cu^I in zeolites [32–36].

In Fig. 3, IR absorption spectra of all four samples during CO adsorption is shown. The background subtracted spectra have been normalized to the sample weight. The last spectra in all four series is recorded at ~8 mbar equilibrium CO pressure. These precautions ensure a fair comparison when discussing the band intensities of the four samples. As the samples are exposed to incremental doses of CO, the bands typical for mono- and eventually dicarbonyl adducts on Cu^I sites will be formed [37]. The band(s) related to the formation of monocarbonyl species are highlighted with a grey background. This appears as a growing band at 2158 and 2157 cm⁻¹ for Cu^I-MOR and Cu^I-ZSM-5, while for Cu^I-FAU and Cu^I-BEA, the monocarbonyl species form two distinct bands at 2161/2147 and 2159/2151 cm⁻¹. These two separate bands have previously been correlated in literature to two structurally distinct Cu-sites [37, 38]. Cu^I-BEA seems to have fewer accessible Cu-sites, as shown by the lower intensity for the monocarbonyl bands for this material than the corresponding band(s) for the other zeolites. This is also corroborated by the appearance of the band at 2143 cm⁻¹ at high coverages for the Cu^I-BEA sample, since this is the vibrational frequency of gaseous CO, indicating that all possible adsorption sites are already covered. We postulate that this is related to the low Al concentration, and hence high Cu ion loading on this sample, relative to available exchange sites, resulting in the formation of copper agglomerates.

As more CO is dosed onto the samples, a band starts appearing in the 2178–2182 cm⁻¹ region. This is the symmetric stretch of Cu^I-(CO)₂, and is a clear indication that dicarbonyl species are forming. For all samples, the asymmetric stretch of Cu^I-(CO)₂ is also present at lower wavenumbers (~2149–2152 cm⁻¹), although, this is distorted by a broad tail, indicating that another band is also appearing in that area. Indeed, there seems to be a band/shoulder at around 2135 cm⁻¹, which is likely due to the presence of Cu₂O nanoparticles formed during the exchange procedure [37]. The intensity of the symmetric and asymmetric stretch for Cu^I-(CO)₂ for the Cu^I-MOR sample was further compared to the same vibrational frequencies from CO on the 0.30Cu^I-MOR sample as well as a liquid ion exchanged (LIE) Cu-MOR (Cu/Al=0.28) with the same Si/Al ratio as the MOR investigated herein, previously published by Pappas et al. [39]. A figure comparing the three samples can be

found in the SI (Fig. S4). By first comparing the high and low loaded CuCl exchanged samples, it is evident the highly exchanged sample also have more available Cu^I to form monocarbonyl adducts, as the band intensity for monocarbonyl is higher in the Cu^I-MOR sample compared to 0.30Cu^I-MOR. However, comparing the symmetric dicarbonyl band at 2178 cm⁻¹, the two samples show approximately the same intensity, indicating that the same amount of Cu^I-(CO)₂ is formed on the two samples. It is important to note that these values are not normalized to Cu content, indicating that 0.30Cu^I-MOR has a higher ratio of Cu sites available for dicarbonyl formation. Even so, when comparing both samples to the LIE sample published previously by Pappas et al., it is evident that the LIE sample has markedly higher bands for the dicarbonyl adducts, even though it has the same Cu content as 0.30Cu^I-MOR. Higher intensities of the symmetric and asymmetric stretch for Cu^I-(CO)₂ have been previously attributed to Cu-zeolites with a larger concentration of low-coordination Cu sites, more likely to be able to activate the C-H bond in methane [40]. This indicates that the SSIE method used for the Cu^I-zeolites herein, yields fewer Cu sites that are in a coordination state and position preferred for reaction with methane, compared to LIE. This could partially be due to less accessibility to the sites because of nanoparticle formation blocking the pores as observed with the reduction in specific surface area for all the zeolites. Another possibility is that some of the Cu sites are coordinated to Cl, thus limiting the coordination environment available for CO and only allowing for monocarbonyl species to form. The latter can also be corroborated by the observation of CuCl₂ nanoparticles with XRD after testing.

3.3 Investigating the redox properties with CH₄-TPR

To further explore the propensity of the samples for reaction with methane, CH₄-TPR experiments were used. This technique probes the redox properties of the materials. FT-IR indicated the lack of Brønsted acid sites in the material, while CO adsorption showed that only some of the Cu sites were available to form dicarbonyl adducts. Such adducts have been linked to efficient methane activation [41]. With CH₄-TPR, it is possible to determine if these properties affect the reactivity of materials towards methane. Figure 4 shows the CH₄ consumption (a) and the CO₂ production (b) against temperature during CH₄-TPR over the four materials highly exchanged materials. In Fig. 4 (c) and (d), Cu^I-MOR is compared to 0.30Cu^I-MOR.

The CH₄ consumption trace obtained with this method should be considered to be only semi-quantitative, due to the quite small changes of the intensity of the methane m/z fragments. We will therefore focus on the most distinct

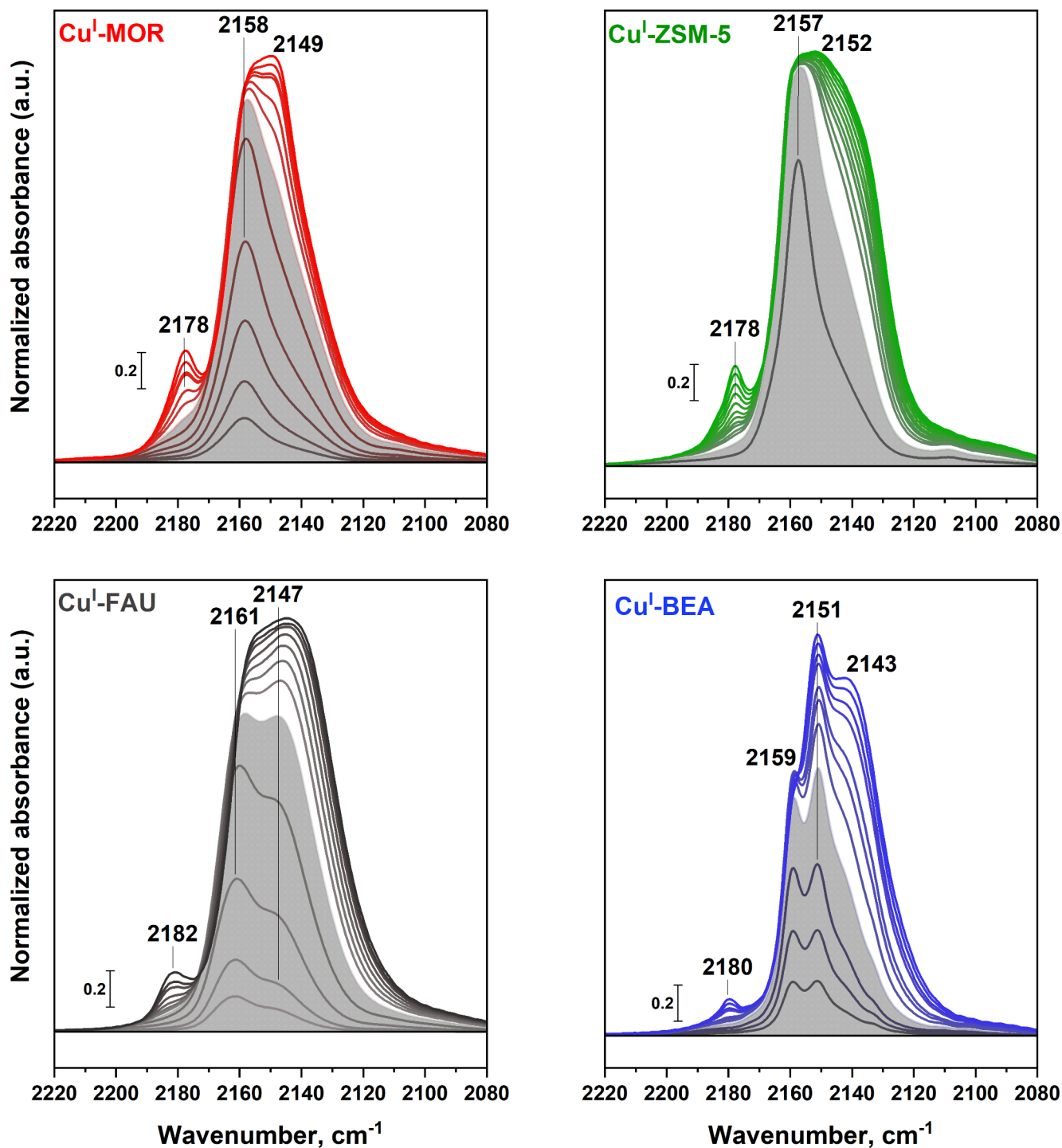


Fig. 3 FT-IR spectra showing the $\nu(\text{CO})$ stretching region of the four Cu^{I} -zeolites during CO adsorption. The spectra have been collected with increasing CO pressure. All spectra are normalized to their framework overtone and background subtracted using the spectrum taken

after pretreatment at 450 °C in vacuum. The last spectrum in all graphs is obtained after an equilibrium pressure of ca. 8 mbar was achieved. The grey area gives the last spectrum taken before the total CO pressure was large enough for dicarbonyl adducts to develop

differences that can be observed between the samples in this discussion. First, as observed in Fig. 4 (a), it is noteworthy that the onset of CH_4 consumption for the highly exchanged MOR, BEA and ZSM-5 seems to start around

the same temperature, whereas the methane consumption occurs at considerably higher temperature for FAU. Further, a considerably larger quantity of methane is consumed over Cu^{I} -MOR and Cu^{I} -FAU compared to the other

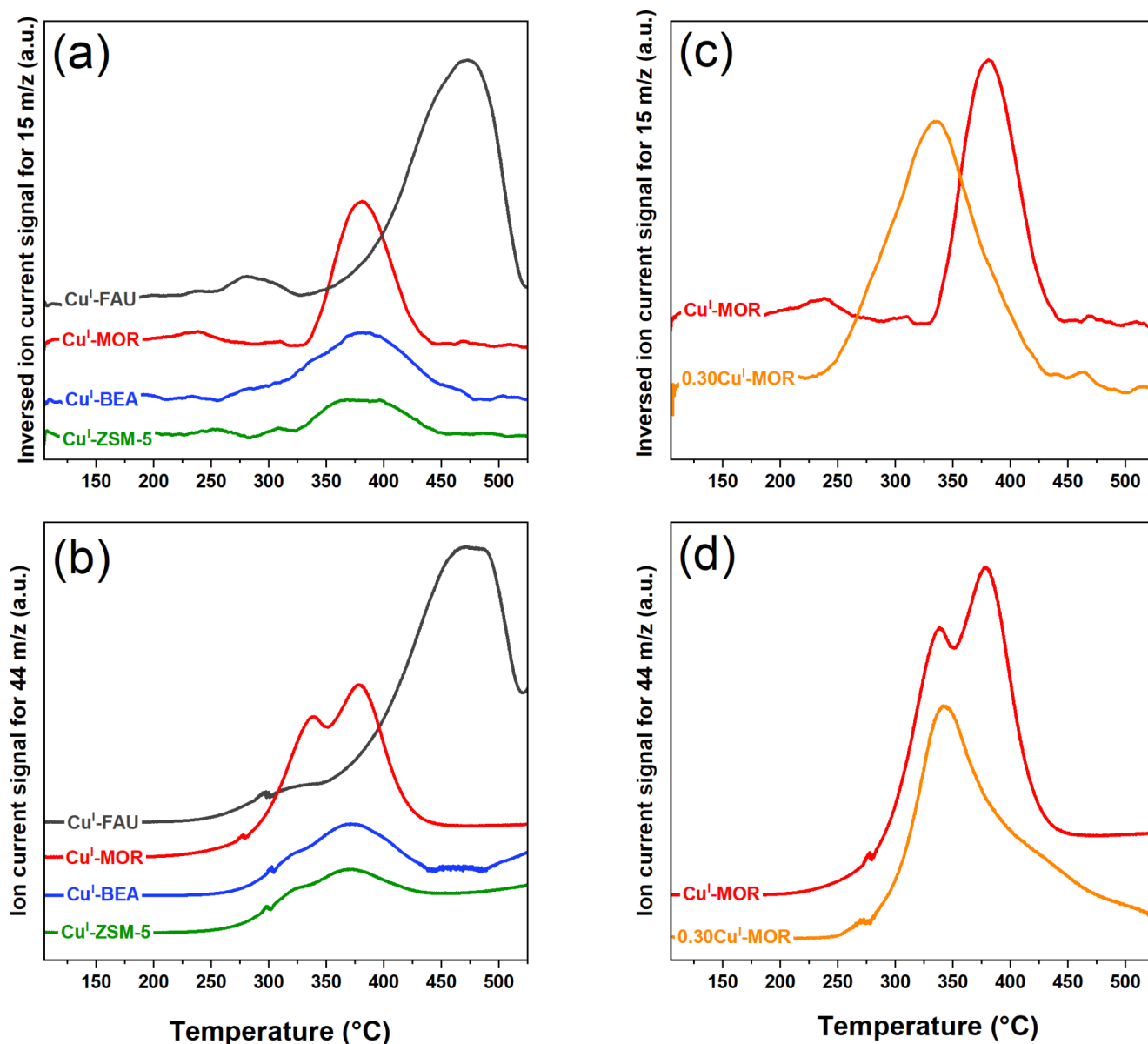
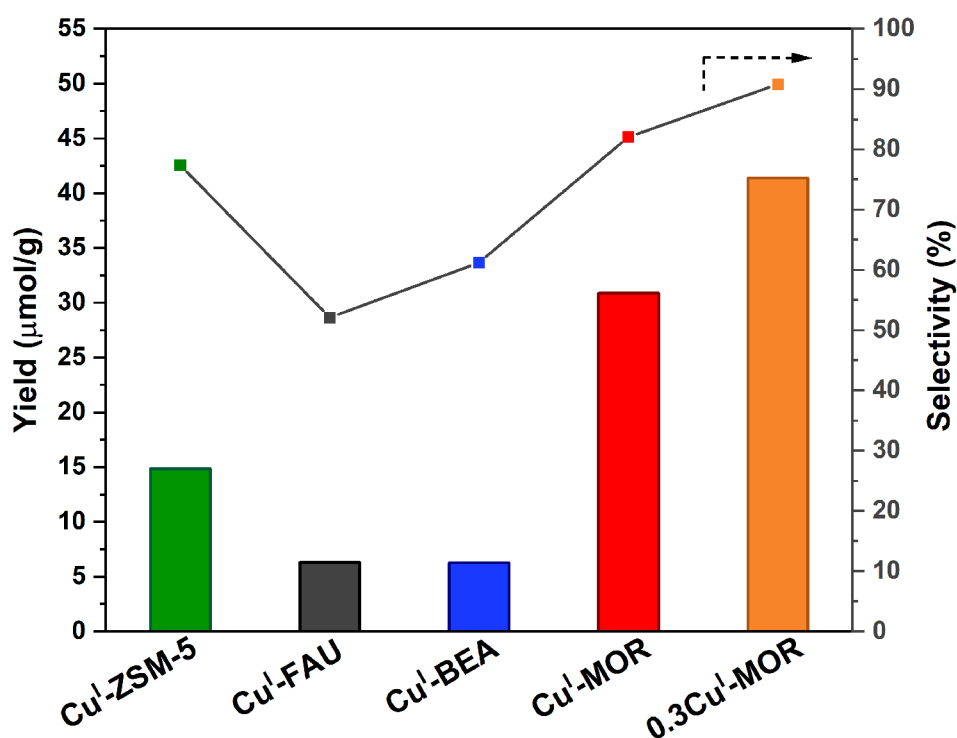


Fig. 4 CH_4 -TPR signals for all four materials. On the left is the CH_4 consumption, and on the right is the corresponding CO_2 production. The graphs have been vertically adjusted for easier comparison

two materials. Sorting the materials based on the temperature of their maximum consumption rate gives $\text{Cu}^{\text{I}}\text{-ZSM-5} < \text{Cu}^{\text{I}}\text{-MOR} < \text{Cu}^{\text{I}}\text{-BEA} < \text{Cu}^{\text{I}}\text{-FAU}$. This order is in line with the results previously reported by Sushkevich and van Bokhoven for CH_4 consumption on ion-exchanged Cu-zeolites [28]. When comparing the highly exchanged $\text{Cu}^{\text{I}}\text{-MOR}$ to the $0.30\text{Cu}^{\text{I}}\text{-MOR}$ sample though (Fig. 4 (c)), there appears to be a significant difference in the temperature for maximum consumption rate among the two. This earlier methane consumption may suggest that $0.30\text{Cu}^{\text{I}}\text{-MOR}$ has a higher reactivity towards methane than $\text{Cu}^{\text{I}}\text{-MOR}$, likely coming from more accessible Cu_xO_y -sites.

When inspecting the CO_2 production (Fig. 4 (b) and (d)), it should be remarked that $0.30\text{Cu}^{\text{I}}\text{-MOR}$, $\text{Cu}^{\text{I}}\text{-MOR}$ and $\text{Cu}^{\text{I}}\text{-FAU}$ produce more CO_2 than the other zeolites. The CO_2 production is also shifted to higher temperatures for FAU, in line with the higher temperature onset for CH_4 consumption. Sushkevich and van Bokhoven correlated the temperature difference for $\text{Cu}^{\text{I}}\text{-FAU}$ to a higher fraction of monomeric Cu active sites, which require a higher temperature to activate methane. Further, it can be observed that the production of CO_2 occurs as two peaks for the highly exchanged samples, especially visible for $\text{Cu}^{\text{I}}\text{-MOR}$. Over $0.30\text{Cu}^{\text{I}}\text{-MOR}$, on the other hand, there is one main peak with just a broad shoulder towards higher temperatures. For

Fig. 5 Activity data for the methane to methanol reaction over the Cu^I-zeolites. The left axis gives the yield in μmol of total amount of methanol per gram of zeolite. On the right axis is the selectivity. In the reaction protocol, the materials were exposed to the following gas flows (15 ml/min) and temperatures; 100% O₂ (500 °C, 8 h), 100% He (200 °C, 1 h), and then, isothermally, 100% CH₄ (3 h), 100% He (1 h), and 10% H₂O in 10% Ne/He (~2 h)



the highly exchanged sample, it does appear as if the onset of CO₂ release occurs before appreciable methane consumption. However, as pointed out above, the true starting point for the uptake of CH₄ is very difficult to determine precisely. The first CO₂ peak appears at around 320 °C for all samples. As this is the main peak in 0.30Cu^I-MOR, the sample with the least Cu agglomerates and nanoparticles, it is likely that this is the temperature corresponding to the products formed from selective C-H activation at the active Cu-sites. Alternatively, it could be suggested that since there is a shift of methane consumption to higher temperatures for the Cu^I-MOR vs. 0.30Cu^I-MOR, the second CO₂ peak for the highly exchanged samples, which overlays well with their CH₄ consumption, is actually the one linked to CH₄ oxidation over the active Cu-sites for these species. If this is the case, it could indicate that the higher Cu-loading has led to more monomeric Cu active sites, also for the other zeolites, and not only FAU. A similar effect with methane consumption being at higher temperatures due to different framework properties was also shown comparing two different CHA frameworks (SAPO-34 vs. SSZ-13) in a previous publication by Kvande et al. [27]. Another possibility is that the higher amount of Brønsted sites in 0.30Cu^I-MOR aids in the reactivity towards methane, and that this is the reason behind the clear difference in CH₄ consumption temperature between the two MOR we observe herein, and not necessarily the formation of different types of Cu-oxo sites. Since it has been shown previously that Brønsted sites are

important for stabilizing the methoxy intermediates, this is a plausible scenario [30].

3.4 Performance studies in the methane to methanol reaction

The propensity of Cu^I-zeolites (Cu^I-ZSM-5, Cu^I-FAU, Cu^I-BEA, Cu^I-MOR) towards producing methanol from methane was investigated by performing a well-established stepwise reaction protocol [7]. The test results on the four Cu^I-zeolites are presented in Fig. 5 below. The yield is presented in bar columns as μmol of total amount of methanol per gram of zeolite. The squared points represent the selectivity to the total amount of methanol. The unwanted byproduct of the reaction is CO₂. It should be noted that CH₃Cl is also observed as a product from the reaction but has not been included in the quantified yield or selectivity. As mentioned previously, the Cl is a remnant from the SSIE, and from EDX analysis after testing, it was observed that a large fraction of the Cl in the framework disappeared after one test, as shown in Table S2.

Excitingly, all four samples show the ability to produce methanol, although only Cu^I-ZSM-5 and Cu^I-MOR show a selectivity towards methanol similar to that previously reported for ion-exchanged zeolites [7, 11]. The appreciable yields of methanol are somewhat surprising, considering that the FT-IR study revealed very few Brønsted sites in these materials, which have been suggested to be needed for methanol formation. Thus, the results presented here might

suggest that some Cu-species can be capable of selectively converting methane to methanol without facilitation by Brønsted sites. However, formation of some Brønsted sites during the reaction protocol cannot be ruled out. Cu^I-ZSM-5 and Cu^I-MOR also give the highest yield of methanol of the four samples, with Cu^I-MOR clearly outperforming the others, in line with what has been observed previously for ion exchanged materials at these reaction conditions [4, 28]. These results are also very much in line with Cu^I-MOR being the sample that was able to consume most methane at the lowest temperature area during TPR (Fig. 4). However, Cu-FAU also has a high consumption of methane in TPR, but this occurs at higher temperature. We note that Sushkevich and van Bokhoven were able to show that Cu-FAU yielded much higher amounts of methanol when the methane activation was performed at higher temperatures [28]. Interestingly, in the same study they obtained a higher yield for BEA compared to ZSM-5, which is opposite to the results presented herein. However, this difference could be due to several unknown factors like a difference in methane loading pressure between the two studies, or it could be the higher Si/Al for BEA in this study, as well as the large over-exchange of Cu, causing fewer accessible active sites as observed by CO-adsorption with FT-IR.

To place the yields obtained in this study into perspective, the Cu^I-MOR can be compared to a previous publication by Dyballa et al. [4]. There, two different commercial mordenites (Si/Al=7 and 11) were studied, starting with both H- and Na-form. A comparison between two different Cu-loading procedures was performed, i.e. liquid ion exchange (LIE) and incipient wetness impregnation (denoted SSIE in the paper). This thorough study showed that Cu exchanged onto the H-form generated more productive materials than when the ion exchange was carried out starting with the Na-form. In addition, LIE led to better Cu-mordenites with better methanol productivity than incipient wetness impregnation. The Cu^I-MOR used in the present study is based on the commercial MOR, CBV21A, which is the same parent material as the material with Si/Al=11 in the paper by Dyballa et al. [4]. When comparing the total methanol yield obtained over the Cu^I-MOR (38 μmol/g) to the yields obtained previously (16–169 μmol/g), it is apparent that the total methanol yield of Cu^I-MOR is comparable to those achieved for Cu-zeolites obtained with LIE over the Na-form. However, the large fraction of inactive Cu as presented above results in an appreciably lower methanol productivity per copper for the Cu^I-MOR (0.03 mol_{methanol}/mol_{Cu}) compared to those presented by Dyballa et al. (>0.06). From these initial results, it is suggested that a precise method is necessary to obtain a high fraction of active sites.

To investigate if we could obtain a higher fraction of active sites, and hence increase the productivity by reducing the Cu exchange degree, a Cu^I-MOR with a Cu/Al≈0.30 was synthesized via SSIE. Indeed, this material exhibits a higher methanol productivity (0.10 mol_{methanol}/mol_{Cu}) as well as a higher yield of methanol, as shown in Fig. 5. The increase can likely be attributed to the formation of less nanoparticles and Cu agglomerates. Alternatively, based on the CH₄-TPR results discussed above, one could also argue that the increased productivity is related to a higher fraction of Brønsted sites present in this sample compared to the higher Cu loaded samples. However, to unravel this question would require a more extensive study where measures are taken to minimize the presence of unwanted Cu species. Interestingly, the productivity of 0.30Cu^I-MOR is within the range of the productivities obtained by Dyballa et al. (0.17–0.19) on most of the materials with Si/Al=11. However, LIE of Cu on the H-form still generates Cu-MOR with 0.25 mol_{methanol}/mol_{Cu} at comparable Cu-content, outperforming the 0.30Cu^I-MOR reported here.

The 0.30Cu^I-MOR sample was also tested over three repeated reaction cycles to see if the removal of Cl through CH₃Cl formation had an impact on the methanol yield by potentially freeing up Cu-sites for C-H bond activation. Only a small increase was observed (from 38 to 42 μmol/g, see Fig S5), even though a qualitative analysis of the amount of CH₃Cl formed revealed a significant reduction in the CH₃Cl production from cycle to cycle (Fig S6). Previously it has been shown that repeating the test over several cycles tends to lead to a minor increase in methanol productivity [7]. Based on this, it seems that the removal of Cl from the material does not lead to an increase in methanol productivity for the samples.

4 Conclusion

Herein an alternative approach to liquid ion exchange for introducing Cu into zeolites has been investigated in the context of selective partial methane oxidation. Extensive characterization of the Cu-zeolites suggests the solid state ion exchange (SSIE) method reported here leads to a significant fraction of Cu nanoparticles and agglomerates. This is believed to hinder the ability of the materials to effectively activate methane. However, the performance data do suggest that methanol is produced on these materials, possibly without the need of Brønsted sites, indicating that methoxy intermediates can be stabilized on other surface sites. To improve on the low methanol yields however, it is necessary with the presence of more Cu-oxo species and possibly Brønsted sites, as well as higher accessibility to all of these sites, which could be achieved with a more fine-tuned

technique. As a proof of concept, we showed that the introduction of a lower amount of Cu via SSIE does result in the formation of a higher fraction of active and accessible Cu-oxo species, more Brønsted sites and a subsequently higher methanol yield. Therefore, we believe that a SSIE method, with some reduction in the amount of Cu exchanged, and a change in Cu-source that does not lead to Cl-based byproducts, could be a viable option in the future for efficient and scalable synthesis of Cu-zeolites for the methane to methanol reaction.

Supplementary Information The online version contains supplementary material available at <https://doi.org/10.1007/s11244-022-01763-7>.

Funding This publication forms a part of the iCSI (industrial Catalysis Science and Innovation) Centre for Research-based Innovation, which receives financial support from the Research Council of Norway under contract no. 237922. FS, PP and SC thank the Centre National de la Recherche Scientifique (CNRS), University of Strasbourg, and the French Ministry of Research for financial support. FS also thanks the French Ministry of Research for a Ph.D. fellowship. Open access funding provided by University of Oslo (incl Oslo University Hospital)

Declarations

Conflict of interest The authors declare no conflict of interest.

Open Access This article is licensed under a Creative Commons Attribution 4.0 International License, which permits use, sharing, adaptation, distribution and reproduction in any medium or format, as long as you give appropriate credit to the original author(s) and the source, provide a link to the Creative Commons licence, and indicate if changes were made. The images or other third party material in this article are included in the article's Creative Commons licence, unless indicated otherwise in a credit line to the material. If material is not included in the article's Creative Commons licence and your intended use is not permitted by statutory regulation or exceeds the permitted use, you will need to obtain permission directly from the copyright holder. To view a copy of this licence, visit <http://creativecommons.org/licenses/by/4.0/>.

References

- Labinger JA (2004) Selective alkane oxidation: hot and cold approaches to a hot problem. *J Mol Catal A: Chem* 220:27–35
- Horn R, Schlögl R (2015) Methane activation by heterogeneous catalysis. *Catal Lett* 145:23–39
- Ravi M et al (2019) Misconceptions and challenges in methane-to-methanol over transition-metal-exchanged zeolites. *Nat Catal* 2:485–494
- Dyballa M et al (2019) On how copper Mordenite Properties govern the Framework Stability and Activity in the methane-to-methanol Conversion. *ACS Catal* 9:365–375
- Sushkevich VL et al (2017) Selective anaerobic oxidation of methane enables direct synthesis of methanol. *Science* 356:523–527
- Alayon EM et al (2012) Catalytic conversion of methane to methanol over Cu-mordenite. *Chem Commun* 48:404–406
- Pappas DK et al (2017) Methane to methanol: structure-activity Relationships for Cu-CHA. *J Am Chem Soc* 139:14961–14975
- Wulfers MJ et al (2015) Conversion of methane to methanol on copper-containing small-pore Zeolites and Zeotypes. *Chem Commun* 51:4447–4450
- Groothaert MH et al (2005) Selective oxidation of methane by the bis(μ -oxo)dicopper core stabilized on ZSM-5 and mordenite zeolites. *J Am Chem Soc* 127:1394–1395
- Woertink JS et al (2009) A $[\text{Cu}_2\text{O}]^{2+}$ Core in Cu-ZSM-5, the Active Site in the Oxidation of Methane to Methanol. *Proc. Natl. Acad. Sci. USA* 106:18908–18913
- Pappas DK et al (2018) The nuclearity of the active site for methane to methanol Conversion in Cu-Mordenite: a quantitative Assessment. *J Am Chem Soc* 140:15270–15278
- Prodinger S et al (2022) Synthesis–structure–activity relationship in Cu-MOR for partial methane oxidation: Al Siting via Inorganic structure-directing agents. *ACS Catal* 12:2166–2177
- Knorpp AJ et al (2018) Copper-exchanged omega (MAZ) Zeolite: copper-concentration dependent active Sites and its unprecedented methane to methanol Conversion. *ChemCatChem* 10:5593–5596
- Kvande K et al (2020) Advanced X-ray absorption spectroscopy analysis to Determine structure-activity Relationships for Cu-Zeolites in the Direct Conversion of methane to methanol. *ChemCatChem* 12:2385–2405
- Sushkevich VL et al (2021) Identification of Kinetic and Spectroscopic Signatures of Copper Sites for Direct Oxidation of methane to methanol. *Angew Chem Int Ed Engl* 60:15944–15953
- Dinh KT et al (2019) Continuous partial oxidation of methane to methanol catalyzed by diffusion-paired copper dimers in copper-exchanged Zeolites. *J Am Chem Soc* 141:11641–11650
- Vennestrøm PNR et al (2014) Influence of lattice stability on hydrothermal deactivation of Cu-ZSM-5 and Cu-IM-5 zeolites for selective catalytic reduction of NO_x by NH₃. *J Catal* 309:477–490
- Shwan S et al (2015) Solid-state ion-exchange of copper into Zeolites facilitated by Ammonia at Low Temperature. *ACS Catal* 5:16–19
- Le HV et al (2017) Solid-state ion-exchanged Cu/Mordenite catalysts for the Direct Conversion of methane to methanol. *ACS Catal* 7:1403–1412
- Bozbag SE et al (2016) Methane to methanol over copper Mordenite: yield improvement through multiple cycles and different synthesis techniques. *Catal Sci Technol* 6:5011–5022
- Kuhn P et al (2009) Probing Cu-USY Zeolite Reactivity: design of a Green Catalyst for the synthesis of Dienes. *J Phys Chem C* 113:2903–2910
- Chassaing S et al (2017) Zeolites as Green Catalysts for Organic synthesis: the cases of H-, Cu- & Sc-Zeolites. *Curr Org Chem* 21:779–793
- Chassaing S et al (2018) Green catalysts based on zeolites for heterocycle synthesis. *Curr Opin Green Sustainable Chem* 10:35–39
- Clerc A et al (2020) Chan-Lam-type azidation and One-Pot CuAAC under CuI-Zeolite Catalysis. *ChemCatChem* 12:2060–2065
- Schlimpen F et al (2022) From A3/KA2 to AYA/KYA multicomponent coupling reactions with terminal ynamides as alkyne surrogates – a direct, green route to γ -amino-ynamides. *Green Chem* 24:6467–6475
- Schlimpen F et al (2021) α -Tertiary propargylamine synthesis via KA2-Type coupling reactions under Solvent-Free CuI-Zeolite Catalysis. *J Org Chem* 86:16593–16613
- Kvande K et al (2020) Comparing the nature of active Sites in Cu-loaded SAPO-34 and SSZ-13 for the Direct Conversion of methane to methanol. *Catalysts* 10:191

28. Sushkevich VL, van Bokhoven JA (2019) Methane-to-Methanol: activity descriptors in copper-exchanged Zeolites for the Rational design of materials. *ACS Catal* 9:6293–6304
29. Llewellyn P et al (2006) Characterization of porous solids VII. *Stud Surf Sci Catalysis*; Elsevier 160:748
30. Dyballa M et al (2019) Zeolite Surface Methoxy Groups as Key Intermediates in the Stepwise Conversion of methane to methanol. *ChemCatChem* 11:5022–5026
31. Sushkevich VL et al (2020) Pathways of Methane Transformation over copper-exchanged Mordenite as revealed by In-Situ NMR and IR Spectroscopy. *Angew Chem Int Ed* 59:910–918
32. Alayon EMC et al (2015) Bis(μ -oxo) Versus mono(μ -oxo) dicopper cores in a Zeolite for converting methane to methanol: an *in situ* XAS and DFT Investigation. *Phys Chem Chem Phys* 17:7681–7693
33. Borfecchia E et al (2015) Revisiting the nature of Cu sites in the activated Cu-SSZ-13 Catalyst for SCR reaction. *Chem Sci* 6:548–563
34. Larsen SC et al (1994) Electron Paramagnetic Resonance Studies of Copper Ion-Exchanged ZSM-5. *J Phys Chem* 98:11533–11540
35. Llabrés i Xamena FX et al (2003) Thermal reduction of Cu^{2+} -Mordenite and Re-oxidation upon Interaction with H_2O , O_2 , and NO . *J Phys Chem B* 107:7036–7044
36. Sushkevich VL, van Bokhoven JA (2018) Revisiting copper reduction in zeolites: the impact of autoreduction and sample synthesis procedure. *Chem Commun* 54:7447–7450
37. Giordano F et al (2013) Characterization of Cu-Exchanged SSZ-13: a comparative FTIR, UV-Vis, and EPR Study with Cu-ZSM-5 and Cu-beta with similar Si/Al and Cu/Al Ratios. *Dalton Trans* 42:12741–12761
38. Palomino GT et al (2000) XRD, XAS, and IR characterization of copper-exchanged Y Zeolite. *J Phys Chem B* 104:8641–8651
39. Pappas DK et al (2021) Influence of Cu-speciation in mordenite on direct methane to methanol conversion: Multi-Technique characterization and comparison with NH_3 selective catalytic reduction of NO_x . *Catal Today* 369:105–111
40. Pappas DK et al (2019) Understanding and optimizing the performance of Cu-FER for the direct CH_4 to CH_3OH Conversion. *ChemCatChem* 11:621–627
41. Palomino GT et al (2002) Vibrational and optical spectroscopic studies on copper-exchanged ferrierite. *Stud Surf Sci Catal* 142:199–206

Publisher's Note Springer Nature remains neutral with regard to jurisdictional claims in published maps and institutional affiliations.

SUPPORTING INFORMATION

Copper-zeolites prepared by solid-state ion exchange - characterization and evaluation for the direct conversion of methane to methanol

Karoline Kvande^{1*}, Sebastian Prodinge¹, Fabian Schlimpen², Pablo Beato³, Patrick Pale², Stefan Chassaing², Stian Svelle¹

- 1 Center for Materials Science and Nanotechnology (SMN), Department of Chemistry, University of Oslo, 1033 Blindern, 0315, Oslo, Norway
- 2 Laboratoire de Synthèse, Réactivité Organiques et Catalyse (LASYROC), Institut de Chimie, CNRS-UMR7177, Université de Strasbourg, 4 rue Blaise Pascal, Strasbourg 67070, France
- 3 Topsoe A/S, Haldor Topsøes Allé 1, DK-2800 Kgs. Lyngby, Denmark

* Correspondence: karoline.kvande@smn.uio.no (K.K.)

Table of Contents

1. Elemental mapping with EDX.....	1
2. N ₂ -physisorption data	2
3. XRD results after testing	2
4. Additional FT-IR spectroscopy data	3
5. Elemental analysis with EDX	5
6. Repeated performance tests over 0.30Cu(I)-MOR.....	5
References.....	7

1. Elemental mapping with EDX

In addition to the elemental analysis shown in the main text, also Energy Dispersive X-ray Mapping was performed on the samples to investigate the behavior of Cu in the samples. Fig. S1 show a very inhomogeneous Cu distribution over two of the samples, Cu(I)-USY and Cu(I)-ZSM-5. This is in good agreement with the SEM and backscatter images presented in the main text.

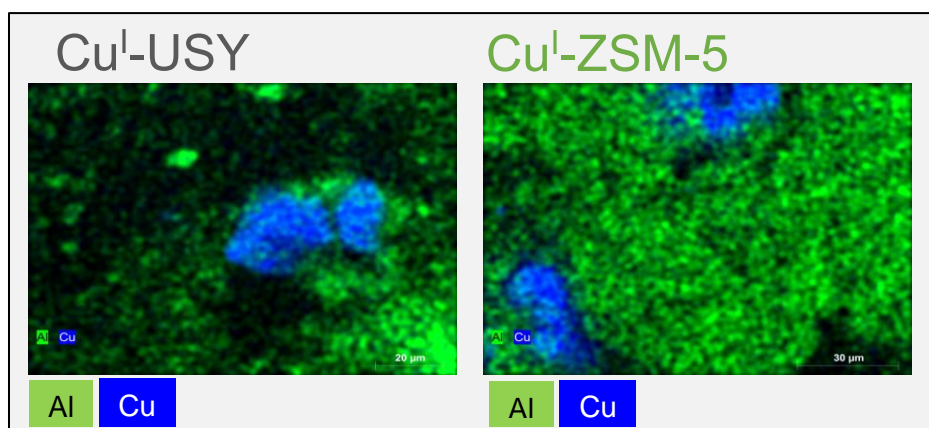


Fig. S1 EDX mapping of Cu(I)-FAU and Cu(I)-ZSM-5. The blue areas are agglomerations of Cu around the zeolite framework shown by the mapping of Al (green area).

2. N₂-physisorption data

Table S1. N₂-physisorption data analyzed with BET

Sample name	SSA (m ² /g)
CBV5020 (H-ZSM-5)	431
Cu ^I -ZSM-5	347
ZEOCAT PB/H (H-BEA)	620*
Cu ^I -BEA	577
CBV21Ads (H-MOR)	532
Cu ^I -MOR	221
0.3Cu ^I -MOR	466
CBV500 (H-USY)	600*
Cu ^I -USY	388

*Values obtained from the manufacturers (Zeochem international and Zeolyst international).

3. XRD results after testing

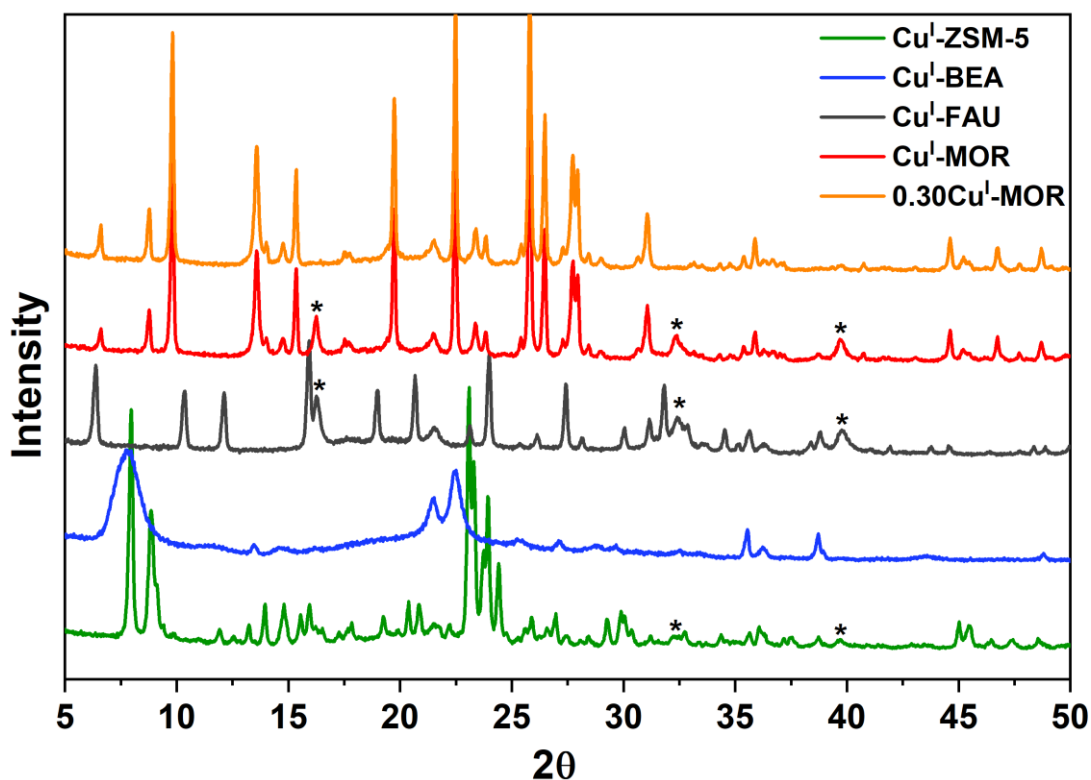


Fig. S2 XRD results after testing. The asterix marks peaks that are not part of the zeolite crystal pattern. The additional peaks belong to CuCl_2 ($2\theta = 16^\circ$) and CuO ($2\theta = 32$ and 40°).

4. Additional FT-IR spectroscopy data

To understand the behavior of the Cu(I)-zeolites when they were subjected to FT-IR spectroscopy, the Cu(I)-MOR zeolite were compared to the H-form of the parent MOR (CBV21A). In Fig. S3, the $\nu(\text{OH})$ stretching region of the Cu(I)-MOR sample and the H-form of the parent MOR is compared. It is evident from this figure that the band at xx cm^{-1} , related to the Si(-OH)Al stretch is completely absent in the Cu(I)-MOR sample, suggesting that this sample have negligible Brønsted acidity left after SSIE.

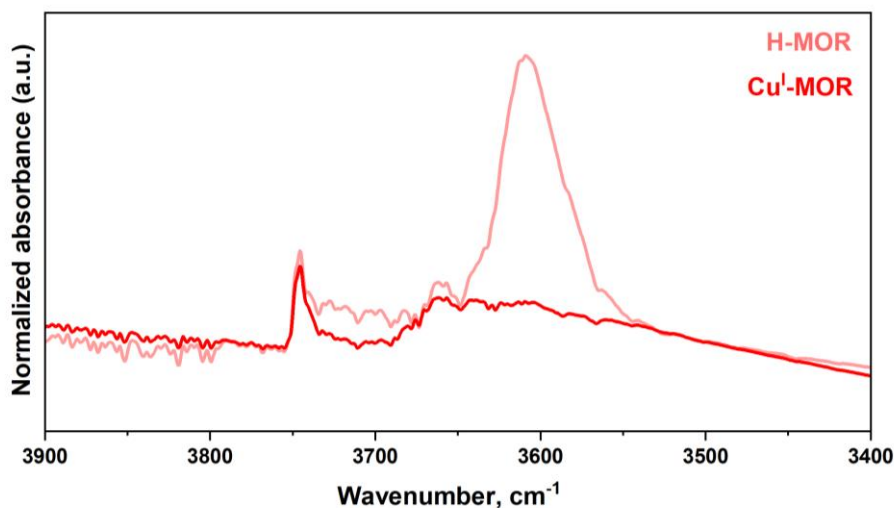


Fig. S3 FT-IR spectra of the $\nu(\text{OH})$ stretching region. The light red color is the spectra of the H-form of the parent MOR (CBV21A) after pretreatment at 450 °C in vacuum. The red spectrum is of Cu(I)-MOR.

For the CO adsorption experiments, the Cu(I)-MOR is here further compared to a liquid ion exchanged (LIE) Cu-sample of the same parent with a $\text{Cu}/\text{Al} = 0.28$ (Fig. S4), and the 0.30Cu^{I} -MOR. The spectra of the LIE Cu-MOR have been published previously, but is replotted here for comparison [1]. The final spectrum in all graphs is obtained with an equilibrium pressure around 8 mbar in the system. The area marked in grey reveal approximately the absorbance intensity coming from the monocarbonyl adducts ($2158/2159\text{ cm}^{-1}$). Then, as the Co pressure increases, two bands appear, one at higher and one at lower wavenumbers, being the symmetric and asymmetric stretching of dicarbonyl species, respectively. The bands correlated to dicarbonyl species are more intense and more defined in the LIE MOR-sample.

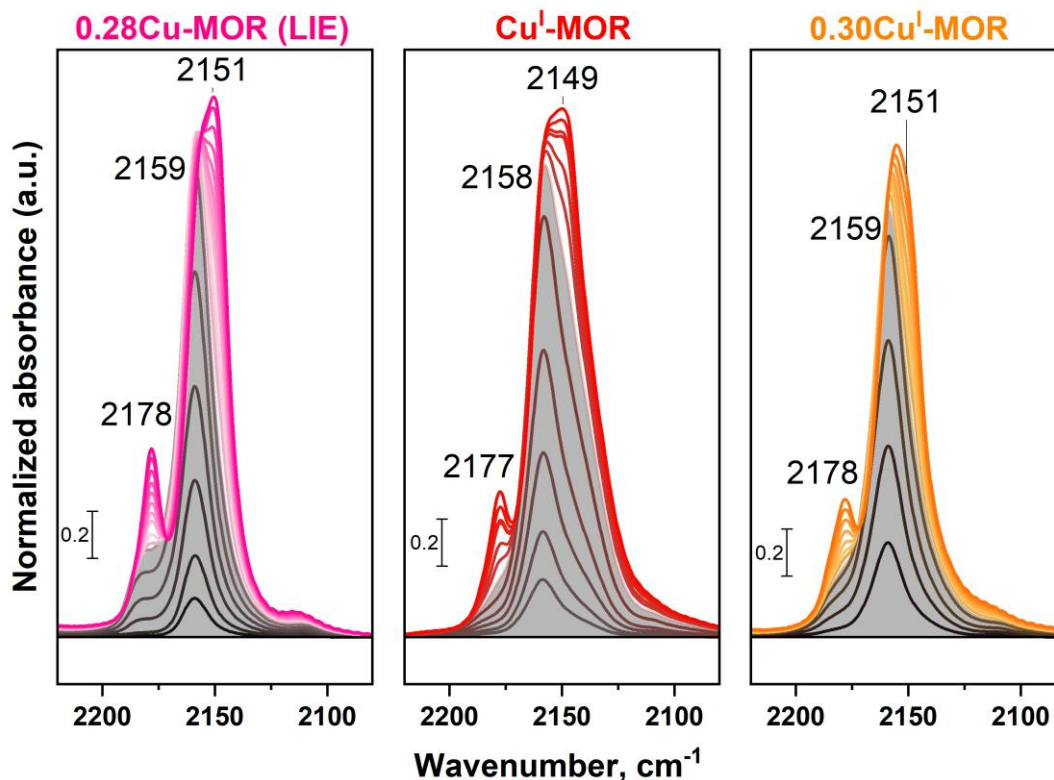


Fig. S4 CO adsorption FT-IR spectra of Cu(I)-MOR made from SSIE and tested in this paper (on the left) compared to Cu-MOR made from LIE on the right [1]. Both samples were pretreated in vacuum at 450 °C before subjected to incremental doses of CO up to 8 mbar of equilibrium pressure.

5. Elemental analysis with EDX

For most of the elemental analysis, MP-AES was used, as this is a very reliable technique requiring external standards for all elements tested. However, for a quicker, more qualitative analysis, EDX is a great tool to use. Therefore, we checked the samples before and after performance testing to see the impact on the Cl content. Cu(I)-ZSM-5 is shown as an example in Table S2, clearly showing how the Cl/Cu relationship was significantly reduced from before to after testing.

Table S2 Summary of elemental analysis measured with EDX on the Cu(I)-ZSM-5 sample.

Sample name	Si/Al	Cu/Al	Cl/Cu
Cu^I-ZSM-5	12.2	1.2	0.7
Cu^I-ZSM-5 tested	9.6	0.7	0.3

6. Repeated performance tests over 0.30Cu(I)-MOR

In order to see if the removal of Cl had an impact on the test results by revealing more Cu-sites available for methane activation, the 0.30Cu(I)-MOR sample were run for 3 cycles, heating

directly up in O₂ from 200 °C after the steam extraction. Fig. S5 shows the change in methanol yield (bar plot – left axis) and selectivity (line/symbol – right axis).

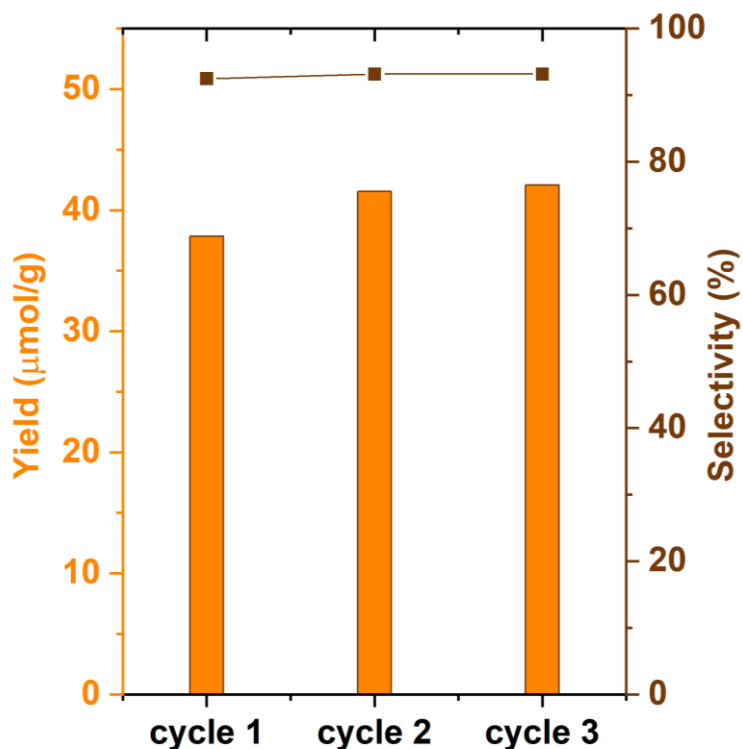


Fig. S5 Total yield of methanol produced over the 0.30Cu(I)-MOR sample for three consecutive cycles. The yellow bars represent the yield given as µmol of methanol per gram of zeolite (left axis). The selectivity in % (right axis) is displayed with brown squares.

Fig. S6 depicts the change in CH₃Cl production over the three cycles. The amounts have not been quantified, and the MS fragment for CH₃Cl ($m/z = 50$) is plotted for qualitative comparison.

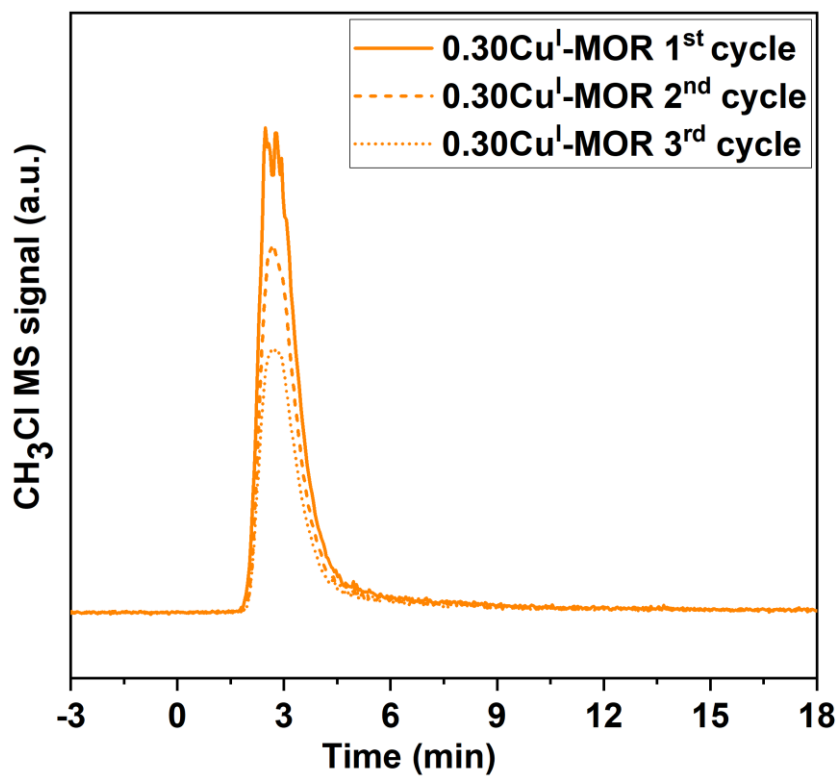


Fig. S6 The plot shows the change in MS signal output for CH₃Cl ($m/z = 50$) over the three cycles.

References

- [1] Pappas D K, et al. (2021) Influence of Cu-speciation in mordenite on direct methane to methanol conversion: Multi-Technique characterization and comparison with NH₃ selective catalytic reduction of NO_x. *Catal. Today* 369:105-111



Paper IV



Paper V



Cite this: DOI: 10.1039/d3cc00948c

 Received 27th February 2023,
Accepted 18th April 2023

DOI: 10.1039/d3cc00948c

rsc.li/chemcomm

Cu-loaded zeolites enable the selective activation of ethane to ethylene at low temperatures and pressure†

 Karoline Kvande,^a Sebastian Prodingler,^a Bjørn Gading Solemsli,^a Silvia Bordiga,^b Elisa Borfecchia,^b Unni Olsbye,^a Pablo Beato^c and Stian Svelle^{a*}

Cu-zeolites are found to activate the C–H bond of ethane already at 150 °C in a cyclic protocol and form ethylene with a high selectivity. Both the zeolite topology and Cu content are found to impact the ethylene yield. Ethylene adsorption studies with FT-IR, demonstrate that oligomerization of ethylene occurs over protonic zeolites, while this reaction does not occur over Cu-zeolites. We postulate that this observation is the origin of the high ethylene selectivity. Based on the experimental results, we propose that the reaction proceeds via the formation of an ethoxy intermediate.

The global demand for gas is expected to rise continuously over the coming years, and the situation is confounded by the recent unrest in Europe.¹ Furthermore, finding less energy-intensive pathways for the conversion of the components of natural gas remains a high-priority issue. Many direct reaction pathways for methane have been suggested. One of the more promising is a stepwise conversion route over oxygen-activated Cu-zeolites. These can oxidize methane and, with the assistance of water, produce methanol with a selectivity of around 90%.² The research on this approach has revealed that after oxygen activation, Cu-oxo moieties are formed as the active sites,³ and upon exposure to methane, a methoxy species forms at these active sites in the framework.⁴ Since the Cu-sites can activate methane, we found it important to investigate whether these sites also are capable of activating other hydrocarbons, like ethane, by applying the same reaction procedure. Today the industrially applied method for converting ethane is by steam cracking to ethylene at 800–900 °C, requiring large amounts of

energy.⁵ Non-oxidative (EDH) and oxidative (ODH) dehydrogenation of ethane are among the most studied pathways for direct ethane conversion.⁶ EDH typically requires high temperatures and low pressures to push the equilibrium toward product formation due to the endothermic nature of the reaction. However, high temperatures can lead to less controllable gas phase reactions between the reactants and products and therefore often lead to equilibrium constraints for EDH reactions. ODH however, is exothermic, and can therefore be operated at lower temperatures. The typical range is 300–700 °C, and a variety of supported metals, oxides, and mixed-metal catalysts have been investigated for the reaction.^{6b} The main drawback of ODH is that measures need to be taken to limit the product over-oxidation to CO₂ and to find safe operational modes due to the highly exothermic nature of the reaction.

Partial oxidation of ethane with H₂O₂ at 50 °C over Fe and Fe/Cu-loaded zeolites is another interesting pathway that has been suggested by Forde *et al.*⁷ The authors show that different reaction pathways occur, depending on the ion-exchanged metal. Cu promotes the formation of ethylene, while Fe promotes acetic acid. It is also interesting to note that the partial oxidation of ethane at low temperatures (~75 °C) has been shown to be possible over an iron-based MOF. The MOF can form Fe-oxo intermediates upon oxidation in N₂O, and these species can be used to activate ethane to form ethanol and acetaldehyde.⁸

Herein, we explore the conversion of ethane based on a stepwise conversion route, optimized for methane to methanol (MTM) conversion,⁹ over various Cu-loaded zeolites, namely, MOR, ZSM-5, and SSZ-13. All the samples have been well characterized with techniques like XRD, SEM, elemental analysis, and N₂-physisorption, in previous publications.^{9,10} The relevant elemental composition and the samples corresponding activity in the methane to methanol (MTM) conversion is reported in Table S1 in the ESI.† In this fundamental study, we report a new pathway for ethane conversion over Cu-zeolites, and we explore the structural and compositional requirements

^a Centre for Materials Science and Nanotechnology (SMN), Department of Chemistry, University of Oslo, 1033 Blindern, 0315, Oslo, Norway. E-mail: stian.svelle@kjemi.uio.no

^b Department of Chemistry, NIS Center and INSTM Reference Center, University of Turin, via P. Giuria 7, 10125 Turin, Italy

^c Topsoe A/S, Haldor Topsoes Alle 1, DK-2800 Kgs. Lyngby, Denmark

† Electronic supplementary information (ESI) available: Experimental methods, physicochemical data, experiment protocol as well as supporting test results and FT-IR spectra (PDF). See DOI: <https://doi.org/10.1039/d3cc00948c>



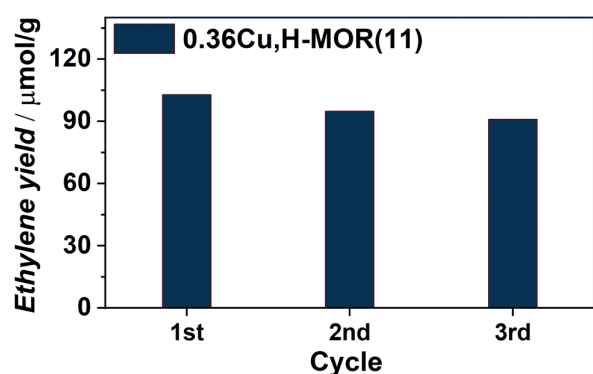


Fig. 1 Ethylene yield ($\mu\text{mol g}^{-1}$) obtained for three consecutive reaction cycles as defined in the ESI,[†] Scheme S1.

for an effective reaction. All experimental methods are reported in the ESI,[†] Section S1.

Already from our initial results, following the scheme reported in ESI,[†] Section S1.2, it was evident that a Cu-loaded MOR zeolite, 0.36Cu,H-MOR(11), where 0.36 is the Cu/Al ratio and 11 is the Si/Al ratio, was able to activate the C–H bond in ethane. The main product was ethylene, with $\sim 95\%$ hydrocarbon selectivity during the steam extraction step (ESI,[†] Fig. S1(a)) as determined with GC-FID. The only other products detected were butene and ethanol. Small traces of CO_2 were also observed qualitatively with the MS (ESI,[†] Fig. S1(b)). When following the productivity throughout three reaction cycles, the reactivity seems to be quasi-stable, with only a small decrease in ethylene yield for each cycle (Fig. 1).

Fig. 2 shows the yield of ethylene obtained over different material topologies and zeolite compositions. Several interesting features of the reaction can be observed. 0.36Cu,H-MOR(11) is used as reference material for the discussion. First, the reaction was performed over three test materials. A Cu-loaded silica (5 wt%Cu– SiO_2) containing CuO clusters, a Cu-loaded aluminosilicate with similar Al and Cu content as the reference

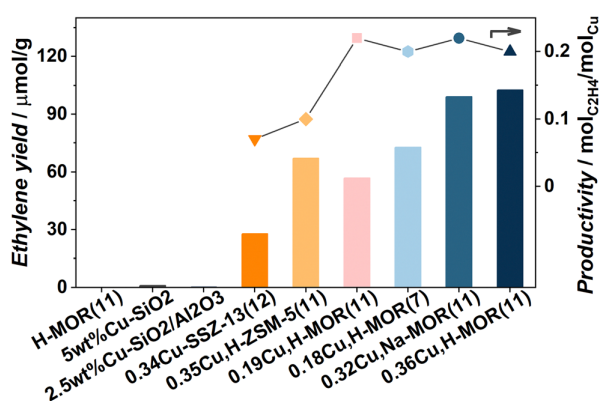


Fig. 2 (left axis) Bar plot comparing the ethylene yield ($\mu\text{mol g}^{-1}$) produced over different materials. The right axis shows the ethylene productivity ($\text{mol}_{\text{C}_2\text{H}_4} \text{mol}_{\text{Cu}}^{-1}$) for the Cu-zeolites. The line connecting the symbols is for visual guidance.

material that contains $[\text{AlO}_4]^-$ for Cu and H exchange, and an H-MOR zeolite (a porous zeolite framework with acid sites, but no Cu). They all yielded negligible amounts of ethylene and other products, confirming that both well-defined Cu sites and the zeolite framework with restricted exchange sites, are necessary to promote the activation of ethane. Further, a Na-based, Cu-exchanged MOR zeolite (0.32Cu,Na-MOR(11)) with similar Cu-content as the reference material, but less Brønsted sites (see the ESI,[†] Fig. S2), displayed a similar ethylene yield and product distribution (ESI,[†] Fig. S1). This implies that the Brønsted sites are not that crucial for ethylene production. This is in contrast to previous findings for the MTM reaction that show that the Brønsted sites play an important part in stabilizing methoxy intermediates for methanol production.^{4c,11} A Cu-loaded ZSM-5 with similar Cu/Al and Si/Al as our reference material produced significantly lower yield, and thus lower productivity ($0.10 \text{ mol}_{\text{C}_2\text{H}_4} \text{mol}_{\text{Cu}}^{-1}$). This was somewhat surprising, as ZSM-5 has been proposed in other ethane activation reactions, e.g. exchanged with Pt, Zn, Ga, or Fe.^{7,12} Nevertheless, the same trend between the zeolites has also been observed in the MTM reaction,¹³ highlighting the similarity of the two reactions. Also a Cu-loaded SSZ-13 was tested in the reaction and proved less productive than both MOR and ZSM-5 ($0.07 \text{ mol}_{\text{C}_2\text{H}_4} \text{mol}_{\text{Cu}}^{-1}$). This evidences a trend, where the productivity increases with increasing pore size: CHA (8r) < MFI (10r) < MOR (12r).

When employing a Cu-mordenite with both a lower Si/Al and Cu/Al ratio (0.18Cu,H-MOR(7)) that previously has been found to have a remarkably high yield in MTM reaction (ESI,[†] Table S1), unremarkable results are found when ethane is the reactant. This indicates that the Cu species in 0.18Cu,H-MOR(7) are more efficient at activating methane than ethane, which is surprising given the higher reactivity of ethane (the bond dissociation energies of the first C–H bond in CH_4 and C_2H_6 are 439 vs. 422 kJ mol^{-1} , respectively¹⁴). Based on this conspicuous difference, and the lack of a detrimental effect of Na, we conjecture that there might be some subtle differences in the site requirements for methane and ethane activation.

Upon comparing the reference to a sample based on the same zeolite but with lower Cu content (0.19Cu,H-MOR(11)) it is evident that 0.36Cu,H-MOR(11) has the highest yield. The normalized ethylene productivity of the Cu-loaded zeolites ($\text{mol}_{\text{C}_2\text{H}_4} \text{mol}_{\text{Cu}}^{-1}$) is plotted on the right axis of Fig. 2. The productivity is the same for all four MOR samples ($\sim 0.20 \text{ mol}_{\text{C}_2\text{H}_4} \text{mol}_{\text{Cu}}^{-1}$), suggesting that regardless of Si/Al ratio or Cu content, the number of active sites increases linearly with the amount of Cu present. In contrast, a volcano-type behavior is typically observed within the same range of Cu content for MTM with the productivity peaking at intermediate Cu-loadings.^{3a,15} This major difference between the two reactions again indicates different Cu site requirements for C–H activation in ethane vs. methane.

In an attempt to optimize the performance of the reaction, 0.36Cu,H-MOR(11) was exposed to different ethane loading times and temperatures (Fig. 3). First, the results revealed that a somewhat lengthy exposure time was necessary for ethane activation. However, the ethane activation observed herein is



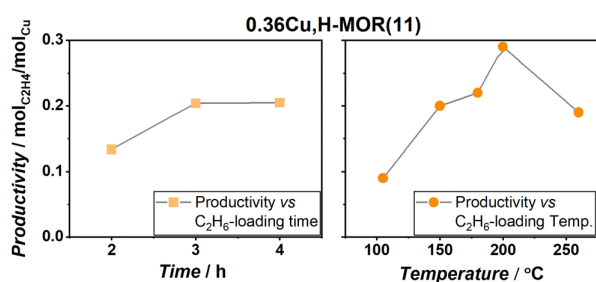


Fig. 3 Normalized ethylene productivity ($\text{mol}_{\text{C}_2\text{H}_4}/\text{mol}_{\text{Cu}}$) obtained during a systematic study of the reaction conditions. The change in productivity is reported vs. the exposure times (left column – squares) and the temperature (right column – circles). The water extraction step was always kept isothermal to the ethane exposure temperature. The grey lines are only present as a guide for the eye.

much faster than methane activation in the same protocol, as Pappas *et al.* deemed an exposure time of 6 h necessary to optimize the MTM reaction protocol over Cu-CHA.⁹ Secondly, upon comparing the ethane loading temperature, a peak productivity of $0.29 \text{ mol}_{\text{C}_2\text{H}_4} \text{ mol}_{\text{Cu}}^{-1}$ was found at 200 °C, before the reactivity started to decrease again at higher temperatures. This behavior is very similar to the MTM reaction.

To study the interaction of the ethylene product with the materials, 0.36Cu,H-MOR(11) and H-MOR were investigated with FT-IR spectroscopy upon incremental doses of ethylene. The full spectra, including a more detailed description, are reported in ESI† (Section S4, Fig. S3 and S4), while the $\nu(\text{C-H})$ region is shown in Fig. 4. Below 3000 cm^{-1} , several new bands evolve for H-MOR(11), but not for the Cu-containing sample. These bands are related to the formation of saturated CH_2 (2928 and 2857 cm^{-1}) and CH_3 (2960 and 2873 cm^{-1}) groups, indicating that ethylene starts to be polymerized in the H-MOR zeolite. This has also been shown to occur over other H-zeolites.¹⁶ Interestingly, this behavior is only observed in the pure, protonic zeolite, and not in the Cu-containing sample, even though 0.36Cu,H-MOR(11) still has a significant amount of Brønsted sites, as seen in the $\nu(\text{O-H})$ region of the spectrum before dosing ethylene (ESI,† Fig. S2).

To further support that the bands observed for the H-MOR sample indeed originate from oligomerized ethylene, the samples were cooled to 100 K and then outgassed for a longer period up to room temperature (RT). All bands related to oligomerized species that were formed during ethylene dosing remained in the FT-IR spectra after outgassing (ESI,† Fig. S5). We posit that the ability of the Cu-exchanged zeolites to suppress oligomerization might be the key to the high ethylene selectivity. When Cu-zeolites are used in the ETE reaction, the ethylene-derived intermediates are stabilized on the Cu-sites, thus preventing further oxidation or chain growth.

Based on the experimental data obtained, we have tried to identify possible reaction routes for ethylene formation from ethane over activated Cu-sites. The reaction pathways considered are displayed in Scheme 1. No in-depth depiction of the nature of the Cu sites is provided, as this would require

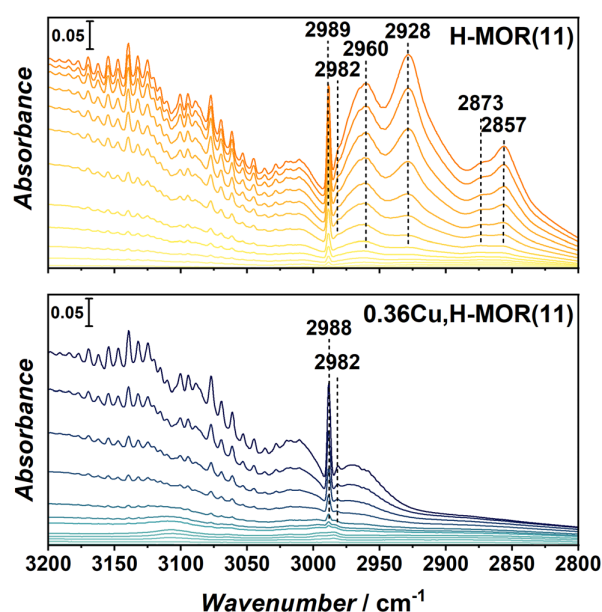
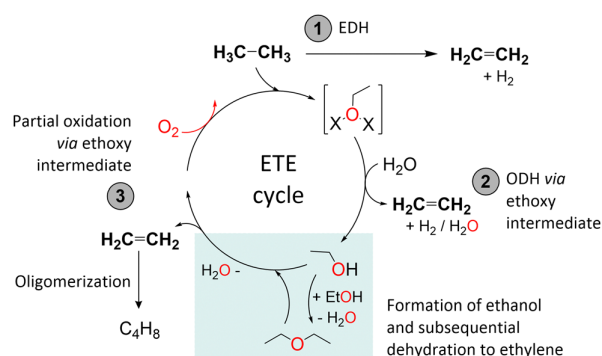


Fig. 4 FT-IR spectra of the $-\text{CH}$ stretch region obtained for adsorbed ethylene at RT on H-MOR(11) (top panel) and 0.36Cu,H-MOR(11) (bottom panel). The spectra are reported in difference with respect to the spectrum of the activated sample and are normalized to the framework overtones.

advanced characterization and a deeper understanding of the Cu speciation, especially after ethane activation, which goes beyond the scope of this study. There are in principle three pathways for ethylene formation, marked (1)–(3) in Scheme 1. Pathway (1) involves the direct dehydrogenation of ethane and the formation of molecular hydrogen in an endothermic reaction. However, as we have shown that oxidized Cu species are an important factor for ethylene production, and since also C_2 oxygenates are observed as (minor) byproducts, it is considerably more likely that the reaction proceeds *via* an ethoxy intermediate. Accordingly, two exothermic, oxidative reaction pathways, (2) and (3), are proposed. Analogous to methoxy formation in the MTM reaction, ethane could react with some



Scheme 1 Possible routes derived from the experimental data obtained herein for the ETE reaction. EDH and ODH stand for non-oxidative and oxidative dehydrogenation of ethane, respectively. The colored box highlights the dehydration processes.



type of Cu_xO_y -moieties leading to ethoxy formation. Pathway (2) is a direct oxidative dehydrogenation of ethane *via* ethoxy intermediate species. Water facilitates the desorption of ethylene, and H_2O (or possibly H_2 if the Cu is re-oxidized in this step) is formed as the byproduct. Pathway (3) involves C_2 oxygenates (ethanol and possibly diethyl ether (DEE) from dehydration) as free intermediates. Initially formed ethoxy species are detached from the active site upon contact with water. Then, a dehydration process occurs, either instantaneously at the acid sites or some point down the bed, and ethylene is the main product detected in the effluent. To confirm the likelihood of dehydration, we exposed 0.36Cu, H-MOR(11), H-MOR(11), and 0.32Cu,NaMOR(11) directly to ethanol after activation in oxygen, which indeed led to a significant formation of ethylene over all three materials.

Pathway (3) is supported by the observation of trace amounts of ethanol in the effluent. We consider it unlikely that ethanol is formed from acid-catalyzed hydration of ethylene in pathway (2) as the product distribution is the same over both Na-based and H-based Cu-MOR and thus unaffected by the density of Brønsted acid sites (ESI,† Fig. S1). Additionally, since an oxidative dehydrogenation to ethylene, as suggested by pathway (2), should be feasible without the addition of H_2O , it is more conceivable that the reaction is proceeding *via* ethanol formation (pathway (3)). Consequently, the main experimental observations favor reaction pathway (3), and we surmise that the reported ethane activation protocol results in the formation of ethoxy intermediates. We note that this might lay the foundation for a search for a process to form ethanol directly from ethane, by looking for the right reaction conditions and metal-zeolite.

The results reported herein expand the scope of Cu-zeolites in the activation of C–H bonds of lower alkanes. We report, for the first time, a low-temperature, ambient pressure, and highly selective pathway to form ethylene from ethane. The reaction is clearly akin to the well-investigated, stepwise MTM reaction, with about the same temperature needed for C–H activation, but there are also marked differences between these two reactions. Screening of a number of Cu-loaded zeolites indicate that the active site requirements are different for the two substrates. Our work is reconcilable with the formation of an ethoxy intermediate, which might present the opportunity for the selective formation also of ethanol by tuning reaction parameters. As a topic for further studies, we highlight a more detailed investigation that might enable the establishment of a steady-state process, similar to what has been recently described for methane, albeit at very low conversions. This could be an important contribution to the direct C–H activation research.

This publication forms a part of the iCSI (industrial Catalysis Science and Innovation) Centre for Research-based Innovation, which receives financial support from the Research Council of Norway under contract no. 237922. M. Signorile is

acknowledged for insightful discussions and G. Deplano for synthesizing the Cu,H-ZSM-5 sample. TOC is created with Biorender.com.

Conflicts of interest

There are no conflicts to declare.

References

- Gas Market Report, Q3-2022*, IEA, Paris <https://www.iea.org/reports/gas-market-report-q3-2022>, accessed: 06.10.2022.
- M. A. Newton, A. J. Knorpp, V. L. Sushkevich, D. Palagin and J. A. van Bokhoven, *Chem. Soc. Rev.*, 2020, **49**, 1449–1486.
- (a) D. K. Pappas, A. Martini, M. Dyballa, K. Kvande, S. Teketel, K. A. Lomachenko, R. Baran, P. Glatzel, B. Arstad, G. Berlier, C. Lamberti, S. Bordiga, U. Olsbye, S. Svelle, P. Beato and E. Borfecchia, *J. Am. Chem. Soc.*, 2018, **140**, 15270–15278; (b) S. Grundner, M. A. Markovits, G. Li, M. Tromp, E. A. Pidko, E. J. Hensen, A. Jentys, M. Sanchez-Sanchez and J. A. Lercher, *Nat. Commun.*, 2015, **6**, 7546–7554; (c) M. H. Groothaert, P. J. Smeets, B. F. Sels, P. A. Jacobs and R. A. Schoonheydt, *J. Am. Chem. Soc.*, 2005, **127**, 1394–1395.
- (a) E. M. C. Alayon, M. Nachtegaal, A. Bodi and J. A. van Bokhoven, *ACS Catal.*, 2014, **4**, 16–22; (b) K. Narsimhan, V. K. Michaelis, G. Mathies, W. R. Gunther, R. G. Griffin and Y. Roman-Leshkov, *J. Am. Chem. Soc.*, 2015, **137**, 1825–1832; (c) M. Dyballa, K. Thorshaug, D. K. Pappas, E. Borfecchia, K. Kvande, S. Bordiga, G. Berlier, A. Lazzarini, U. Olsbye, P. Beato, S. Svelle and B. Arstad, *ChemCatChem*, 2019, **11**, 5022–5026.
- T. Ren, M. Patel and K. Blok, *Energy*, 2006, **31**, 425–451.
- (a) H. Saito and Y. Sekine, *RSC Adv.*, 2020, **10**, 21427–21453; (b) Y. Gao, L. Neal, D. Ding, W. Wu, C. Baroi, A. M. Gaffney and F. Li, *ACS Catal.*, 2019, **9**, 8592–8621; (c) X. Liu, T. Liang, R. Barbosa, G. Chen, H. Toghiani and Y. Xiang, *ACS Omega*, 2020, **5**, 1669–1678.
- M. M. Forde, R. D. Armstrong, C. Hammond, Q. He, R. L. Jenkins, S. A. Kondrat, N. Dimitratos, J. A. Lopez-Sanchez, S. H. Taylor, D. Willock, C. J. Kiely and G. J. Hutchings, *J. Am. Chem. Soc.*, 2013, **135**, 11087–11099.
- D. J. Xiao, E. D. Bloch, J. A. Mason, W. L. Queen, M. R. Hudson, N. Planas, J. Borycz, A. L. Dzubak, P. Verma, K. Lee, F. Bonino, V. Crocellà, J. Yano, S. Bordiga, D. G. Truhlar, L. Gagliardi, C. M. Brown and J. R. Long, *Nat. Chem.*, 2014, **6**, 590–595.
- D. K. Pappas, E. Borfecchia, M. Dyballa, I. A. Pankin, K. A. Lomachenko, A. Martini, M. Signorile, S. Teketel, B. Arstad, G. Berlier, C. Lamberti, S. Bordiga, U. Olsbye, K. P. Lillerud, S. Svelle and P. Beato, *J. Am. Chem. Soc.*, 2017, **139**, 14961–14975.
- (a) M. Dyballa, D. K. Pappas, K. Kvande, E. Borfecchia, B. Arstad, P. Beato, U. Olsbye and S. Svelle, *ACS Catal.*, 2019, **9**, 365–375; (b) G. Deplano, M. Signorile, V. Crocellà, N. G. Porcaro, C. Atzori, B. G. Solemsli, S. Svelle and S. Bordiga, *ACS Appl. Mater. Interfaces*, 2022, **14**, 21059–21068.
- V. L. Sushkevich, J. A. Van Bokhoven and R. Verel, *Angew. Chem., Int. Ed.*, 2020, **59**, 910–918.
- (a) K.-H. Steinberg, U. Mroczek and F. Roessner, *Appl. Catal.*, 1990, **66**, 37–44; (b) J. A. Biscardi and E. Iglesia, *J. Catal.*, 1999, **182**, 117–128; (c) V. B. Kazansky, I. R. Subbotina, N. Rane, R. A. van Santen and E. J. M. Hensen, *Phys. Chem. Chem. Phys.*, 2005, **7**, 3088–3092.
- M. B. Park, S. H. Ahn, A. Mansouri, M. Ranocchiari and J. A. van Bokhoven, *ChemCatChem*, 2017, **9**, 3705–3713.
- B. Ruscic, *J. Phys. Chem. A*, 2015, **119**, 7810–7837.
- S. Proding, K. Kvande, B. Arstad, E. Borfecchia, P. Beato and S. Svelle, *ACS Catal.*, 2022, **12**, 2166–2177.
- G. Spoto, S. Bordiga, G. Ricchiardi, D. Scarano, A. Zecchina and E. Borello, *J. Chem. Soc., Faraday Trans.*, 1994, **90**, 2827–2835.



ELECTRONIC SUPPLEMENTARY INFORMATION

Cu-loaded zeolites enable the selective activation of ethane to ethylene at low temperature and pressure

Karoline Kvande,^a Sebastian Prodinge,^a Bjørn Gading Solemsli,^a Silvia Bordiga,^b Elisa Borfecchia,^b Unni Olsbye,^a Pablo Beato,^c and Stian Svelle.^{a,*}

^a Center for Materials Science and Nanotechnology (SMN), Department of Chemistry, University of Oslo, 1033 Blindern, 0315, Oslo, Norway.

^b Department of Chemistry, NIS Center and INSTM Reference Center, University of Turin, via P. Giuria 7, 10125 Turin, Italy

^c Topsoe A/S, Haldor Topsøes Allé 1, DK-2800 Kgs. Lyngby, Denmark

*Correspondence:

stian.svelle@kjemi.uio.no (S.S.)

Innholdsfortegnelse

1.	Experimental section	1
1.1.	Material preparation and characterization	1
1.2.	Ethane activation measurements	2
1.3.	Fourier Transform Infrared (FT-IR) spectroscopy	3
2.	Material summary	3
3.	Product selectivity derived from GC-FID	4
4.	FT-IR spectroscopy	4
5.	References	7

1. Experimental section

1.1. Material preparation and characterization

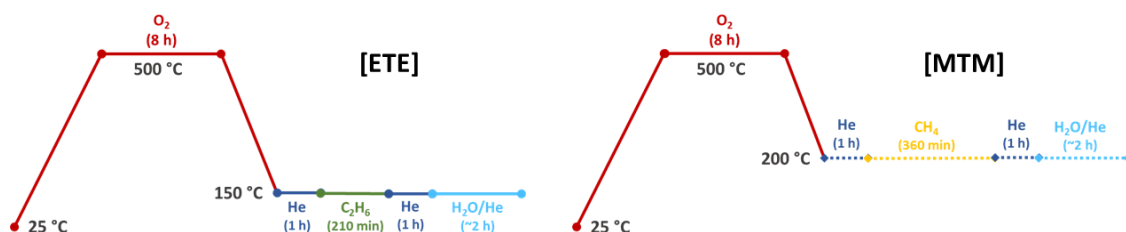
Cu-zeolites with different composition and cations have been investigated for the reaction. The nomenclature of the zeolite samples is $y\text{Cu}_x\text{-ZEOLITE}(z)$, where y is the Cu/Al ratio of the sample, x is the cation present, either H or Na, and z is the Si/Al ratio of the zeolite. The zeolites used herein is either mordenite (MOR), CHA (SSZ-13) or an MFI type framework (ZSM-5). The MOR samples were made from commercially available material from Zeolyst, namely CBV21A (Si/Al = 11) and CBV10Ads (Si/Al = 7). The ZSM-5 sample used for this

study came also from Zeolyst, CBV 2314 (Si/Al = 11.5), while SSZ-13 was prepared in a procedure described elsewhere [1]. In addition to Cu-zeolites, also an H-form of CBV21A (H-MOR(11)) and Cu exchanged SiO₂ (ecoChrom MP Silica 100-200, 60 Å) and SiO₂/Al₂O₃ (Sigma Aldrich, grade 135, Al = 6.5 %) were tested in the reaction. The Cu-source for SiO₂ and SiO₂/Al₂O₃ was Cu(NO₃)₂×3H₂O (Sigma Aldrich). A 5wt%-CuSiO₂ and 2.5wt% Cu-SiO₂/Al₂O₃ sample was prepared following the procedure reported by Prodingler et al. [2], and the Cu wt.% of the samples is determined based on the intended ratio between Cu and SiO₂ or aluminium, respectively, before exchange.

Basic characterization of the MOR zeolites have been performed previously and was reported by Dyballa et al. [3] Characterization of 0.34Cu-SSZ-13 is reported by Pappas et al. [4], and characterization of the ZSM-5 sample is reported in a publication by Deplano et al. [5].

1.2. Ethane activation measurements

The testing was performed with a customized set-up previously used for the MTM conversion [4, 6-8]. 100 mg sample (~85 mg of dry weight, sieve fraction: 425 – 250 μm) was placed inside a straight quartz tube reactor (i.d. = 6 mm). The temperature of the oven was calibrated prior to the measurements using a thermocouple inside a quartz sheet on top of the reactor bed. The flow of gases was controlled using four different MFCs and fed separately onto the sample with the help of stop- and 4-way valves. The activity of the materials towards ethane activation was tested with a very similar protocol to the optimized stepwise conversion route for MTM [4]. For the standard protocol, the only difference to what has been reported previously was a lower temperature for C_xH_y loading and subsequent water extraction from 200 to 150 °C. A shorter C₂H₆ loading time (210 min instead of 360 min) was also utilized, similar to our latest work within the MTM reaction [7, 9]. Scheme S1 represents the optimized protocol for the MTM process reported for CHA by Pappas et al [4], and the ethane activation protocol (ETE) applied herein. The reaction protocol involves three main steps. First, the sample is activated in O₂ (100 %) 500 °C for 8 h. Then the reaction temperature is lowered to 150 °C (5 °C/min) and flushed with He for 1 h, before C₂H₆ (5 %/rest. He) was introduced for 210 min. A second flushing step was performed in He, before a water-saturated 10 % Ne/He stream was introduced isothermally. The saturator was heated to 45 °C to obtain ~ 10 % water in the feed. All flows were kept to 15 ml/min. The effluent was monitored with an online quadrupole mass spectrometer (Omnistar GSD320, Pfeiffer). For quantitative analysis of the main product, a microgas chromatograph (μGC 3000A, Agilent) equipped with a Plot U column with an FID detector and He as the carrier gas, was employed.



Scheme S1. Reaction protocol for the ETE protocol applied herein and the previously applied MTM process on the materials.

1.3. Fourier Transform Infrared (FT-IR) spectroscopy

FT-IR spectroscopy was performed on a Bruker Vertex 70 instrument with a Mercury-Cadmium-Telluride (MCT) detector. The interaction of ethylene adsorption on the 0.36CuMOR11 and H-MOR11 samples at RT was investigated. Each sample was pressed with 2-3 tons into self-supporting wafers (11.3 mg/cm²) and fitted inside gold envelopes. The envelopes were placed in a low temperature vacuum cell with KBr windows and heated under vacuum at 450 °C for 1.5 h (ramp rate = 5 °C/min) for pretreatment. After cooling to RT, individual spectra were collected while small amounts of ethylene were dosed onto the sample, until reaching an equilibrium pressure of 17 mbar. After dosing, the sample was also cooled with LN₂, before it was slowly outgassed and consecutively heated back to RT. FT-IR spectra were collected during all parts of the experiment.

2. Material summary

For the purpose of this study, a library of well-studied Cu-zeolites in the MTM reaction were chosen in order to be able to directly compare the effect of the reaction protocols. Table S1 summarizes the characteristics of all samples.

Table S1. Chemical composition and MTM performance of the materials used herein.

Sample name	Si/Al	Cu/Al	Cu wt. %	MTM Productivity (mol _{MeOH} /mol _{Cu})	MTM Yield (μmol _{MeOH} /g _{zeolite})
H-MOR(11) ¹⁾	11	-	-	-	-
0.19Cu,H-MOR(11) ¹⁾	11	0.19	1.67	0.24	64
0.36Cu,H-MOR(11) ¹⁾	11	0.36	3.18	0.25	123
0.32Cu,Na-MOR(11) ¹⁾	11	0.32	2.83	0.17	74
0.18Cu,H-MOR(7) ¹⁾	7	0.18	2.33	0.47	172
0.35Cu,H-ZSM-5(11) ²⁾	11.5	0.35	2.88	0.10	43
0.30Cu,H-SSZ-13(12) ¹⁾	12.1	0.34	2.68	0.16	67
2.5wt%-Cu/SiO₂/Al₂O₃	14.6	0.38	2.5	-	-
5wt%-CuSiO₂	-	-	5	-	-

- 1) Elemental composition, such as Si/Al, Cu/Al and Cu wt.%, along with the MTM productivity and yield of the Cu-exchanged MOR zeolites and the 0.30Cu,H-SSZ-13(1) sample have been determined by Svelle and co-workers in previous publications [3, 4, 6]. The protocol for MTM is reported in Scheme S1.
- 2) The MTM activity of 0.35Cu,H-ZSM-5(11) was measured herein with the instrumentation and protocol reported in our previous study by Prodinger et al. [9]. Elemental composition, such as Si/Al, Cu/Al and Cu wt.% was previously reported by Deplano et al. [5].

3. Product selectivity derived from GC-FID

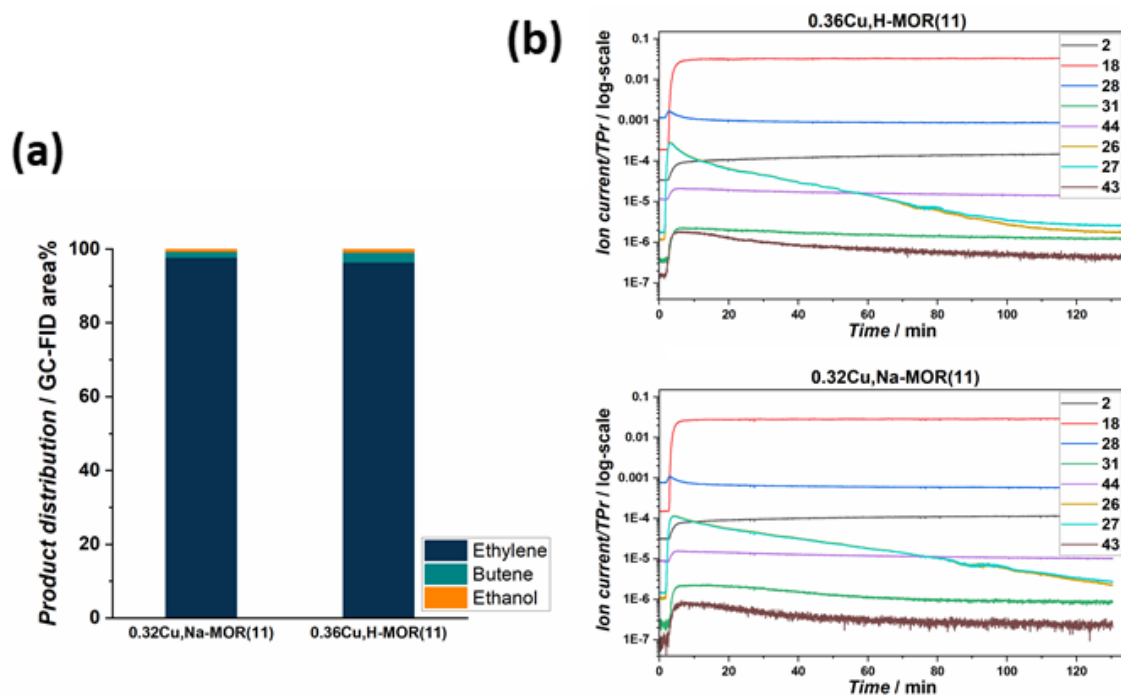


Figure S1. Bar plot (a) comparing the product distribution during the ETE protocol reported in Scheme 1 in the main text as observed by GC-FID for 0.32Cu,Na-MOR(11) and 0.36Cu,H-MOR(11). A selection of mass fragments (b) collected during the water extraction step, as observed by an online MS is reported. The y-axis represents ion current divided by the total pressure of the mass spectrometer in log-scale, and the time in minutes (min) is reported on the x-axis from right after water was introduced to the reactor.

4. FT-IR spectroscopy

To see the remaining Brønsted acid sites in 0.32Cu,Na-MOR(11) compared to 0.36Cu,H-MOR(11), and the pure H-MOR zeolite, the FT-IR spectra of vacuum activated (450 °C) samples were compared. Figure S2 shows the normalized $\nu(\text{O-H})$ stretch region, and the band at 3610 cm^{-1} is linked with the $\nu(\text{O-H})$ stretch of Brønsted acid sites (Si-(O-H)-Al).

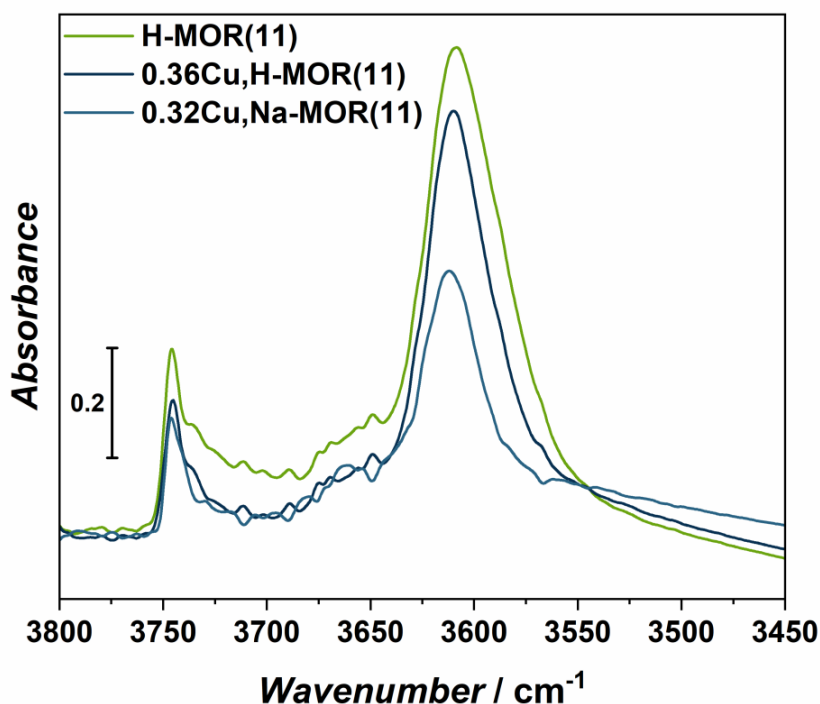


Figure S2. FT-IR spectra of the $\nu(\text{O-H})$ stretch region of 0.32Cu,Na-MOR(11), 0.36Cu,H-MOR(11), and H-MOR(11).

In both 0,36Cu,H-MOR(11) and H-MOR, the features related to gaseous ethylene appear quite fast, as observed from the strong symmetric stretching band of CH_2 at 2989 cm^{-1} . However, the band appearing at 2982 cm^{-1} is likely a downward shift of the same functional group, confirming that the C_2H_4 gas is also perturbed by the framework by forming a $\text{C}_2\text{H}_4\text{-OH}$ π -complex [10]. This is also evident by the shift to lower frequency for the Brønsted $\nu(\text{O-H})$ stretching bands (

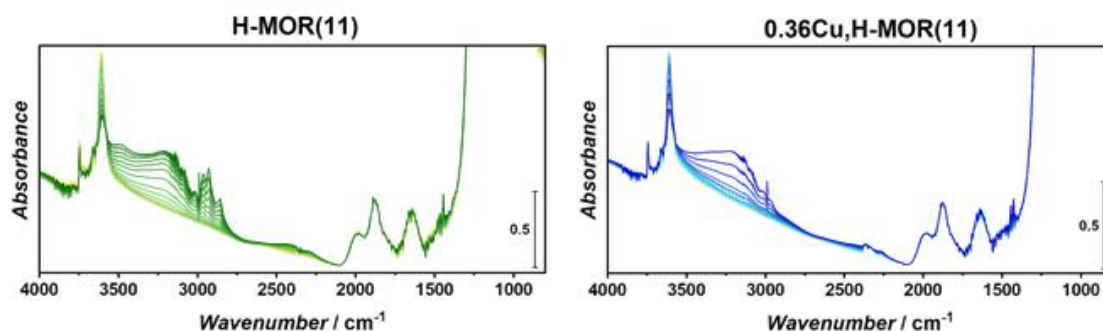


Figure S3) and the band appearing at 1340 cm^{-1} , which is a bending mode of CH_2 that is IR-inactive in the free molecule (Figure S4). For the ethylene molecule, a second, IR-active, bending mode for CH_2 should also be present in the IR spectra. The bands at 1444 and 1428 cm^{-1} , as observed in Figure S4, can be attributed to this bend in the free molecule as well as perturbed by Cu^+ , respectively. Due to spectral noise, it is not possible to separate out any downward shift of the band at 1444 cm^{-1} related to the adsorption on the framework.

Upon scrutinizing the spectra in Figure S4, only small indications of the IR inactive $\nu(\text{C}=\text{C})$ stretch vibration on Brønsted sites ($\sim 1612 \text{ cm}^{-1}$) are observed [10, 11]. However, as this is almost indistinguishable from the background, the FT-IR spectra obtained under the conditions reported here can unfortunately not be used to search for the ethylene molecules preferential siting (H- or Cu-) inside the Cu-zeolite framework.

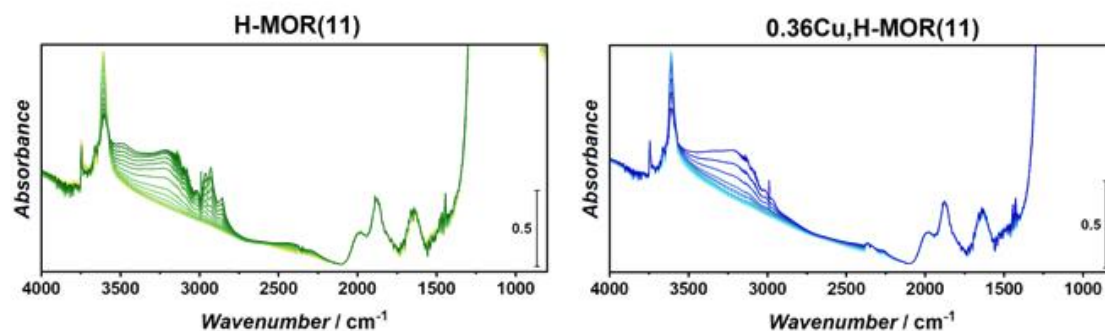


Figure S3. FT-IR spectra of the full region obtained for adsorbed ethylene at RT on H-MOR(11) (left panel) and 0.36Cu,H-MOR(11) (right panel). Each spectrum is obtained after sending incremental doses of ethylene onto the sample from about 50 μbar to 17 mbar of equilibrium pressure. Before dosing, the samples were pretreated under vacuum at 450 $^{\circ}\text{C}$ for 1.5 h (ramp rate = 5 $^{\circ}\text{C}/\text{min}$). The spectra are normalized to the framework overtone.

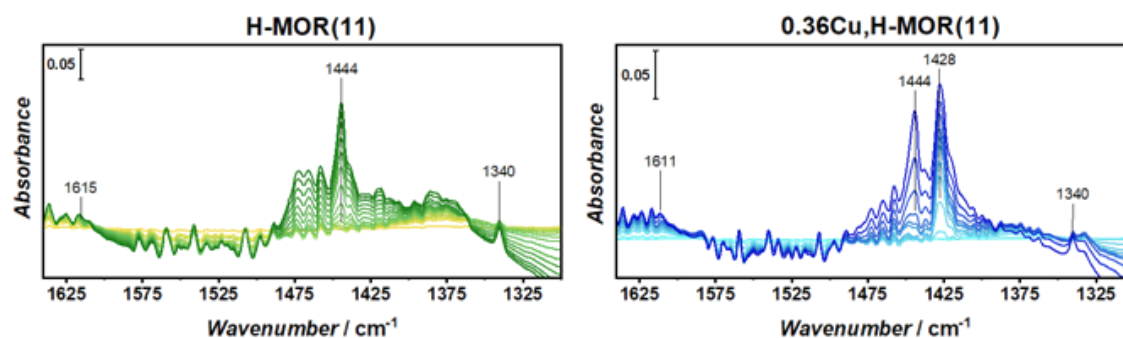


Figure S4. FT-IR spectra of the C=C stretch and -CH bend region obtained for adsorbed ethylene at RT on H-MOR(11) (left panel) and 0.36Cu,H-MOR(11) (right panel). Each spectrum is obtained after sending incremental doses of ethylene onto the sample from about 50 μbar to 17 mbar of equilibrium pressure. Before dosing, the samples were pretreated under vacuum at 450 $^{\circ}\text{C}$ for 1.5 h (ramp rate = 5 $^{\circ}\text{C}/\text{min}$). The spectra are normalized to the framework overtone and background subtracted. All additional bands (noise) are due to atmospheric moisture affecting spectra.

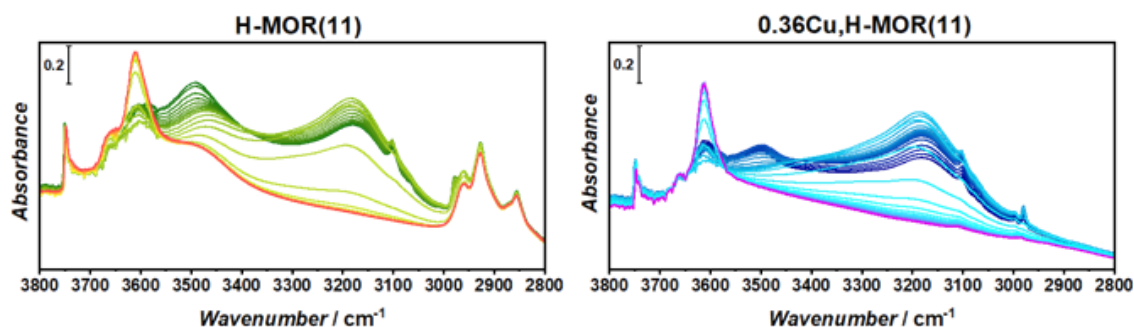


Figure S5. FT-IR spectra of the -OH and -CH stretch region showing the desorption of ethylene over time from 100 K to RT. The spectra show which bands are disappearing, and which are remaining upon outgassing and heating to RT. For H-MOR(11) (left panel), dark green spectrum represents the bands present at 100 K, while the orange spectrum represents completely outgassed at RT. For 0.36Cu,H-MOR(11) (right panel), dark blue spectrum represents the bands present at 100 K, while the pink spectrum represents completely outgassed at RT. Before outgassing, the ethylene dosed samples were cooled to 100 K (with LN₂).

5. References

- [1] T. V. W. Janssens, H. Falsig, L. F. Lundegaard, P. N. R. Vennestrøm, S. B. Rasmussen, P. G. Moses, F. Giordanino, E. Borfecchia, K. A. Lomachenko, C. Lamberti, S. Bordiga, A. Godiksen, S. Mossin and P. Beato, *ACS Catal.* **2015**, 5, 2832-2845.
- [2] S. Prodingler, M. F. K. Verstreken and R. F. Lobo, *ACS Sustainable Chem. Eng.* **2020**, 8, 11930-11939.
- [3] M. Dyballa, D. K. Pappas, K. Kvande, E. Borfecchia, B. Arstad, P. Beato, U. Olsbye and S. Svelle, *ACS Catal.* **2019**, 9, 365-375.
- [4] D. K. Pappas, E. Borfecchia, M. Dyballa, I. A. Pankin, K. A. Lomachenko, A. Martini, M. Signorile, S. Teketel, B. Arstad, G. Berlier, C. Lamberti, S. Bordiga, U. Olsbye, K. P. Lillerud, S. Svelle and P. Beato, *J. Am. Chem. Soc.* **2017**, 139, 14961-14975.
- [5] G. Deplano, M. Signorile, V. Crocellà, N. G. Porcaro, C. Atzori, B. G. Solemsli, S. Svelle and S. Bordiga, *ACS Appl. Mater. Interfaces* **2022**, 14, 21059-21068.
- [6] D. K. Pappas, A. Martini, M. Dyballa, K. Kvande, S. Teketel, K. A. Lomachenko, R. Baran, P. Glatzel, B. Arstad, G. Berlier, C. Lamberti, S. Bordiga, U. Olsbye, S. Svelle, P. Beato and E. Borfecchia, *J. Am. Chem. Soc.* **2018**, 140, 15270-15278.
- [7] K. Kvande, D. K. Pappas, M. Dyballa, C. Buono, M. Signorile, E. Borfecchia, K. A. Lomachenko, B. Arstad, S. Bordiga, G. Berlier, U. Olsbye, P. Beato and S. Svelle, *Catalysts* **2020**, 10, 191.
- [8] D. K. Pappas, E. Borfecchia, M. Dyballa, K. A. Lomachenko, A. Martini, G. Berlier, B. Arstad, C. Lamberti, S. Bordiga, U. Olsbye, S. Svelle and P. Beato, *ChemCatChem* **2019**, 11, 621-627.
- [9] S. Prodingler, K. Kvande, B. Arstad, E. Borfecchia, P. Beato and S. Svelle, *ACS Catal.* **2022**, 12, 2166-2177.
- [10] G. Spoto, S. Bordiga, G. Ricchiardi, D. Scarano, A. Zecchina and E. Borello, *J. Chem. Soc. Faraday trans.* **1994**, 90, 2827-2835.
- [11] J. Datka and E. Kukulska-Zajac, *J. Phys. Chem. B* **2004**, 108, 17760-17766.

